ELASTOMER-BASED MICROCABLE ELECTRODES FOR ELECTROPHYSIOLOGICAL APPLICATIONS

A Dissertation
Presented to
The Academic Faculty

by

Maxine Alice McClain

In Partial Fulfillment
of the Requirements for the Degree
of Doctor of Philosophy in the
School of Electrical and Computer Engineering

Georgia Institute of Technology
May 2010

ELASTOMER-BASED MICROCABLE ELECTRODES FOR ELECTROPHYSIOLOGICAL APPLICATIONS

Approved by:

Dr. Mark Allen, Advisor
School of Electrical and Computer Engineering
Georgia Institute of Technology

Dr. Robert Butera
School of Electrical and Computer Engineering
Georgia Institute of Technology

Dr. Michelle LaPlaca, Co-Advisor
School of Biomedical Engineering
Georgia Institute of Technology

Dr. Stephen DeWeerth
School of Electrical and Computer Engineering
Georgia Institute of Technology

Dr. Pamela Bhatti
School of Electrical and Computer Enginering
Georgia Institute of Technology

Dr. Kenneth Gall
School of Materials Science and Engineering
Georgia Institute of Technology

Date Approved: 3/17/2010

ACKNOWLEDGEMENTS

I would like to thank my advisors, Mark Allen and Michelle LaPlaca for their mentoring during my PhD. I am grateful for their guidance. As a student in their groups, I also greatly admire their integrity and commitment research. They are both enthusiastic, supportive, and work to produce students who have a well-developed view of the critical problems in their field. My committee has also been very constructive and I'm grateful for the attention they have given to this project. They have seen many iterations of my experimental plans and have been helpful at every round.

The work in this thesis could not have happened without the generosity in both time and knowledge of several collaborators and research staff at Georgia Tech. Richard Shafer worked with me to develop the electromechanical testing set-up and the laser machined stencils. Dr. Laura O'Farrell and her staff at the PRL were conscientious and always available for surgeries and all the unexpected eventualities. Charlie Suh and the rest of the cleanroom staff have been tireless and amazing. Hanno Leisen was a great help with the MRI imaging. I would like to also thank my peers, particularly Sarah Stabenfeldt, Jim Ross, Isaac Clements, and Zhan (Jen) Liu who have all lent their expertise to my project. Sarah helped with the fibrin characterization and was an all-around resource for the wet side of this project. Jim helped me use and interpret the data from his house-built electrode impedance monitoring system. Isaac also helped with electrical characterization by testing my electrodes in a peripheral nerve recording protocol. Jen helped interpret the tensile behavior of the elastomer samples. With their help, I avoided months of misunderstood data and trial-and-error experimentation. The LaPlaca group, especially Chris Lessing, JT Shoemaker, and Brock Wester taught me surgical techniques. JT has been a great help in troubleshooting and planning the histology. Brock's artistic intuition and command of Adobe Illustrator were relied on for many of the schematics and figures in this thesis. The MSMA group was a wealth of knowledge, both in and out of the cleanroom. I enjoyed (and miss) the 7:30 am group meetings at Starbucks, with Dr. Allen, Seong-Hyok, Swami, Florian and Jen, where I received much helpful insight, whether it was experimental design or data analysis.

My dear parents will be happy when this is over. My siblings have been an unflinchingly loyal pack, as always. The team at Axion has been continuously upbeat and has helped motivate me to finish and join them on the other side, where all the offices have windows, and the Earl Grey is never acrid. My friends, a number of whom have become like family, have been optimistic and encouraging and were always available for commiseration. Days of failed experiments were redeemed by Friday afternoons at ABC, bike rides, races, swim-practice, and all forms of yoga, from hokey to just plain hard. I hope I always have these people in my life.

TABLE OF CONTENTS

LIST OF TABLES

LIST OF FIGURES

SUMMARY

The goal of this thesis work was to make a compliant microcable electrode that could fit into spatially constrained spaces, including deployment into the cortical layers of the cortex. Previous studies have indicated that reducing the bending stiffness of an implanted cortical electrode also reduces the injury and inflammatory response at the implant site. The electrode was designed in a microcable geometry that can be used either individually or in an array, as a shank-style electrode or as a string-like electrode that can be threaded around features such as the peripheral nerve.

The fabrication process, using spin cast μmolding (SCμM), is simple and adaptable to different patterns. We have successfully demonstrated the fabrication of both sinusoidal and straight microcables. SCμM patterning was also used on the substrate that framed the microcables, as an open, net-like sheet, as well as the patterning of the recording sites on the microcable electrodes. The creation of these different features, and their implementation in microelectrode fabrication demonstrates the versatility of a simple process technique. The microcables were fabricated using polydimethyl siloxane (PDMS) and the conductive element for the electrodes was thin-film gold.

The microcable electrode recording sites were electrically characterized using frequency-based impedance modeling and the impedance parameters were compared and shown to agree with the estimated values and trends from a circuit-based model. The microcables were also threaded around a peripheral nerve and used to record elicited action potentials to demonstrate functionality as compliant electrodes.

The thin metal film and the low tensile modulus of the PDMS substrate created an electrode with a composite tensile modulus lower than other compliant electrodes described in the literature. The gold film increased the composite modulus approximately three-fold compared to the unaltered PDMS. The durability of the electrodes and tolerance for stretch was also tested. The microcables were found to be conductive up to 6% strain and to regain conductivity after release from multiple applications of 200% strain. As the number of 200% strain applications increased (1,000-5,000), the electrodes lost conductivity at lower strains (1-2%). The tolerance for high-strain shows that the electrodes can be deployed for use and stretched or pulled into place as needed without damaging the conductivity.

The microcable electrodes were also tested for a suitable insertion mechanism for use as shank-style cortical electrodes. The microcables were coated on one side with fibrin, which when dry, stiffens the microcables for insertion into the cortex. A 28-day implant study comparing fibrin coated PDMS microcable electrodes showed a positive, but relatively low inflammatory response, as measured by glial fibrillary astrocytic protein (GFAP; indicating activated astrocytes) immediately at the tissue edge of the implant site. The response of the control, silicon shank-style electrodes, was varied, but also trended toward low levels of GFAP expression. The GFAP staining was possibly due to the clearance of the fibrin from the implant site or low-grade gliosis. Implant studies extending beyond 28 days are necessary to determine whether and to what degree the inflammation persists at the PDMS microcable implant site.

CHAPTER 1

INTRODUCTION

1.1 Introduction

The goal of this thesis is to create electrical-tissue interfaces that bear more similarity to biological tissue than to a circuit board. Specifically, the aims center on the development and testing of durable, low-profile, low Young's modulus electrodes that can meet the varied needs of electrophysiological interfaces. Examples of potential applications include wrapping an electrode around a peripheral nerve or over an irregularly shaped organ or tissue mass such as the heart, integrating an electrode array into a spliced peripheral nerve for prosthetic applications, or inserting an electrode into the brain without inducing an encapsulating response from the tissue. The electrical components described here are a step to that end, but they are also relevant to other applications. External prosthetics do not have the rigorous requirements of implants, but still stand to benefit from "soft" and low profile electrical components. The electrode arrays developed here are flexible microcables that mechanically resemble strands of cooked pasta. The microcables can be arranged so that they are free on one end, arranged like a row of shank electrodes. The microcables can also be joined at either end, to create a net-like structure. The utility of a net-like profile is minimizing the confinement of the tissue onto which the array is placed. This could be advantageous in artificial prosthetic skins, for example, where a net-like set of electrodes is more breathable than a continuous sheet. The capacity for micropatterning the electrode shape or incorporating topographical features is also relevant for novel cell culture and tissue engineering applications. The work described here progresses as follows:

1) the development of a fabrication process for elastomer-based shank and net-like arrays of electrodes
2) impedance characterization and electrophysiological testing of the electrode
3) electro-mechanical fatigue testing of microcable arrays
4) implant testing to assess the tissue response to low-modulus electrodes.

The *in vivo* applications demonstrated here are peripheral nerve recording and the cortical tissue response to implantation. Neural electrodes have a number of potential and realized applications as therapeutic devices, including restoration of visual, cochlear, peripheral, cardiac, GI, and urinary function. It is expected that most of the aforementioned areas could benefit from a more tissue-like electrode design. The background will focus on electrodes for cortical applications because it is the focus of multiple areas of neurological research and much of the microfabrication technology development has been devoted to this application. The three primary contributions of the thesis, which span development and application of the microelectrodes are as follows:

1) facile fabrication schemes,
2) low-profile, compliant, durable electrodes
3) the assessment of tissue damage after fibrin-assisted implantation of compliant electrodes.

The fabrication of microfabricated electrodes with a PDMS substrate typically included a plasma etch step, although other methods such as laser ablation have also been employed [6-7]. Plasma etching must be carefully calibrated and requires access to a well-maintained reactive etch system, as contaminants from previous processes can have a residual effect on subsequent use. This is not necessarily a trivial point, as in the

author's experience, the cleaning times can rival the actual etch times. Using RIE or laser ablation can also attack the metal forming the conductive lead. If the metal layer is several hundred nanometers thick, this may not be an issue, but when the film is 30 nm and subject to mechanical strain, etch-related degradation becomes a concern. The use of spin-casting on a reusable mold and creating exposed sites over thin metal films with photoresist, which is easily patterned and dissolved, avoids these limitations.

The electrodes were designed to be low profile, compliant and durable arrays. The previously reported literature has described low profile electrodes, compliant, such as metalized Kevlar filaments [8]. The durability of the metalized film has not been described, but string-like electrodes can be expected to undergo mechanical deformations that may cause delamination and fracture of the conductive film on the filament. Additionally, a strategy for arranging the string-like electrodes into an array requires some consideration. Polyimide and parylene-based electrodes have also been reported for compliant electrode applications, including configurations in an array format [9-11]. Because of the qualities of these polymers, polyimide and parylene based electrodes can be expected to be relatively durable as long as they do not suffer plastic deformation [12-13]. The elastic modulus of these electrodes is still several orders of magnitude greater than that of neurological tissue [12, 14-15], making the cross-sectional area of the electrode critical for achieving adequate compliance. Silicone-based electrodes have the advantage of having an intrinsically low compliance, reducing the necessity of a small foot-print. The small footprint has other advantages that are related to achieving contact with the region of interest in the biological tissue. The electrodes described here were designed to that end. Because they are fabricated on an elastomeric substrate, plastic

deformation is not a concern, allowing the devices to be bent, bundled, or otherwise deformed in their deployment.

The Young's modulus of the electrodes developed in this thesis is such that they cannot be inserted into tissue (e.g. brain) without an additional mechanism for insertion. The use of a coating was tested for its ability to successfully insert the electrode and for the degree of inflammation and damage it caused. Delicate electrodes have previously used a PEG coating for insertion [16]. The effect of PEG, at locally very high concentrations, is a concern for cell viability in the localized region [17-18]. Fibrin is a biologically derived alternative that is naturally resorbed over a period of weeks [19]. Histological metrics were used to assess fibrin's utility as a temporary stiffening agent that does not cause damage to the surrounding tissue.

1.2 Goals of chronic neural electrodes

In acute and chronic settings, microwire electrodes have been used to monitor and stimulate neural activity. Recordings done in acute or *ex-vivo* preparations can give a perspective on the organization of the brain[20], how the networks organize to processes information [21], and examine the electrophysiological dysfunction of disease induced states [22-24]. Chronic recordings involve either growing dissociated neurons on an electrode array *in vitro* or surgically implanting electrodes in an animal[25-26]. *In vitro* activity is useful for studying cell-level mechanisms while *in vivo* activity is useful for investigation at the network or systemic level. The chronic study of neural activity can be used to provide a time-dependent view of the aforementioned phenomena; however, one of the driving factors in developing neural electrode implants with long-term stability is the realization of a prosthetic brain machine interface (BMI)[27]. The successful

development of BMI technology holds broad therapeutic promise for patients that have mobility- or sight-related morbidity [28-30].

1.2.1 Chronic electrodes: origin and history

Implanted electrodes have been neurological research tools for the past half-century. As early as 1958, microwires were used to record ensemble activity from neurons in unrestrained squirrels [31]. In current research on implanted electrode arrays, efforts focus on optimizing the interface to preserve the quality of recordable neural activity. Over time, the population of successful recording electrodes decreases; this is due to inter-related variables thought to be initiated by the implant's effect on surrounding tissue [32]. If the neural interface could be preserved over years the electrode arrays could be used as a clinically useful therapy to communicate with a computer or robotic system. Long term recording has been demonstrated, but the signal loss over time is a limiting factor [33]. Achieving long-term continuity between electronics and neural tissue at the clinical level faces several roadblocks, the most prominent of which may be the change in tissue morphology the electrodes cause to the surrounding tissue that inhibits successful recording over time [34-35].

1.2.2 Strategies to improve performance

Electrode arrays have been designed to minimize the damage caused to the tissue by increasing the lead density on electrode shanks and reducing the shank cross-section [36-37] and by coating the electrodes with materials to decrease the level of inflammation[38-42]; however, glial scarring and decreased proximal neuron density are persistent problems[43]. The technology and strategy for making the implanted electrode as unobtrusive as possible can be expected to create a long-term closed-loop neural

prosthetic. The work toward this goal, however, has been driven by studies using simple microwire electrode arrays [43-54]. The motivations for microwire use may be due to the cost of microelectronics-based electrode technology or the adequate, if sub-optimal, spatial sampling and durability provided by conventional microwire arrays.

Acute and chronic experiments have been done using hand-bundled microwires arranged in an electrode array [43, 54-56]. Evoked neural activity from various external stimuli, (e.g. tactile [21, 57], auditory [56] , gustatory [58-59]) has been collected. The spatial locations and neural activity in brain respective to its modality, e.g. the cortex, have also been investigated [47, 55, 60-62]. Additionally, the network behavior regarding synchronization, changes in firing patterns, and other variables in network activity has been used to understand the mechanisms of learning and to investigate the mechanisms of neurological dysfunction as it relates to disorders such as epilepsy [45, 51] stroke [53], and Alzheimer's [24] as well as systemic syndromes such as diabetes [63]. The microwire arrays have a flexible format, as the lengths of the wires can be varied, the planar 2D array of spikes can be made with over 700 electrodes [33], to meet the requirements of different applications.

1.2.3 Fabrication technology

The disadvantage of microwire arrays is that they are largely hand-made and are limited by the wire diameter [49, 62]. Efforts toward using microelectronics processing to increase the electrode density and take advantage of parallel processing technology have led to the Utah array [64]and to the Michigan array [65]. Both are now commercially available from Cyberkinetics Inc. (Foxboro, Ma) and Neuronexus (Ann Arbor, MI), respectively. In addition, polymer-based electrode arrays for cortical

applications have been made from polyimide [11, 66-69] and parylene [9, 70]. Non-cortical applications have used more compliant substrates such as silicone rubber [71].

1.2.4 Commercially-available electrodes

The Utah array is made from a monolithic material and etched into an array of high-aspect ratio spikes [64]. The substrate begins as a thick (1.5 mm) n-type silicon wafer. The sites of the electrodes are doped to p-type footprints. The wafer is then diced 1.5 mm deep, so that the footprints are the substrates to be etched into an array of posts. The posts are etched, metallized and insulated so that they are functional electrodes. The electronic contacts are made on the backside of the wafer, at the p-type footprints. The electrode array is a 3-D set of spikes, each 100 μm wide at the base and μm wide at the tips (Figure 1.1). The process is amenable to production and electronics packaging allowing the arrays to be made commercially available for research use. The Utah array was initially made with even spike heights (for 2-D recording capabilities), although a variable height conformation has also been demonstrated [2]. The variable height can be important in several instances: for recordings intended to sample activity at multiple levels or to remain at the same depth in one level by following the curvature of the brain. Multiple depths also allow different regions to be sampled with the location of the activity of interest has not been localized in prior studies. Although the electrode shanks are a 3D array, the recording is two-dimensional if the electrodes are all the same height. Full, three-dimensional sampling is possible the post recording sites are staggered, since the electrode tips all end in the same plane. While the height of the electrodes can be specified, depth placement is still critical for recording in specific regions, i.e. different cortical layers.

The Michigan electrode, is a planar or two-dimensional device, but circumvents the dimensional restrictions by having recording sites at multiple points along the probe [65]. Given that cortex is organized in a lamellar format, having the recording density in the vertical rather than horizontal plane may provide more flexibility in obtaining useful recordings [72]. The Michigan-style probes have also been demonstrated in a stackable configuration for true three-dimensional recording capabilities [4] (Figure 1.3). The array is fabricated on a planar silicon substrate with the row of shanks having multiple electrodes patterned onto each shank. The electrodes are photolithographically patterned lines that extend in parallel along the length of the silicon shank. Because micropatterning rather than bulk silicon doping is used to create the leads, the density of individual recording sites per volume of the implanted device is increased by about 40 fold, although by comparison, a Michigan-style probe has between 16 and 64 recording sites on four to eight shanks and the Utah electrode has 96 recording sites on 96 shanks. The cross-sections of the shanks, which can be made several millimeters long, taper from approximately 100 μm at the base to a point at the tip and are 15 μm thick, occupying approximately 10% of the total volume of an individual microwire. The active site can tailored for either single unit recordings (approximate active site diameter: 15 μm, or multi-unit field activity (40 μm). The Michigan electrodes are also useful as cochlear implants because their high modulus and thin cross-section make them well suited to curving with the shape of the cochlea [73-75].

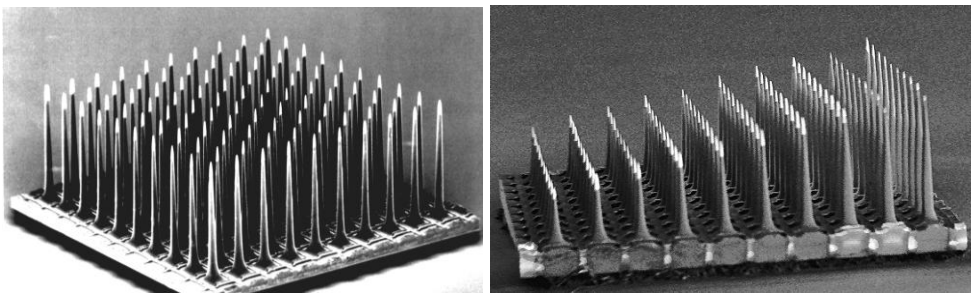

Figure 1.1: The Utah electrode array is shown in two configurations above. The shank array is etched from a monolithic piece of silicon and the recording site is confined to an exposed region at the shank tip. (a) the array with all shanks the same height (b) the array with staggered heights. [2]

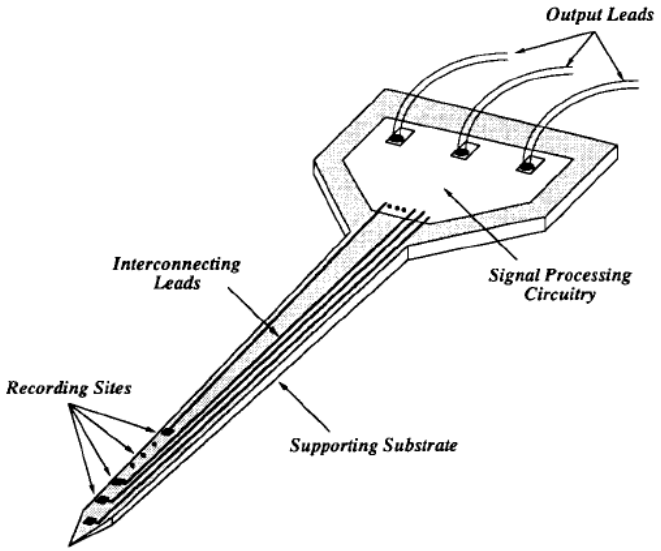

Figure 1.2: A schematic of a single shank of the Michigan electrode is shown. The design had several innovations including on-chip signal processing capabilities and multiple recording sites per shank. The shanks were also fabricated in a row-format (Figure 1.4) for recordings at multiple locations and multiple depths in one plane The design was based on planer silicon and was able to leverage silicon-based microelectronics processing [5].

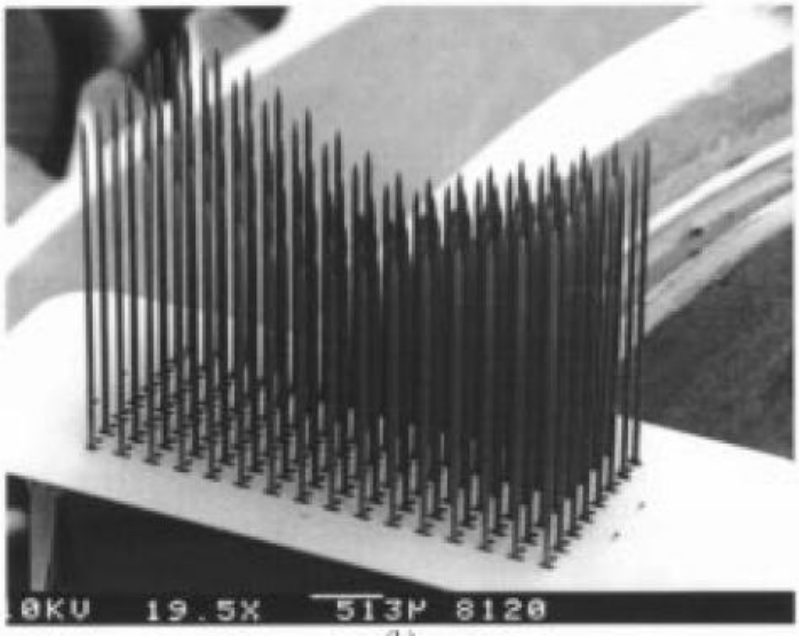

Figure 1.3: The Michigan electrodes are adaptable to a 3D array format by packaging rows of shank electrodes into an assembly tray. This matched the 3D geometry of the Utah array and enabled multiple recording sites per shank. [4]

The Michigan electrodes also have developed an implant-compatible CMOS circuit interface incorporated into the electrode array[65, 76]. The system was designed to incorporate multiplexing and frequency-specific amplification; bidirectional signaling over a single lead and self-testing of the electrodes using the integrated system were demonstrated [65, 76]. Variations in the Michigan electrode fabrication strategy have been used for other electrode designs because it conforms to general wafer-level fabrication processes.

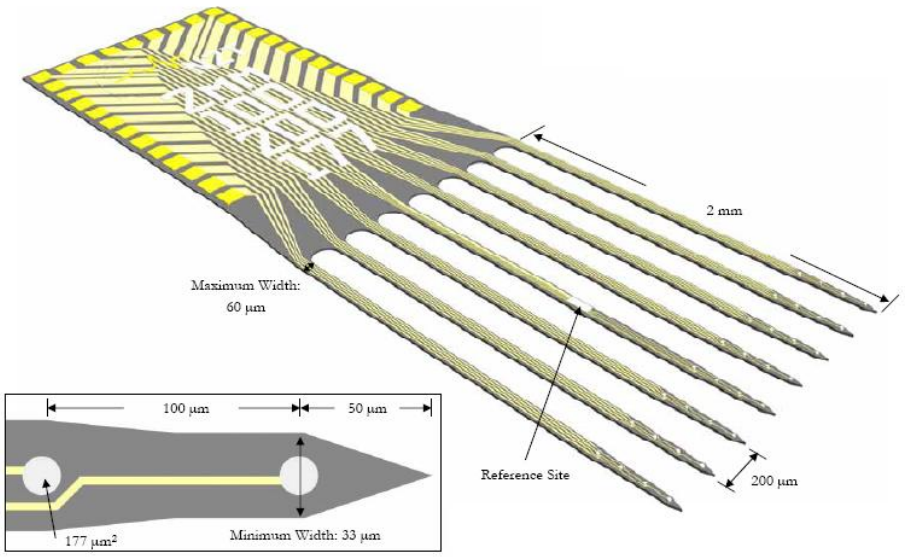

Figure 1.4: The Michigan probes and a compatible data acquisition system are commercially available for research applications. A sample probe is shown from the NeuroNexus (Ann Arbor, MI) catalog above. The shank geometry and number are specifiable as are the active site geometries [1].

1.3 Biological response to chronic electrode implantation

Chronic electrodes for cortical stimulation and recording have been used successfully in clinical and research settings [77-79]. The performance of the electrode implants is somewhat variable and one of the reasons for variability, besides the issue of addressing a complex network of neurons correctly and efficiently, is that the implanted electrode changes the tissue in its vicinity [80-81]. Although the electrode injures the tissue during implantation, this event is not thought to be a significant contribution in the development of an encapsulating glial scar and a loss of neurons proximal to the implant

[82]. The glial scar and the decrease in proximal neuronal populations 1) increases impedance for both stimulation and recording and 2) reduces the likelihood of a useful neural recording by increasing distance between the electrode and neural activity [81]. The probable reason why these events accompany electrode implantation is the chronic, low-level inflammatory response at the implant site [80-81]. Inflammation and disruption of the blood brain barrier has toxic effects on neurons and the glial scar is a CNS self-protection mechanism to isolate neural tissue from the site of trauma and its neurotoxic events [81]. However, this response may also contribute to poor electrode performance.

As mentioned earlier, the initial implant event is not thought to be the main mechanism of scaring and neuronal loss. Previous studies have compared implanted electrodes to stab wounds, where the electrode is inserted and then removed [3, 66, 82]. The inflammation and neuronal loss four weeks after the surgery are minimal compared to electrodes that were inserted and removed after four weeks. The difference is likely due to the presence of the electrode over time. Concurrently, the performance of the electrodes suffers in chronic applications. These changes in electrode performance are temporally correlated to the aforementioned tissue changes and are limiting the scope of CNS electrode-based therapies and research [35, 80].

1.3.1 Degradation of electrode performance over time

The collected neural activity from implanted electrode arrays can be applied for several applications. The recorded signals are also used for research purposes to monitor electrophysiological activity to environmental or chemical stimuli [21, 83-84]. Clinical applications include neuromotor prostheses and brain-computer interfaces (BCIs). These

therapies have used cortical signals that can be transduced to a robotically controlled actuator or computer for actuating movement or controlling a computer. Functionality has been demonstrated in both primates and humans [26, 33, 35, 85-86]. The signal is routed from the brain through electrodes instead of the spinal cord and peripheral nerves to develop therapies for full or partial paralysis. The recorded signal can also be used as feedback for deep brain stimulation (DBS), which is currently electrophysiologically only feed-forward [87-88]. The success of the therapy must be measured in a change in symptoms and the optimization that occurs over days to weeks [89-90].

Because of the complexity of signaling, the electrode must record selective neural activity with a high signal to noise ratio [80]. To differentiate a useful signal from background noise, the electrode arrays often target single-unit (single-cell) activity [43]. The single unit potentials are assembled from the array of recording electrodes and used as an ensemble to determine its significance [26].

In non-clinical research studies, the quality of recordable signals changes with time and varies within the implanted array and between animals. For example, in microwire implants in monkeys, the number of functional electrodes in a microwire array dropped by 40% between one and 18 months after implantation [33]. Similarly, Rouche also reported a decrease with time (5 mo) with the Utah array in cats [91]. Generally, the initial studies on the chronic electrode tissue response were on the order of 1-6 months for electrodes made of microwire or silicone [43, 92].

The signal degradation over time and the change in tissue surrounding the electrode are temporally linked; the change in tissue that occurs with the degradation in recording signals and may also be linked to the inconsistency of stimulation-based

therapies. The design of an electrode that does not cause glial scaring or neuronal loss, or at least mitigates the degree to which they do occur, has been a goal of several recent studies. The effect of coatings on the electrode surface, the electrode surface area to volume ratio, and the mechanical properties of the electrode substrate have been investigated [3, 39, 41, 66]. The goal of these modifications has been either to increase the mechanical coupling or to decrease the mechanical mismatch of the electrode/brain interface. The implanted electrodes are stiffer than the brain tissue (by 5-9 orders of magnitude). The effect of the mechanical mismatch is amplified by micromotion of the electrode. Micromotion occurs from cardiac and respiratory rhythms and ambulatory motion of the animal or person with the implant. The micromotion causes a strain in the surrounding tissue and the persistent incidence of this strain becomes a chronic low-level trauma. The micromotion from physiological factors (vascular and respiratory) in rats have been measured in the range of 10-30 μm for respiratory effects and 2-4 μm for vascular pulsatility [93]. The effect of ambulation and head movement on the electrode can also be expected to contribute.

Strain simulations on the tissue near the electrode have also been done for a hypothetical electrode that oscillates in line with its long axis [94]. The tether on the electrode has the potential to apply tension to the electrode shank; a vertical up and down translation is a simple test of a hypothetical dynamic. The simulation of the electrode and tissue interface was tested under with cases of minimal and very strong adhesion between the tissue and the electrode. The low adhesion case, assuming that the tissue was not attached to the electrode and it was able to slide along the tissue with a finite level of friction generated strains of 0.1-0.01 in the tissue around the tip of the electrode. It was

noted that the active site is normally at the tip, and so the location of the strain had particular significance. Conversely, when the tissue is presumed to be attached to the electrode and there is no slip at the interface, the strains were lower by a order of magnitude and had an even distribution along the shank length, rather than concentrating at the tip of the electrode [95].

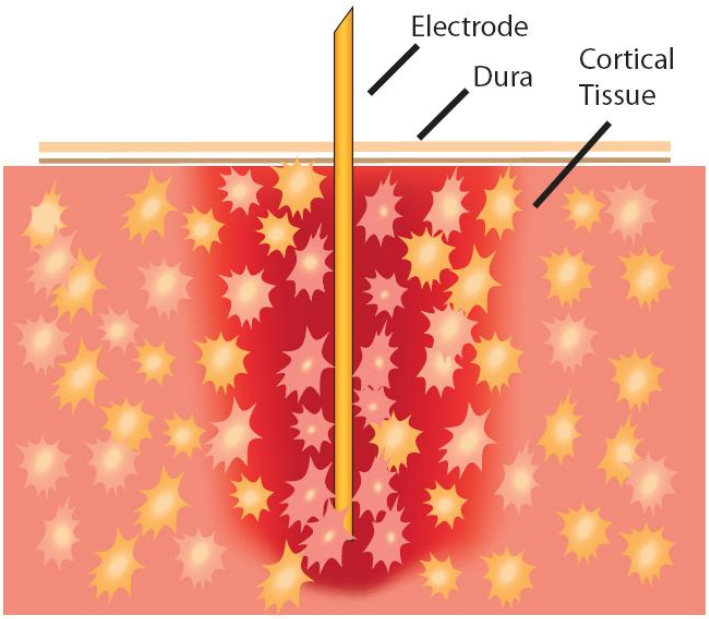

Figure 1.5: A schematic view of the inflammation around the electrode is shown above. The astrocytes in the vicinity of the electrode become activated, indicating an inflammatory state. The neuronal population close to the electrode decreases.

The effect of micromotion on inflammation has been supported by an *in vitro* study testing the response of astrocytes and microglia, the CNS cell types mediating neuroinflammation, to 24 hrs of 5% strain at a frequency close to physiological levels (30 cycles/min) [81]. The astrocytes showed an increase in inflammatory markers TGF-beta1, GFAP, and neurocan. TGFβ1 is involved in the glial scaring response, GFAP is indicative of activated astrocytes and neurocan inhibits axonal regeneration. The

microglia, showed an increase in IL-1β but not TNFα, both of which are inflammatory markers.

The data on floating vs. directly fixed electrodes supports the hypothesis that the mechanical differences cause continuous low-level injury [96]. The rigid electrodes described above suffer from attenuated or lost signals in chronic experiments. This is hypothesized to be due to the disparity in stiffness and inertial movement between the electrode and brain tissue. The tethering of a rigid microelectrode array in the skull induces more encapsulation and neural signal loss over time than a "floating" electrode array.

The array is considered to be floating if the electrodes are coupled to the brain rather than the skull. In mounting schemes that are not floating, the electrodes are fixed to the skull after insertion into the brain. The inertial shifting and settling of the brain within the skull causes damage to the tissue around the electrodes if the electrodes are fixed in place relative to the skull [97]. Allowing the electrodes to move with the brain reduces their tendency to injure the tissue. Alternative fixation mechanisms commonly include making the electronics bundle a flexible cable and fixing it to the skull without inducing tension in the line to the implanted electrodes [1]. Because the cable is flexible, and not in tension, the implanted array is able to mechanically couple with the brain tissue rather than with the electronics and skull.

The floating arrays improve performance by making the electrode's effective mechanical behavior closer to that of brain tissue [97]. The mechanical mismatch can generate undesirable strain fields in the brain tissue [94]. The chronic small deformations in the surrounding brain tissue of the person or animal with the implant occur

continuously with movement and settling of the brain in the skull. The deformation is injurious and the consequential glial response is therefore sustained and indefinitely present [98].

1.4 Polymeric approaches

One of the strategies that has been adopted to improve the mechanical coupling between the tissue and the electrode has been to make the electrode out of a lower Young's modulus material. The planar fabrication process to create a two-dimensional array of shanks lends itself to fabrication from a number of different materials [9, 11, 66-70]. The use of polymer substrates such as polyimide has provided electrodes with a lower effective elastic modulus [66, 99-100]. Similar to reducing the strain induced by tethering, implanting a more compliant electrode is expected to cause less mechanical damage to the tissue under chronic implant environments [94]. A difference in the elastic modulus of approximately five orders of magnitude still exists between polyimide and brain tissue, however it is much reduced from the approximately nine orders of magnitude in silicon probes [94]. The bending stiffness may affect the inflammation in the tissue in a chronic-recording environment. The material composition and geometry are both factors in determining the bending stiffness; e.g. a high modulus electrode with a small cross-section may have a smaller bending stiffness than a larger cross-section probe of a slightly softer material. Additionally, if the cells surrounding the electrode have mechanically coupled to the electrode surface, the shear strain from the electrode to the tissue may be reduced and electrode movement is more effectively coupled to the tissue. The effective adhesion and mechanical coupling between two materials with several orders magnitude difference in elastic modulus appears to necessarily include an

intermediate layer with a transitional elastic modulus [101]. Consequently, in practice, improved adhesion and its protective effects may also be coupled with encapsulation; however, the development of a surrounding fibrous layer which is developed to protect the surrounding tissue also acts to distance the electrode from the neurons.

The hypothesis that the difference in mechanical properties between the implanted electrode and brain leads to injury causing signal loss has inspired much of the research in relatively compliant polymeric materials. The polymer technology primarily includes polyimide and parylene electrodes. Rousche *et al.* designed a polyimide array similar to the Michigan silicon arrays in 2001[66]. Parylene has been used by Takeuchi *et al.* to make a multi-functional microfluidic, micro electrode, with the fluidic channel temporarily loaded with PEG to aid insertion [70].

The biological data on implanted polymer electrodes are less extensive than for silicon and microwire devices. However, the data available suggest that reducing the stiffness of the implant correspondingly improves the neuronal density in the vicinity of the electrode and reduces glial fibrillary astrocytic protein (GFAP) positive (i.e. activated) astrocyte and microglial density [99, 102]. Unfortunately the studies lack adequate controls. An implant study of polyimide electrodes showed GFAP staining comparable to that found with a stab wound, although the stab wound data cites was from another publication. Despite these promising results, further corroborating data is lacking. Parylene is similar to polyimide in that it is a chemically inert, low-k dielectric polymer that is used in flexible electronics. Although no studies were found comparing parylene-based implants to silicon probes, Seymour et al conducted a study testing the effect of implant size in parylene-based probes [103]. The control “large” probe was

approximately 50 x 70 μm, while the smaller probe section is comprised of a fin that had lattice patterns that varied from solid to mostly open (Figure 1.6). After four weeks, neuronal cell loss and the presence of microglia were more positively correlated with the tissue surrounding the "large" shank region and the fins with less open area. The hypothesis driving this work is that smaller features (< 15 μm) or better coupling between the electrode and tissue cause a reduced macrophage response; however, the reduced material cross-section reduces the bending stiffness, which appears to be the effective net variable.

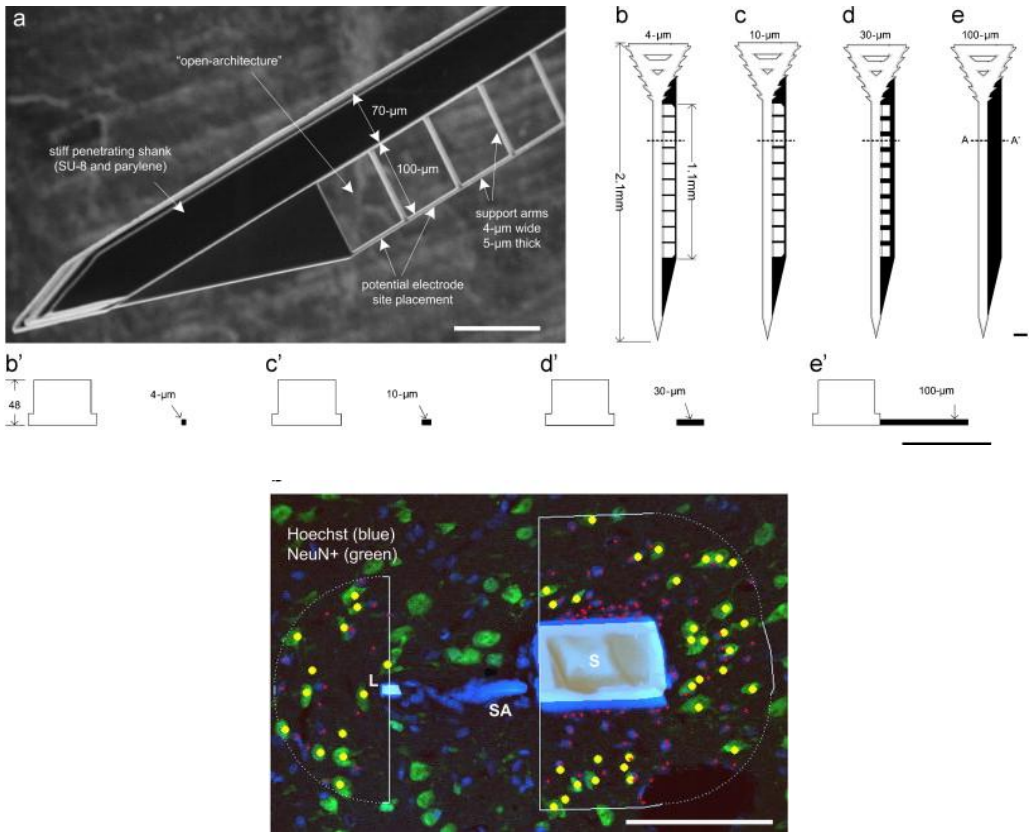

Figure 1.6: The probe geometries tested by Seymour *et al.* are shown top (a). A sample histological image is shown bottom (b). The red dots indicate non-neuronal cells, which were more populous around the shank (right) than the fin (left) [3]. Scale: 100 μm.

The lack of histological data on polymer electrodes may be due to their relatively recent use. Polyimide electrodes were first presented in 1989 [104] with the first cortical electrodes presented in and parylene has a documented history of use as an electrode insulator [105] and was published as a cortical electrode in 2005 [70]. The disparity in use is also possibly due to accessibility issues or technique-related insertion difficulties that are inherent in lower modulus designs. Probe coatings are commonly used. Examples of temporary coatings that dissolve after implantation are PEG [70, 106], collagenase [107], sucrose [108], and specialized temperature-sensitive polymers[108]. The coating dissolves or melts after it is implanted, however the coating is temporarily disruptive to the surrounding cells and hinders electrophysiological recording immediately after implant, which is used to verify accurate placement during surgery. Alternatives to a temporary coating involve fabricating the electrode on a substrate that has high-modulus regions [100, 109] or has a temperature sensitive change in the stiffness [110].

1.5 Conclusion

The Michigan electrodes have been consciously designed to minimize the space the electrodes occupy in the brain, while the Utah array adapted the microwire array format into a monolithic substrate. Many of the subsequent flexible electrode arrays are based on the Michigan electrode's planar fabrication process. The work toward flexible arrays recognized that the stiffness of microwires and silicon presented compatibility concerns with brain tissue. The large disparity in mechanical properties and the inertial movement due to factors as subtle as respiration, and cardiac rhythm has been calculated to cause electrode movement against the tissue [81]. Chronic inflammation and a loss of the

neuronal population in the vicinity of electrode implants has been noted and preliminary data suggest that it is correlated to the stiffness of the electrode. The histological changes around the electrode limit electrode function with time and consequently limit the clinical utility of potential therapies. The development of more compliant electrodes that can be easily fabricated is a goal the research community is working towards. Studies to date suggest that more compliant electrodes cause less damage and inflammation to the tissue.

1.6 Citations

1. Neuronexus, *Silicon Microelectrode Array Research Product Catalog and Manual*. 2008: Ann Arbor MI.
2. Kindlmann, G.N., RA. Badi, A. Bigler, J. Keller, C. Coffey, R. Joens, GM. Johnson, CR. . *Imaging of Utah Electrode Array, Implanted in Cochlear Nerve*. in *NIH Symposium on Biocomputation & Bioinformation Digital Biology*. 2003: Bethesda MD.
3. Seymour, J.P. and D.R. Kipke, *Neural probe design for reduced tissue encapsulation in CNS.* Biomaterials, 2007. **28**(25): p. 3594-3607.
4. Bai, Q., K.D. Wise, and D.J. Anderson, *A high-yield microassembly structure for three-dimensional microelectrode arrays.* Ieee Transactions on Biomedical Engineering, 2000. **47**(3): p. 281-289.
5. Ji, J., K. Najafi, and K.D. Wise, *A SCALED ELECTRONICALLY-CONFIGURABLE MULTICHANNEL RECORDING ARRAY.* Sensors and Actuators a-Physical, 1990. **22**(1-3): p. 589-591.
6. Garra, J., et al., *Dry etching of polydimethylsiloxane for microfluidic systems.* Journal of Vacuum Science & Technology a-Vacuum Surfaces and Films, 2002. **20**(3): p. 975-982.
7. Graubner, V.M., et al., *Incubation and ablation behavior of poly(dimethylsiloxane) for 266 nm irradiation.* Applied Surface Science, 2002. **197**: p. 786-790.
8. McNaughton, T.G. and K.W. Horch, *Metallized polymer fibers as leadwires and intrafascicular microelectrodes.* Journal of Neuroscience Methods, 1996. **70**(1): p. 103-110.
9. Rodger, D.C., et al., *Flexible parylene-based multielectrode array technology for high-density neural stimulation and recording.* Sensors and Actuators B-Chemical, 2008. **132**(2): p. 449-460.
10. Lacour, S.P., et al., *Polyimide micro-channel arrays for peripheral nerve regenerative implants.* Sensors and Actuators a-Physical, 2008. **147**(2): p. 456-463.
11. Myllymaa, S., et al., *Fabrication and testing of polyimide-based microelectrode arrays for cortical mapping of evoked potentials.* Biosensors & Bioelectronics, 2009. **24**(10): p. 3067-3072.

12. DuPont, *Kapton Technical Data Sheet.*
13. Parylene Coating Services, I., *Properties of Parylene.* 2010.
14. Green, M.A., L.E. Bilston, and R. Sinkus, *In vivo brain viscoelastic properties measured by magnetic resonance elastography.* Nmr in Biomedicine, 2008. **21**(7): p. 755-764.
15. Borschel, G.H., et al., *Mechanical properties of acellular peripheral nerve.* Journal of Surgical Research, 2003. **114**(2): p. 133-139.
16. Suzuki, T., Mabuchi, K. Takeuchi, S. *A 3D flexible parylene probe array for multichannel neural recording*. in *Proceedings of the 1st International IEEE EMBS Conference on Neural Engineering*. 2003.
17. Herold, D.A., et al., *Evidence for the toxicity of polyethylene-glycol.* Veterinary and Human Toxicology, 1981. **23**(5): p. 363-363.
18. Montaguti, P., E. Melloni, and E. Cavalletti, *Acute intravenous toxicity of dimethyl-sulfoxide, polyethylene-glycol-400, dimethylformamide, absolute ethanol, and benzyl alcohol in inbred mouse strains.* Arzneimittel-Forschung/Drug Research, 1994. **44-1**(4): p. 566-570.
19. Adams, R.A., et al., *Manifold roles for fibrin.* Molecular Interventions, 2004. **4**(3): p. 163-176.
20. Wu, C.P., et al., *Size does matter: Generation of intrinsic network rhythms in thick mouse hippocampal slices.* Journal of Neurophysiology, 2005. **93**(4): p. 2302-2317.
21. Boloori, A.R. and G.B. Stanley, *The dynamics of spatiotemporal response integration in the somatosensory cortex of the vibrissa system.* Journal of Neuroscience, 2006. **26**(14): p. 3767-3782.
22. Vlkolinsky, R., et al., *Acute exposure to CXC chemokine ligand 10, but not its chronic astroglial production, alters synaptic plasticity in mouse hippocampal slices.* Journal of Neuroimmunology, 2004. **150**(1-2): p. 37-47.
23. Tebano, M.T., et al., *Adenosine A(2A) receptor blockade differentially influences excitotoxic mechanisms at pre- and postsynaptic sites in the rat striatum.* Journal of Neuroscience Research, 2004. **77**(1): p. 100-107.
24. Freir, D.B., C. Holscher, and C.E. Herron, *Blockade of long-term potentiation by beta-amyloid peptides in the CA1 region of the rat hippocampus in vivo.* Journal of Neurophysiology, 2001. **85**(2): p. 708-713.
25. Rolston, J.W., DA. Potter, SM., *Precisely timed spatiotemporal patterns of neural activity in dissociated cortical cultures.* Neuroscience Letters, 2007. **148**(1): p. 294--303.
26. Carmena, J.M., et al., *Learning to control a brain-machine interface for reaching and grasping by primates.* Plos Biology, 2003. **1**(2): p. 193-208.
27. Allison, B.Z., E.W. Wolpaw, and A.R. Wolpaw, *Brain-computer interface systems: progress and prospects.* Expert Review of Medical Devices, 2007. **4**(4): p. 463-474.
28. Di Pino, G., E. Guglielmelli, and P.M. Rossini, *Neuroplasticity in amputees: Main implications on bidirectional interfacing of cybernetic hand prostheses.* Progress in Neurobiology, 2009. **88**(2): p. 114-126.
29. Elder, J.B., et al., *The future of cerebral surgery: A kaleidoscope of opportunities.* Neurosurgery, 2008. **62**(6): p. 1555-1579.

30. Tonet, O., et al., *Defining brain-machine interface applications by matching interface performance with device requirements.* Journal of Neuroscience Methods, 2008. **167**(1): p. 91-104.
31. Green, J.D., *Simple microelectrode for recording from the central nervous system.* Nature, 1958. **182**(4640): p. 962-962.
32. Velliste, M., et al., *Cortical control of a prosthetic arm for self-feeding.* Nature, 2008. **453**(7198): p. 1098-1101.
33. Nicolelis, M.A.L., et al., *Chronic, multisite, multielectrode recordings in macaque monkeys.* Proceedings of the National Academy of Sciences of the United States of America, 2003. **100**(19): p. 11041-11046.
34. Butson, C.R. and C.C. McIntyre, *Tissue and electrode capacitance reduce neural activation volumes during deep brain stimulation.* Clinical Neurophysiology, 2005. **116**(10): p. 2490-2500.
35. Ryu, S.I. and K.V. Shenoy, *Human cortical prostheses: lost in translation?* Neurosurgical Focus, 2009. **27**(1).
36. Csicsvari, J., et al., *Massively parallel recording of unit and local field potentials with silicon-based electrodes.* Journal of Neurophysiology, 2003. **90**(2): p. 1314-1323.
37. Kim, C. and K.D. Wise, *A 64-site multishank CMOS low-profile neural stimulating probe.* Ieee Journal of Solid-State Circuits, 1996. **31**(9): p. 1230-1238.
38. Pierce, A.L., et al., *Thin-film silica sol-gel coatings for neural microelectrodes.* Journal of Neuroscience Methods, 2009. **180**(1): p. 106-110.
39. He, W., G.C. McConnell, and R.V. Bellamkonda, *Nanoscale laminin coating modulates cortical scarring response around implanted silicon microelectrode arrays.* Journal of Neural Engineering, 2006. **3**(4): p. 316-326.
40. Klaver, C.L. and M.R. Caplan, *Bioactive surface for neural electrodes: Decreasing astrocyte proliferation via transforming growth factor-beta 1.* Journal of Biomedical Materials Research Part A, 2007. **81A**(4): p. 1011-1016.
41. Purcell, E.K., et al., *In vivo evaluation of a neural stem cell-seeded prosthesis.* Journal of Neural Engineering, 2009. **6**(2).
42. Rennaker, R.L., et al., *Minocycline increases quality and longevity of chronic neural recordings.* Journal of Neural Engineering, 2007. **4**(2): p. L1-L5.
43. Williams, J.C., R.L. Rennaker, and D.R. Kipke, *Long-term neural recording characteristics of wire microelectrode arrays implanted in cerebral cortex.* Brain Research Protocols, 1999. **4**(3): p. 303-313.
44. Kish, L.J., M.R. Palmer, and G.A. Gerhardt, *Multiple single-unit recordings in the striatum of freely moving animals: effects of apomorphine and D-amphetamine in normal and unilateral 6-hydroxydopamine-lesioned rats.* Brain Research, 1999. **833**(1): p. 58-70.
45. Fanselow, E.E., A.P. Reid, and M.A.L. Nicolelis, *Reduction of pentylenetetrazole-induced seizure activity in awake rats by seizure-triggered trigeminal nerve stimulation.* Journal of Neuroscience, 2000. **20**(21): p. 8160-8168.
46. Chen, M.T., et al., *In vivo extracellular recording of striatal neurons in the awake rat following unilateral 6-hydroxydopamine lesions.* Experimental Neurology, 2001. **171**(1): p. 72-83.

47. Chiu, C.Y. and M. Weliky, *Spontaneous activity in developing ferret visual cortex in vivo.* Journal of Neuroscience, 2001. **21**(22): p. 8906-8914.
48. Scherberger, H., et al., *Magnetic resonance image-guided implantation of chronic recording electrodes in the macaque intraparietal sulcus.* Journal of Neuroscience Methods, 2003. **130**(1): p. 1-8.
49. Tsai, M.L. and C.T. Yen, *A simple method for fabricating horizontal and vertical microwire arrays.* Journal of Neuroscience Methods, 2003. **131**(1-2): p. 107-110.
50. Rennaker, R.L., et al., *An economical multi-channel cortical electrode array for extended periods of recording during behavior.* Journal of Neuroscience Methods, 2005. **142**(1): p. 97-105.
51. Simonotto, J.D., et al., *Nonlinear analysis of high-resolution microwire electrode data from a chronic limbic epilepsy model over the latent period.* Epilepsia, 2005. **46**: p. 124-124.
52. Sanchez, J.C., et al., *Structural modifications in chronic microwire electrodes for cortical neuroprosthetics: A case study.* Ieee Transactions on Neural Systems and Rehabilitation Engineering, 2006. **14**(2): p. 217-221.
53. Zhang, X.G., et al., *Measurement of neuronal activity of individual neurons after stroke in the rat using a microwire electrode array.* Journal of Neuroscience Methods, 2007. **162**(1-2): p. 91-100.
54. Van Gompel, J.J., et al., *Phase I trial: safety and feasibility of intracranial electroencephalography using hybrid subdural electrodes containing macro-and microelectrode arrays.* Neurosurgical Focus, 2008. **25**(3).
55. Patil, P.G., et al., *Ensemble recordings of human subcortical neurons as a source of motor control signals for a brain-machine interface.* Neurosurgery, 2004. **55**(1): p. 27-35.
56. Witte, R.S., P.J. Rousche, and D.R. Kipke, *Fast wave propagation in auditory cortex of an awake cat using a chronic microelectrode array.* Journal of Neural Engineering, 2007. **4**(2): p. 68-78.
57. Pantoja, J., et al., *Neuronal activity in the primary somatosensory thalamocortical loop is modulated by reward contingency during tactile discrimination.* Journal of Neuroscience, 2007. **27**(39): p. 10608-10620.
58. de Araujo, I.E., et al., *Food reward in the absence of taste receptor signaling.* Neuron, 2008. **57**(6): p. 930-941.
59. Simon, S.A., et al., *Multisensory Processing of Gustatory Stimuli.* Chemosensory Perception, 2008. **1**(2): p. 95-102.
60. Nicolelis, M.A.L., et al., *Reconstructing the engram: Simultaneous, multisite, many single neuron recordings.* Neuron, 1997. **18**(4): p. 529-537.
61. Lebedev, M.A., J.E. O'Doherty, and M.A.L. Nicolelis, *Decoding of temporal intervals from cortical ensemble activity.* Journal of Neurophysiology, 2008. **99**(1): p. 166-186.
62. Lo, R.C. and Y.M. Yu, *Improved flexible microwire array electrode for intracortical signals recording.* Biomedical Engineering-Applications Basis Communications, 2009. **21**(1): p. 39-50.
63. De Araujo, I., et al., *Insulin administration modulates satiety-sensitive neurons in a rat model of obesity and type 2 diabetes.* International Journal of Obesity, 2007. **31**: p. S101-S101.

64. Campbell, P.K., et al., *A SILICON-BASED, 3-DIMENSIONAL NEURAL INTERFACE - MANUFACTURING PROCESSES FOR AN INTRACORTICAL ELECTRODE ARRAY.* Ieee Transactions on Biomedical Engineering, 1991. **38**(8): p. 758-768.
65. Najafi, K. and K.D. Wise, *An implantable multielectrode array with on-chip signal-processing.* Ieee Journal of Solid-State Circuits, 1986. **21**(6): p. 1035-1044.
66. Rousche, P.J., et al., *Flexible polyimide-based intracortical electrode arrays with bioactive capability.* Ieee Transactions on Biomedical Engineering, 2001. **48**(3): p. 361-371.
67. Metz, S., et al., *Flexible polyimide probes with microelectrodes and embedded microfluidic channels for simultaneous drug delivery and multi-channel monitoring of bioelectric activity.* Biosensors & Bioelectronics, 2004. **19**(10): p. 1309-1318.
68. Seo, J.M., et al., *Biocompatibility of polyimide microelectrode array for retinal stimulation.* Materials Science & Engineering C-Biomimetic and Supramolecular Systems, 2004. **24**(1-2): p. 185-189.
69. Kato, Y.X., et al., *Development of surface microelectrode array based on photosensitive polyimide for recording from the auditory cortex.* Neuroscience Research, 2008. **61**: p. S178-S178.
70. Takeuchi, S., et al., *Parylene flexible neural probes integrated with microfluidic channels.* Lab on a Chip, 2005. **5**(5): p. 519-523.
71. Meacham, K.W., et al., *A lithographically-patterned, elastic multi-electrode array for surface stimulation of the spinal cord.* Biomedical Microdevices, 2008. **10**(2): p. 259-269.
72. Kandel, E.S., J. Jessell, T., *Principles of Neural Science*. 3rd ed, ed. A.a. Lange. 1991, Norwalk.
73. Bell, T.E., K.D. Wise, and D.J. Anderson, *A flexible micromachined electrode array for a cochlear prosthesis.* Sensors and Actuators a-Physical, 1998. **66**(1-3): p. 63-69.
74. Bhatti, P.T. and K.D. Wise, *A 32-site 4-channel high-density electrode array for a cochlear prosthesis.* Ieee Journal of Solid-State Circuits, 2006. **41**(12): p. 2965-2973.
75. Wang, J.B. and K.D. Wise, *A Thin-Film Cochlear Electrode Array With Integrated Position Sensing.* Journal of Microelectromechanical Systems, 2009. **18**(2): p. 385-395.
76. Sodagar, A.A., K.D. Wise, and K. Najafi, *A fully integrated mixed-signal neural processor for implantable multichannel cortical recording.* Ieee Transactions on Biomedical Engineering, 2007. **54**(6): p. 1075-1088.
77. Kralik, J.D., et al., *Techniques for long-term multisite neuronal ensemble recordings in behaving animals.* Methods, 2001. **25**(2): p. 121-150.
78. Gubellini, P., et al., *Deep brain stimulation in neurological diseases and experimental models: From molecule to complex behavior.* Progress in Neurobiology, 2009. **89**(1): p. 79-123.
79. Awan, N.R., A. Lozano, and C. Hamani, *Deep brain stimulation: current and future perspectives.* Neurosurgical Focus, 2009. **27**(1).

80. Polikov, V.S., P.A. Tresco, and W.M. Reichert, *Response of brain tissue to chronically implanted neural electrodes.* Journal of Neuroscience Methods, 2005. **148**(1): p. 1-18.
81. He, W.B., R., *A molecular perspective on understanding and modulating the performance of chronic central nervous system recording electrodes*, in *Indwelling neural implants: strategies for contending with the in vivo environment*, W.M. Reichert, Editor. 2008, CRC Press: Boca Raton.
82. McConnell, G.C., et al., *Implanted neural electrodes cause chronic, local inflammation that is correlated with local neurodegeneration.* Journal of Neural Engineering, 2009. **6**(5).
83. Albert, G.C., et al., *Deep brain stimulation, vagal nerve stimulation and transcranial stimulation: An overview of stimulation parameters and neurotransmitter release.* Neuroscience and Biobehavioral Reviews, 2009. **33**(7): p. 1042-1060.
84. Centonze, D., et al., *Impaired excitatory transmission in the striatum of rats chronically intoxicated with manganese.* Experimental Neurology, 2001. **172**(2): p. 469-476.
85. Kennedy, P.R., et al., *Direct control of a computer from the human central nervous system.* Ieee Transactions on Rehabilitation Engineering, 2000. **8**(2): p. 198-202.
86. Hochberg, L.R., et al., *Neuronal ensemble control of prosthetic devices by a human with tetraplegia.* Nature, 2006. **442**(7099): p. 164-171.
87. Johnson, M.D. and C.C. McIntyre, *Quantifying the Neural Elements Activated and Inhibited by Globus Pallidus Deep Brain Stimulation.* Journal of Neurophysiology, 2008. **100**(5): p. 2549-2563.
88. Chao, P.K., et al., *Classifying deep brain neuronal activities by bursting parameters.* International Journal of Innovative Computing Information and Control, 2009. **5**(4): p. 847-854.
89. McIntyre, C.C., et al., *How does deep brain stimulation work? Present understanding and future questions.* Journal of Clinical Neurophysiology, 2004. **21**(1): p. 40-50.
90. Journee, H.L., A.A. Postma, and M.J. Staal, *Intraoperative neurophysiological assessment of disabling symptoms in DBS surgery.* Neurophysiologie Clinique-Clinical Neurophysiology, 2007. **37**(6): p. 467-475.
91. Rousche, P.J. and R.A. Normann, *Chronic recording capability of the Utah Intracortical Electrode Array in cat sensory cortex.* Journal of Neuroscience Methods, 1998. **82**(1): p. 1-15.
92. Liu, X.M., DB. Carter, RR. Bullara, LA. Yuen, TG. Agnew, WF., *Stability of the interface between neural tissue and chronically implanted intracortical microelectrodes.* Ieee Transactions on Rehabilitation Engineering, 1999. **7**(3): p. 315-326.
93. Gilletti, A. and J. Muthuswamy, *Brain micromotion around implants in the rodent somatosensory cortex.* Journal of Neural Engineering, 2006. **3**(3): p. 189-195.
94. Subbaroyan, J.M., D.C.;Kipke, D.R., *A finite-element model of the mechanical effects of implantable microelectrodes in the cerebral cortex.* Journal of Neural Engineering, 2005. **2**(4): p. 10.

95. Lee, H.B., R. Sun, W. Levenston, M., *Biomechanical analysis of silicon microelectrode-induced strain in the brain.* Journal of Neural Engineering, 2005. **2**(81-89): p. 81-89.
96. Subbaroyan, J. and D.R. Kipke, *The role of flexible polymer interconnects in chronic tissue response induced by intracortical microelectrodes--a modeling and an in vivo study.* Conf Proc IEEE Eng Med Biol Soc, 2006. **1**: p. 3588-91.
97. Biran, R., D.C. Martin, and P.A. Tresco, *The brain tissue response to implanted silicon microelectrode arrays is increased when the device is tethered to the skull.* Journal of Biomedical Materials Research Part A, 2007. **82A**(1): p. 169-178.
98. Griffith, R.W. and D.R. Humphrey, *Long-term gliosis around chronically implanted platinum electrodes in the Rhesus macaque motor cortex.* Neuroscience Letters, 2006. **406**(1-2): p. 81-86.
99. Cheung, K.C., et al., *Flexible polyimide microelectrode array for in vivo recordings and current source density analysis.* Biosensors & Bioelectronics, 2007. **22**(8): p. 1783-1790.
100. Lee, K., et al., *Polyimide based neural implants with stiffness improvement.* Sensors and Actuators B-Chemical, 2004. **102**(1): p. 67-72.
101. Miserez, A., et al., *The transition from stiff to compliant materials in squid beaks.* Science, 2008. **319**(5871): p. 1816-1819.
102. Mercanzini, A., et al., *Demonstration of cortical recording using novel flexible polymer neural probes.* Sensors and Actuators a-Physical, 2008. **143**(1): p. 90-96.
103. Stice, P., et al., *Thin microelectrodes reduce GFAP expression in the implant site in rodent somatosensory cortex.* Journal of Neural Engineering, 2007. **4**(2): p. 42-53.
104. Vanderpuije, P.D., C.R. Pon, and H. Robillard, *Cylindrical cochlear electrode array for use in humans.* Annals of Otology Rhinology and Laryngology, 1989. **98**(6): p. 466-471.
105. Loeb, G.E., et al., *Parylene as a chronically stable, reproducible microelectrode insulator.* Ieee Transactions on Biomedical Engineering, 1977. **24**(2): p. 121-128.
106. Plexon, *Commercially available microwire arrays coating in PEG.* . (Dallas, TX).
107. Paralikar, K.J. and R.S. Clement, *Collagenase-aided intracortical microelectrode array insertion: Effects on insertion force and recording performance.* Ieee Transactions on Biomedical Engineering, 2008. **55**(9): p. 2258-2267.
108. Singh, A., H. Zhu, and J. He. *Improving mechanical stiffness of coated benzocyclobutene (BCB) based neural implant.* in *Conf Proc IEEE Eng Med Biol Soc.* 2004. San Francisco, CA: IEEE.
109. Lee, K.K., et al., *Polyimide-based intracortical neural implant with improved structural stiffness.* Journal of Micromechanics and Microengineering, 2004. **14**(1): p. 32-37.
110. Sharp, A., et al., *Toward a self-deploying shape memory polymer neuronal electrode.* Journal of Neural Engineering, 2006. **3**(4): p. L23-30.

CHAPTER 2

PROCESS FLOW DEVELOPMENT

2. 1 Introduction

The objectives of the fabrication portion of this thesis are:

- producing electrode arrays that were out of a compliant material and that had a profile similar to the shank-style electrode arrays.
- developing a process that was easy to implement so that the fabrication would not limit the number of arrays available for testing

2.1.1 Overview of materials and process selection

Silicone rubber is well-suited as a material for biological applications; it is, generally speaking, biologically inert and many formulations have relatively low Young's modulus [1-6]. Silicone has a history of use as an implant material because it is well tolerated by the body [7][1]. Silicone also has a low, but not zero, chemical reactivity, meaning it is relatively stable as an implant material [7, 10]. (Some chemical changes, such as calcification [7], occur over time and must be taken into account for the application). Regarding mechanical compliance (tensile modulus), many biological

---

[1] Silicone does not elicit the same level of immune response that many other materials elicit, possibly because there is a minimal or absent antibody response [8]. Antibody tagging is part of the foreign body response and its mitigation may reduce the body's efforts to digest and wall-off an implant [9].

tissues are in the kPa range while the range of many common and micro-electronics-related polymers is several orders of magnitude larger (see Tables 2.1-2.2). Achieving an efficient interface to the biological target can require similar mechanical properties. The elastomeric properties and low tensile modulus of silicone make it well suited to relatively "soft," living systems.

Table 2.1: Young's modulus values for polymers commonly used in bioMEMS.

Polymer	Young's modulus		
Poyldimethyl siloxane	~1	MPa	[11]
Parylene C	4.5	GPa	[12]
SU-8	3.5-7.5	GPa	[13]
Polystyrene	204	GPa	[14]
Polyimide (Kapton ®)	2.4-3.2	GPa	[15]
Polypropylene	0.15- 1.1	GPa	[16]

Table 2.2: Young's modulus values for biological tissues

Tissue type	Young's modulus		
Brain	3.15	kPa	[17]
Peripheral nerve	576 $\pm$ 160	kPa	[18-19]
Cardiac	1003 $\pm$ 10.7	kPa	[18-19]
Skeletal muscle	24.7 $\pm$ 3.5	kPa	[18-19]
Endothelial	1.4 $\pm$ 0.1 - 6.8$\pm$ 0.4	kPa	[18-19]

Biomedical MEMS for *in vivo* or *in vitro* applications utilize small feature sizes to unobtrusively monitor biological processes or effectively interface with cellular-level targets. Lab-on-chip and microscale cell cultures systems are some examples of PDMS-based, biomedical devices with microscale features. The surface features on the PDMS substrate are frequently designed to either aid the processing or analysis of a liquid or suspended or sample, to improve the interface to cells, or to directly obtain information

on a local scale from the sample [20-24]. PDMS is an attractive alternative for devices that must be made in large quantities, such as single use diagnostics, because the patterning is easily done with micromolding and because the micromold can be readily made using standard techniques, prototyping varations on a device is also feasible [25]. Silicon or PDMS may be molded very effectively and efficiently on the microscale, however standard micromolding does not create free-standing microscale features or through-holes [26]. Patterning free-standing microscale features in PDMS has relied on specialized and time-intensive techniques, such as reactive ion etching and laser micromachining[27-28]. The use of spin-cast micromolding (SCμM) to create microscale vias in PDMS was presented in 2000 [26]; however its utility expands beyond PDMS membranes with patterned microscale vias. The through-hole creation from SCμM can be used to create other features to form microcables and microwebs in a multilayered device. An example of using SCμM to fabricate a more complex device is described here.

2.1.2 Design and fabrication criteria

A simple process flow has been developed for arrays of electrically functional, elastomer microcables. The microcable geometry further improves on one of the primary advantages of PDMS-based electronics: the conformability of the PDMS substrate. The design presented here changes the substrate from a continuous sheet to an array of cables. Each microcable can conform to the topography it is in contact with without interference from other features or irregularities on the target surface. Conversely, in a sheet, the surrounding features can limit or prevent contact between the device and target surface

(see Figure 2.1) An elastomeric sheet can be made to conform to irregular geometries such as the example in Figure 2.1 by the application of stretch. However, this alternative is generally undesirable because stretching the device can interfere with the function of the electrical components or apply unintended pressure on the substrate. The second advantage of the microcable array is that it is more "breathable," compared to the same array patterned on a sheet-like substrate. The "breathability" is particularly desirable if sensors and electronics are to be placed on the skin. A third advantage of the microcable array is that the footprint becomes dynamic in that it can be bunched up or separated as needed (Figure 2.2).

Figure 2.1 (a) A cross-sectional view of the contact between a flexible sheet and (b) an array of flexible microcables to a hypothetical irregular substrate. The precise degree of contact in the first image depends on the thickness and stiffness of the sheet and the radius of curvature of the substrate. Replacing the sheet with a microcable array removes this uncertainty, as the primary limitation to contact is the width of the microcable.

Figure 2.2: Schematic of a compliant electrode array. The design for microcable electrodes includes a PDMS substrate and a thin film gold conductive layer. The low modulus of the PDMS and the minimal thickness of the gold layer are both useful in creating a compliant microcable electrode array.

The prior literature on PDMS-based electronics includes structures intended to be either compliant or compliant and stretchable [29-30]; however PDMS is elastomeric, so the devices are stretchable regardless of whether it is desirable for the application. Elastomeric electronics are generally comprised of an elastomer that integrates an electrical conductor in some fashion, commonly by mixing conductive particulates into the bulk elastomer. Examples of conductive particulates include conductive polymers, carbon nanotubes, and graphite [31-33]. Using bulk electrically conductive elastomers in micropatterned devices presents challenges in controlled, precise patterning of the conductive media and in incorporating the conductive component with selectively insulated and exposed regions. Thin-film gold metallization of PDMS addresses these considerations as gold is frequently patterned in microfabricated devices and silicone can tolerate some but not all standard process techniques [30]. Additionally, gold has relatively soft and ductile mechanical properties, which are advantageous for use in elastomer electronics. It also does not form a surface oxide, making it suitable for features such electrode recording sites.

2.1.3 PDMS micropatterning techniques

PDMS shape and topography can be controlled by several mechanisms, including photosensitive polymerization, laser ablation, reactive ion etching (RIE), and micromolding [27-28, 34-35]. While these techniques have been critical in developing silicone-rubber microstructures, they have limitations in applicability or convenience. Reactive ion etch micropatterning of PDMS for electrical devices is a time intensive process [29]. Laser ablation is traditionally a serial process, and in some instances, may

require registration. Photopatternable commercially available PDMS, may have a higher elastic modulus than desired for low-modulus applications (160 MPa, approximately two orders of magnitude greater than the PDMS used here) [30].

2.1.4 Comparison of PDMS to other materials

Sylgard 184 has an elastic modulus lower than other polymers commonly used in microelectronics (table 2.1). A low modulus is desirable in those biological applications in which it is beneficial for the stiffness of the device to match the stiffness of the tissue. PDMS still has a higher Young's modulus than many tissues (see table 2.2), but it is significantly lower than the alternative materials.

2.2 Fabrication approach

Micromolding when used alone does not create vias or other through-hole features. Although micromolding has been used extensively to pattern PDMS for non-electrical applications, molded microstructures with electrical functionality are less prevalent [35-36]. The advantages of micromolding include the reusable mold, potential bench-top fabrication. The simplicity of the design makes it amenable to high-through-put fabrication. Micromolding can be combined with spin-casting to create through-hole-containing PDMS membranes, and electrically insulating structures with selective exposure sites [26], [37].

The electrodes were made using a sequence of micromold-patterned spun-cast films, with the conductive material patterned via standard metallization techniques. The basic process flow is shown in Figure 2.3. The micromold was designed to pattern an

array of cable-like features that were framed within a larger sheet-like membrane. Depending on the process parameters, the sheet could be made to include perforations, so that it was net or web-like, to make the structure more permeable to gas and fluid circulation.

The micromold was made by patterning SU-8 on a standard 4" silicon wafer (step 1). The release layers and PDMS was spun-cast using standard spinner tools designed to pattern photoresist (step 2). The metallization was done via thermal evaporation (step 3). Thermal evaporation deposits the metal with less energy to the substrate than E-beam evaporation or ion-beam sputtering. Using a low-energy method was a consideration because the PDMS is susceptible to mechanical property changes due to radiation[38]. The metal patterning was done using both photoresist-based lift-off and stenciling (step 4). The microcables' top insulating layer and their recording sites were defined using photoresist (step 5). After the photoresist was patterned, the insulating PDMS layer was spun and cured (step 6). The photoresist and release layers were dissolved to produce the free-standing microcable electrode array.

The though-holes created by spun-cast, micromolding (SCμM) can be used to create net-like membranes by spinning the film until its thickness is less than the height of the mold features. The net-like geometry is useful in biological applications because it is more conformal than a planar sheet and does not isolate the target structure from gas and fluid exchange. A simple micromold and its released elastomer membrane, demonstrating the SCμM concept, are shown in Figure 2.4. The released membrane is a net-like structure with through-holes created by the mold posts. SCμM has been used

here to create an electrically active net-like array, the strands of which are referred to here as microcables. The multiple layers of molds and traditional metallization patterning are combined in the process described here to create arrays of microcables.

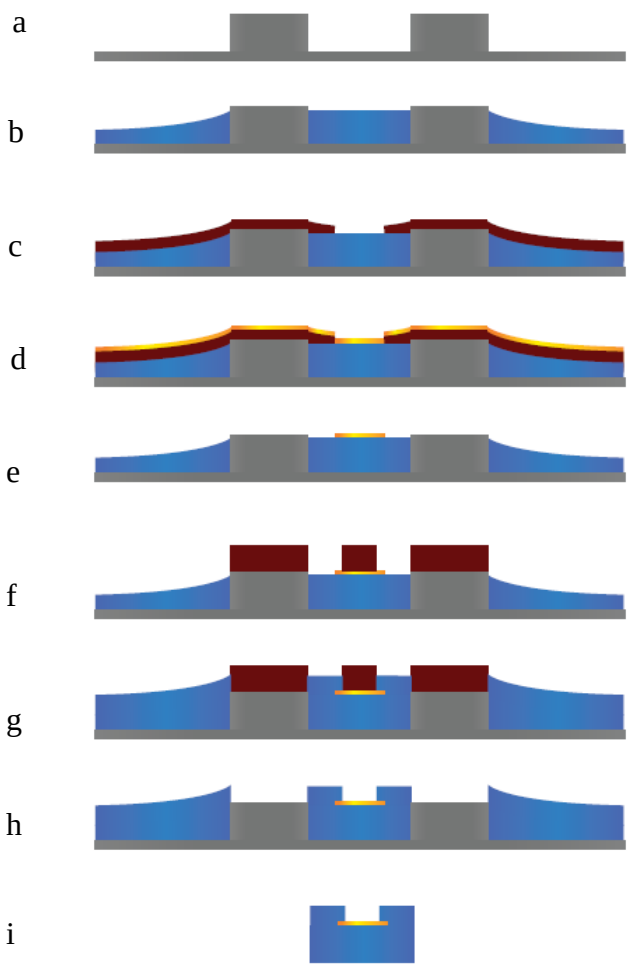

Figure 2.3. The three dimensional process flow is shown to the left, with the two-dimensoinal view of the layers during the process shown right. The mold (a) is sequentially covered with dextran and agarose release layers and PDMS (b). The thickness of the PDMS across the membrane varies depending on the spacing and geometry of the mold features. The electrical lead patterning is done using traditional metallization lift-off (c-e). A negative image of the leads is patterned with photoresist (c) and metal is deposited over the sample (d). Dissolving the photoresist leaves the patterned metal trace on the PDMS substrate (e). The top insulating layer is defined using a sacrificial photoresist mold (f-h). The sidewalls of the microcable and the access node are defined with photoresist (f). The top insulating layer of PDMS is spun-cast and cured (g). The photoresist is dissolved (h) and the microcables are released from the mold (i).

The stretch-tolerant microcables were fabricated in a dog-bone configuration that could be converted into a straight-shank-style array. The dog-bone configuration was

designed for the purpose of stretch tests and converted into a shank array for *in vivo* testing and implantation (Figure 2.5). The arrays for implantation and *in vivo* testing were cut along one edge of the frame to create and array of shanks that were free at the distal end.

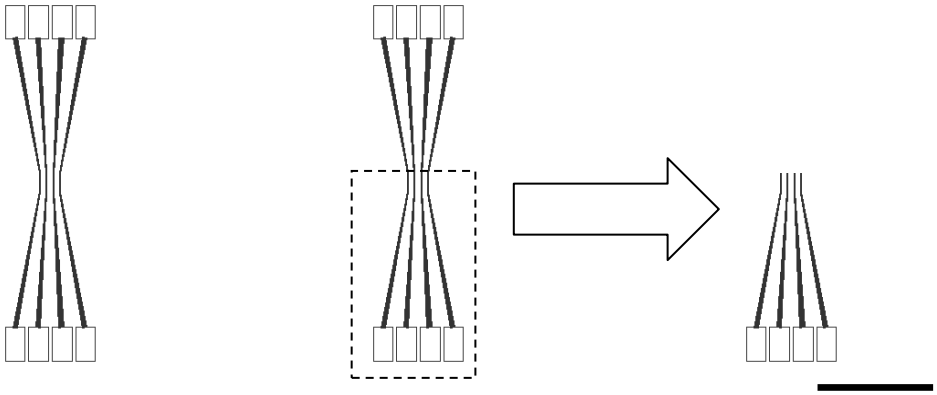

Figure 2.4: The dog-bone style is shown to the left. To convert the dog-bone configuration to a shank-style array, the portion outside the dotted box (center) was cut away. The shank-style array is shown to the right. Scale bar is 1 cm.

2.2.1 Methods

The mold for the array was photolithographically patterned with SU-8 photoepoxy. The photomasks were emulsion-printed mylar sheets (Fine Line Imaging; Colorado Springs, CO). The mold was made with multiple layers of SU-8. A test-grade silicon wafer was coated with a 2 μm layer of SU-8 2002, (spin recipe: 500/100/5, 1000/500/30; SB, 95° C hotplate 2 m) flood exposed (50 mJ) and hard baked. (95 ° C hotplate 2 m) A second 16 μm thick layer of SU-8 2015 was spun-cast (spin recipe: 500/100/5, 2000/500/30; SB: 95° C hotplate , 3.5 m) , patterned (145 mJ; post-exposure

bakes: 95° C hotplate , 4.5 m), and developed as the mold substrate. A third layer, 26 μm thick, of SU-8 2015 was deposited on the substrate (spin recipe: 500/100/5, 2000/500/30; SB: 95° C hotplate , 3.5 m, exposes: 200 mJ, post exposure bake: 95° C hotplate , 4.5 m, developed using SU-8 developer) to increase the height of a sub-set of the mesh posts (26 μm vs. 16 μm) to create mesh through-holes throughout the membrane. The heights of the molds were confirmed with an optical micrometer (Quadra-Chek 200, Metronics; Bedford, NH). All posts were 3600 μm^2 in area, spaced 20 μm edge-to-edge. The walls creating the microcables were 30 μm wide.

The release layer, 20 % v/w dextran (Sigma; St Louis MO) in water was spun on the mold after a 30 second plasma discharge (EMS 100 glow discharge unit, Electron Microscopy Sciences; Hatfield, PA). The dextran was applied twice, followed by a 1% w/v agarose (Sigma) in water spin coat. The dextran and agarose were spun 40s at 800 rpm, and each layer was dried (hotplate, 100 ° C, 30s) before the next application. Applying the agarose required heating it until the gel melted and spin-casting the melted solution. Sylgard 184 PDMS was then spun onto the mold at 4000 rpm for 4 min. The thickness of the spun cast silicone was 16 μm. Figure 2.5 A1&2 shows the first layer of PDMS on the SU-8 mold. The micrographs of this step, Figure 2.5 A3&4, show the mold before and after the PDMS layer.

The gold leads were patterned using lift-off metallization and thermal deposition (Figure 2.5 B1&2). Before the lift-off resist was applied, the silicone substrate was treated with a 30s negative plasma discharge to improve photoresist dispersion on the PDMS. Negative resist, NR9-8000 (Futurrex; Franklin, NJ) was deposited 9 μm thick, pre and post-exposure baked on a hotplate at 95 °C, for 60 s and developed with RD-6

developer (dilute tetramethyl ammonium hydroxide (TMAH), with a proprietary additive, Futurrex). The exposure dose was 125 mJ, which is lower than the dose recommended by the manufacturer; however, the resulting undercut in the resist improved its release during lift-off. PVD 75 filament evaporator (Kurt J Lesker; Clairton, PA) was used for the thermal deposition of a 5 nm chrome adhesion layer and a 50 nm gold layer. The deposition was done at 10^{-5} Torr. After deposition, the lift-off resist was removed with aqueous RR3 resist stripper (Futurrex; concentrated tetramethyl ammonium hydroxide), rinsed with deionized water and dried. The film thickness was confirmed by doing a simultaneous metallization of a glass slide. The thickness of the deposition was determined by a resistance measurement of the metallized slide, via a four-point probe (Signatone; Gilroy, CA).

The photoresist posts used to pattern a sacrificial mold are shown in Figure 2.6C. The photoresist mold preserves the microcable structure and creates electrical access nodes along the cable length. The NR9-8000 photoresist is spun 30 μm thick, pre and post exposure baked in an oven at 85 °C, for five minutes, patterned with an exposure dose of 850 mJ, and developed with RD-6 developer. In Figure 2.5 C, the cable and mold are shown before and after another layer of PDMS is spun-cast. (4000rpm, 8 min; cured at 100° C for 10 min.) After curing, the photoresist is removed with RR3, leaving the metal exposed at a selectively uninsulated access node (Figure 2.5 D). Note that in the process, the photoresist shields the gold surface from contact with the PDMS. After the PDMS is cured, dissolving the photoresist in a bath of TMAH creates an uninsulated site. The array is then released in a water bath to dissolve the agarose and dextran. A

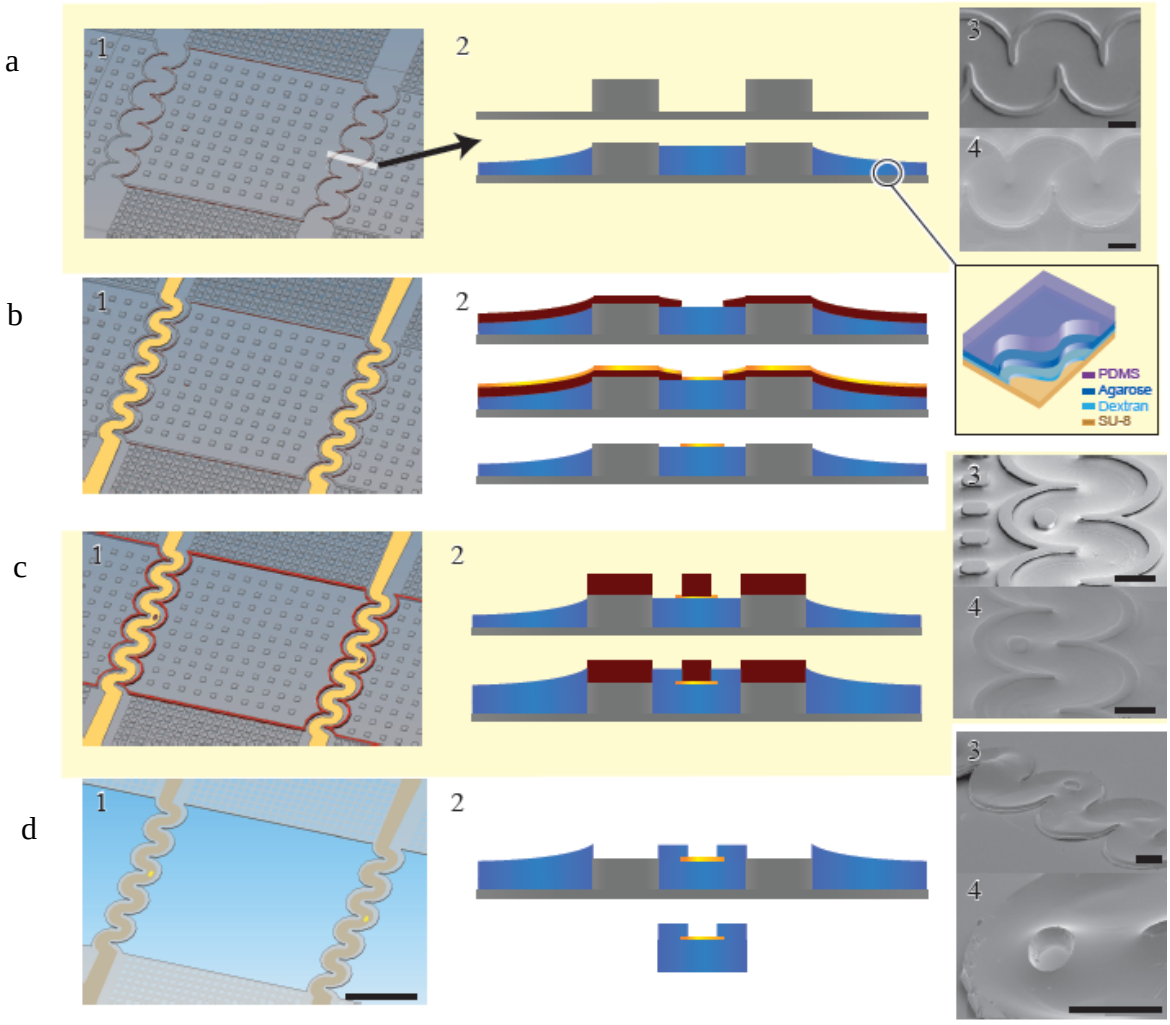

Figure 2.5: The main steps in the process flow are shown in graphical sequence. The three dimensional representation (left) highlights specific steps in the process, while the corresponding process flow is shown in its entirety in the middle column. Relevant scanning electron micrographs of the microcables during processing are shown in the right column. (a3-4) The mold is shown with and without the PDMS layer. (c3-4) The photoresist pattern for defining the top insulating layer is shown before and after the top layer is spun-cast and cured. (d3-4) The microcable is shown after release, with a an enlarged view of the recording site. The microcable array is shown in micrographs with the photoresist mold and (c4) after the top layer of PDMS has been spun cast. (d1-2) After the photoresist is dissolved, the access node is exposed and the device is ready to be released. (d3-4) A water bath is used to dissolve the agarose and dextran and the microcable array is separated from the mold. The scale bars are 500 μm for the drawing (left) and 100 μm for the micrographs (right).

single released microcable is shown in Figure 2.5 D3. The access node is shown in a magnified view in Figure 2.5 D4**.** The 4" wafer on which the reusable molds were patterned is shown in Figure 2.6. The molds were arranged equidistant from the center of the wafer so that they received similar centripetal force on the spinner, and thus, similar PDMS thicknesses. After release, the array is placed on a microscope slide for mechanical support. For electrical tests, the pads at the ends of the leads are connected to hook-up wire with electrically conductive silicone (Silicone Solutions; Twinsburg, OH). A multimeter (Fluke 179 True RMA multimeter, Fluke Inc.; Everett, WA) was attached to the hook-up wire on either end of each microcable for the resistance measurement.

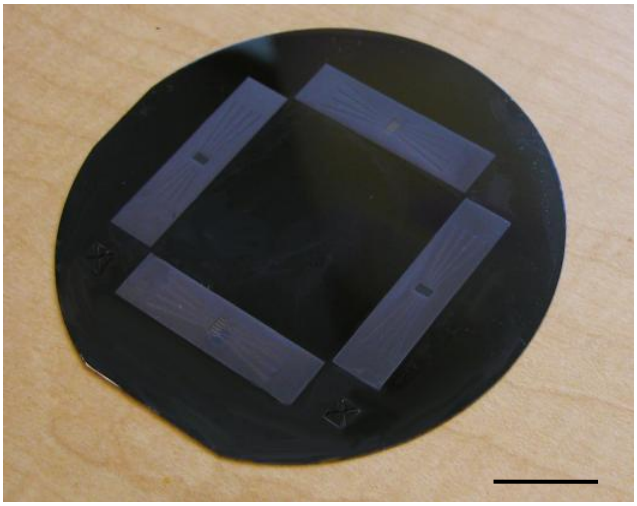

Figure 2.6: The wafer with for molds for the electrode arrays is shown above on a 4" wafer. The molds are arranged so that the centripetal force is approximately the same for each mold and across the span of each mold. The ends of the mold will see a higher force than the center because they are farther from the center of the wafer. However, because of the placement of the molds on the periphery of the wafer, the relative difference in distance from the center of the individual elements in each mold is minimal. Therefore, the discrepancies are not significant enough to be noticeable in the performance of the electrode array. Scale bar is two cm.

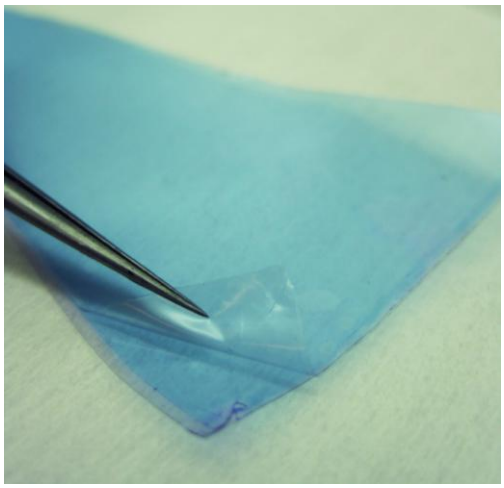

Figure 2.7: Riston© dry resist is a photosensitive (blue) film. It is stored between two layers of cellophane. One layer of cellophane is removed in order to attach the Riston© to the substrate. In typical use, after exposure, the top layer of cellophane is removed so the film may be developed. In this instance, the top layer was removed after the top layer of PDMS was spun-cast, and before it was cured.

The pads were covered with dry-film photoresist (Riston MultiMaster115; Dupont, Wilmington, DE) prior to the application of the top insulating PDMS layer. The film was 40 μm thick. Prior to application it was cut into squares that spanned the length of the four bond pads. One side of the cellophane backing was removed (Figure 2.7). The exposed side was pressed into place on the wafer by hand and heated on the hotplate at 85 °C for five minutes for improved adhesion. After the PDMS was spun on the wafer and cured at 100 °C for ten minutes, the top cellophane layer of the dry-film resist was peeled off with tweezers, taking a thin coating of PDMS with it (Figure 2.8). The resist, which has not been exposed to UV in this process, was removed using RBP DX-40 (DuPont), a potassium carbonate developer.

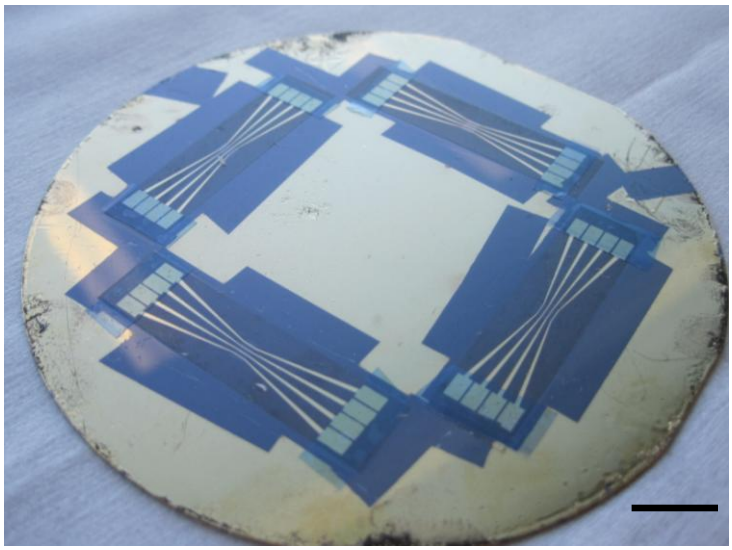

Figure 2.8: The Riston© is shown after it has been applied to the bond-pads of the electrode arrays. The microelectrode arrays, at this point, have the bottom layer of PDMS, the patterned metal (the pattern on the whole wafer is due to the stencils, which are taped into place during metallization), and the photoresist patterning the exposure sites on the microcables. After the top layer of PDMS is spun cast, the top cellophane layer on the Riston is removed. The PDMS is cured, and then the (unexposed) Riston is dissolved in its developer, leaving the bond pads exposed. Scale bar is 1 cm.

2.2.2 Fabrication results

The microcables were 2 mm long and 200 μm wide. The access sites on the top insulated area were ovals 50 x 100 μm (approximate area: 4000 μm^2). The gold leads on the microcables were 100 μm wide. The microcable array leads were centered within a larger elastomer substrate for ease of handling (Figure 2.9**)**. The electrical leads transitioned into wider gold tracks on the substrate that terminated in square pads that could be easily attached to hook-up wires for testing.

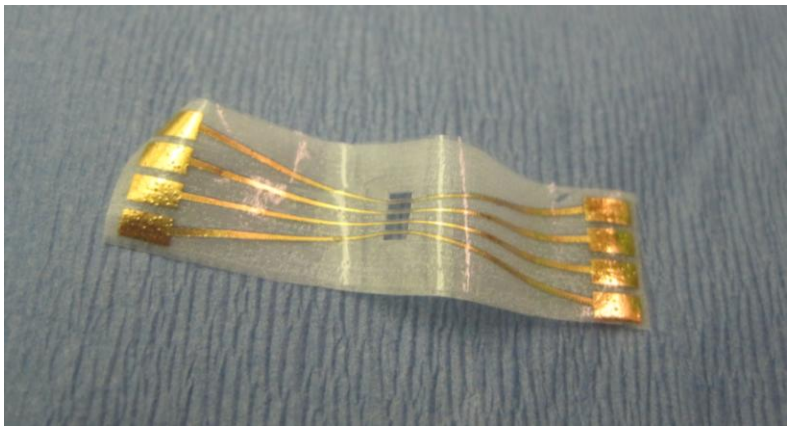

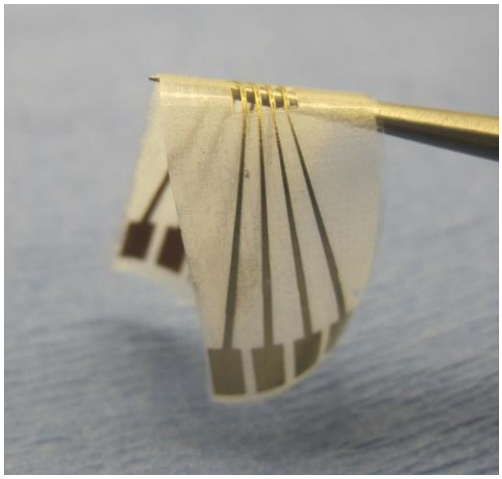

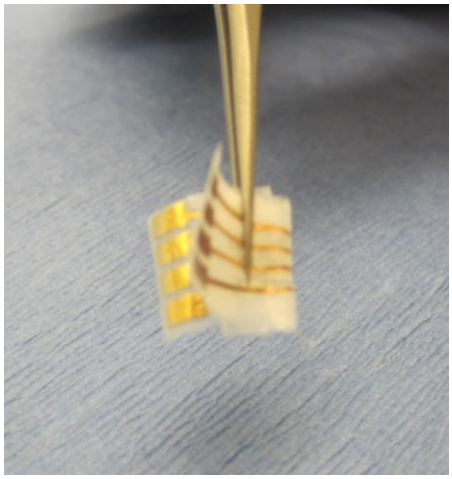

Figure 2.9 a-c: The device is shown in several configurations to highlight the flexibility and conformability of the array. The design shown here, described as a "dog-bone" style (where each lead is exposed at two ends), was chosen for ease of use in electrical resistance monitoring, which was a component in cyclic strain fatigue tests (see table 3). The dog-bone style is adaptable to shank-style probes by physically cutting the array in half, at the end of the window defining the microcables. A mold can also be made specifically for microcables, however, for research purposes, the design described here was found to be easily adaptable. Scale bar: 1 cm.

The SU-8 micromold and thick photoresist have been used to specify the geometry of an elastomer-based microelectrode array. The walls and posts define microcables and through-holes in the spun-cast PDMS membrane. As an example of the types of structures that can be fabricated using this process, consider the free-floating microcables shown in Figures 2.11. The straight microcables have been placed flat on a

slide to show their planar shape (a) and in a water bath to demonstrate their mechanical compliance (b). The membrane framing the microcable array has through-holes from a subset of the posts, demonstrating that the SCμM process can be used to make micropatterned membranes several square centimeters in area. The recording site, patterned with sacrificial photoresist is shown on one of the microcables in Figure 2.12. The sligltly wrinkled texture of the gold film is visible in Figure 2.13

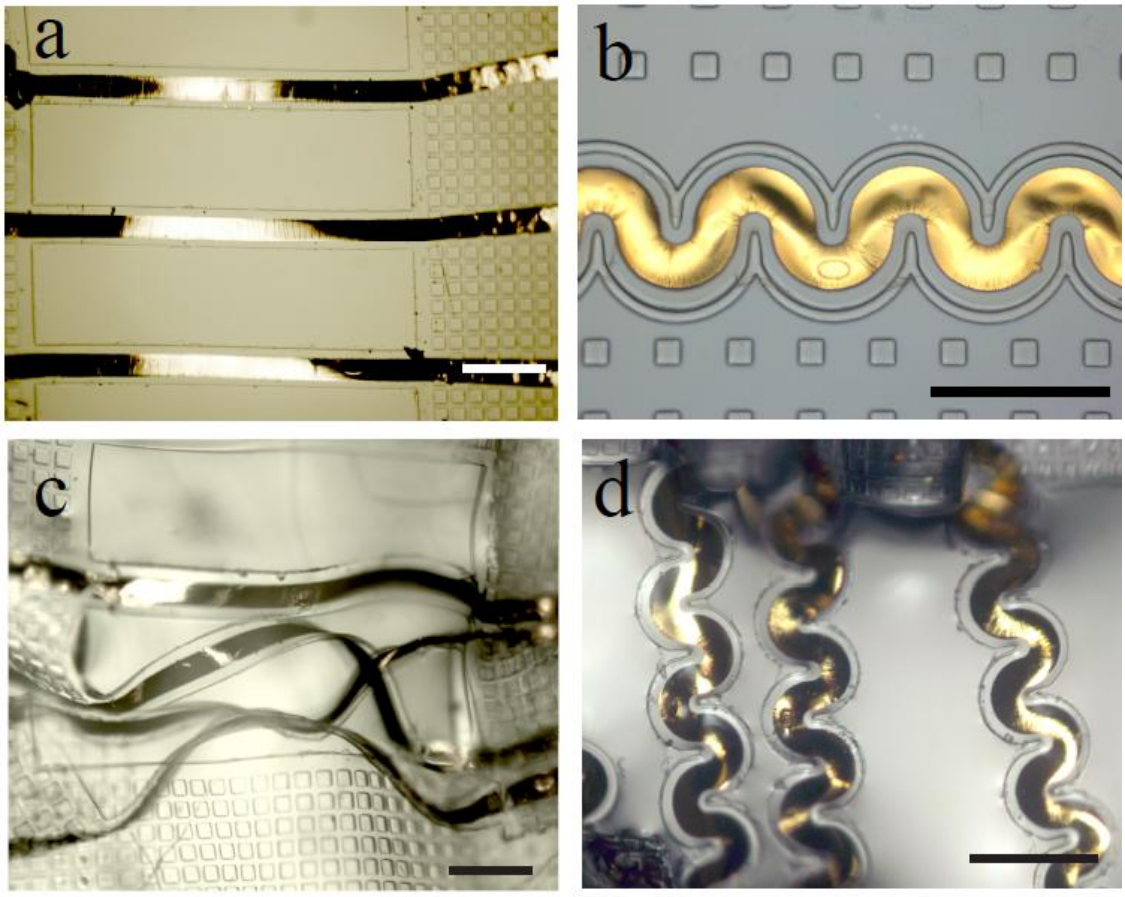

Figure 2.11: The photomicrographs show completed devices of straight (left) and sinusoidal (right) microcables. The arrays are shown laid flat (a-b) and in a water bath (c-d). The microcables are flexible and compliant after release, as demonstrated by their free-form conformation in the water bath. The scale bars are 400 μm.

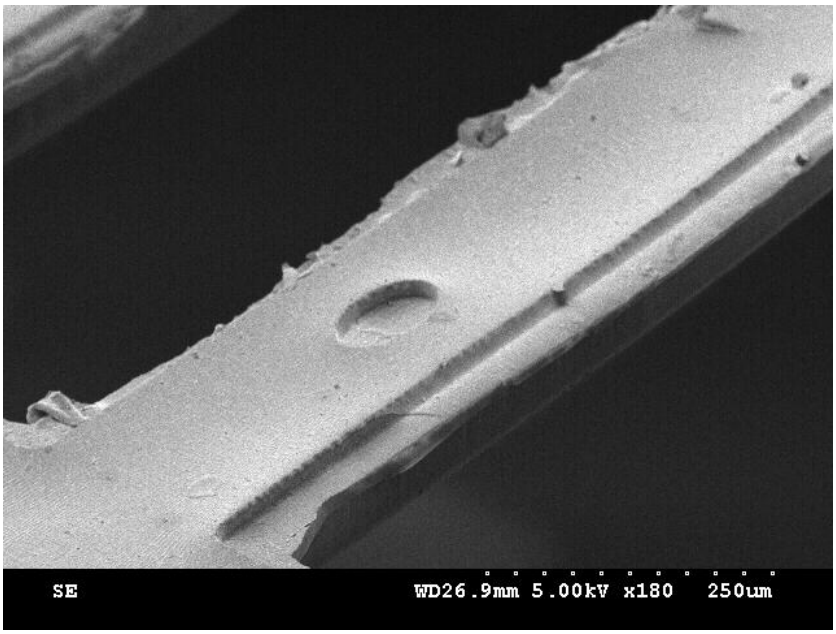

Figure 2.12: The straight microcable array was successfully patterned and released and an example microcable is shown above. The top PDMS layer is differentiable from the bottom by the step profile. The top PDMS layer was patterned using photoresist and spin casting.

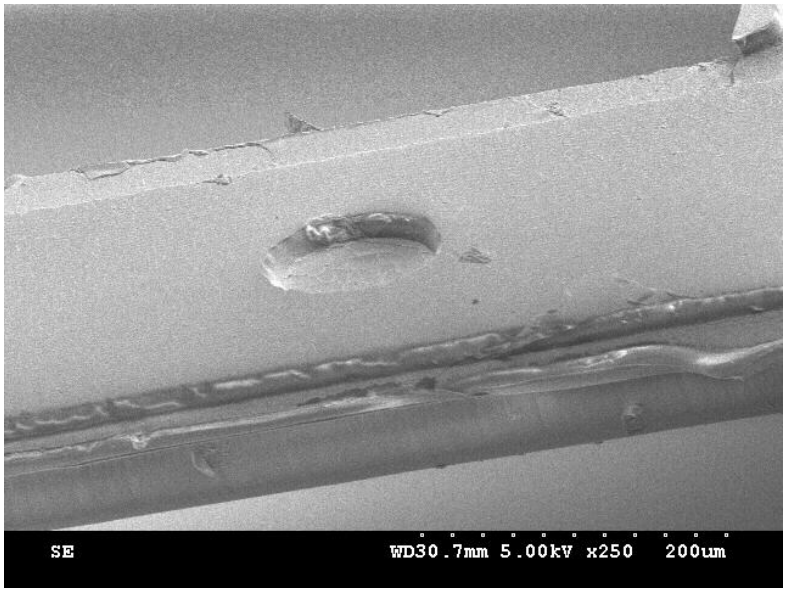

Figure 2.13: An expanded view of the recording site is shown above. The cracks in the gold film differentiate it by texture from the PDMS, indicating that the gold surface is successfully exposed.

The dry-film resist was used to insulate the gold film. There were several criteria that made dry-film resist better suited than more common sacrificial materials. The spin-casting layer leaves a PDMS film on larger topologies. The SU-8 mold features were tens of microns wide. In the spin casting process, a larger feature will retain a layer of PDMS that is thick enough to act as a barrier to chemical etches or to remain mechanically intact after the separation from the mold. When the feature is increased in width to several hundreds of microns, the feature retains a thicker layer of PDMS; the through-hole patterning is only functional for features that are within a size limit. The estimated size limit is a span of over 200 μm, as determined from earlier mask designs not detailed here. The bond pad area is larger than this limit and so it cannot be patterned with photoresist in the same manner the electrical access sites are. The dry-film resist has the top layer of cellophane which can be peeled off to remove this PDMS layer. At the same time, because the dry-film resist remains, it can be done without damaging the gold film. The dry-film resist develops away cleanly without leaving a residue. The developer is relatively gentle and does not give any indication of damaging the gold film or the PDMS.

2.2.3 Electrical and metrological characterization results

The average resistance for each lead after release was 136 Ω (n=6, SD= 30 Ω) as measured individually via a multimeter. The conductive silicone used to attach the hook-up wire to the contact pads (Figure 2.14) at either end of the cable had a reported volume resistance of 0.01 Ω·cm [39], and so was expected to contribute minimally to the total

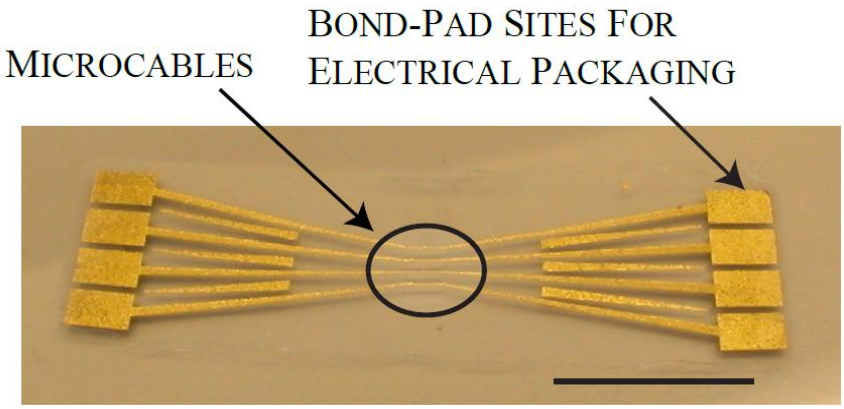

Figure 2.14: The microcable array is centered within a larger membrane, shown above, that has a footprint approximately 1.5 x 4 cm. The rectangular gold pads on each end are to facilitate packaging for electrical testing. The gold, triangle-shaped features between the leads were created to ease resist removal during metallization lift-off by reducing the contiguous area to be attacked by the resist stripper. As these features are artifacts of processing they are not electrically functional components of the array. The scale bar is 1 cm.

resistance, assuming it was in good contact with the sample. The thickness (50 nm) was determined by measuring the resistance via a four point probe (Signatone; Gilroy, CA) and Wyko optical profilometer (Veeco; Plainview, NY) of a film deposited on a glass slide under the same conditions. The calculated value for the leads, with 50 nm of gold is 50 Ω. Prior to release of the microcables from the mold, the average resistance was 89 Ω (n=6; SD=6 Ω) the resistance and standard deviation increases suggest microcracks. Cracking of gold thin-films on elastomers has been documented in the literature [30]; when the film is well-adhered to the substrate, the cracks that are formed in the strained film remain localized because the substrate responds to the strain evenly and prevents stress localization thereby limiting the propagation of individual cracks in the film. The larger than expected resistance in the unreleased leads (i.e. prior to any microcracking) may be due to the thinness of the film. The grain size ranged from approximately 25 to

40 nm as measured from scanning electron microscope imaging (data not shown). The proximity of the grain size values to the film thickness, combined with the stress induced from the wrinkled topography of the gold and may have contributed to the increased resistance because this disparity was not found in films deposited on rigid glass slides.

2.3 Considerations when using the SCμM process

2.3.1 Mold Design

When designing a mold for a SCμM structure, the spacing of the mold features and the resulting effect on material retention must be taken into account. PDMS is retained between the posts during the spin-casting in a space and geometry dependent manner; if the mold is an array of posts with the same size and spacing, the membrane will have a consistent thickness. An example of a membrane released from its mold is shown in Figure 2.15. If different features (e.g. posts) have different shapes and spacing, the parameters of one feature set will constrain the spacing and shape of the surrounding features; otherwise, the thickness of the membrane will be inconsistent (Figure 2.16**),** and the thinner areas can make the membrane fragile and difficult to handle.

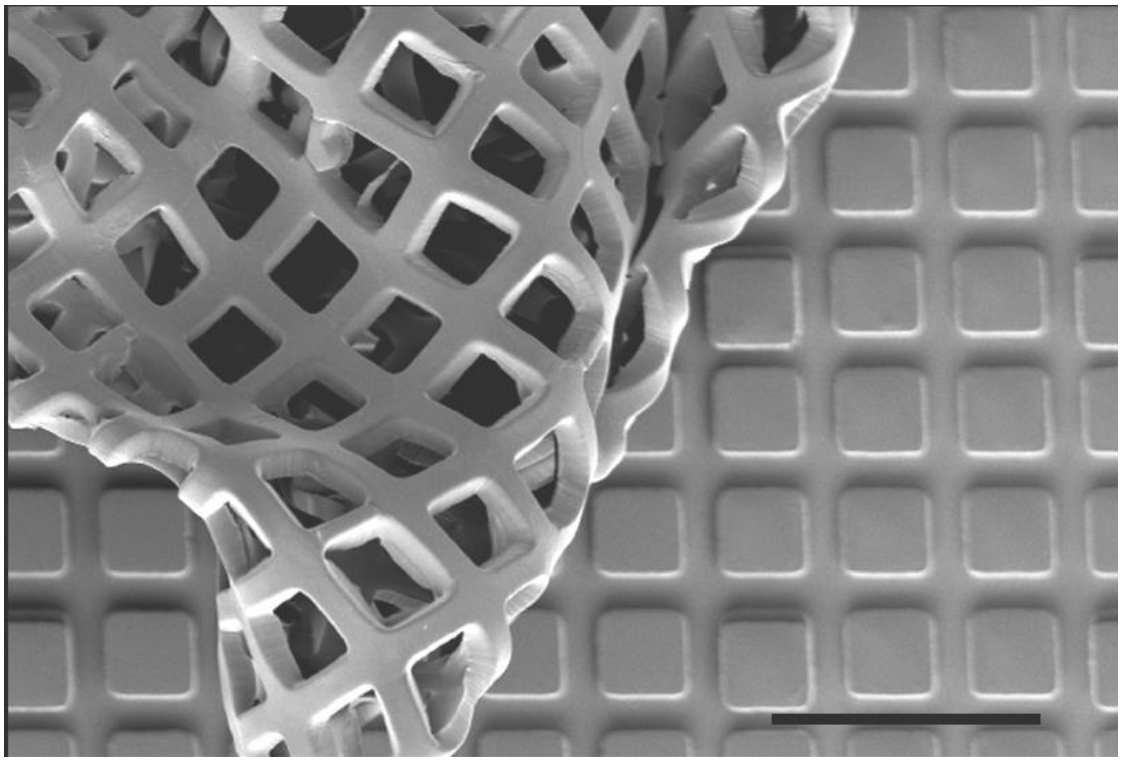

Figure 2.15: A PDMS membrane is shown as it is pulled back from the SU-8 on which it was spun-cast. The PDMS was spun-cast thin enough on the SU-8 mold so that through holes in the membrane are created. The membrane thickness and mold height are both 16 μm. The scale bar is 200 μm

The amount of PDMS retained for a given spin speed and duration depends on the post spacing, with narrower post spacings retaining more PDMS. This feature can be exploited intentionally if variations in thickness are desirable; it is used here to facilitate the separation of the microcables by creating thin, easily removed segments that become open spaces after the membrane is released from the mold. The mold design for the surrounding membrane was constrained by the dimensions and geometry of the microcables. The sinusoidal walls define the cables and the surrounding posts retain PDMS to create a membrane that frames the microcable array (Figure 2.17). If the mold

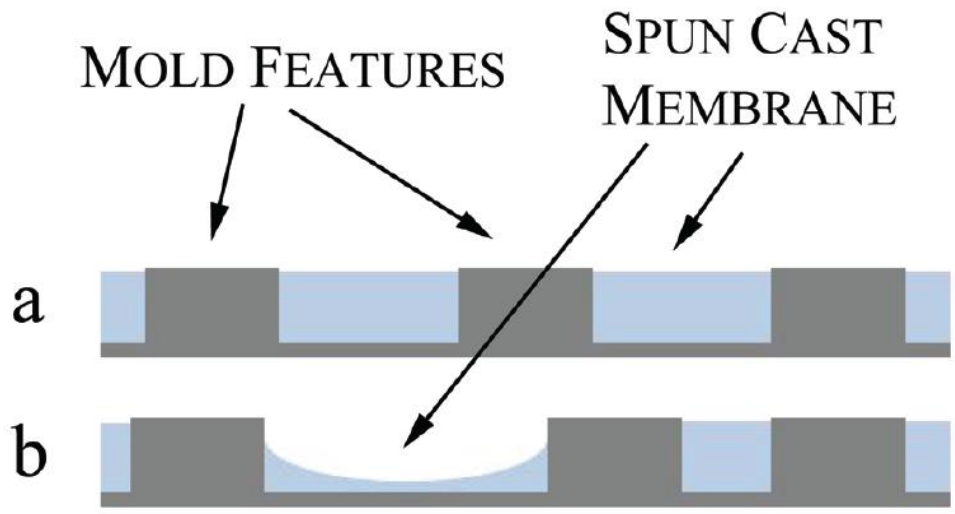

Figure 2.16: The feature spacing determines the thickness of a spun-cast film. (a) Evenly spaced mold features (within a finite spacing limitation) produce membranes with an even thickness. (b) Variations in the feature spacing create differences in the film thickness.

consisted solely of the microcable features, the surrounding area required for handling and packaging would be too thin and too fragile to handle without breaking. The posts were selectively removed from metalized areas to prevent an electrical discontinuity due to post placement. The membrane framing the microcables maintains a semi-open geometry with though holes created by the subset of taller posts (Figure 2.18). The post spacing, 20 μm, edge to edge, is smaller than the 200 μm wall spacing for the microcables because it has been observed experimentally that longer features, orthogonal to the spin casting centrifugal force retain more PDMS retained; the 2 mm long microcable-defining walls, two millimeters long, retain approximately as much PDMS as the 60μm square post features even though the spacing between the microcable defining walls is 200 μm and the post spacing is 30 μm.

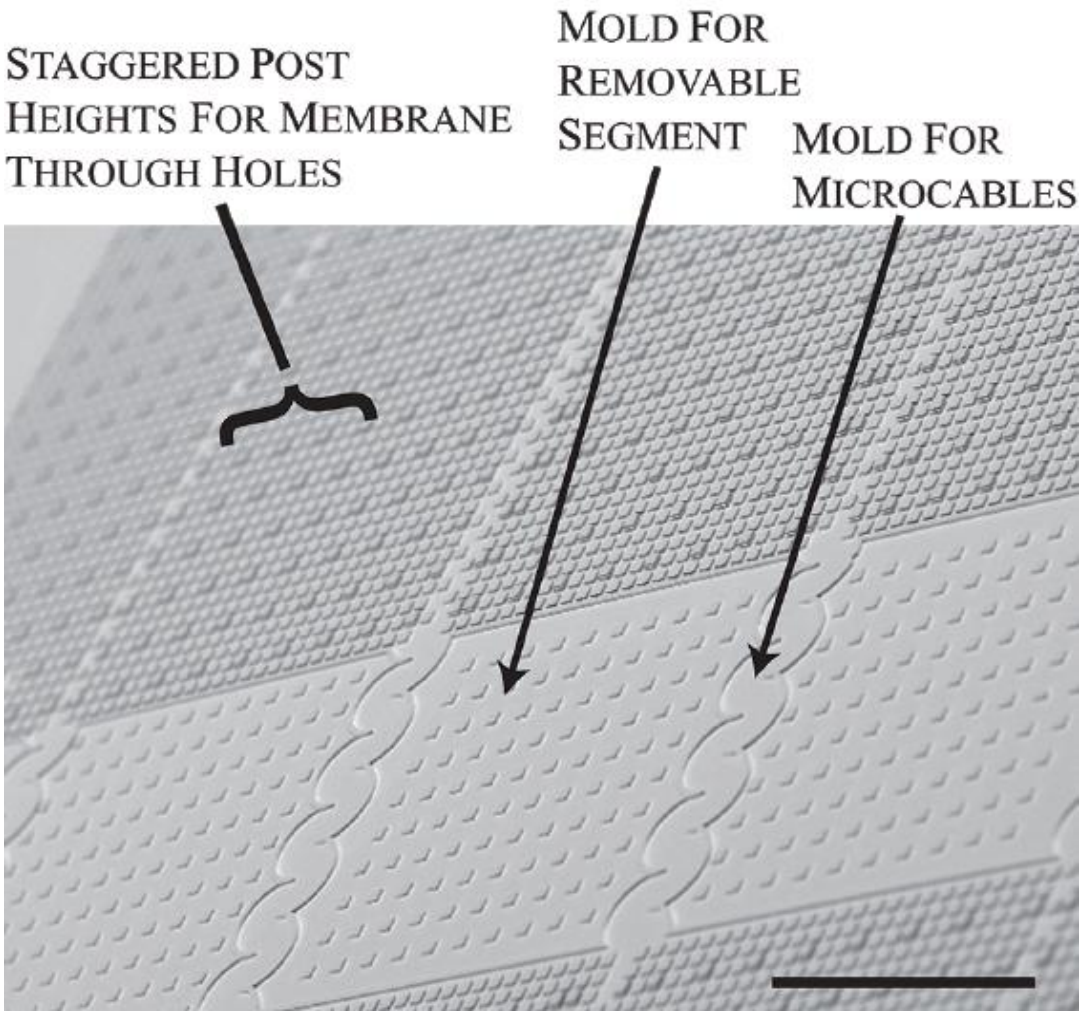

Figure 2.17: The SU-8 mold for the net-like array includes sinusoidal lines and multi-height posts to create an array of microcables and through holes in the surrounding membrane. The spacing of the posts between the microcable features is farther apart than the spacing in the rest of the mold because the wider post spacing allows for a thinner film, which is easily removed during the release of the microcable array from the mold. The scale bar is 1 mm.

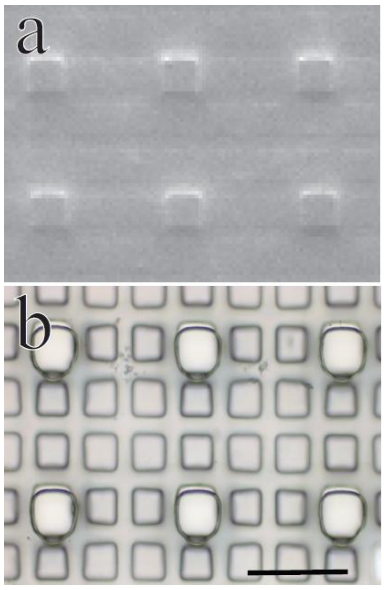

Figure 2.18: The SU-8 mold is coated with PDMS (a). The mold features are still visible through the cured layer of PDMS. As seen in the released PDMS membrane (b), the taller posts make through holes, while the shorter surrounding posts do not. The shorter set of posts created a substrate with a thickness and durability suitable for handling and metallization patterning. The taller set of posts was designed to allow fluid and gas exchange across the membrane. The scale bar is 200 μm.

2.3.2 Selecting process-related chemicals for PDMS-based devices

The chemicals traditionally used for feature patterning in microelectronics processing are not generally suitable for use on PDMS because it absorbs many organics and is vulnerable to degradation from some highly acidic and alkaline aqueous solutions. PDMS absorption or degradation by common solvents and solutions used in chemical and microelectronics processing were systematically tested by Lee *et al* [40]. The compatibility to 38 polar and nonpolar solvents is listed based on absorption and the degradative effect of acidic or basic solutions is tested. Many organics are absorbed by PDMS, which may or may not be a problem depending on the application. Concentrated

sulfuric and as well as dipropylamine and fluoride containing compounds (e.g. HF) either degraded or dissolved the PDMS.

The problems this generates are two-fold. First, microfabrication processing frequently relies on organic or strongly alkaline/acidic etchants or developers. If the etchant or developer partitions into the substrate, its residue can interfere with subsequent steps. Additionally, we have observed that if the PDMS is patterned with metal, the swelling from absorption of organics causes the metal to fracture, destroying the electrical continuity.

The processing here uses aqueous materials when possible. When resists and developers are used, the parameters were optimized to minimize exposure to the substrate. The release layers to remove the microcable array from the SU-8 mold are dextran, a water-soluble starch molecule, and agarose, a water-soluble polysaccharide molecule that deters the dextran dissolution during processing, particularly the metallization lift-off. The dextran dissolves easily in water and has been used previously as a release layer for microfabrication [41]. The aqueous-based processing dissolves enough of the dextran (when used alone) that it partially releases the microcables off the SU-8 mold. This is problematic because the top, insulating PDMS layer is patterned using an aligned photomask, requiring the features to be in their original orientation on the mold. The agarose layer acts as a slowly dissolving seal over the quickly dissolving dextran. The agarose was not simply used in place of the dextran because it gels at room temperature at very low concentrations (<1% w/v solution with water), making its application as bulk release layer difficult. The dextran release layer (20% w/v solution in water; liquid at room temperature), by contrast, was applied over two applications, and

supplies enough bulk dissolvable material to facilitate release of the cables. When the microcables are ready for release, the mold is placed in a water bath at room temperature for several hours to allow the agarose and dextran to dissolve. After the release layers are solubilized, the microcables are easily pulled from the SU-8 mold with a pair of tweezers. The mold is clean after the cable release, so can it be reused multiple times.

2.4 Optimization of the fabrication process

The process was iteratively improved for more both more durable structures and an improved yield. For example, the delicacy of the metallization lift-off was substituted by a cleaner, simpler stencil-patterning step. The yield of the electrodes improved after the PDMS substrate was mixed to include a higher tear strength component. The first prototype described here was electrically conductive after release, but was frequently not measurably conductive after the device was packaged for use, i.e. the electrodes were compliant and could tolerate careful handling, but their fragility was a practical limitation for the application. The contributing factors were identified from the literature on the fracture behavior thin metal films mounted to substrates with an elastic modulus several orders of magnitude lower than that of the bulk metal. Generally, the durability and integrity of the film is a function of the film and substrate thickness and relative elastic moduli, and of the adhesion between the two materials. These factors were integrated into a second process flow for durable, conductive electrodes.

The factors that we varied to increase the stretch-tolerance of a gold film on an elastomer substrate were:

- Optimizing the mold for thicker substrates
- Decreasing gold film thickness
- Increasing the ultimate tensile strength and increasing the elastic extensibility per unit load on the substrate

Other variables not tested but identified as plausible contributing factors in the literature, include the modulus of the substrate and the metal and the film-substrate adhesion [42-43]. The deleterious effects of processing on the film were shown to increase the film resistance, but we did not test whether there was also an effect on stretch-tolerance.

The substrate thickness was increased to 85 μm to improve the durability of the microcables. The mold needed to be made taller for the thicker features. The mold design also needed to be revised to account for a change in the aspect ratio from features that were approximately three to four times as wide as the height to features that had a taller height than width. This change in aspect ratio made the demolding more difficult for densely spaced features. The feature spacing was increased and simplified until devices could be successfully demolded without tearing.

The metallization was done via a stencil that was fixed to the substrate prior to deposition. The use of a stencil instead of photoresist-based lift-off precluded the need for the agarose sealing of the dextrose and it was subsequently left off the final protocol. The top insulating layer was patterned with photoresist in the same manner described above.

The polymer was also changed to a polymer mix: Sylgard 184 and Sylgard 186 in a 1:1 wt ratio. The Sylgard 186 is described as having higher tear and tensile strengths [44-45] and was added to improve the durability of the microcable arrays. It was not used exclusively because it is not easily spin-castable as its viscosity is 65000 centipoise, compared to 3900 centipose for Sylgard 184 (a difference of approximately 17-fold) [46]. Because of the high-viscosity, it does not spin-cast into a smooth film; however a mixture of the two polymers can be spin-cast into a smooth film. The polymer mixture also shows improved durability as identified by qualitative experience in handling the two versions of the spun-cast membranes. The quantification of the mechanical properties will be described below.

2.4.1 Optimizing the mold

The mold for the array was photolithographically patterned with multiple layers of SU-8. A test-grade silicon wafer was coated with a 2 μm layer of SU-8 2002, flood exposed and hard baked. A second 80 μm thick layer of SU-8 2025 was spun-cast, patterned, and developed as the mold substrate (Figure 2.18-19). The heights of the molds were confirmed with an optical micrometer (Quadra-Chek 200). All posts were 360 μm^2 in area, spaced 20 μm edge-to-edge. The walls creating the microcables were 30 μm wide.

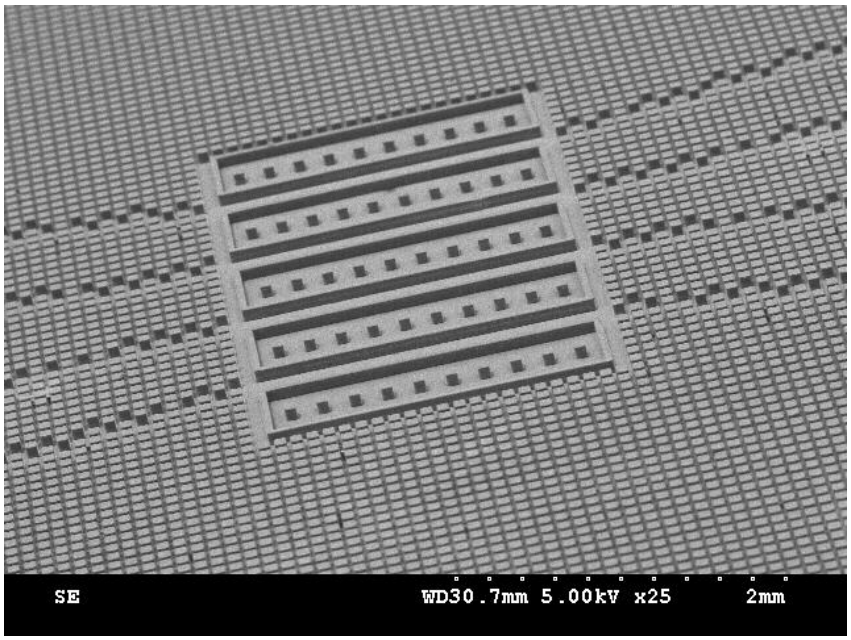

Figure 2.18: The second version of the mold used straight microcables, that were aligned more closely for the intended application of shank-style electrode array. The use of a rat as the animal model, constrained the size of the array.

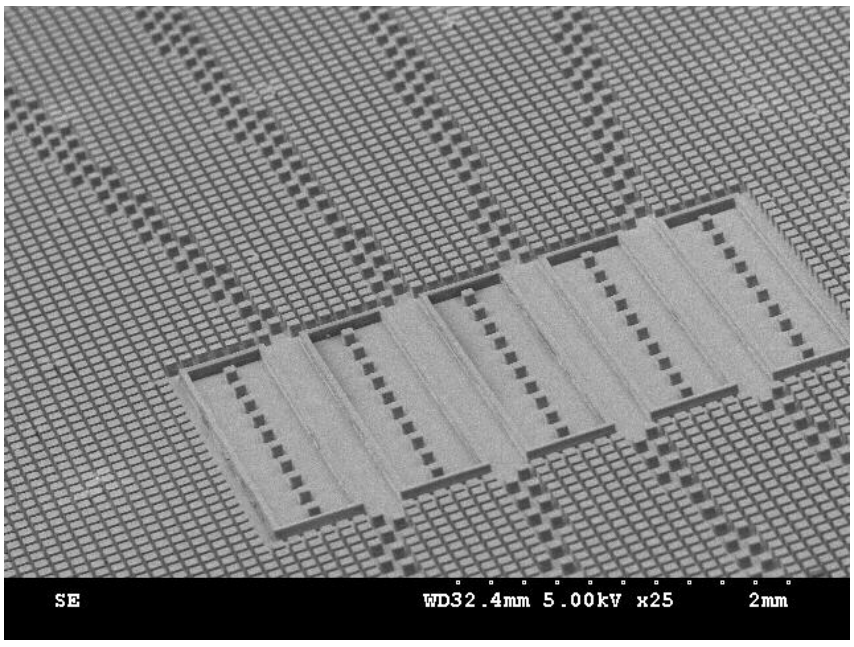

Figure 2.19: The second mold, shown from a second perspective, was increased in height to 80 μm. The spacing and geometry of the surrounding posts was kept the same.

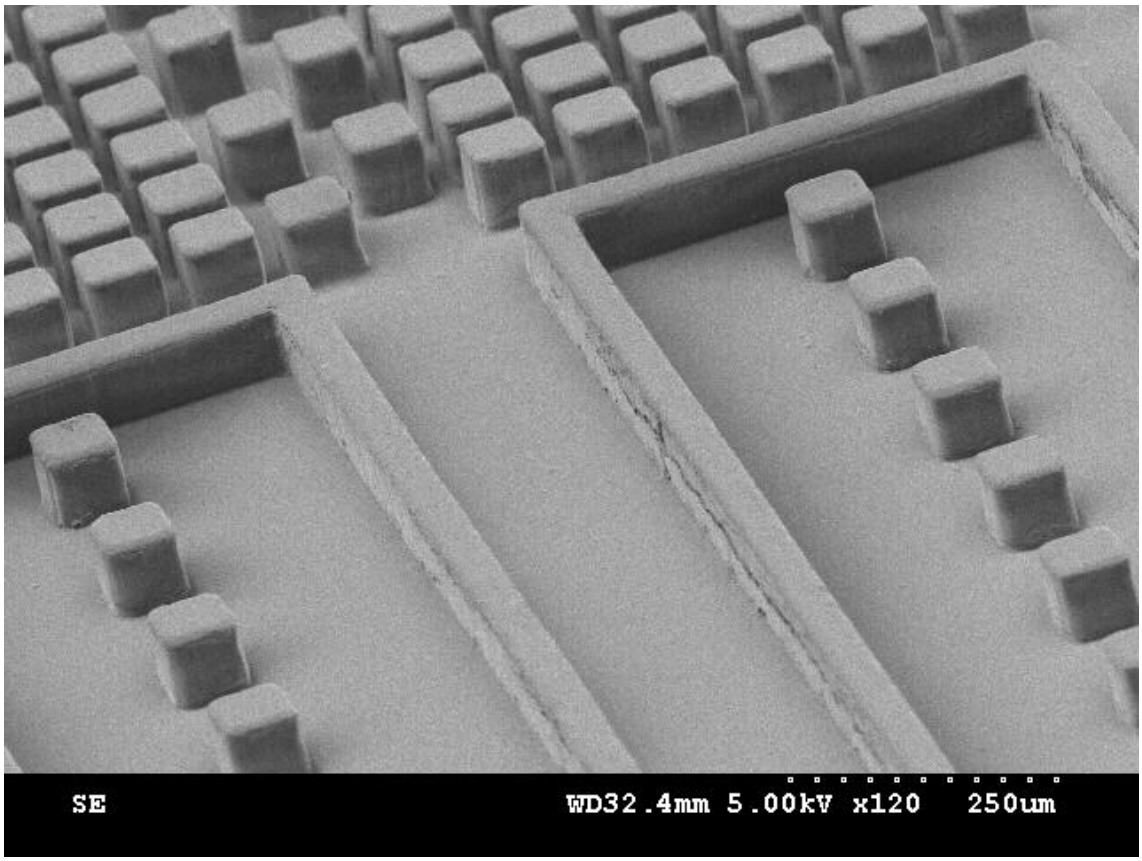

Figure 2.20: An expanded view of the mold shows the vertical profiles of the SU-8 features. The mold is shown after being used to fabricate a microcable array. The array releases cleanly from the mold enabling the mold to be used for the fabrication of multiple microcable arrays.

The release layer, 20 % v/w dextran (Sigma; St Louis MO) in water was spun on the mold after a 30 second plasma discharge (EMS 100 glow discharge unit, Electron Microscopy Sciences; Hatfield, PA). The dextran was applied twice, spun 40 s at 800 rpm, and each layer was dried (hotplate, 100 ° C, 30s) before the next application. Sylgard 184 and Sylgard 186 PDMS were mixed together in a 1:1 wt ratio and spun onto the mold at 4000 rpm for 30 s. The thickness of the spun cast silicone was approximately 85 μm. The heights of the microcables were confirmed with an optical micrometer (Quadra-Chek 200).

The posts, highlighted in Figure 2.20 were too close to allow for quick removal of the array, instead, requiring a prolonged soak. The center posts also retained too much PDMS when microcables were spun 80 μm thick. The extra PDMS retained in the spacers made them more substantial, and made their removal more difficult. Additionally, the current mold could was difficult to make with SU-8 thicker than 80 μm. Efficiently clearing the unexposed SU-8 from between the posts without incurring a delamination of the microcable-defining troughs due to extended exposure to developer proved difficult. To address these limitations, a third mold was designed, shown in Figures 2.21-22. The third mold had more space between the posts to allow for easier developing of the SU-8 and removal of the PDMS after processing. The posts in the center of the spacers were changed to a sparser set of tabs that reduced the retention effect compared to the posts and helped anchor the microcable troughs while the SU-8 was developed.

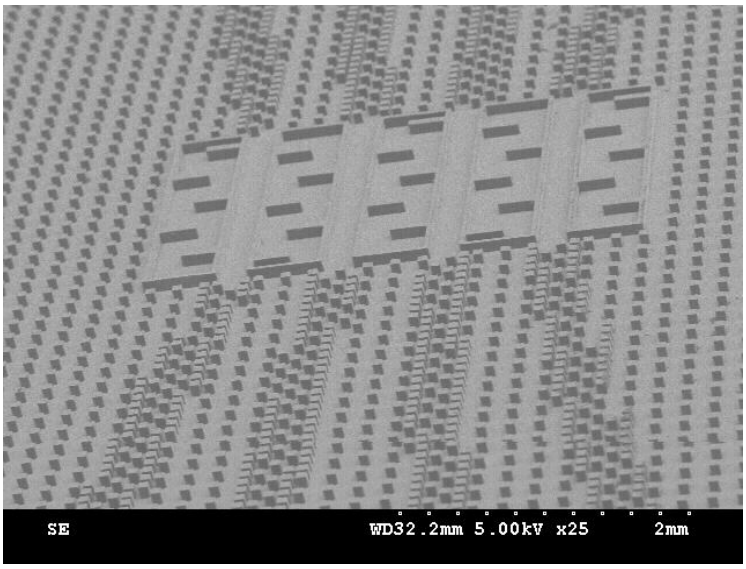

Figure 2.21: The third mold has an increased spacing in post height and change in spacer design. The increase in post spacing made developing the SU-8 mold and releasing the PDMS easier. The post spacing in the regions patterned with gold was kept in its original configuration to make alignment of the metallization stencil easier.

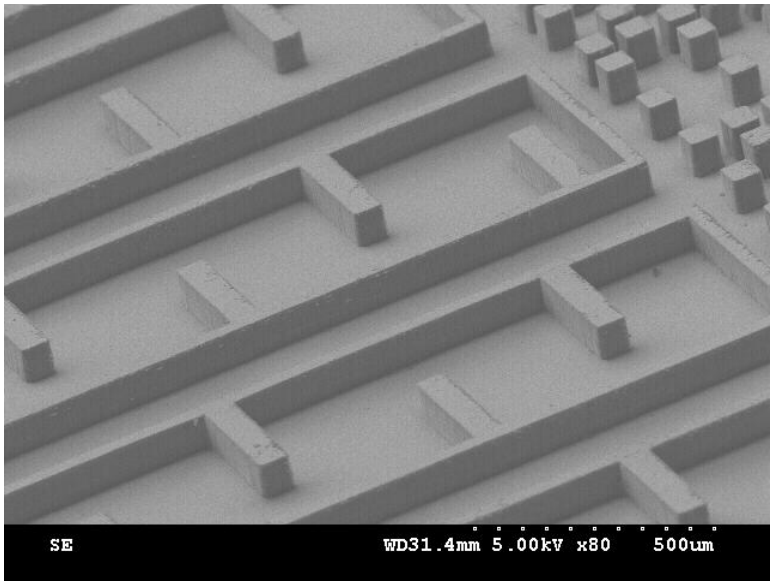

Figure 2.22: The close up view of the microcable troughs and spacers. The side-tabs replaced the posts to help anchor the trough walls. The density of the side-tabs was reduced compared to the posts to reduce the amount of PDMS retained in the spacer regions. Thinner layers of PDMS in the spacer regions correspond with their easier removal.

2.4.2 Optimizing the metallization

The gold leads were stencil patterned using thermal deposition. The stencils were made of 125 μm thick brass sheets, cut using an IR laser (Figure 2.23). After the pattern was cut, the brass was etched with muriatic acid to smooth the side walls. The stencils were aligned under a stereomicroscope and taped to the substrate using Kapton tape. Prior to deposition, the wafer was oxygen plasma treated for 60 s. PVD 75 filament evaporator (Kurt J Lesker; Clairton, PA) was used for the thermal deposition of a 5 nm chrome adhesion layer and a 50 nm gold layer. The deposition was done at 10^{-5} Torr. After deposition, the stencils were removed by hand.

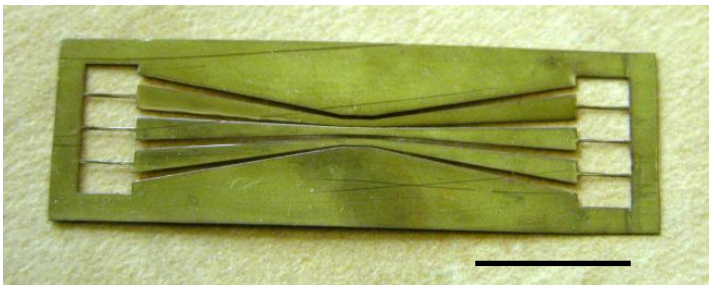

Figure 2.23: The stencil used to pattern the microelectrode array leads is shown above. The pattern is cut into a 125 μm thick brass sheet using an IR laser. Prior to deposition the stencil is taped in place on the wafer. The scale bar is 1 cm.

The photoresist posts used to pattern a sacrificial mold were patterned with NR9-8000 photoresist, spun 30 μm thick, pre and post exposure baked in an oven at 85 °C, for five minutes, patterned with an exposure dose of 850 mJ, and developed with RD-6 developer. The PDMS is spun-cast (4000 rpm, 8 min; cured at 100° C for 10 min.). After curing, the photoresist is removed with RR3, leaving the metal exposed at a selectively uninsulated access node in the same manner as the originally described process. The array is then released in a water bath to dissolve the dextran.

2.4.3 Optimizing the substrate mechanical properties

The Young's modulus of the mixed 184:186 Sylgard was compared with 184 Sylgard using the lower strain region of the tensile test curve. The stress-strain curve of elastomers tends to have an S shape. The Young's modulus can be obtained by the linear region in the lower part of the S, i.e. at low strains. The material was spun on an SU-8 mold in the same manner used to fabricate the microcable electrodes. The spin-times for the 184-only samples were increased to provide the same thickness microcable that is produced for the 184/186 samples. The elastic modulus was measured from the stress-strain curve of a tensile test using linear curve fitting from IGORPro software (WaveMetrics; Lake Oswego, OR). The modulus was also measured using a HysitronTriboindenter, however, the data are highly dependent on the scan and tip parameters and the optimized scans were not conducted on all the samples. Consequently, the data were used in preliminary tests to examine a difference between the two polymer mixes, rather than to measure the absolute value of the Young's modulus.

The stress-strain curves were conducted on single microcables that were glued to a paper frame with a 1.33 mm window. The 1.33 mm was used as the reference for determining the level of strain for a given displacement. The paper frame, coupled to a screw with a piece of polyimide is shown in Figure 2.24. The screw fit into the load cell and the bottom of the paper frame was held in place by a clamp mounted on the Instron machine (Figure 2.25). The pictures show a microcable patterned with gold that was tested in chapter 4. The microcables were shown with gold here in chapter 2 for visibility in the figure and were not coated in gold for the tests.

The tensile tests were done using an Instron-like machine, designed for millimeter and sub-millimeter displacement (Bose Electroforce 3100 test instrument, Bose; Eden Prairie, MN). As shown in Figure 2.24, the microcable was mounted on a piece of paper with a slit 1.33 mm wide cut out of the middle. The microcable on the paper frame is coupled to the force sensor (1.0 N Interface Advanced Force and Torque Measurement; Scottsdale, AZ), which was mounted in-line with the microcable in the Instron machine. After the sample was mounted, the sides of the paper frame were cut so that only the tensile properties of the microcable were measured. Each microcable was tested with a monotonically increasing displacement to the point of failure.

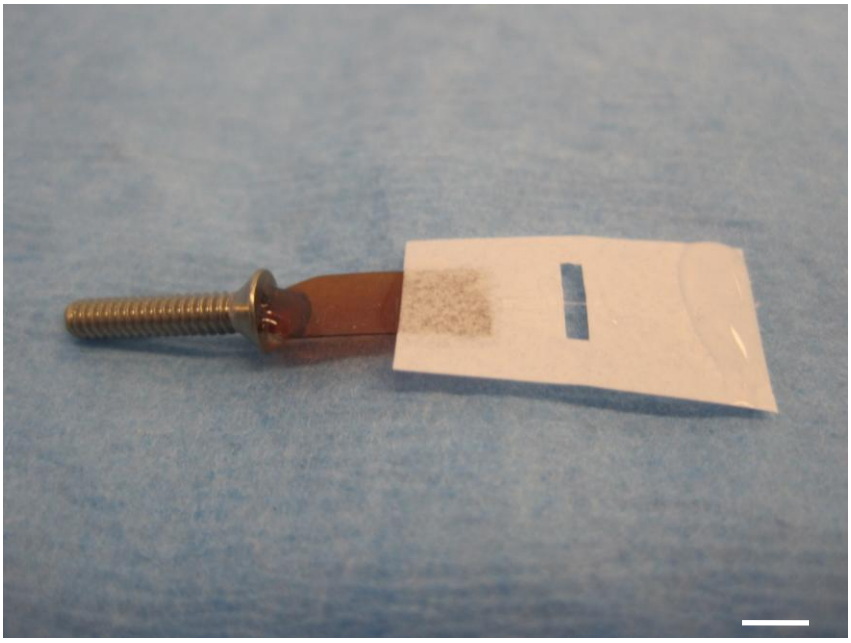

Figure 2.24: The microcable is mounted on a strip of paper and attached to the force sensor using a screw and piece of polyimide. The polyimide was coupled to the screw because it could easily be glued the screw in a vertical orientation. It served as a linkage to ensure the microcable and paper housing could be attached to the force sensor without introducing unintended distortions in the microcable orientation. The PDMS tensile tests were conducted on samples without gold. Scale bar is 2 mm.

Figure 2.25: The microcable sample is shown in the test set-up. Prior to the test, the sides of the paper are cut away so that only the microcable is measured in the tensile test. The load cell (indicated by the white arrow) measures the force that is incurred from tensile stretch. The displacement transducer is housed in the black housing about the load cell. The bottom clamp is stationary.

2.4.4 Results from optimization

The resistance before release was 106 Ω (n=6, SD= 15 Ω). The resistance after release was 128 Ω (n=6, SD= 19 Ω). The resistance before release is higher than the previous process (average: 89 Ω) even though the gold film thickness was reduced from

50 nm to 30 nm; however, it is slightly closer to the calculated value for a 30 nm thick microcable (83 Ω) than the experimental data was for the lift-off deposited 50 nm film (89 Ω vs 50 Ω for experimental and calculated, respectively). The arrays were able to be packaged while changing minimally in conductivity for the stretch tests and *in vivo* tests.

The electrode arrays, with integrated leads showed a qualitative increase in durability, while remaining extremely flexible, as shown in Figure 2.26. The bond pads are the large row of squares at either end of the array.

2.4.5 Increasing the tensile modulus of the substrate results

The elastic modulus PDMS mix of Sylgard 184/186 and Sylgard 184 was obtained from the 0-10% strain region of a second set of samples. The resolution of the high-strain tests was inadequate to examine the stress-strain curve at low strain levels. The modulus was calculated for four samples in each group. The stress-strain curves for those samples are shown in Figures 2.26. The calculated modulus is on the lower end of reported values. The Young's modulus from the literature of Sylgard 184 ranges from 0.75 MPA to 3 MPa [47-49].

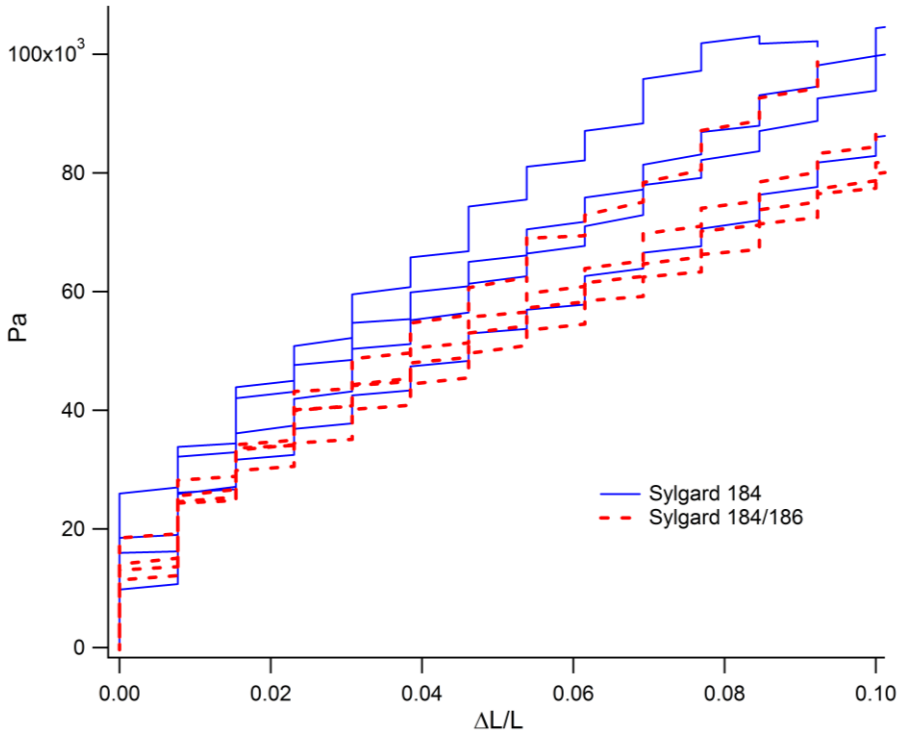

Figure 2.26: The low strain regions of the stress-strain curves of three Sylgard 184 microcables are shown above. The dashed lines show the curve fitting to obtain the Young's modulus.

Table 2.3: The Young's modulus calculations from the 10% strain region of the tensile tests are given below. The difference in the two groups was not statistically significant for a 95% confidence interval.

Sample	Young's Modulus	Standard Deviation
Sylgard 184 a	0.72 MPa	
Sylgard 184 b	0.78 MPa	
Sylgard 184 c	0.78 MPa	
Sylgard 184 d	0.60 MPa	
Average	**0.72 MPa**	**0.084 MPa**
Sylgard 184/186 a	0.58 MPa	
Sylgard 184/186 b	0.85 MPa	
Sylgard 184/186 c	0.60 MPa	
Sylgard 184/186 d	0.69 MPa	
Average	**0.68 MPa**	**0.18 MPa**

The stress-strain curve for the ultimate tensile strength of the two polymers is shown in Figures 2.27-29. The shape is slightly sigmoidal, with an increase in the modulus of both polymers between 100-150% strain. The second inflection point is broader, occurring at over 200% strain. The stress-strain curve in Figure 2.26 shows that at 0-10% strain, the 184/186 mixture and 184-only samples had equivalent tensile moduli. The stress-strain curve for the tensile load tests shows a slightly different perspective. The stress-strain profile in the high-load test was highly variant at 0-10% strain and was not useful in a modulus assessment. The stress-strain profile at higher strains shows a larger increase in the stress for the 186/184 samples than the 184 samples. The significance of this is that the 184/186 is stretched out of shape less easily during handling than the 184 alone.

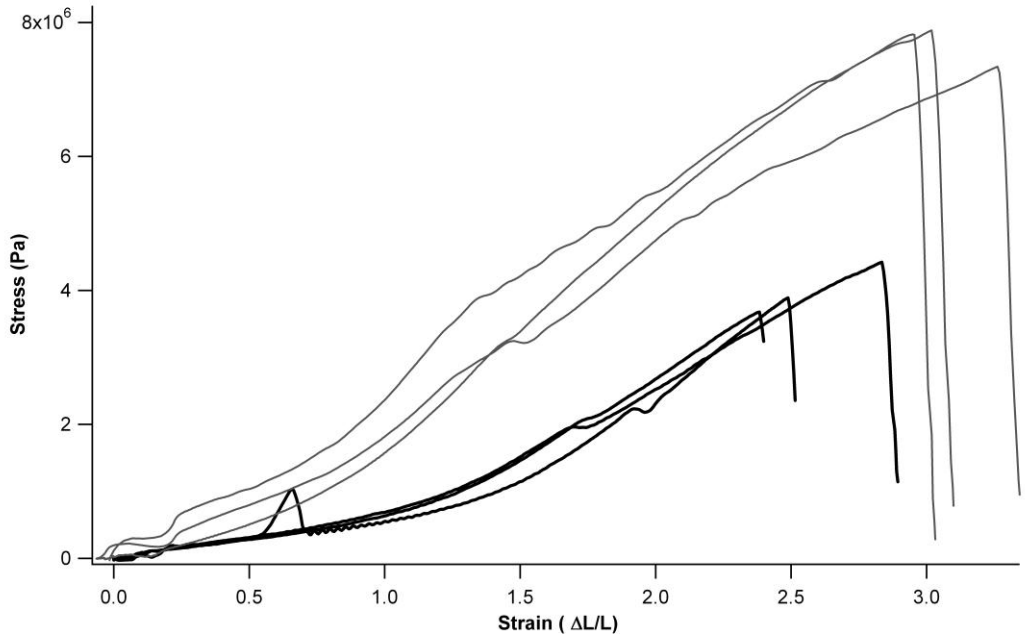

Figure 2.27: The stress-strain measured to failure for microcables made from 184 (black) and 186/184 (grey) is shown above.

Table 2.4: The PDMS 184/186 mixture had a higher tensile strength and load at failure than the Sylgard 184 alone.

186/184 Sample	Strain (%)	Load at failure (MPa)
1	296%	7.82
2	301%	7.88
3	326%	7.34
Average	**308%**	**7.68**
184 Sample		
1	239%	4.42
2	238%	3.68
3	249%	3.88
Average	**242%**	**4.00**

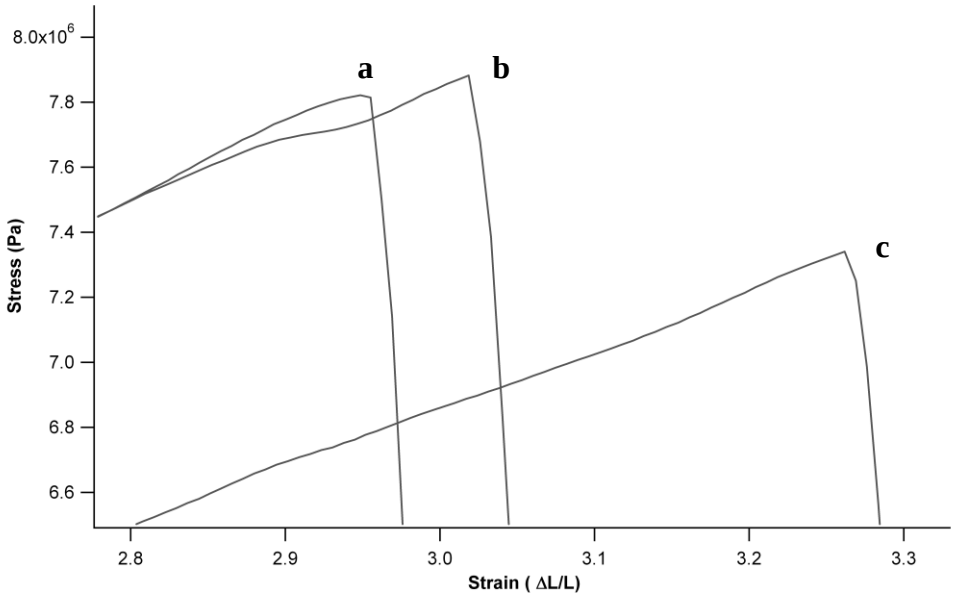

Figure 2.28: An expanded view of the failure points of the 186/184 polymer mix (3 samples.)

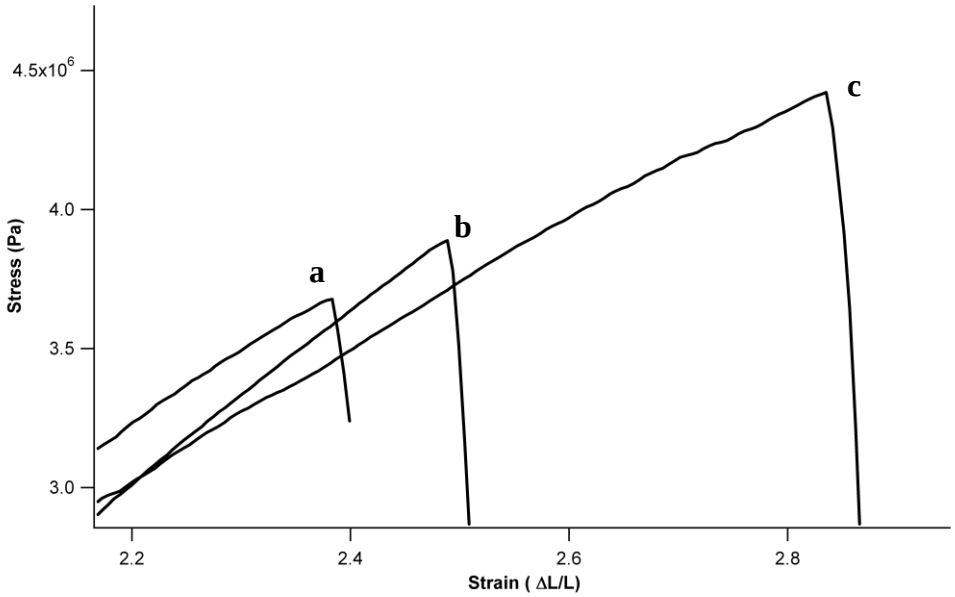

Figure 2.29: An expanded view of the failure points of the 184 polymer samples (3 samples.)

A one-way ANOVA comparing the on the load at failure and the displacement values for the 184/186 and the 184 only samples showed a significant difference in the load at failure and tensile strength. Tukey HSD test indicated significance with a 99% confidence interval.

2.4.6 Discussion of revisions to the fabrication process

The preliminary resistance measurements suggest that the changes to the fabrication process have contributed to a more durable microcable array. Process A had a thinner more compliant substrate and a thicker metal layer while Process B had a thicker, less compliant substrate and a thinner metal layer. The differences are compared in table 2.5.

Table 2.5**:** A side-by-side comparison of the changes in the microcable fabrication process.

	Process A	**Process B**
Substrate	Sylgard 184	50/50 Sylgard 184/Sylgard 186
Substrate thickness	16 um	85 um
Gold film thickness	50 nm	30 nm
Metal patterning method	Photoresist lift-off	Micropatterned stencil

The changes in the processing reduced the resistance after device release even though the metal film thickness for Process B was 60% the thickness for Process A. As shown by the comparison of resistance averages for the microcables (Table 2.5), Process A had a lower initial resistance, as would be expected by the thinner gold film (the mechanisms are described in chaper 4), although the difference is not proportional and the resistances for both processes are higher than the resistances for a film on glass or from theoretical calculations. The standard deviation is higher; this may be due the film thickness and a resulting increased susceptibility to stress in the substrate/film interface. After release Process B has a lower resistance and a lower standard deviation, suggesting that the film is more tolerant for the deformations related to handling the array.

Table 2.6: The average resistance values are given for two different processes used to fabricate the microcable arrays. The averages and standard deviations were calculated from n=6.

	Before device release	**After device release**
Process A	89 Ω (SD:6Ω)	136 Ω (SD:30Ω)
Process B	106 Ω (SD:15Ω)	128 Ω (SD:19Ω)

The ultimate tensile strength of the PDMS 186/184 mix was greater than the Sylgard 184. The properties of bimodal polymer silicone mixtures have been documented in the literature [50-51]. The molecular mechanisms are hypothesized to allow the two distributions to form overlaying networks in which properties of the

original polymers, such a high tensile strength are largely preserved. The polymers combined here were mixed to create a higher tensile strength, smoothly spincastable PDMS. Sylgard 186 has an average molecular weight estimated in excess of 5,000 kDaltons and is viscous enough that it does not spin-cast into a smooth film, but it marketed as a high-tensile strength polymer [45]. Sylgard 184, which does spin-cast into a smooth film, has an average molecular weight that was two orders of magnitude lower, estimated at 25 kDaltons [52]. The reaction for both products is platinum catalyst driven and the cross-linker for 184 polymerizes the 186 prepolymer, so the networks likely cross-link with each other instead of being intertwined, but separate branches, but the molecular distribution is bimodal.

The durometer of the two materials is given by Dow on the product information sheet. Sylgard 184 has a slightly higher durometer (50 shore) than Sylgard 186 (24 shore) [44-45]. The relation between durometer and the stress-strain derived Young's modulus has a correlation described by Qi *et al*. [53]. Durometer testing of bulk materials and AFM testing for thinner films measures the force-depth profile from an innenting tip of prescribed geometry. In elastomers, as long as the limiting extensibility is adequate (> 5) the modulus can be approximated from the hardness. Although the correlation is not directly proportional, the reduced hardness of the Sylgard 186 correlates with the tensile modulus data.

The ultimate tensile strength is measured at the break point of the sample. The stress-strain curve prior to failure had a roughly sigmoid shape. The initial inflection point is explained by the literature as the region at which medium and large elongation at initiated (0.85-1.15 strain) [53-54]. The stress-strain curve at low strains has been more

frequently characterized and can be approximated by classical Gaussian rubber elasticity theory. The shear modulus of the material is the defining parameter in the stress-strain slope. At medium to large elongation (~50-150%), the stress shows an increase in slope that deviates from the low-strain model [54]. The increase in slope is determined by the extensibility limit of the polymer. Generally, an increase in cross-linking density or a shortening of chains causes a loss of extensibility. The loss of extensibility translated to a decrease in elongation at break. The second inflation point is not described by the elastomer stress-strain theory. The slope of the stress-strain curve decreases above 200% strain to approximately the same value found at the low strain region. The decrease in the stress-strain slope is broader than the point at which the slope increased. The broad region in which the slope changed might allude to a progressive degradation in the sample. Similarly shaped, a decrease in the slope for plastic (i.e. non-elastomeric) samples is found at the yield stress [55]. It may be that the decrease observed in the samples shown here is also due to a plastic deformation referred to as permanent set [56]. This potential mechanism could be identified by measuring a change in the length of the samples at strains above the second inflection point. This must be done within a predetermined time point after the tensile test because in elastomers, the permanent set is often reduced over extended periods.

The strain of inflection point is increased for the 186/184 mixture, suggesting an increased durability. Because the change in slope suggests degradation in the polymer, routinely using the device in this range is undesirable, although it does not necessarily mean device failure. The microcable electrodes could potentially be exposed to the high strain region during placement. If they are used as chronic implants, the low stress region

of the stress-strain curve does not appear to cause imminent failure, although the cumulative effects in an *in vivo* environment bear further investigation. It is the low strain region that appears most probable with movement of the tissue at the implant site being the primary mechanism.

2.5 Summary and potential applications

The use of patterned photoresist and SU-8 to create multi-layered devices with through-holes is a useful technique when applied to multi-layer electronic devices, but it also has potential applications in mechanical and micro-fluidic PDMS-based device where a patterned film of PDMS is desirable. Its compliance could make it a useful microscale "seal" for protection of electronic components from integrated fluidics or conversely, for directly facilitating fluidic containment. The substrate conformability and suitability for spin-casting were motivations for using Sylgard 184 (Dow Corning; Midland, MI), which has a low Young's modulus (1.78 MPa, [13]) and can be spun cast and thermally cured *in situ*.

The spin times are on the order of a few minutes, the metallization uses a standard process and the SU-8 molds are reusable. The electrode arrays can be fabricated relatively rapidly, allowing large quantities of the arrays to be easily made. This is beneficial because biological studies require a relatively large number of consistently manufactured samples. To encourage the use of elastomer-based electrodes as a biological tool, it is desirable to minimize supply limitations that might impact their implementation.

The microcable nets can also be made in a range of geometries to fit the requirements of the application. The sinusoidal leads shown in Figure 2.12 provide

more conformability than the straight leads. The extra extension or deformation available in the sinusoidal microcables may be useful; alternately accurate placement may be easier with straight microcables.

The microcables have potential applications in neural and cardiac recording applications. The access sites are available for surface modification and could be used to stimulate or record electrophysiological signals. The compliance and open web-like conformation of the microcable array are conducive to recording over irregular or curved bodies, such as the surface of the brain or heart and do not create a barrier to fluid and gas exchange. The microcables are adaptable for use as shank-style electrodes (providing a temporary coating is applied to aid insertion[57]), wrapping around small features, such as peripheral nerves, or integration into cell and tissue culture systems.

The multilayer feature allows conductive material to be insulated and selectively exposed. Our implementation of SCμM in a multilayer electronic structure demonstrates a simple, relatively rapid process that can be used to make highly compliant electronic structures with patternable geometries.

2.6 Citations

1. Levier, R.R., et al., *What is silicone* Journal of Clinical Epidemiology, 1995. **48**(4): p. 513-517.
2. Pelzer, H. and N. Heimburger, *Evaluation of the in vitro and ex vivo blood compatibility of primary reference materials.* Journal of Biomedical Materials Research, 1986. **20**(9): p. 1401-1409.
3. Polyzois, G.L., A. Henstenpettersen, and A. Kullmann, *An assessment of the physical-properties and biocompatibility of 3 silicone elastomers.* Journal of Prosthetic Dentistry, 1994. **71**(5): p. 500-504.
4. Haug, S.P., et al., *Effects of environmental-factors on maxillofacial elastomers .3. physical-properties.* Journal of Prosthetic Dentistry, 1992. **68**(4): p. 644-651.
5. Belanger, M.C. and Y. Marois, *Hemocompatibility, biocompatibility, inflammatory and in vivo studies of primary reference materials low-density*

polyethylene and polydimethylsiloxane: A review. Journal of Biomedical Materials Research, 2001. **58**(5): p. 467-477.
6. EncyclopædiaBritannica (2010) *industrial polymers, major*. Encyclopædia Britannica Online.
7. Jung, D.H., et al., *Gross and Pathologic analysis of long-term silicone implants inserted into the human body for augmentation rhinoplasty: 221 revision cases.* Plastic and Reconstructive Surgery, 2007. **120**(7): p. 1997-2003.
8. Backovic, A., et al., *Simultaneous analysis of multiple serum proteins adhering to the surface of medical grade polydimethylsiloxane elastomers.* Journal of Immunological Methods, 2007. **328**(1-2): p. 118-127.
9. Roitt, I.B., J. Male, D., *Immunology*. 2001, Edinburch: Mosby.
10. Christenson, E.M., et al., *Biostability and macrophage-mediated foreign body reaction of silicone-modified polyurethanes.* Journal of Biomedical Materials Research Part A, 2005. **74A**(2): p. 141-155.
11. Sun, Y.J., B. Akhremitchev, and G.C. Walker, *Using the adhesive interaction between atomic force microscopy tips and polymer surfaces to measure the elastic modulus of compliant samples.* Langmuir, 2004. **20**(14): p. 5837-5845.
12. Pornsin-Sirirak, T. and Y. Tai, *Flexible parylene actuator for micro adaptive flow control*, in *MEMS 2001*. 2001.
13. Al-Halhouji, A.T., et al., *Nanoindentation testing of SU-8 photoresist mechanical properties.* Microelectronic Engineering, 2008. **85**(5-6): p. 942-944.
14. Kaliappan, S.K. and B. Cappella, *Temperature dependent elastic-plastic behaviour of polystyrene studied using AFM force-distance curves.* Polymer, 2005. **46**(25): p. 11416-11423.
15. DuPont, *Kapton Technical Data Sheet*.
16. Gracias, D.H. and G.A. Somorjai, *Continuum force microscopy study of the elastic modulus, hardness and friction of polyethylene and polypropylene surfaces.* Macromolecules, 1998. **31**(4): p. 1269-1276.
17. Green, M.A., L.E. Bilston, and R. Sinkus, *In vivo brain viscoelastic properties measured by magnetic resonance elastography.* Nmr in Biomedicine, 2008. **21**(7): p. 755-764.
18. Mathur, A.B., et al., *Endothelial, cardiac muscle and skeletal muscle exhibit different viscous and elastic properties as determined by atomic force microscopy.* Journal of Biomechanics, 2001. **34**(12): p. 1545-1553.
19. Borschel, G.H., et al., *Mechanical properties of acellular peripheral nerve.* Journal of Surgical Research, 2003. **114**(2): p. 133-139.
20. Wlodkowic, D., et al., *Biological Implications of Polymeric Microdevices for Live Cell Assays.* Analytical Chemistry, 2009. **81**(23): p. 9828-9833.
21. Ramalingam, N., et al., *Real-time PCR array chip with capillary-driven sample loading and reactor sealing for point-of-care applications.* Biomedical Microdevices, 2009. **11**(5): p. 1007-1020.
22. Lui, C., et al., *Low-power microfluidic electro-hydraulic pump (EHP).* Lab on a Chip. **10**(1): p. 74-79.
23. Karuwan, C., et al., *Flow injection based microfluidic device with carbon nanotube electrode for rapid salbutamol detection.* Talanta, 2009. **79**(4): p. 995-1000.

24. Jha, S.K., et al., *Electrochemical cell lysis on a miniaturized flow-through device.* Current Applied Physics, 2009. **9**(4): p. E301-E303.
25. Xia, Y.N. and G.M. Whitesides, *Soft lithography.* Annual Review of Materials Science, 1998. **28**: p. 153-184.
26. Ostuni, E., et al., *Patterning mammalian cells using elastomeric membranes.* Langmuir, 2000. **16**(20): p. 7811-7819.
27. Garra, J., et al., *Dry etching of polydimethylsiloxane for microfluidic systems.* Journal of Vacuum Science & Technology a-Vacuum Surfaces and Films, 2002. **20**(3): p. 975-982.
28. Graubner, V.M., et al., *Incubation and ablation behavior of poly(dimethylsiloxane) for 266 nm irradiation.* Applied Surface Science, 2002. **197**: p. 786-790.
29. Meacham, K.W., et al., *A lithographically-patterned, elastic multi-electrode array for surface stimulation of the spinal cord.* Biomedical Microdevices, 2008. **10**(2): p. 259-269.
30. Yu, Z., et al., *A new tool to study post-traumatic neuronal dysfunction: Stretchable microelectrode arrays.* Journal of Neurotrauma, 2006. **23**(6): p. P49.
31. Maiti, M., M. Bhattacharya, and A.K. Bhowmick, *ELASTOMER NANOCOMPOSITES.* Rubber Chemistry and Technology, 2008. **81**(3): p. 384-469.
32. Mark, J.E., *Some novel polymeric nanocomposites.* Accounts of Chemical Research, 2006. **39**(12): p. 881-888.
33. Someya, T., et al., *A large-area, flexible pressure sensor matrix with organic field-effect transistors for artificial skin applications.* Proceedings of the National Academy of Sciences of the United States of America, 2004. **101**(27): p. 9966-9970.
34. Sayah, A., V.K. Parashar, and M.A.M. Gijs, *LF55GN photosensitive flexopolymer: A new material for ultrathick and high-aspect-ratio MEMS fabrication.* Journal of Microelectromechanical Systems, 2007. **16**(3): p. 564-570.
35. Sia, S.K. and G.M. Whitesides, *Microfluidic devices fabricated in poly(dimethylsiloxane) for biological studies.* Electrophoresis, 2003. **24**(21): p. 3563-3576.
36. Wolfe, D.B., et al., *Fabrication of planar optical waveguides by electrical microcontact printing.* Applied Physics Letters, 2004. **84**(10): p. 1623-1625.
37. Nam, Y., K. Musick, and B.C. Wheeler, *Application of a PDMS microstencil as a replaceable insulator toward a single-use planar microelectrode array.* Biomedical Microdevices, 2006. **8**(4): p. 375-381.
38. Maxwell, R.S., et al., *Quantification of radiation induced crosslinking in a commercial, toughened silicone rubber, TR55 by H-1 MQ-NMR.* Polymer Degradation and Stability, 2009. **94**(3): p. 456-464.
39. SiliconeSolutions, *SS-27 Product Description*.
40. Lee, J.N.P., C. Whitesides, GM, *Solvent Compatibility of Poly(dimethylsiloxane)-Based Microfluidic Devices.* Analytical Chemistry, 2003. **75**(23): p. 6544.
41. Linder, V., et al., *Water-soluble sacrificial layers for surface micromachining.* Small, 2005. **1**(7): p. 730-736.

42. Li, T. and Z. Suo, *Deformability of thin metal films on elastomer substrates.* International Journal of Solids and Structures, 2006. **43**(7-8): p. 2351-2363.
43. Li, T. and Z. Suo, *Ductility of thin metal films on polymer substrates modulated by interfacial adhesion.* International Journal of Solids and Structures, 2007. **44**(6): p. 1696-1705.
44. DowCorning, *Sylgard 186 Silicone Elastomer Kit Technical Data Sheet*. 2009.
45. DowCorning, *Sylgard 184 Silicone Elastomer Kit Technical Data Sheet*. 2009.
46. Dow Corning, C., *Sylgard Product information Sheet*.
47. Schneider, F., et al., *Mechanical properties of silicones for MEMS.* Journal of Micromechanics and Microengineering, 2008. **18**(6).
48. She, H.Q. and M.K. Chaudhury, *Estimation of adhesion hysteresis using rolling contact mechanics.* Langmuir, 2000. **16**(2): p. 622-625.
49. Engel, J.M.C., J. Bullen, D. Liu, C. *Polyurethane rubber as a MEMS material: characterization and demonstration of an all-polymer two-axis artificial hair cell flow sensor*. in *18th IEEE International Conference onMicro Electro Mechanical Systems, 2005*. 2005.
50. Shah, G.B., *Bimodality and increased amount of crosslinker enhances tensile properties of the silicone networks.* E-Polymers, 2007.
51. Shah, G.B. and R.W. Winter, *Effect of bimodality on tear properties of silicone networks.* Macromolecular Chemistry and Physics, 1996. **197**(7): p. 2201-2208.
52. Flowers, G. and S. Switzer, *Background material properties of selected silicone potting compounds and raw materials for their substitutes*, O.o.S.a.T. Information, Editor. 1978, Department of Energy (Lawrence Livermore Laboratory).
53. Qi, H.J., K. Joyce, and M.C. Boyce, *Durometer hardness and the stress-strain behavior of elastomeric materials.* Rubber Chemistry and Technology, 2003. **76**(2): p. 419-435.
54. Meissner, B., *Tensile stress-strain behaviour of rubberlike networks up to break. Theory and experimental comparison.* Polymer, 2000. **41**(21): p. 7827-7841.
55. Beer, F.R., J. , *Mechanics of Materials*. 1992, New Yprk: McGraw-Hill, Inc.
56. Smith, L., *The language of rubber*. 1993, Oxford: Butterworth Heineman.
57. Palmer, C., *Microwire technique for recording single neurons in unrestrained animals.* Brain Research Bulletin, 1978. **3**(3): p. 285-289.

CHAPTER 3

ELECTRODE IMPEDANCE CHARACTERIZATION

3.1 Introduction

The electrode impedance in a physiological solution indicates the signal range the electrode is used in; therefore, this metric can be used as a basic measure of electrode functionality. Factors that determine electrode impedance at the recording or stimulation site include the following:

- geometric area: the footprint of the active site
- total surface area: a planar or three-dimensional surface
- surface chemistry: the capacity for charge injection

These variables shape the functional range of the recorded or stimulated signal. Neural recording electrodes and their instrumentation are optimized for a high signal-to-noise ratio because the target signal is frequently in the μV range. This optimization endeavors to create a low impedance value relative to the geometric area. The geometric area itself can be increased to help lower impedance, but not without decreasing spatial resolution, which also generally hinders the signal-to-noise ratio. An alternative to increasing the geometric area is to increase the surface area within the geometric area by depositing a film at the active site that has three-dimensional morphology. Sometimes the surface chemistry properties are also improved by the three-dimensional film if the respective material's charge transfer capacity is better than that of the native electrode material.

Stimulating electrodes have a different set of requirements. Signal to noise is not as great a concern as avoiding electrochemically induced corrosion of the stimulating

surface. The surface chemistry for stimulating electrode surfaces is often a dielectric, the polarization of which is used to propagate the signal [1]. Non-dielectric surfaces are also used, but are designed so that the charge injection during stimulation is largely reversible and does not cause a net loss of ions from the electrode surface [2]. The design criteria of the electrode for both recording and stimulation can be understood using a circuit model that approximates the electrical properties of the geometric area, surface area, and surface chemistry [3].

3.2 Components in the electrode impedance model

The impedance has been modeled as an equivalent circuit with the characteristics of the electrode's active site modeled as resistive and capacitive circuit components: the interfacial resistive and capacitive elements (constant phase angle impedance), charge transfer resistance, and the spreading resistance. The relation of these components is shown in the circuit in Figure 3.1[3].

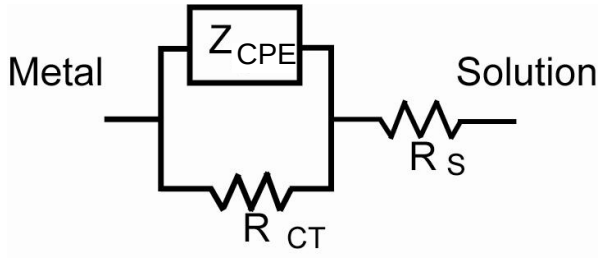

Figure 3.1: The impedance at the electrode surface is modeled as a constant phase element (Z_{CPE}), charge transfer resistance (R_{CT}) and spreading resistance (R_S).

3.2.1 Interfacial capacitance

The interfacial capacitance is determined by the organization of the electrolyte medium on a molecular level at the electrode surface. The characteristics of this organization are determined by the medium composition and concentration, and the

applied potential at the interface [4]. The surface topography of the electrode active site is also a contributing factor.

Of the molecular effects on capacitance, the most immediate layer, the inner Helmholtz plane, is an oriented layer of water molecules, aligned with the positive hydrogen groups against the negatively charged metal (Figure 3.2). The negative dipole of the water layer is coupled to the positive water dipole of hydrated ions. The hydrated ions form a layer that is more closely packed at the surface of the electrode and decreases in density with distance from the electrode surface. The inner layer of hydrated ions is called the outer Helmholtz plane. The more diffuse organization of hydrated ions beyond the Helmholtz plane is the Gouy-Chapman layer [5]. As a field is applied via the electrode and induces a polarization in the molecules, the capacitance decreases as the thickness of the Helmholtz layer reduces due to the close packing of the hydrated ions. The theoretical model of the interfacial elements is the series capacitance addition of the inner and outer Helmohltz layers (C_H) and the Gouy-Chapman diffuse layer (C_G, equation (3.1)). The capacitance can also be understood as the summation of the thickness of the double layer (d_{OHP}) and the Debye length (L_D), as shown in the second part of equation (3.1).

$$\frac{1}{C_I} = \frac{1}{C_H} + \frac{1}{C_G} = \frac{d_{OHP}}{\varepsilon_o \varepsilon_r} + \frac{L_D}{\varepsilon_o \varepsilon_r} \cosh\left(\frac{z\phi_o}{2U_t}\right) \tag{3.1}$$

$$L_D = \sqrt{\frac{\varepsilon_o \varepsilon_o U_t}{2n^o z^2 q}} \tag{3.2}$$

in which ε_0 is the permittivity of free space; ε_r is the permittivity of the double layer; z is the ion charge; ϕ_0 is the applied electrode potential; U_t is the thermal voltage; n^0 is the ion concentration in the bulk solution; and q is the electron charge.

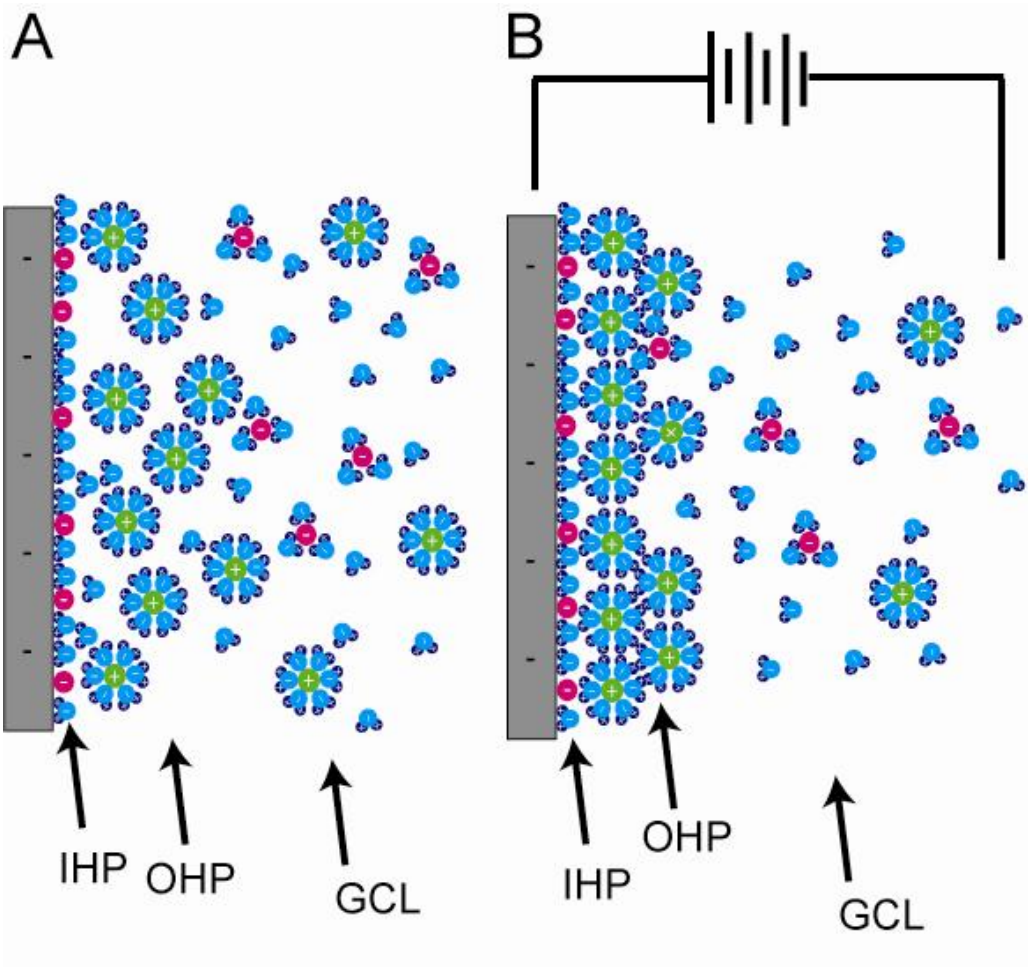

Figure 3.2: The layers contributing to interfacial capacitance are represented in the schematic above. The inner Helmholtz plane (IHP) is composed of a layer or water molecules and negative ions. The Outer Helmholtz plane is a layer of hydrated ions that is slightly diffuse (A) but compresses under the presence of an applied field (B). The Gouy-Chapman layer (GCL) is a more diffuse layer of hydrated ions that transitions into the bulk solution.

The Helmholtz capacitance is determined by the electrolyte's dielectric permittivity, the electrode area, and the distance of the outer Helmholtz plane from the

electrode surface. The Gouy-Chapman capacitance is determined by the thickness of the solvated ion layer, the voltage at the electrode surface, and the thermal voltage (equation (3.1). The constant phase element impedance is used instead of the capacitive molecular layers for modeling because there is an interfacial resistive component in addition to the capacitive components at the molecular level, the degree of which depends on the presence of fractal-like surface topology. The constant phase element (CPE) is used in circuit models of impedance to fit a capacitive-like element produced from the electrolyte double layer [6]. The relation is defined by equation (3.3), where the exponent, n, when equal to zero or one, indicates pure resistance or capacitance, respectively [3].

$$Z_{CPE}(\omega) = \frac{1}{(jwQ)^n} \tag{3.3}$$

Q is a magnitude-related variable of Z_{CPE}. The fractal dimension of the electrode surface is correlated to the value of n. For a fractal dimension, D, the value of n is given in equation (3.4).

$$\mathrm{n} = \frac{1}{\mathrm{D} - 1} \tag{3.4}$$

If the surface is smooth, the fractal dimension is 2 (n=1); If the surface is very rough then D = 3 and n = 0.5. CPE behavior can also be induced by variations in reaction rates at the electrode surface, the surface coatings, or current distribution.

3.2.2 Charge transfer resistance

Increasing the surface area of the electrode generates an increase in the interfacial capacitance but also significantly decreases the charge transfer resistance. The surface

area can be increased while maintaining the same geometric area by plating a three-dimensional conductive coating onto the recording site. A coating like platinum black deposits in a porous or highly branched three-dimensional configuration at the recording site [7]. The increase in surface area can decrease the total impedance by several orders of magnitude, depending on the plating parameters [8].

The resistance is determined by the surface available for charge transfer of the respective electrical signal. The signal propagation through the electrode interface occurs when a potential is applied relative to the equilibrium value, termed the overpotential (η). The overpotential generates a current that is composed of the following components (equation (3.5)): charge transfer in the double layer (η_t), a diffusion of reactants (η_d), and the resulting reactions (η_r), and the crystallization of metal atoms into the electrode metal's lattice structure (η_c) [5]. In the regime of neural electrodes, the charge transfer overpotential is the dominant component in the equation. The crystallization of metal atoms into the electrode's metallic lattice structure is negligible. The diffusion of reactants and resulting reactions is also negligible if the electrode is suitably designed for physiological applications.

$$\eta = \eta_t \, \eta_d \, \eta_r \, \eta_c \tag{3.5}$$

The charge transfer resistance is determined via the equilibrium exchange current density (J_o) and related to the charge transfer overpotential by equations (3.6) and (3. 7).

$$R_{CT} = \frac{U_t}{J_o z} \tag{3.6}$$

$$\mathrm{J} = \frac{\eta_t}{R_{CT}} \tag{3.7}$$

Whether the electrode is considered polarizable depends on the value of J_o, with ideally polarizable and non-polarizable electrodes having J_o values of zero and infinity, respectively.

The charge injection capacity of the metal and the characteristics of the electrolyte interface both contribute to the value of J_o. A more polarizable electrode is desirable because it allows a wider range of operating voltages without inducing irreversible electrochemical reactions [5]. An infinitely large theoretical current exchange density means no overpotential develops and the electrode is ideally nonpolarizable. Conversely, a low current exchange density creates an ideally polarizable surface. The Bulter-Volmer equation (3.8) relates the interfacial current produced from an applied voltage for a given current exchange density [5].

$$J = J_o \left[e^{\frac{(1-\alpha) z \eta_t}{U_t}} - e^{\frac{-\alpha z \eta_t}{U_t}} \right] \tag{3.8}$$

In equation (3.8), α and 1- α are the transfer coefficients for cathodic and anodic currents, respectively. When the surface is rough or porous, the overpotential used to calculate the transfer coefficients has to be adapted to account for ohmic drop effects[1] [9]; however, for smooth electrode surfaces and small overpotentials in the linear regime, it is possible to approximate R_{CT} by the equations described above ((3.6), (3.7)).

---

[1] Ohmic drop effects are voltage drops that occur across an ohmic resistance. The charge transfer resistance is non-ohmic.

3.2.3 Spreading Resistance

The electrode's active geometric area and geometry contribute to the spreading resistance (Rs), which describes the dispersion of current to the tissue or surrounding medium. The geometric area is a function of the surface area of the recording site, assuming the recording site surface is perfectly planar. The spreading resistances for a circular and square shaped active site are given below and are shown to be functions of the radius, r, and side length, l [3]. The medium (electrolyte) resistivity is given by ρ.

$$R_{s,circle} = \frac{\rho}{4r} \tag{3.9}$$

$$R_{s,square} = \frac{\rho \ln 4}{\pi l} \tag{3.10}$$

Increasing the size of the active site decreases its spreading resistance. Increasing the perimeter-to-area ratio also lowers spreading resistance, as shown in the elliptical areas of varying aspect ratios (Table 3.1). The more elongated the ellipse, the lower its spreading resistance is [10]. This relation is somewhat intuitive, given that spreading resistance is analogous and shares the same geometrical relations to heat transfer dynamics [10]. For many simple microwire electrodes, the most straightforward way to control the impedance is to vary the area of wire exposed from the insulating sheath.

Table 3.1: The effect of the perimeter-to-surface area ratio on spreading resistance. Increasing the perimeter for a given surface area will cause a decrease in the spreading resistance.

a/b elliptical ratio	Spreading resistance coefficients relative to a circle per unit area
1:1	1
1:2	0.971
1:4	0.892
1:8	0.782

3.3 Electrical impedance and electrophysiological testing for neural electrodes

Neural electrodes are used to stimulate and record from electrically excitable biological tissue. Stimulation and recording encompass a wide range of applications specified in part by the following parameters:

- acute or chronic time ranges
- the location of the recorded tissue, i.e., peripheral or central
- the volume of tissue targeted, i.e., single cell or tissue/field

In this discussion, a neural electrode is considered to be a microwire (< 1mm diameter), or a microwire bundle, that records extracellular electrical activity of neurons *in vivo* or stimulates *in vivo* neural populations. The electrode's application determines the desired geometric area of the recording area and the impedance level. (As mentioned previously, the geometric area is also a variable in the impedance value.)

3.3.1 Impedance factors for recording electrodes

Relatively high impedances (i.e., in the mega-ohm range) only record activity in an extremely small vicinity around the electrode, creating electrodes that only record

single-cell potentials. The geometric area of the electrode recording area is also very small for this application, with a diameter in the range of several microns [11]. A larger geometric area for the same impedance value reduces the spatial resolution of the recording. Reducing the impedance to the kilo-ohm range extends the spatial extent of the recording, allowing for populations of neural activity to be recorded [12].

3.3.2 Impedance factors for stimulating electrodes

Stimulation must occur in a power density range that does not cause damage to the tissue, either because of joule heating and subsequent denaturation of the tissue or because of ionic efflux from the electrode and resulting toxicity. These adverse effects are avoided by designing an electrode with sufficient charge transfer capacity. The impedance (ohms) correlates with a large charge transfer in the relation described in equation (3.11). The power of the signal is set at the threshold for successful tissue stimulation. This value can be limited, particularly in chronic stimulation environments, by prolems such as degradation of the electrode surface, damage or undesirable interference to surrounding tissue, and power considerations with implantable batteries.

$$Z_{ELECTRODE} = R_s + \frac{1}{\left(\frac{1}{Z_{CPE}} + \frac{1}{R_{CT}}\right)} \qquad (3.11)$$

The interface of the electrode to neural tissue is designed to enable the electrode to record or stimulate a desired volume of tissue as specifically as possible. Unintended effects on neural function or on neuron-to-electrode communication are often due to electrode degradation or tissue changes in response to the electrode. Tissue changes, which are driven by the immune and or injury response, are harder to modulate and will be

discussed in chapter five. Electrode degradation is avoidable to a significant extent if the electrode site is designed appropriately for the application.

Electrodes are frequently optimized for capacitive or non-Faradic charge transfer, i.e., the regime of operation when there is no permanent exchange of ions between the electrode and electrolyte. The capacitive charge transfer is a transient rearrangement of charged ions in the electrolyte under the applied field. The interface is purely capacitive. Faradic charge transfer occurs when oxidative or reductive processes occur at the electrode interface. Capacitive and resistive elements account for the activity at the electrode surface. Cathodic potentials at the electrode surface cause the addition of an electron to the electrode surface, while anodic potentials cause the removal of an electron. The transfer of charge is non-reversible if the products are able to diffuse away from the electrode. When the applied potential is close to equilibrium, the reaction is determined by the magnitude of the voltage and is referred to as being under kinetic control. At sufficiently high voltages, the reaction rate is not dependent on the voltage but on mass transport at the electrode surface; reactions occurring under these circumstances are under mass transport control. The kinetic domain is considered to be reversible because the large proportion of reactants remains close to the site relative to the amount of kinetic products in the reaction. If the polarity is reversed, the stored reactants are available for the reverse reaction.

When mass transport dominates, the products are removed from the reaction site more quickly than the kinetics can occur. In this regime there is no storage of reactants to reverse the process if the potential is reversed. If the reactant is particularly soluble in the electrolyte and precipitates out of solution or becomes a gas, the reaction is irreversible.

Irreversible reactions are undesirable because they cause a local change in the chemical composition near the electrode site, which can translate to deleterious effects on the tissue. Some materials, such as platinum, are commonly used for stimulation because they have a pseudocapacitive quality [2]. The Faradic reaction occurs, but the product remains attached, making the reaction reversible when the polarity is changed.

During stimulation, irreversible Faradic activity is undesirable because the reactants can induce toxicity in the surrounding tissue. The irreversible processes also tend to corrode the electrode in chronic systems. The reversible charge injection limit is used to identify the electrode's stimulation capacity without generating irreversible reactions. The double-layer capacitance, pseudocapacitance, and reversible Faradic reaction capacity all contribute to the reversible charge injection limit.

The choice of voltage- or current-controlled signals also determines the effectiveness of electrode stimulation. Current-controlled stimulation is generally favored although the instrumentation is more complex. Voltage-controlled stimulation is not used as frequently because it can be inconsistent for effective tissue stimulation. Voltage stimulation has a maximal current at the beginning of the pulse, which falls as the double layer is charged and Faradic processes begin, versus a constant current in a current controlled stimulation [2]. Cellular depolarization is driven by current, so voltage control is less reliable at inducing cellular depolarization than current control pulsing. The decrease in current over the duration of a voltage-controlled pulse correspondingly changes the volume of tissue targeted over the pulse duration. Any changes in resistance within the system will also change the stimulation parameters.

3.3.3 Peripheral nerve recording background

The nervous system is divided into the central and peripheral system. The central nervous system is the brain and spinal cord while the peripheral nervous system includes ganglia and peripheral nerves. The somatic peripheral system comprises sensory neurons of the dorsal root and cranial ganglia that extend throughout the body to provide feedback to the CNS about the environment and the body's relation to it. The somatic motor neurons extend from the CNS but are considered peripheral [13]. The sciatic nerve is a relatively large peripheral nerve that extends from the spinal cord and enervates the rat hind limb. The sciatic nerve is frequently used in studies on nerve injury and regeneration [14].

3.4 Methods

3.4.1 Methods for impedance characterization

In this section, the experimental impedance measurements from the electrodes described in chapter two are compared with values derived from the circuit-element model. The circuit element model was tested with hypothetical and fitted values using Matlab (Mathworks; Natick, MA). The experimental setup is described as follows. The patterned active site is an elliptically shaped surface, 100 x 50 μm, with an area of 15,707 μm^2. Impedance measurements were taken over a frequency sweep from 1 Hz to 100 k Hz using a dynamic signal analyzer (Stanford Research Systems, Model SR785; Sunnyvale, CA), the parameters for which were set using custom written Matlab code [8]. The impedance of the active site was measured in phosphate buffered saline, with a platinum counter electrode. The platinum black was deposited at the electrode site using

pulse plating via a function generator (HP 33102A, Hewlett Packard; Palo Alto, CA). Each channel was individually plated with a 50% duty cycle, 1 kHz square wave for 9,000 pulses. The plating parameters had been previously optimized and the plating duration was empirically determined as the duration required to cause an impedance drop of approximately an order of magnitude [15]. The stimulation tests were conducted in phosphate buffered saline (150 mM, with 10% fetal bovine serum) buffered to physiological pH (7.2). The physiological saline with serum was chosen so that the chemistry at the electrode interface would be similar to that of an *in vivo* setting. The impedance of the recording site was measured at two points: after $1.5*10^6$ and after $9*10^6$ cycles of biphasic pulses. The pulse was cathodic, current controlled 200 μs, 50% duty cycle, 100 μA (current density: 2.5 A/cm^2).

3.4.2 Methods for electrophysiological measurements

The microcable electrodes were prepared as described in chapter two. The recording set-up is designed for differential recording between two electrodes. The differential recording between two electrodes of known spacing can be used to determine nerve conduction velocity, which is a measure of functional integrity. In this setting, it was used in a healthy rat to verify electrode function. The microcables were divided into either groups of two or isolated into single electrodes so that placement could be varied for the differential measurement.

The electrodes were connected to fine, Teflon-insulated wire with silver-coated aluminum filled RTV silicone (Silicone Solutions). The connections were then coated with RTV silicone elastomer for electrical insulation and mechanical support. The

microcables were glued on to a wedge piece of PDMS for ease of handling as shown in figure 3.3.

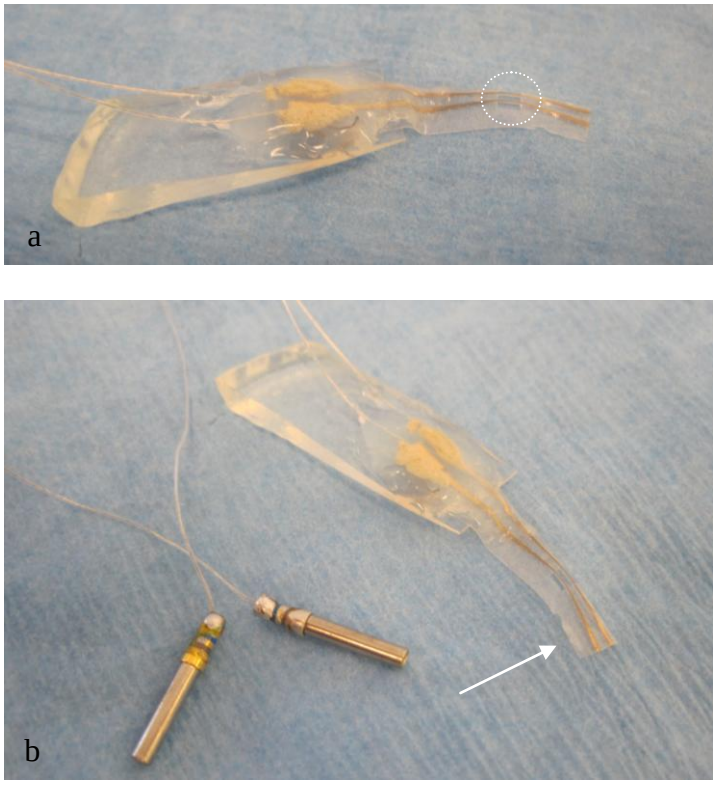

Figure 3.3: A double microcable array is shown above. (a) The recording sites are in the microcable region, shown circled. The recording sites are the only uninsulated regions on the electrode. (b) The extra length, indicated by the arrow, was left attached for ease of handling while setting the microcables in position to the peripheral nerve. The electrodes were connected to the amplifier via the pins shown above (b).

To assess the capability of the PDMS electrodes to record biological signals, acute electrophysiological testing was performed to record compound nerve action potentials from the sciatic nerve of an adult Sprague-Dawley rat. The rat was deeply anesthetized with isofluorane gas, and a skin incision made along the femoral axis. The underlying thigh muscles were delineated with a blunt probe to expose the sciatic nerve,

which was freed from overlying connective tissue. The nerve was then draped across a pair of microcable PDMS electrodes, spaced 1 cm apart, and the cavity was moistened with mineral oil warmed to 37ºC. Next, a portion of the posterior tibial nerve branch, located near the ankle was exposed, and attached to a pair of stainless steel bipolar hook electrodes. This distally positioned pair of electrodes was attached to a stimulator (Model S88, Grass Technologies) and stimulus isolation unit (Model SIU5B, Grass), which were used to stimulate the nerve with 100μs square pulses of variable amplitude, applied at a rate of 1Hz.

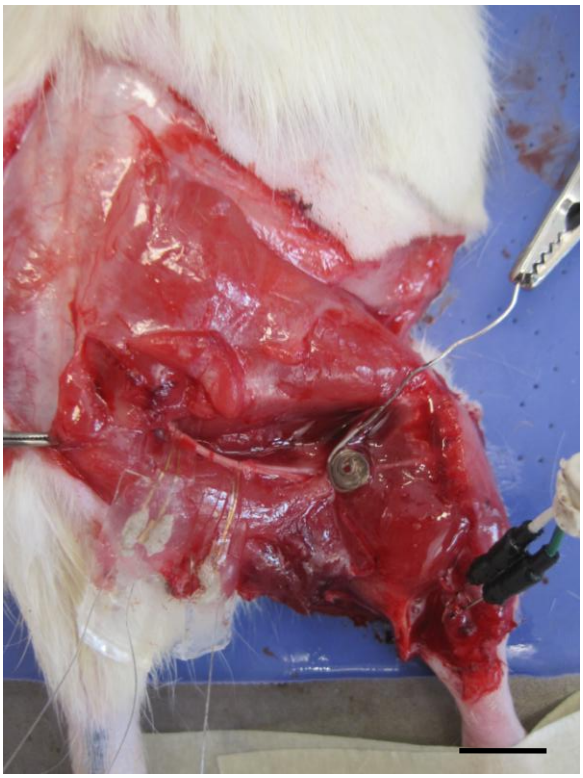

Figure 3.4: The microcable electrodes are shown draped over the sciatic nerve (left). The grounding electrode is the coiled wire to the right. The stimulating electrode is attached to the nerve at the lower hind limb (bottom right). Scale bar is 1 cm

Evoked compound nerve action potentials were recorded upstream from the microcable PDMS electrodes and amplified (G=1000), bandpass filtered (300-5000 Hz,

Model 1700, A-M Systems), and digitally sampled. (25 kS/sec, Multichannel Systems DAQ card.) The recordings were averaged up to 128 times, using a trigger signal provided by the stimulator.

3.5 Results

3.5.1 Impedance characterization results

The results of the simulated model are shown in Figures 3.4 a-d. The values were chosen to show an impedance curve with both poles visible in the plot. As predicted by the theory (equation (3.11)), increasing Z_{CPE} by increasing Q, the magnitude of the constant phase angle impedance, increases the impedance values between the poles and shifts the pole values to slightly higher frequencies. Changing the value of n in Z_{CPA}, to adjust for an increase surface roughness creates changes similar to those generated by changing the Q value. Increasing or decreasing R_S changes high-frequency impedance, and increasing or decreasing R_{CT} changes the low-frequency impedance. The experimental data of the electrodes before and after platinization was fitted with the same model. The three electrodes were fabricated with the same recording site size, and the impedance values are roughly the same for all three before and after platinization, as shown in the plot in Figure 3.6. The fitted circuit model parameters for the experimental data are given in Table 3.2. The Q, n, and R_{CT} values changed as expected, while the R_s value remained unchanged.

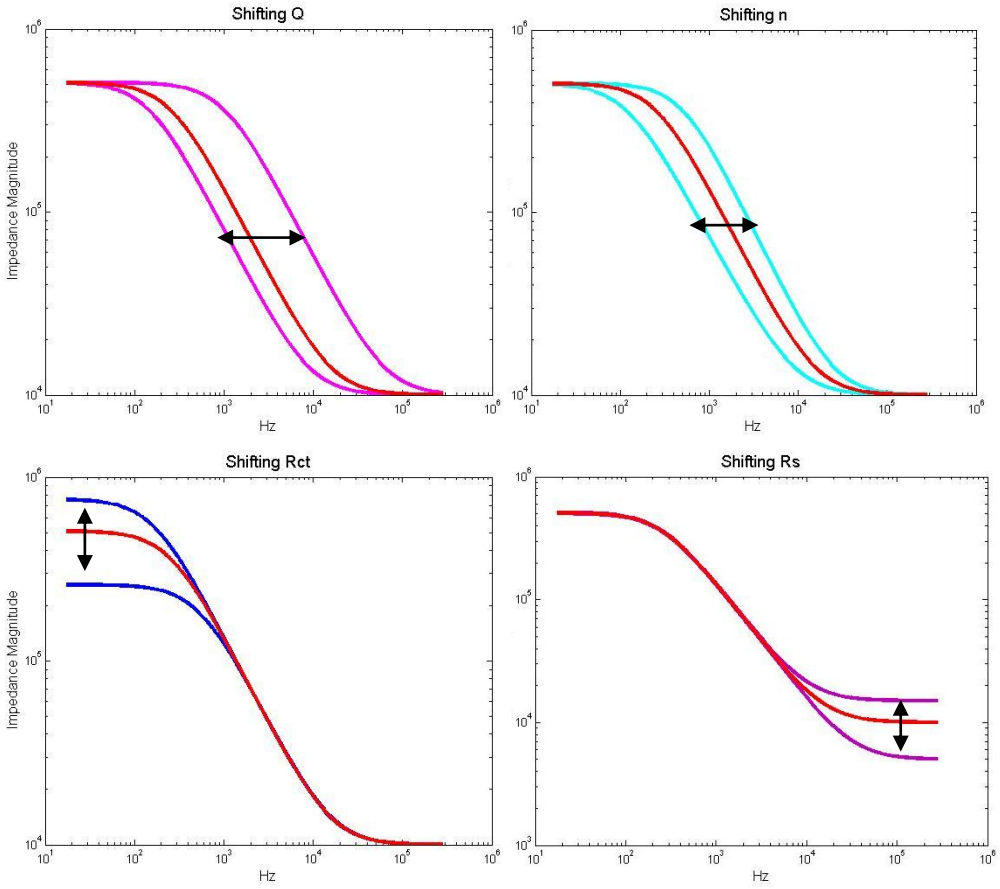

Figure 3.5: The simulations from the circuit-based impedance model are shown above. The four elements in the model were tested for the values given in table 3.2. The increase or decrease in the curve correlating to the increase or decrease in the respective parameter is indicated with bidirectional arrows. The corresponding changes in the above curves shows the variations in the model parameters displays frequency dependent changes.

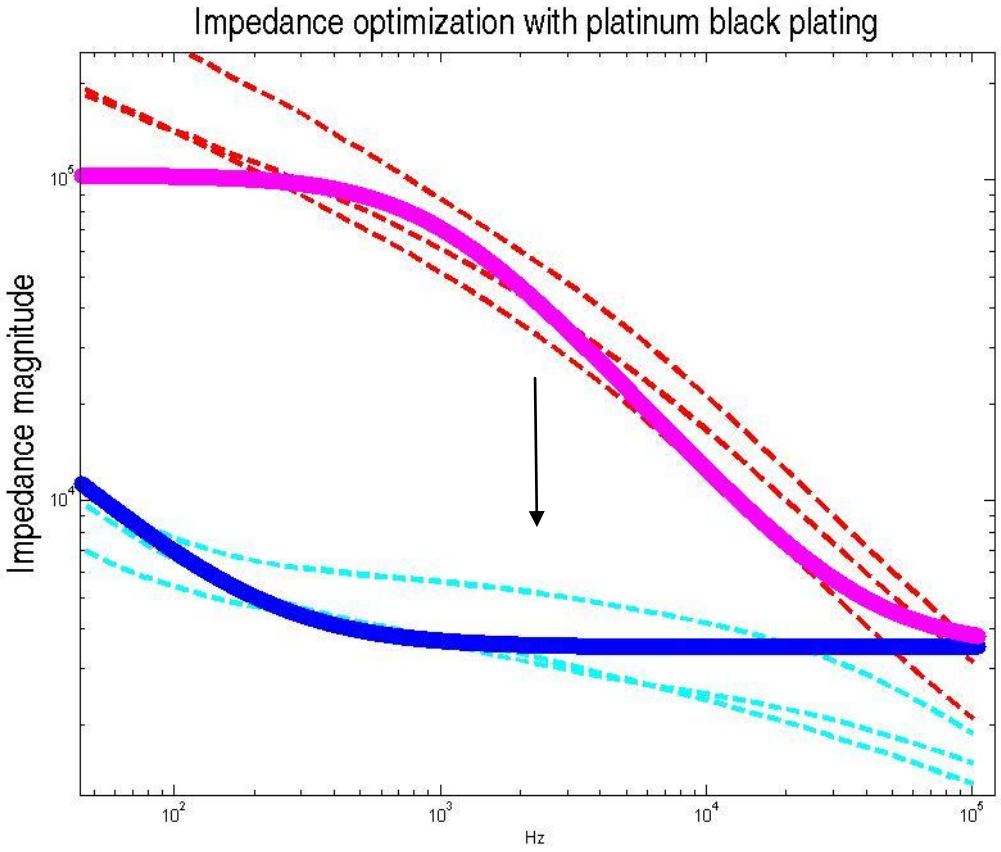

Figure 3.6: The impedance curves for three electrodes before (red) and after (blue) platinization is shown as a function of frequency. The circuit element model (magenta and cayan) is shown with values fitted to the experimental data. The values for the model are given in Table 3.3.

Table 3.2: The test values for the circuit-element impedance models are given here. The changes in the model's impedance curve from the variations in the values are shown in figure 3.3.

Variable	Decreased	Original Curve	Increased
Q	$1*10^{-9}$	$4*10^{-9}$	$7*10^{-9}$
n	0.9	0.95	1.0
R_{CT}	250 k	500 k	750 k
R_S	5 k	10 k	15 k

Table 3.3: The circuit model parameters fitted to the experimental data with the values given in the table. Impedance readings of the electrodes were done before and after platinization.

	Q	n	R_{CT}	R_S
Gold surface	$3*10^{-9}$	0.9	150k	3500
Platinum black surface	$1*10^{-7}$	0.75	40k	3500

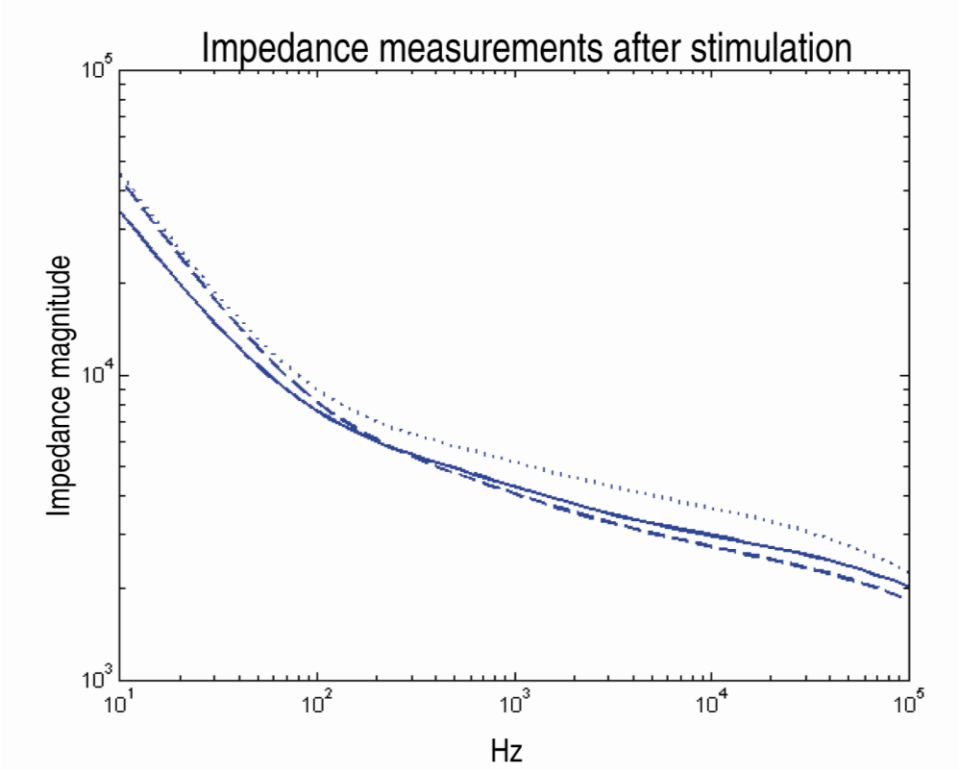

Figure 3.7: Platinum black has the charge injection capacity for a stable stimulating interface at the hypothetical parameters tested in the methods section. The original impedance curve is shown as a solid line. The impedance of the recording site is measured after $1.5*10^6$ cycles of biphasic pulses (dashed) and after $9*10^6$ biphasic pulses (dotted). A slight increase in the impedance is visible after $9*10^6$ pulses. (pulse-width :200 μs, current:100 μA).

3.5.2 Electrophysiological testing results

The electrode placement is shown in figure 3.8. The array of two microcables was threaded under the sciatic nerve. An additional single microcable is shown threaded around the nerve approximately 1 cm distal from the double electrode array.

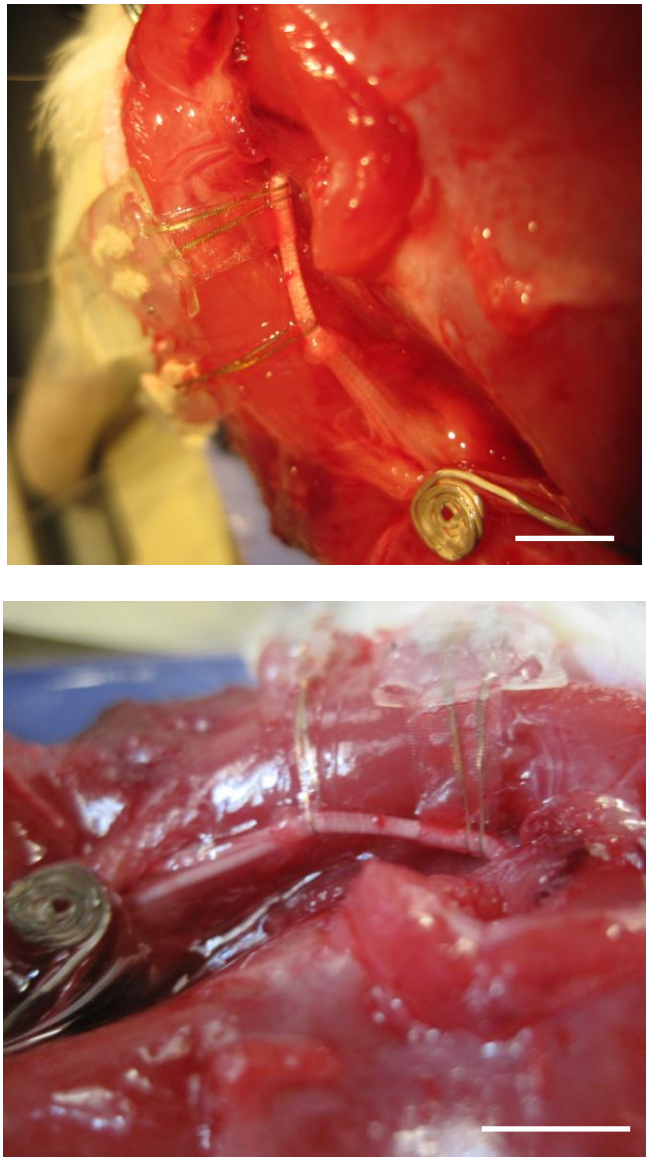

Figure 3.8: The microcable arrays are in close contact with the nerve. The electrodes were threaded under the nerve and pulled through to the other side with tweezers for secure positioning. The recording demonstrates that the electrodes can be bent into position around a small anatomical feature and obtain a successful recording. Scale bar is 1 cm.

The electrophysiological recordings are shown in figure 3.9 (a-c). The control recording, done with a pair of uninsulated wire electrodes verified the nerve could be properly stimulated. The stimulus artifact is the sharp initial peak, while the differentially recorded amplitude occurs directly afterward. The two differential

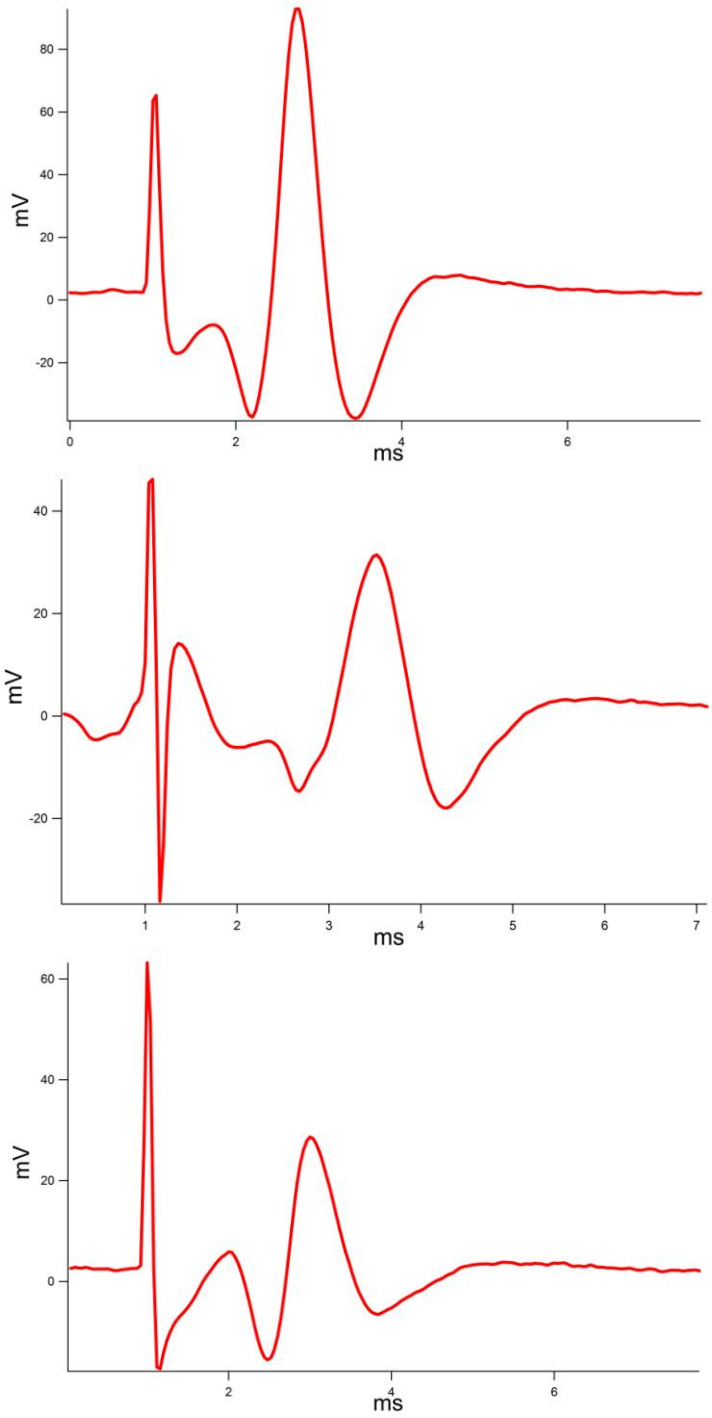

Figure 3.9: The differential recording is shown between (a) a pair of control microwire electrodes approximately 5 mm apart, (b) between the pair of microcables approximately 7 mm apart (c) and between a pair of attached microcables (~ 1 mm apart). The signal is shown after amplification (1000-fold)

recordings from the microcable electrodes are shown in figures 3.9 b-c. The differential recording in 3.9b was obtained from the microcable double array, with a recording site separation of 1 mm. The amplitude is small because the electrodes are spaced relatively close together. The recording in 3.9 c shows the differential amplitude between one of the electrodes in the double array and the third microcable, separated by approximately 5 mm.

3.6 Discussion

The electrodes have been electrically characterized using impedance theory and an experimental electrophysiological model. The two tests were conducted to validate the electrode active rite and the electrode function.

3.6.1 Impedance characterization discussion

The unplatinized gold electrodes have an impedance of approximately 100 kΩ at 1 kHz. After platinization, the constant phase element decreases, as does the charge transfer resistance, and the impedance decreases approximately an order of magnitude to less than 10 kΩ. These changes are due to the increase in surface area at the active site. The platinum black is traditionally useful in reducing the impedance to improve the signal-to-noise ratio for recording applications [3]. It is also a potentially useful coating for non-chronic stimulation purposes. Gold is not used as frequently as a stimulating electrode surface because it has a lower charge storage capacity; during an applied stimulus, gold atoms are irreversibly lost and the surface deteriorates. Platinum, particularly the high-surface area platinum black, has a larger charge storage capacity and a pseudocapacative behavior that is particular to the metal [2].

The values of the fitted parameters are within expected values based on the literature. Because the impedance parameters all depend on the electrode area and the interfacial impedance and charge transfer resistance are dependent on surface area, which is variable for platinum black depending on the plating parameters, a direct correlation is not expected.

Franks *et al.* published the impedance parameters for platinum bright (smooth) and platinum black macro-electrodes (area: 1 cm^2), and platinum black for microelectrodes (area 900 μm^2 or $\approx 10^{-5}$ cm^2) [3]. The values are shown in table 3.4, and compared to the parameters fitted to the electrodes tested here (area: 15,700 μm^2 or $\approx 16 * 10^{-5}$ cm^2). Franks *et al.* plated the platinum black with a current density from 0.3-10 A/cm2, although the duration of the plating was not discussed. The plating described here was pulse plating (9,000 cycles) with a current density of 2.5 A/cm^2. The current density range was similar and the recordings were both done in physiological saline. The parameters are shown vary with the electrode size. n, which is a measure of the fractal properties should not change with the area as long as the fractal character is consistent (i.e. a perfectly flat surface will have an n=1 regardless of the dimensions of the surface). However, the data shown by Franks *et al.* does show a size based variation. The range of current densities was from 0.3-10 A/cm2, which is almost two orders of magnitude and the current density for the respective electrodes was not specified. If the current densities were the same it may have been because the area difference is so large that field inhomogeneities at the edge of the electrode are proportionally larger in the smaller electrode and these inhomogeneties change the deposition characteristics. Rs is approximately proportional for the small electrodes. If the electrodes described here are

approximated as a circle, the calculated radius is 70 μm, while the calculated radius for the published microelectrodes is 18 μm, a factor of 3.9. The spreading resistance increases with the inverse of the radius. The larger electrode (16*10-5 cm2) has a resistance reduced by a factor of 2.1. The influence of the elliptical geometry is minimal (1:0.97) , as stated previously. The effect of scaling on Rs between the $1cm^2$ electrode and the $1*10^{-5}$ cm^2 electrode is also slightly distorted. The radius ratio is 560:1, while inverted the Rs ratio is 2387, large by approximately a factor of four. The platinum black or surface area based resistances are more difficult to approximate because the morphology of the plated material determines the resistance. Given the n decreased more for the electrodes described here (from 0.9 to 0.75) than the n for the electrodes described by Franks *et al*. (0.92 to 0.91 or 0.86) the surface area can be expected to have increased by more and so direct comparisons by geometric area are not possible. The relative changes in charge transfer resistance and Q, when a single electrode is compared before and after, however, is similar. The relative changes (i.e. the initial value relative to the decreased value) in Q and R_{CT} for the 1 cm^2 electrode are $1.3*10^{-2}$ and 0.11, while the relative changes for the $16*10^{-5}$ electrode are $3*10^{-2}$ and 0.27. The ratios of both these changes, i.e. the ratio of the change in Q to the change in R_{CT} is 8.8 for both samples.

Table 3.4: Comparison of impedance parameter values with published data.

Area 16 *10^{-5} cm^2	**Electrode Surface**	**Q**	**n**	**R_{CT}**	**R_S**
	Gold	$3*10^{-9}$	0.90	150k	3.5k
	Platinum black	$1*10^{-7}$	0.75	40k	3.5k
Area 1 cm^2 (Franks *et al.*)					
	Platinum bright	$2.7*10^{-5}$	0.92	450k	28
	Platinum black	$2.1*10^{-3}$	0.91	51k	31
Area $1*10^{-5}$ cm^2 (Franks *et al.*)					
	Platinum black	$8.6*10^{-10}$	0.86	2.7 G	7.4 k

This suggests that although the absolute change in either R_{CT} or Q is dependent on the plating parameters, both parameters will change in a proportion that is constant.

The elastomeric substrate did not affect the impedance data in a noticeable capacity. The experimental data was fit to the theory developed for electrodes on non-elastomeric substrates. PDMS is a relatively low-k dielectric. The dielectric constant of Sylgard 184 is 2.7 (measured at 100 Hz and 100kHz [16]), and the dielectric constant of Sylgard 186 is 2.93 and 2.87 at 100 Hz and 100 kHz, respectively [17]). If the elastomeric nature of the substrate compromised the conductivity of the impedance could be expected to increase. The studies on the conductivity of the thin metal film described in chapter four show that the film remains conductive after reversible stretching of the device.

The applied stimulation under physiologically relevant conditions shows a small change in the shape of the impedance curve after the applied stimulation. This is likely due to both the accumulation of protein at the surface and to irreversible electrochemical activity. The stimulation settings were chosen to be representative of a stimulation protocol *in vivo*; therefore, the stimulation was done in the presence of serum. The literature shows that electrodes exposed to protein have a decrease in interfacial capacitance and an increase in charge transfer resistance. The decrease in interfacial capacitance may be due to an increased efficiency in the charge organization at the interface. The increase in charge transfer resistance may be because the protein is an additional layer through which the charge must pass when a potential is applied. When a charge is applied to the electrode for $1.5*10^6$ cycles, the initial change suggests a slight increase in the constant phase element parameters. This change becomes slightly larger

after $9*10^6$ cycles, although the impedance value is largely unchanged, showing that platinum black can be used for stimulation in a non-chronic application. This is useful because platinum black is relatively convenient to apply. Activated iridium oxide, as an example comparison, is a highly stable electroactive coating but it is more difficult to deposit, requiring a more sophisticated electrochemical system and multiple steps [1]. Platinum black may be useful as an easily applied coating for short-term applications.

3.6. 2 Electrophysiological data discussion

The differential recording of the stimulated action potential demonstrates the recording capability of the microcable electrodes. A positive correlation is shown between the interelectrode spacing of the two recording electrodes and the differential signal, as expected. The signal from the microcable electrodes is comparable to the signal measured with the standard stainless steel hook electrodes used as controls. The impedance of the large control electrodes is extremely low (but not measured) while the impedance for the microcable electrodes was 100 kΩ as measured with an impedance conditioning module (ICM neuro/craft; FHC Inc, Bowdoin, ME). Although direct comparisons between the microcable and control electrodes cannot be made, the prototypic shape of a compound action potential is visible in all recordings. Significantly, the impedance of the microcable electrodes can be varied to suit given applications, by changing the area of the recording site or electroplating platinum black to the exposed recording site. If the microcable electrodes were to be used in a chronic study, it is conceivable from the compliance demonstrated in figure 3.8 that they could be wrapped around the nerve and sutured into a cuff formation.

3.7 Conclusion

The impedance of an electrode site can be optimized for the application by controlling the geometric area, surface area, and surface chemistry. These parameters can be modeled using a resistive and capacitive circuit. The experimentally derived impedance curves can be fitted with the circuit model and the values of the model elements can be estimated to correspond with experimental data. In agreement with theory, increasing the surface area of the electrode decreases the parameters R_{CT}, Q and n, without changing R_S. Additionally, platinum-black coated electrodes can potentially be used for short-term stimulation protocols.

The microcable arrays can be wound around small features such as the peripheral nerve for recording purposes. They successfully tolerated the mechanical handling involved in electrode placement. The electrophysiological signals obtained agree with other recording form control, micro-wire electrodes.

3.8 Citations

1. Meyer, R.D., et al., *Electrodeposited iridium oxide for neural stimulation and recording electrodes.* Ieee Transactions on Neural Systems and Rehabilitation Engineering, 2001. **9**(1): p. 2-11.
2. Merrill, D.R., M. Bikson, and J.G.R. Jefferys, *Electrical stimulation of excitable tissue: design of efficacious and safe protocols.* Journal of Neuroscience Methods, 2005. **141**(2): p. 171-198.
3. Franks, W., et al., *Impedance characterization and modeling of electrodes for biomedical applications.* Ieee Transactions on Biomedical Engineering, 2005. **52**(7): p. 1295-1302.
4. Bard, A.J. and L.R. Faulkner, *Electrochemical methods*. 2nd ed. 2004, Hoboken: John Wiley and Sons.
5. Borkholder, D., *Cell based biosensors using microelectrodes*, in *Electrical Engineering*. 1998, Stanford University: Palo Alto.
6. Jorcin, J.B., et al., *CPE analysis by local electrochemical impedance spectroscopy.* Electrochimica Acta, 2006. **51**(8-9): p. 1473-1479.
7. Ilic, B., et al., *Preparation and characterization of platinum black electrodes.* Journal of Materials Science, 2000. **35**(14): p. 3447-3457.

8. Ross, J., *Microstimulaiton and multicellular analysis: a neural interfacing system for spatiotemporal stimulaiton*, in *Bioengineering*. 2008, Georgia Institute of Technology: Atlanta.
9. Lasia, A., *Impedance of porous electrodes.* Journal of Electroanalytical Chemistry, 1995. **397**(1-2): p. 27-33.
10. Bejan, A., *Heat Transfer Handbook*. 2003, New York: Wiley Interscience.
11. NeuroNexus, *Product Catalog*: Ann Arbor, MI.
12. Gorman, P.H. and J.T. Mortimer, *The effect of stimulus parameters on the recruitment characteristics of direct nerve-stimulation.* Ieee Transactions on Biomedical Engineering, 1983. **30**(7): p. 407-414.
13. Kandel, E.S., JH. Jessell, T., *Principles of Neural Science*. 3rd ed. 1991, East Norwalk: Appleton and Lange.
14. Swett, J.W., RP. Blanks, RH. Swett, AL. Conley, LC., *Motoneurons of the rat sciatic nerve.* Experimental Neurology, 1986. **93**(1).
15. Ross, J., *Microstimulation and multicellular analysis: a neural interfacing system for spatiotemporal stimulation*. 2008, Georgia Institute of Technology: Atlanta.
16. DowCorning, *Sylgard 184 Silicone Elastomer Kit Technical Data Sheet*. 2009.
17. DowCorning, *Sylgard 186 Silicone Elastomer Kit Technical Data Sheet*. 2009.

CHAPTER 4

MECHANICAL CHARACTERIZATION

4.1 Introduction

Compliant and elastomeric electronics are useful for a number of applications that typically require a light-weight, slim-profile, device that can readily conform to a non-planar object e.g. an anatomical surface. There are numerous biomedical applications for these devices, including invasive/implantable electrodes and external electronics, for applications such as human-computer interfaces [1-3]. Additionally, more general applications include paper-like visual displays, strain-based sensors, and electronics that require physical deformation for their deployment into confined spaces [4-7]. Compliant electronics are bendable, wrappable, devices, while elastomeric electronics generally include the properties of compliant devices while also either tolerating or behaving as a function of elastic deformation. Low-modulus electrodes are a current topic of research in endeavors to develop implantable but unobtrusive electrophysiological tools and therapies. Implantable electrodes fabricated on relatively low modulus, substrates such as polyimide have been successfully demonstrated to reduce the trauma to cortical tissue in chronic recording [9-12] These polymer electrodes are durable, and bendable (unlike silicon[1]), and provide microelectronics-level patterning of the leads. The alternative,

---

[1] Wise et al demonstrated the flexible silicon microcables can be used for connection between the electrode array and headstage in implants for animal research. Although the cable is flexible, silicon is still

insulated microwires, are also durable and bendable (if more irreversibly) but are stiffer than polymer or Michigan-style silicon electrodes as evidenced by the fact that they can penetrate the dura without assistance where as the other electrodes require the dura to be snipped before insertion [13-14]. Other examples of compliant electronics, not limited to cortical applications, include fine microwires embedded into a silicone rubber sheet and metallized Kevlar filament for intrafascicular implantation [9, 15-16].

Elastomeric electronics which are both compliant and stretchable have been successfully fabricated using a silicone rubber substrate. The elastomeric property may not be desirable or may provide negligible benefit in some applications, such as a paper-like display. The intended function where compliance is desirable may not benefit or may even be hindered by an elastomeric substrate. In more general applications, if the electronics are composed of integrated circuits, the elasticity of silicone rubber can be dissuading factor.

If integrated circuits are to be used on an elastic substrate, an integrative solution is to pattern the substrate with islands of stiff, or high elastic modulus, material. The fabrication scheme creates an integration of traditional, rigid-substrate electronics, with elastomeric interconnects [17-19]. If highly compliant devices are required, the substrate is sometimes an elastomeric one. Tissue interfaces are an application where a high degree of compliance is often important. Tissue, other than bone, has a range of elastic moduli in

---

extremely brittle and, in the writer's experience, prone to fracture from handling during insertion into the tissue.

the kPa range [20-21], with brain having the lowest value [22] among the excitable tissues listed in the table.

Table 4.1: Young's modulus values for biological tissues. These moduli are lower than the recorded moduli for many plastics (see table 4.2).

Tissue type	Young's modulus
Brain	3.15 kPa [22]
Peripheral nerve	576 ± 160 kPa [20-21]
Cardiac	1003 ± 10.7 kPa [20-21]
Skeletal muscle	24.7 ± 3.5 kPa [20-21]
Endothelial	1.4 ± 0.1 kPa to 6.8± 0.4 kPa [20-21]

Table 4.2: Young's modulus values for polymers commonly used in microfabrication and biomedical devices.

Polymer	Young's modulus
Poyldimethyl siloxane	1 MPa-5 MPa [23]
Parylene C	4.5 GPa [11]
SU-8	3.5-7.5 GPa [24]
Polystyrene	204 GPa [25]
Polyimide (Kapton ®)	2.4-3.2 GPa [26]
Polypropylene	0.15- 1.1 GPa [27]

If electrodes are designed to interface with minimal damage to (low modulus) biological tissue, a highly compliant substrate is desirable, though not necessarily an elastic one; however, because the substrate is elastomeric, the electrodes must not fail due to the stretch incurred during handling and placement.

An electrode's compliance is determined by its bending stiffness, which is the product of the elastic modulus and second moment of inertia. The bending stiffness is the critical parameter in assessing damage to tissue in biological applications. For example, if an electrode array must be wrapped around a peripheral nerve for recording purposes, a

lower bending stiffness reduces the propensity of the electrode to damage the target tissue. The thickness of the substrate, which increases the inertia by the third power, can be reduced to improve the bending stiffness, but the limitation is that using a very thin substrate creates a delicate device susceptible to plastic deformation or breakage. From the materials suitable as substrates for electronics, polydimethyl siloxane has a relatively low elastic modulus (see table 4.2). It is still higher than the modulus of most tissue, but is the lowest of suitable polymers considered here. The second advantage of PDMS is that it is an elastomer, and so can tolerate larger strains than non-elastomer/plastic polymers without suffering plastic deformation.

PDMS has been previously used because of its compliance in electrode arrays without addressing the elastomeric capabilities because the compliance was desirable in its own right [28]; however, the elastic properties of PDMS electronics are desirable for biomedical applications because it adds a dimension of durability to the device, allowing the electrode array to be stretched and pulled over, around and through irregular geometries without risk of breakage. When a thin film is deposited in PDMS, the metal also exhibits elastomeric properties so that the high-compliance is retained without introducing fragility.

Highly-compliant, elastomeric electronics are desirable in general for biomedical applications including externally worn synthetic skins and implantable electrophysiological devices. Synthetic skins have potential applications as biomonitoring devices, either on the body or integrated into clothing [3, 29]. It could also be used in prosthetics as current artificial prosthetic efforts are trying to overcome cumbersome electronics that are dissuasive for wide-spread use [30-32].

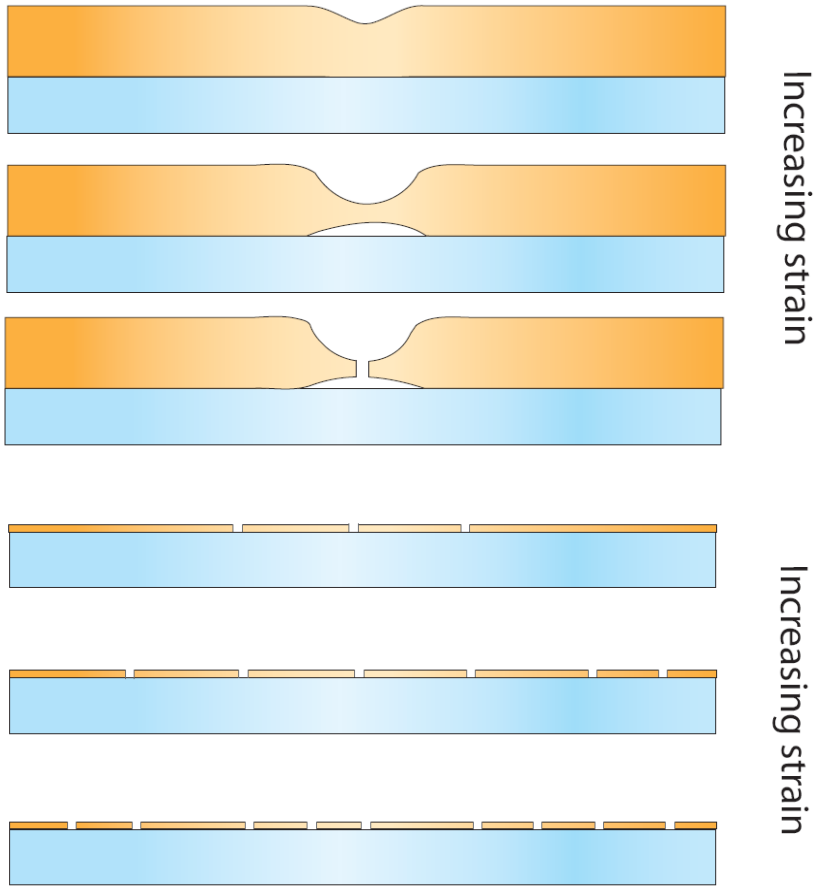

Figure 4.1: The schematic illustrates the difference in fracture patterns between and thick (top) and thin films on an elastomeric substrate under progressively increasing strain.

4.1.1 Background: elastomeric properties of thin-film metal on polymer substrates

When a thin film (<100nm) is deposited on a polymer, the metal layer is able to reduce the crack propagating strain localization that occurs in thick or free-standing films [33]. The strain response of the multilayer structure has been successfully implemented

to create elastomeric or stretch-tolerant electronics. When bonded to a polymer substrate, the thinner films, or free-standing films, have been shown in the literature to be more durable under strain than thicker films because of the way they fracture [34]. The conventional understanding for this trend is that thicker metal films resist the uniformly distributed stress in the substrate and instead concentrate the stress in localized regions forming cracks after a period of plastic deformation (Figure 4.1). The thinner films are better able to deform with the substrate and the stress concentrations because strain-induced cracks are limited by the deformation of the underlying substrate. Thinner films may also be more durable because there is less material available for plastic deformation and subsequent wear induced by topological mismatches at the crack interface is minimized. Examples of the devices are presented below that utilize the fracture properties of thin films as well as describing the strain/resistance profile effect of polymer stiffness, film adhesion, and cyclic strain.

Polyimide substrates with metal films have been stretched up to 20% without suffering a break in the electrical continuity. Although cracks begin to form in the metal, the polyimide responds to strain in a more uniform manner that manages to suppress the propagation of the cracks in the metal film. Xiang *et al*. tested the effects of metal adhesion to the substrate [35]. A plasma treatment was used to improve adhesion to polyimide for a copper film (100 and 170 nm). Without the plasma treatment, the film started to crack and peel off at strains of 2%. Once local thinning occurs the film becomes debonded and behaves like a free standing film, rupturing easily. The plasma treated substrates with Cu films were able to stretch to 10% strain without significant cracks and maintained electrical continuity at 30% strain.

The disadvantage of polyimide is that it plastically deforms, so that once the 20% strain is applied, the substrate and the metal cannot be returned to their original shape. Silicone rubber (PDMS), because it is an elastomer, can be stretched to over 20% without plastic deformation. Li *et al*. tested a 50 nm gold layer (with 5 nm Cr adhesion, 1 mm thick PDMS) on a film that was 25 mm long and 1-2 mm wide [34]. The deposited film was wrinkled, although the wrinkles disappeared after 1% strain. From 3% to 6% strain, the resistance increased linearly, and was electrically open at 8% strain.

Lacour *et al*. demonstrated stretchability with 100 nm thick gold films on PDMS (5 nm Cr adhesion layer) on 1 m thick PDMS [36]. The thin films had a measureable resistance up to 23% strain, at which the resistance was not measureable. The cracks extended across the width of the gold stripe. The relative resistance was less than twice the initial value, until 18% strain, at which point, it began increasing rapidly. The cracks traversed the width of the gold strip at 15%, although electrical continuity was still present. The authors' hypothesis was that a thin conductive layer remains at the bottom of the crack, although it was not detectable.

A 1 mm thick PDMS substrate was stenciled with 200 μm wide, 16 mm long 5nm Cr, 25 nm Au metal [34]. The relative resistance change was measured over 32% strain. After the initial applied strain, the resistance increased approximately 2.5-fold, and the application of 32% strain caused a 6-fold increase in the initial resistance. This behavior was consistent over the course of 100 cycles of applied strain. The cracks were identified as occurring perpendicular to the axis of the applied strain and were 0.2-0.6 μm long at a strain of 20%. It is expected that the cracks will increase in size with the applied strain.

The tolerance for strain has been improved by pre-stressing the substrate, or by creating a substrate with added deformability- i.e., the addition of tri-branched slits to the substrate increases the tolerance for strain of the device without transferring the total strain to the gold film. Similarly, adapting the thin-films to compressive strains involves topographical patterning of the substrate. Patterning a corrugated surface onto the PDMS prior to metallization produced a film that tolerated compression as a function of the wavelength and amplitude of the corrugated pattern [37]. The tolerance for strain without a loss in electrical continuity was improved by maximizing the amplitude of the corrugation relative to the thickness of the film. As the wavelength is increased for a given amplitude, the strain tolerance plateaus, although "wavier" films (those with large amplitude to film thickness ratios) plateaued at longer wavelengths and at higher strain values.

Wrinkling often occurs as part of the deposition process on soft materials [38]; however it can be tailored to maximize the stain tolerance of the film. The metal film can be deposited so that it is compressed on the substrate, extending its conductive range under applied strain, as demonstrated with a gold film is under compressive stress on a PDMS substrate. The thermal expansion mismatch is 14 vs. 960 both 10^{-6}/K, for gold and PDMS respectively so the compression often occurs as part of the deposition process [36]. This can be exploited to further improve the stretchability by stretching the substrate during deposition [4]. The wrinkling wavelength is a function of the thermal expansion mismatch, the pattern of deposition, and the thickness of the two materials. The patterning of lead-like structures (long, thin bars) creates wrinkles orthogonal to the length of the bar-like shape, The organization of the wrinkles is due to the relaxation of

the stress at the edge of the gold, i.e. along the length of the bar. Wrinkling is often present in metal deposited on PDMS and it can be specifically exploited to improve the stretchability of the film.

4.1.2 Alternative and integrative approaches to thin film metal elastomeric electronics

The patterning of thin gold films on elastomers presents several advantages: the system is simple, durable, and well-suited to the requirements of a number of biomedical applications. There are some short comings, however: integrated circuits are not well suited to elastomer substrates and the resistances can be several orders of magnitude higher than the few ohms added from traditional wiring. The power capacity is also attenuated with the reduction in the cross-sectional area of conductive material.

The conductivity of the film varies with the applied strain; this feature could be used as an advantage, but could also present a severe downside to practical implementation; however, these limitations may be overcome by creating stiff islands in the elastomer substrate as described earlier or by using bulk conductive material when a low resistance is necessary. Several examples of elastomeric electronics using bulk conductive material or thin-film metal in a specialized way are described here.

Kim *et al*. have used a room temperature liquid alloy (Indalloy60, Indium Corp, gallium/indium = 75.5/24.5), in a PMDS chip patterned with microfluidic channels (Figure 4.2) [39]. The advantages of using a liquid alloy are the high conductivity, resistance to fatigue, and the smooth response to resistance changes ($\Delta R=0.24\ \Omega$) when stretched up to 100%. The percent change can be modulated via the width of the

microfluidic channel. Narrower channels have a greater percent change in resistance for a given strain.

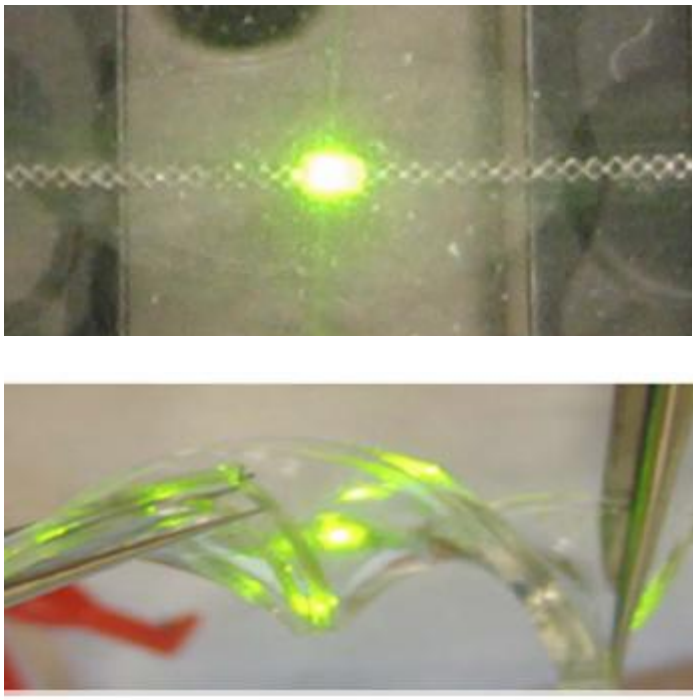

Figure 4.2: A conductive liquid alloy has been filled in microscale channels in PDMS. The liquidity is well-suited to the dynamic nature of a stretchable device, however liquid handling and storage limits the device compatibility [39].

More conventionally, sinusoidal trenches have been formed in PDMS and electroplated to create a gold "wire" (Figure 4.3). This approach also uses micropatterning of bulk material to create a stretchable electrical connection. The wires were patterned in a sinusoidal shape that could be stretched and released as shown in the figure. The authors found than the tolerance for strain could be maximized by decreasing the linewidth and wavelength of the microwires. The wires could be stretched without failure until they were practically straight (57%). The fatigue performance was lower than the films'; the wires could withstand approximately 200 cycles at 25% strain [40].

Patterning the thin-film gold in a stretchable geometry was used in a design described by Befahy *et al*. (Figure 4.4)[41]. PDMS strings were created (400 μm diameter) and twisted prior to metal deposition. After the deposition, the untwisted PDMS strings had a helical gold trace along their length. The number of twists was used to control the width of the gold trace. Although cyclic fatigue data was not reported, electrical continuity was maintained up to 43% strain.

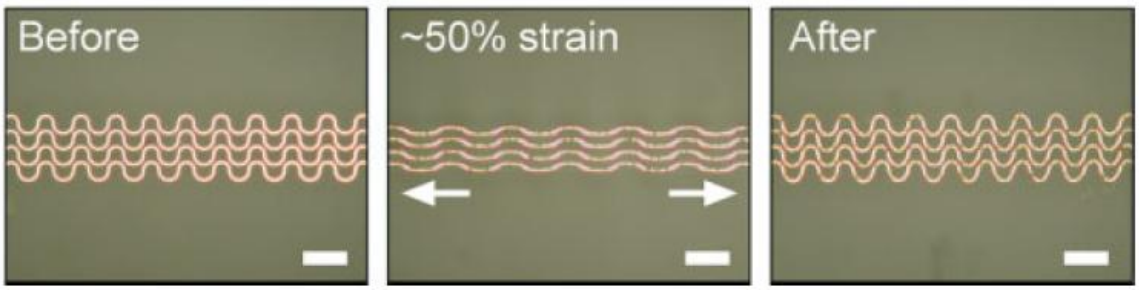

Figure 4.3: Thick, electroplated gold wires were deposited in micromolded trenches. The sinusoidal conformation allows them to be stretched until they are maximally extended [40].

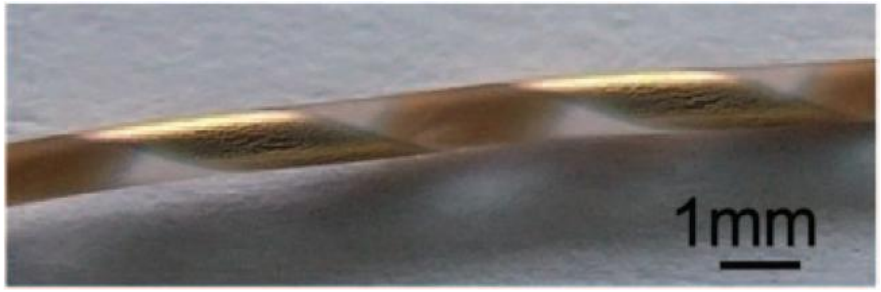

Figure 4.4: The helical patterning of gold on a cylindrical PDMS substrate is another innovative approach to maximize the stretchability [41].

4.1.3 The composite elastic modulus of thin metal film and PDMS structures

PDMS and gold have an elastic modulus difference of approximately four and a half orders of magnitude (90 GPa and 5 MPa for gold [42] and PDMS respectively [43]). The thicknesses difference between these materials in elastomeric electronics is also, typically, in the region of four orders of magnitude (e.g. tens of nanometers of Au on a PDMS substrate hundreds of microns thick). The thin layer of high-modulus gold on the PDMS substrate does increase the effective plane strain modulus compared to the native PDMS as long as the gold film does not have cracks. Once cracks are developed in the film, the stiffening effect is mitigated and the composite structure can have a plane strain modulus equal to that of unmodified PDMS. The analytical relations governing compliant substrates with stiff coatings are proportional to the relative thicknesses and elastic moduli of the respective materials [42].

The plane strain moduli, which account for the Poisson ratio of the material, (eq 4.1-2) and the relative thicknesses (eq 4.3-4) are used in calculating the composite plane strain modulus in the non-cracked system. The simple ratio of the thicknesses and plane-strains is a dimensionless parameter to predict the relative stiffness (eq 4.5). As the thickness of the substrate increases, the relative change in stiffness, S, decreases to 0. The plane strain of the composite with an uncracked film is given in eq 4.6.

Analytical calculations of the plane-strain modulus based on equation (4.x- Begley eq 1)

$$\overline{E_f} = \frac{E_f}{(1-\nu_f^2)} \qquad \text{Eq. 4.1}$$

$$\overline{E_s} = \frac{E_s}{(1-\nu_s^2)} \qquad \text{Eq. 4.2}$$

$$\hat{h}_f = \frac{h_f}{h_f + h_s} \qquad \text{Eq. 4.3}$$

$$\hat{h}_s = \frac{h_s}{h_s + h_f} \qquad \text{Eq. 4.4}$$

$$s = \frac{h_f \bar{E}_f}{h_s \bar{E}_s} \qquad \text{Eq. 4.5}$$

$$\overline{E_o}\varepsilon = [\hat{h}_f \overline{E_f} + \hat{h}_s \overline{E_s}]\varepsilon \qquad \text{Eq. 4.6}$$

The crack spacing, L, and the constant, c, relate the reduced plain strain modulus of the substrate with the cracked film, $\bar{E}_c$.

$$\frac{\bar{E}_c}{\bar{E}_o} = \left[1 + c\left(\frac{h_f \bar{E}_f}{L\bar{E}_s}\right)\left(\frac{\hat{h}_f \bar{E}_f}{\hat{h}_s \bar{E}_o}\right)\right]^{-1} \qquad \text{Eq. 4.7}$$

The constant, c, was determined by a least squares fit of the equation to the data ($c \approx 2$). Experimental data from Begley et al. indicate that eq 4.7 is accurate for

$$\left(\frac{h_f \bar{E}_f}{L\bar{E}_s}\right) < \sim 25 \qquad \text{Eq. 4.8}$$

The relation was tested by the application of strain to the Au-PMDS laminate to generate cracks in the gold layer. When the substrate to film ratio is in the range of four orders of magnitude difference and the film thickness is approximately 100 nm or less, the plane-strain modulus of the cracked sample is a one- to two-fold increase in the plane strain modulus of the substrate, which is much lower than the uncracked sample plane strain modulus (order or magnitude or larger). This analysis shows that although the gold layer

does increase the stiffness of the device, after the cracking that occurs from handling from the packaging, it is likely a modest increase.

The modulus of thin films on elastomers is lower than the calculated values if there is cracking in the gold film. Experimental data was matched with theoretical calculations for an elastomer sandwiched by two films of metal [44]. A 16 nm film deposited on either side of a 162 μm thick elastomer increased the in plane modulus from 1.3 MPa to 27 MPa by calculated values. The large increase is due to the relatively high modulus of the gold film (1251 GPa). After cracking the experimentally measured in plane modulus was 1.6 MPA, very close to the modulus of the elastomer substrate. The calculated value was 1.3 MPa, for an equation based off experimentally measured crack spacing and lengths. The crack parameters are used to estimate the displacements at the cracks under applied strains. Thicker substrates and films were also tested, with the substrate to film ratio ranging from 10:1-20:1. The strains were 3%, and the substrate was assumed to be linearly elastic. The theoretical value trends smaller than the measured value, except for films of ~ 100 nm or greater (96 nm-285 nm), at which the predicted value is larger.

The author observed the dislocation behavior at small volumes as a potential explanation for the discrepancy. Fracture of brittle films preceded by necking/local elongation has a film-thickness dependent behavior. Plastic deformation is reduced in films that are less than 300-500 nm [45]. The limits of plastic deformation are due to the interference of the grain-like morphology of deposited films. For thinner films, the grain structure dominates the cracking behavior, with the grain boundaries acting as crack initiation sites.

The grain size of a film will increase with film thickness (although not proportionally), so studies examining these variables acknowledge the interdependence. Thinner films can be shown to have a better tolerance for repeated cycling, as demonstrated by Sun et al. [18]. Two thicknesses of copper (175 nm and 700 nm) deposited on polyimide were tested for changes in resistance after repeated cycling at 1.3% strain. Although both films are relatively thick and the resistance increased with the number of cycles for both, the failure (i.e. when the resistance increases switched from slight to large) of the 700 nm film began around 1000 cycles and the failure of the 175 nm film began around 5000 cycles. Nanocrystalline metals (grain size < 100 nm) contain a proportionally large surface area of interfacial regions, changing the fracture behavior relative to larger grain sizes. Mechanical effects are an enhanced yield stress and reduced tensile elongation. As grain size decreases, the stress to propagate a dislocation increases [46].

Embedding a 140 nm thick porous gold film in a 40 μm thick layer creates a composite with an experimental modulus of 1.35 MPa, equivalent to the native PDMS. When the film was deflected, it retained electrical continuity that increased "smoothly" up to 25%. The increase or eventual loss in electrical continuity at strains above 25% was not described.

4.1.4 Theory of thin-film crack propagation on compliant substrates

The use of a thin film (< 100 nm) of gold on PDMS has been used in multiple instances to create an elastomeric electronic structure. The thickness of the film, among other variables, determines the device's ability to fracture under cyclic strain without suffering a permanent loss of electrical continuity after the strain is released. As the

theory described here will relate, all other variables being consistent, thick films will have fractures that propagate longer distances (i.e. causing failure) than fractures in thin films. The thin films' fractures propagate for shorter distances and are less prone to causing a loss in continuity. The free standing films rupture at 1-2%, lower stain than required for the fracture and breakage of the bulk material. Examples of stretchable gold/PDMS have been described repeatedly in the literature. The theory for the increased brittleness of free-standing thin films and for the stretchability of the films on elastomers are based on the very small film thickness compared to that of bulk metal. In a thin film the hardening and necking occur on a reduced spatial scale because less material is available in the thin film as demonstrated in the schematic shown in Figure 4.1. Necking (i.e. localized thinning) occurs on a length comparable to the thickness of the film. In a thin film, the local elongation is small and covers a small strain region before rupture occurs, unlike bulk material, which will elongate to a higher strain before fracture. In a free standing film, once a neck occurs the strain becomes very large at that site and reduces over the rest of the film. The localized strain generates a fracture. The displacement localization quickly leads to failure. The support of the substrate acts to suppress the strain localization as demonstrated in the literature [33].

The energy release from the crack propagation is described by the following equations. The crack modeled is a semi-infinite crack on an infinite substrate and film with a difference in elastic properties and Poisson ratios described by the Dundur's parameters, α and β, that described the difference in elastic modulus and Poisson ratio from the two materials.

$$\propto = \frac{\overline{E_f} - \overline{E_s}}{\overline{E_f} + \overline{E_s}} \qquad \text{Eq(4.9)}$$

$$\beta = \frac{E_f(1+\nu_s)(1-2\nu_s) - E_s(1+\nu_f)(1-2\nu_f)}{E_f(1+\nu_s)(1-\nu_s) + E_s(1+\nu_f)(1-\nu_f)} \qquad \text{Eq (4.10)}$$

The stiffness of the substrate and film is S:

$$S = \frac{h_f \overline{E_f}}{h_s \overline{E_s}} \qquad \text{Eq (4.11)}$$

The stress in the film is

$$\sigma_f(x) = \int_0^x \frac{\tau(\tilde{x})}{h_f}\, d\tilde{x} = \frac{\sigma}{h_f}\int_0^x f(\tilde{x})d\tilde{x} = \frac{\sigma \cdot l}{h_f}\phi'(\bar{x}) \qquad \text{Eq (4.12)}$$

for *l* defined as the shear transfer length, which is the distance between the crack tip and the point in the structure where the stain in the film is equal to the stain in the substrate. f(x) and $\phi'(x)$ are dimensionless functions.

$\bar{x} = {}^{x}/_{l}$ is the point being considered relative to the shear transfer distance, *l*.

$$\sigma_s(x) = \frac{\sigma}{\hat{h}_s} - \frac{\hat{h}_f}{\hat{h}_s}\frac{\sigma \cdot l}{h_f}\phi'(\bar{x}) \qquad \text{Eq (4.13)}$$

The strain at the crack boundary is

$$\varepsilon = \frac{\sigma}{E_o}\left[1 + c\left(\frac{h_f \overline{E_f}}{L\overline{E_s}}\right)\left(\frac{\hat{h}_f \overline{E_f}}{\hat{h}_s \overline{E_o}}\right)\right]^{-1} \qquad \text{Eq(4.14)}$$

where c is:

$$c = \frac{1}{\phi'(1)}\left(1 - \frac{\phi(1)}{\phi'(1)}\right) \qquad \text{Eq(4.15)}$$

G is the energy release per unit of area of crack propagation.

$$G_o = \left(\frac{2c}{1-\alpha}\right)\frac{\overline{E_c}\overline{E}_f\varepsilon^2 h_f}{\overline{E_o}} \qquad \text{Eq(4.16)}$$

The energy release increases with the strain moduli of the materials, the thickness of the film, and the difference between the substrate and film plane strain moduli, as expressed by α.

The stiffness of the substrate determines the level of support transferred to the film. The effect of the substrate on crack propagation in a metal film under strain is shown in Figure 4.5. An unsupported film will not have a mechanism to suppress a crack after it has developed; the crack becomes a site for localized stress and the site of failure in the film. Adhesion of the film to a substrate inhibits stress localization and crack propagation as demonstrated by the plasma treatment [35].

A stiffer substrate is expected to inhibit the crack propagation more effectively than a more compliant substrate [33, 42]. The polymer substrate is inclined to a large regime of uniform plastic or elastic response to strain prior to failure. At comparable strains, the metal film is inclined to crack initiation, propagation, and localized failure. The substrate's uniform response inhibits the film's crack propagation. The stiffer the substrate, the more effectively the crack propagation is inhibited. The substrate stiffness is determined by the elastic modulus and the thickness. An insufficient stiffness allows the cracks in the metal film to propagate and break electrical continuity. As the cracks form, the elastomer substrate deforms locally with the cracks. Stiffer substrates prevent the propagation [47].

Attachment to the substrate is critical because once the film has delaminated from the substrate it becomes a free-standing film, rupturing at a few percent strain. The constraint of the adhesive substrate prevents local elongation from continuing to a continuity breaking fracture. Attachment is improved by minimizing substrate contaminants, applying a surface charge to the substrate prior to deposition, and using a thin Cr adhesion layer between the substrate and the metal film [48]. Using a bulk Cr layer is undesirable because Cr is more brittle than other available metals, such as copper or gold, and consequently, fails at lower strains [48].

Figure 4.5: Fracture patterns of a free-standing gold film (top) and a film mounted on a stretchable substrate. The film mounted on the substrate fractures in multiple locations without causing a complete fracture in the film. The substrate inhibits the progression of the fracture.

4.2 Methods

4.2.1 Stiffness characterization

The stiffness of the microcable arrays was tested by measuring the tensile force upon the controlled application of strain. The tensile tests were done using an Instron-like machine, designed for millimeter and sub-millimeter displacement (Bose Electroforce 3100 test instrument, Bose; Eden Prairie, MN). The microcable was mounted on a piece of paper with a slit 1.33 mm wide cut out of the middle. The

microcable was glued to the paper at either end of the slit with RTV silicone elastomer. The microcable on the paper frame was then glued to a small square of polyimide, which was glued to a screw (Figure 4.6) . The screw fit into the force sensor, which was mounted in-line with the microcable in the Instron machine.

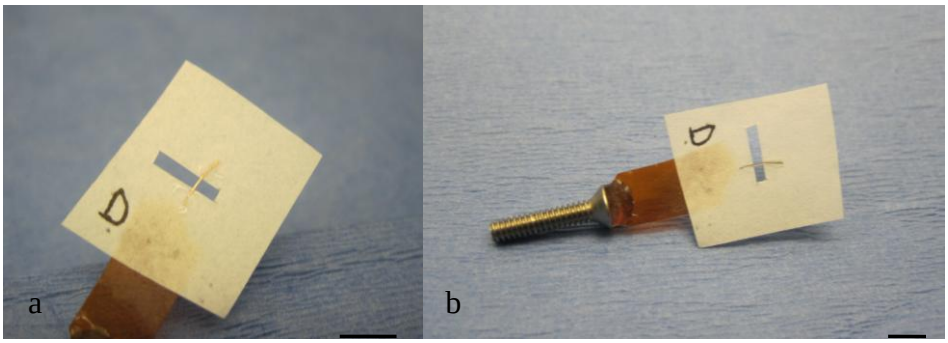

Figure 4.6: The microcable is mounted on a strip of paper and attached to the force sensor using a screw and piece of polyimide. The polyimide was coupled to the screw because it could easily be glued the screw in a vertical orientation. It served as a linkage to ensure the microcable and paper housing could be attached to the force sensor without introducing unintended distortions in the microcable orientation. The testing set-up is the same that was used for the tensile tests in Chapter 2. Scale bar: 2 mm

The microcables were tested in a series of increasing strains to assess if cracking from increased strain levels would measurably reduce the modulus. The strains were applied five times before increasing the strain load. The strain levels were 5, 10, 20, 30 and 40% strain. Higher strain levels were not tested because low strain values are used to obtain the Young's modulus.

The calculated tensile modulus was used to compare the effective bending stiffness of the microcable electrodes relative to silicon and polyimide electrodes from the literature. The bending stiffness of a beam-like structure is dependent on the product of tensile modulus (E) and second moment of inertia (I) for a given beam length. The

calculations were done per unit length to compare the variation in modulus and cross-sectional area. The inertial moments were calculated across both the wide and narrow axis (see Figure 4.7 for the relative aspect ratios). For simplicity in the calculations, the gold was assumed to extend the width of the microcable electrode. The gold was patterned into traces (≤ 15 μm wide) for the polyimide [49] and silicon [14] electrodes and was ignored for simplicity in the calculation. The cross-sectional areas for the polyimide and silicon electrodes were 30 x 80 μm and 15 x 80 μm, respectively [14, 49]. The tensile modulus values for silicon and polyimide used in the calculations were taken from the literature [10, 26].

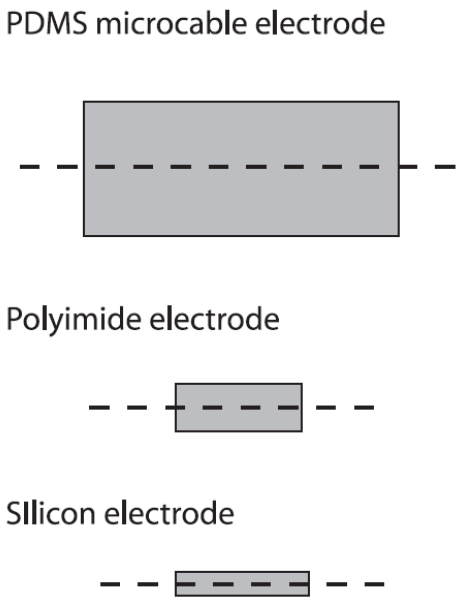

Figure 4.7: The relative aspect ratios for the cross-sections of the PDMS microcables, the polyimide and silicon electrodes are shown above. The second moments of intertia were calculated with respect to the wider axis, as shown by the dotted lines.

For calculations on the microcables, several assumptions were made: the PDMS was treated as one layer, rather than two because only of the layers is only 5 µm thick. The gold tensile modulus was taken from the literature. The gold film in the microcables may be stiffer than bulk gold because of the mechanical properties of thin films [46], but because the film has cracks, it is expected to have less effect than calculated on the microcable composite tensile modulus [44]. The equations for calculating the composite EI from a bilayer structure are presented in Eq 4.17-19 [50].

$$EI_{eq} = \frac{w t_b^3 t_a E_b E_a}{12(t_a E_a + t_b E_b)} K \qquad \text{Eq 4.17}$$

$$K = 4 + 6\frac{t_a}{t_b} + 4\left(\frac{t_a}{t_b}\right)^2 + \frac{E_a}{E_b}\left(\frac{t_a}{t_b}\right)^3 + \frac{E_b}{E_a}\frac{t_b}{t_a} \qquad \text{Eq 4.18}$$

$$I = \frac{bh^3}{12} \qquad \text{Eq 4.19}$$

4.2.2 Electromechanical response to strain

The electrodes were fabricated according to the protocol described in section 2.3 "Revised approach for stretch-tolerant electrodes." The gold surface was imaged using scanning electron microscopy to identify the grain size and to examine the morphology of cracks in the gold deposited on PDMS. The crack propagation at progressively larger strains was also documented using optical microscopy. The microcable electrode was

mounted to a micrometer-controlled stage and the gold on the microcable surface was photographed at discrete applied strains.

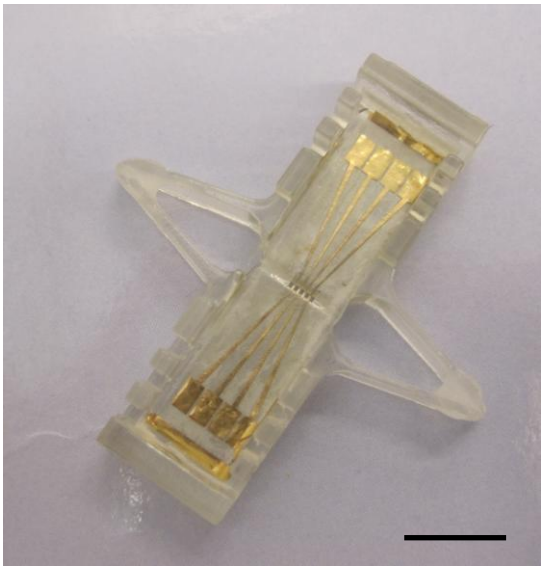

Figure 4.8: The electrode array is shown mounted on the 3D printed frame for mechanical testing. The arrow indicates the region of stretch. The elbows at the sides of the device allow the center region to be stretched while maintaining a fixed space while the electrode array is mounted in the frame and while the frame is mounted in the Instron. The electrode is mounted in the frame with a small amount of slack. Once the piece is mounted in the Instron, the slack is removed by adjusting the Instron spacing. The adjustment is noted in the applied strain. Scale bar: 1 cm

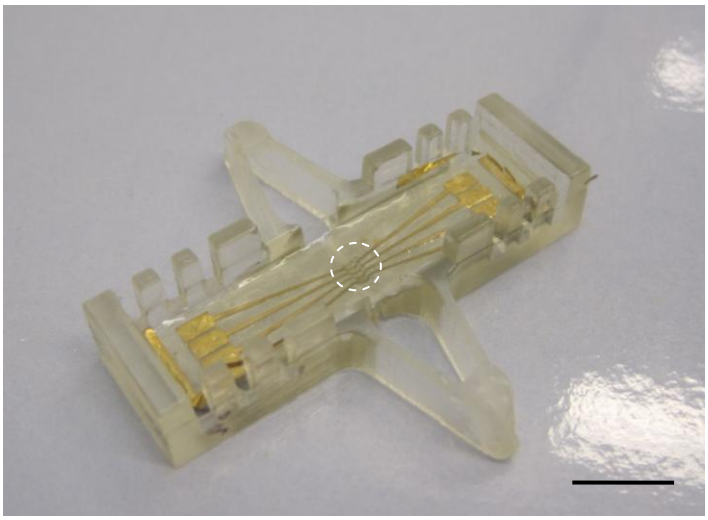

Figure 4.9: The frame and electrode array are shown from a side view. The teeth on the sides of the frame are to hold the wires connecting the array to the resistance measurement set-up. The teeth also recess and protect the wires and electrode array from the clamps. Scale bar: 1 cm

The fatigue testing was done on a Bose Electroforce 3100 test instrument (Bose; Eden Prairie, MN). The strain was applied as a linear-sloped displacement that returned to zero displacement at the same linear rate. The displacement was applied at 1 Hz. The microcables were mounted on a frame as shown in Figure 4.8-9. The frame served to provide a mechanically stable platform for electrical connection and to isolate a testing area, shown as the open region in the center of the frame. The test area, circled in Figure 4.9 varied depending on the degree of strain to maximize the resolution of the test. 2.0 strain (displacement: 2 mm) was tested over a 1 mm span. Strains of 1.0 or less were done over a larger span, 2.4 mm (strain, 1.0: displacement, 2.4 mm). The displacement varied from 2 mm (200%) to 0.25. The frame was printed on a 3D rapid prototyper (Eden 250 Printer, Object Geometries Inc.; Billerica, MA) from a CAD drawing created in SolidEdge (Siemens PLM Software; Plano, TX). The microcables were mounted in the frames with a small amount of slack. Once the microcable/frame assembly was

mounted in the instron (Figure 4.10), the slack was removed in 10 μm increments with resistance measurements taken at every increment. The zero strain was set at 10 μm below the position at which the resistance started to increase.

The electrical resistance recording and strain recipe were on two separate systems and were not linked via trigger. As such, the resistance recording was not time synchronized to the strain profile. To correlate the strain with the resistance, the periodicity of strain was used to calculate the corresponding resistance. For example, the resistance tests (Section 4.2.2) were conducted using a 200% strain applied at 0.2 Hz (5 seconds for a total cycle, 2.5 seconds per increase or decrease in 200% strain). The lowest resistance corresponds to the decreasing/increasing window centered around zero strain. Because the time of that window is given in the resistance data (for example: 0.3 seconds), the strain at which resistance is lost is the displacement (12%) over half that time span (0.15 s).

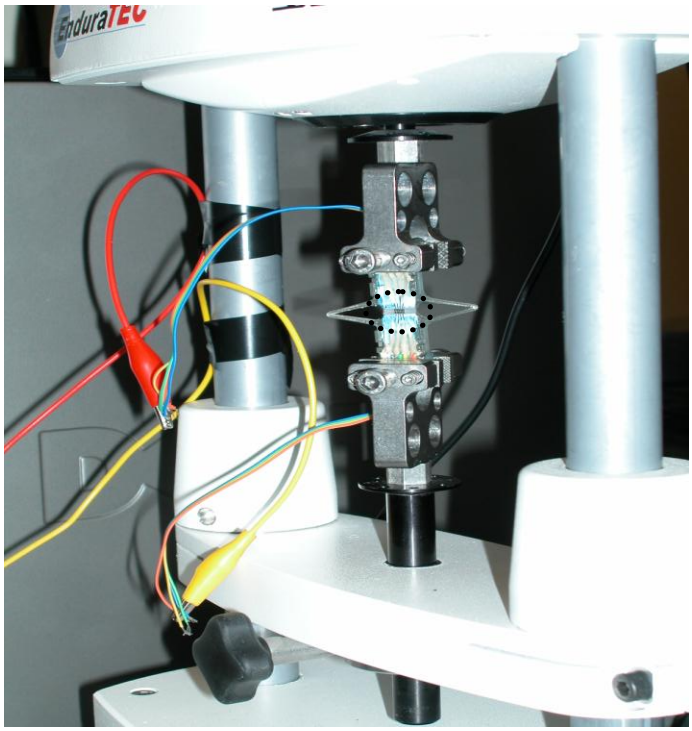

Figure 4.10: The electrode array is shown mounted in the Instron machine. The center region, highlighted by the dashed-line oval, is the 2 mm gap that is stretched.

The electrical resistance was measured with a resistance-tracking program created on a SignalExpress platform (National Instruments; Austin, TX) that measured the resistance as a function of the applied displacement (see Appendix II). The resistance-tracking system was able to monitor the resistance from 0-110 kΩ. The resistance tracking was done at periodic intervals in the sequence of applied strains. The applied strain was slowed to 0.02Hz during recording because of acquisition limitations in the system.

For several tests, the fatigue testing was conducted on a set of two microcable electrodes measured as one resistance value. This was done to maximize the resolution of the test. The resistance value of an individual electrode is calculated by assuming each

electrode has a roughly equal resistance that is measured in a parallel array of four electrodes. Measurements were done prior to testing. Electrode pairs in the tests were selected that had a strain-free resistance within 100 Ω or less.

4.3 Results

4.3.1 Morphology of the gold and qualitative response to stretch

The gold surface has a grain size of approximately 30 nm, as shown in Figure 4.11-14. The cracks are from casual handling of a gold-coated PDMS membrane. The surface morphology demonstrates that the gold film has microscale cracks that have a roughly rectangular or trapezoidal pattern at low strains. Although, as seen in the micrographs documenting the film under progressively increasing strain, the geometry becomes less specific (Figures 4.15-24). Some of the crack formations have a diagonal direction, suggestive of shear fracturing.

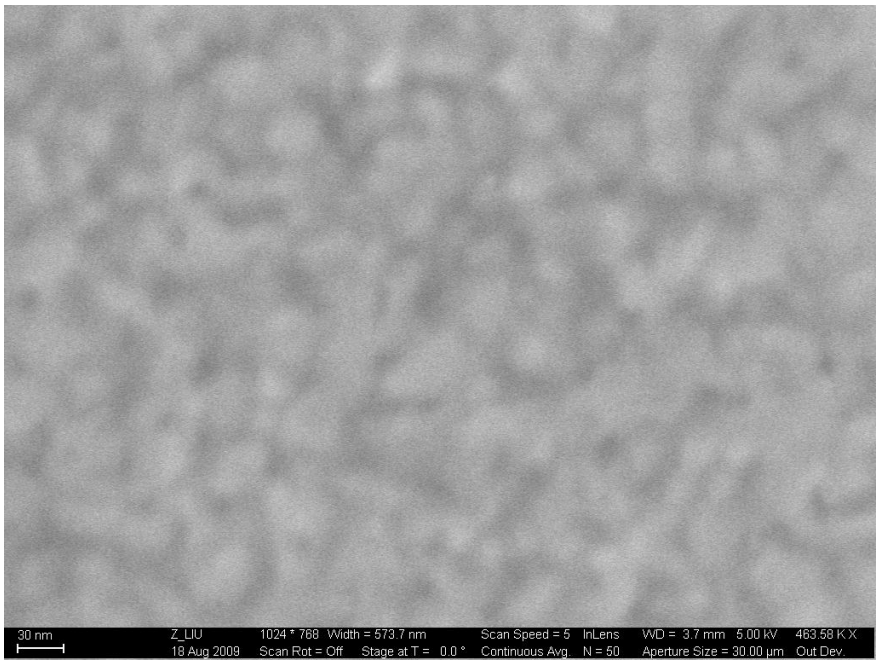

Figure 4.11: The grains in the 30 nm thick gold film on PDMS are somewhat variable in size and shape. The approximate diameter is 25-30 nm.

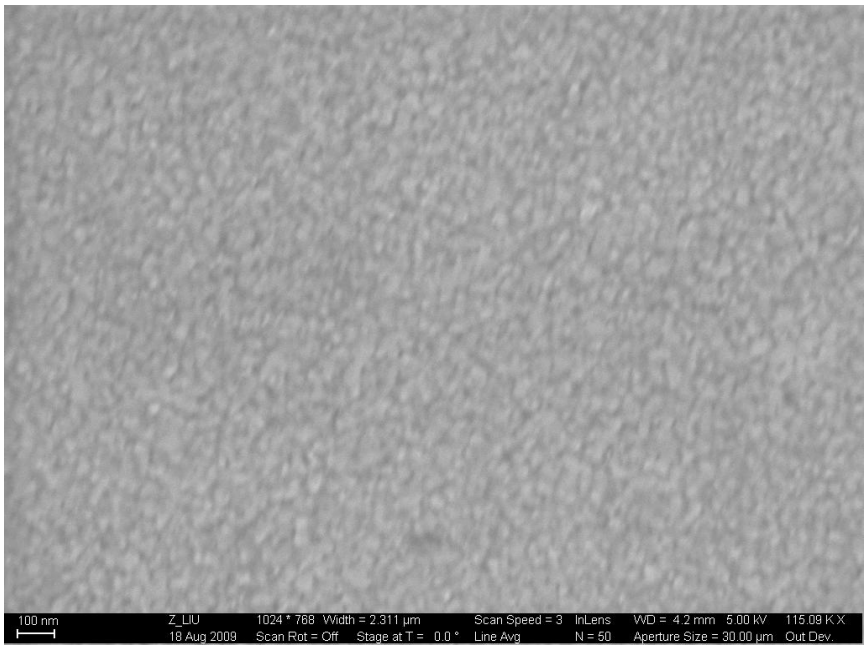

Figure 4.12: The gold film is shown here at a lower magnification to provide a second view of the film morphology.

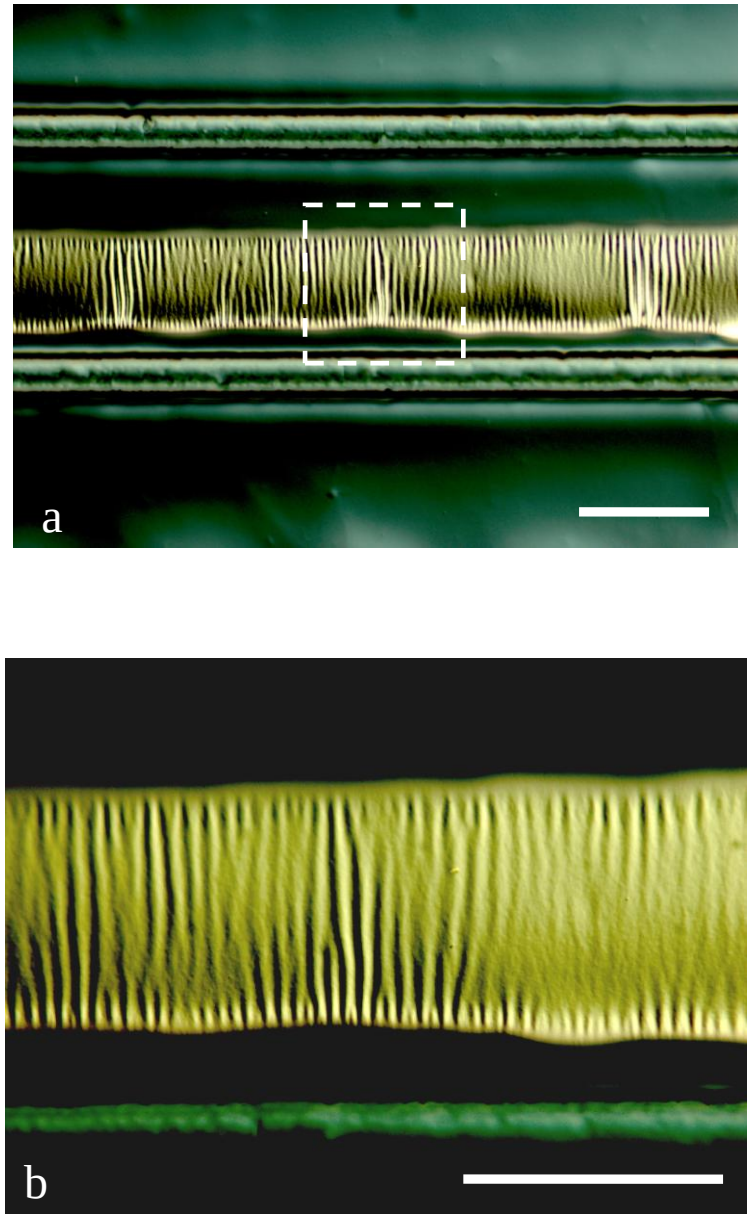

Figure 4.13 a-b: The gold lead of the electrode is shown after patterning, but before it is released from the mold. The highlighted region from a is shown at a higher magnification in b. The uneven edges are a result of both the roughness of the stencil and the degree of contact between the stencil and the substrate. The gold is wrinkled, but not cracked. The scale bars are 100 μm.

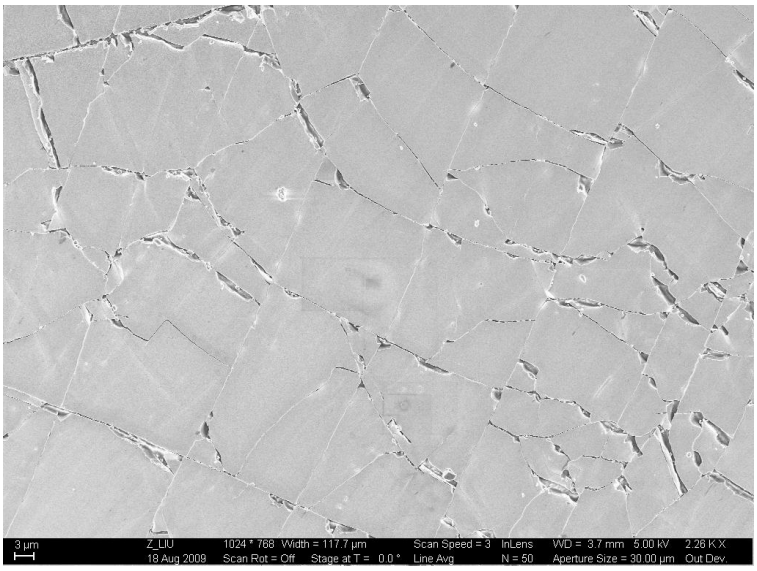

Figure 4.14: Cracking in the 30nm gold on PDMS film is shown above. The cracks follow a somewhat irregular rectangular pattern. When the substrate is not under strain, as shown in the figure, the cracks do not break the continuity of the film.

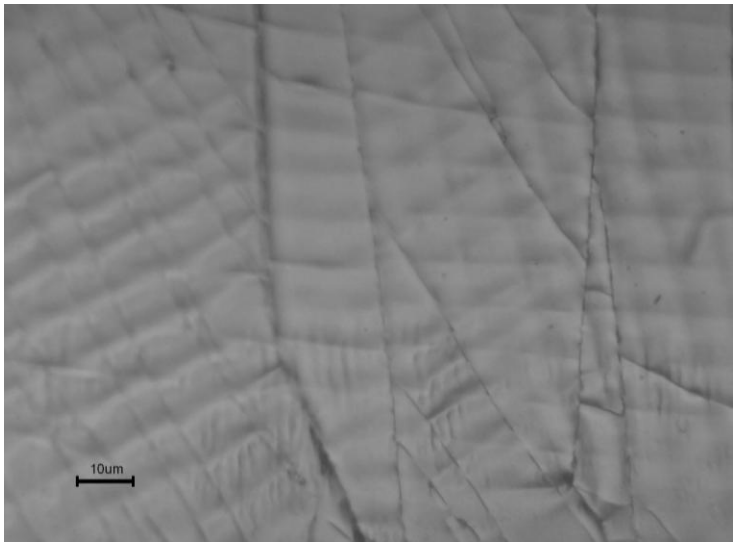

Figure 4.15: The mesoscale view of gold on a PDMS sheet shows two patterns of stress distribution. Cracks and long wrinkles are visible in a randomly oriented pattern. A smaller set of wrinkles, with a periodicity of approximately 10 μm is visible, with an orientation roughly perpendicular to the larger cracks and wrinkles.

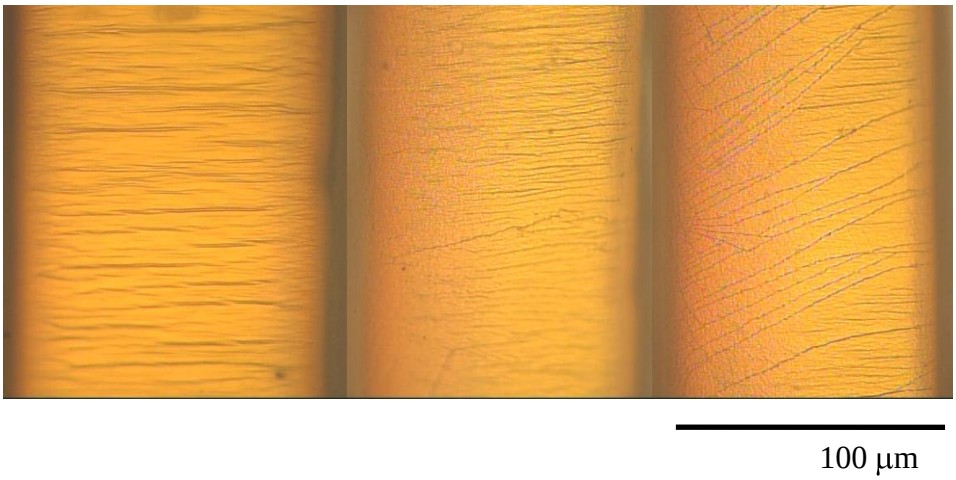

Figure 4.16: The electrodes are shown after release but prior to a specified application of strain. The cracks are visible in most but not all microcables (the far left microcable appears uncracked) and are created by the release from the mold and casual handling. The surface of the film is also seen to vary among microcables. The left most image is grossly, but evenly wrinkled. The middle and right images have a mix of wrinkled regions and unwrinkled regions with a visibly granular morphology. The three microcables shown above are from the same array (and same deposition).

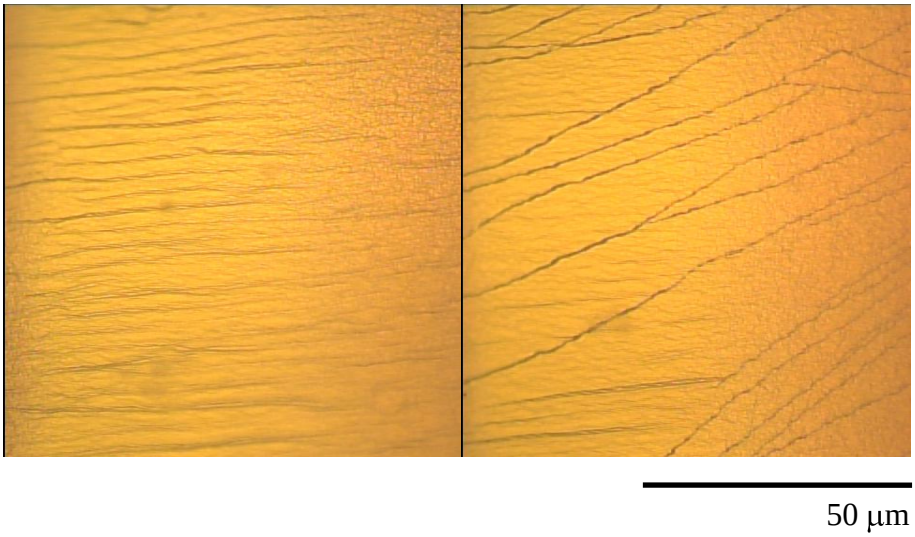

Figure 4.17: The unstrained electrodes are shown at a higher magnification for detail of the surface morphology.

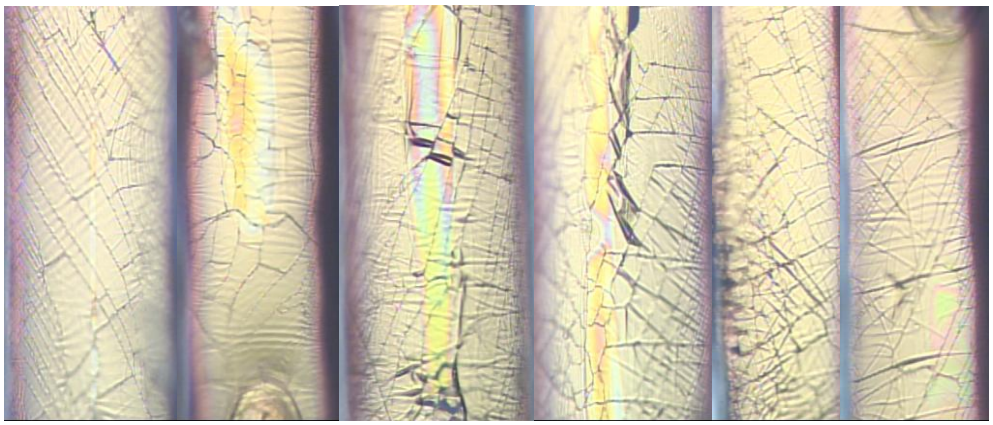

Figure 4.18. The electrodes are stretched 2.5%. The cracks are visible and by be due to casual handling. The crack orientation is diagonal to the long axis of the electrode. Delamination is visible at several points.

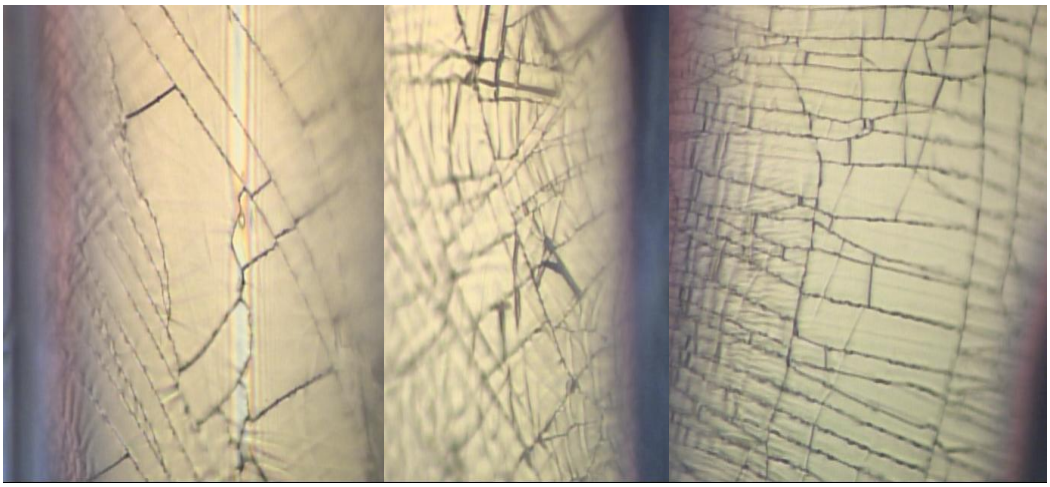

Figure 4.19: The same electrodes, strained to 2.5% shown at 100 x magnification. The cracks have a varying orientation with respect to the long axis of the electrode.

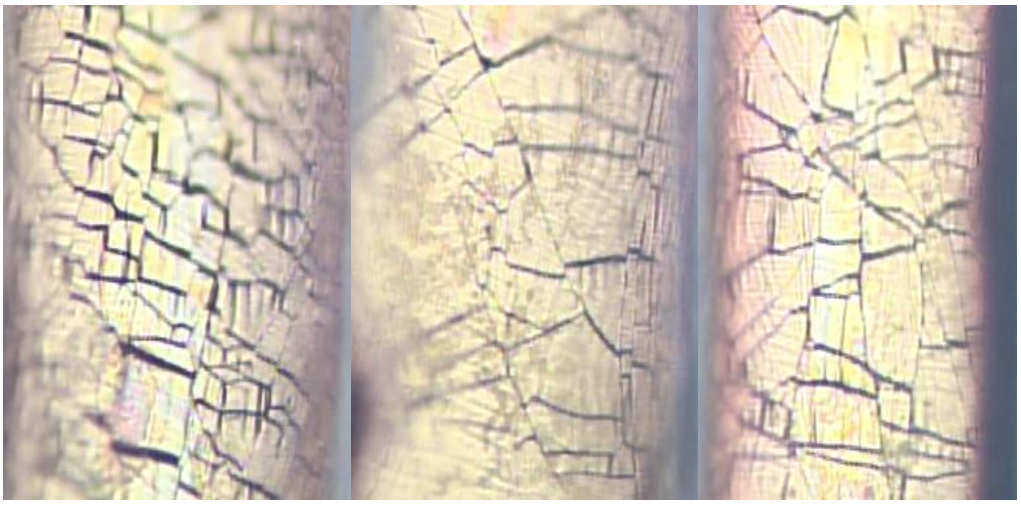

Figure 4.20: The electrodes are shown at 10% strain at 50 x. The strain dependent resistance recordings indicate that the electrode conductivity has decreased approximately two orders of magnitude.

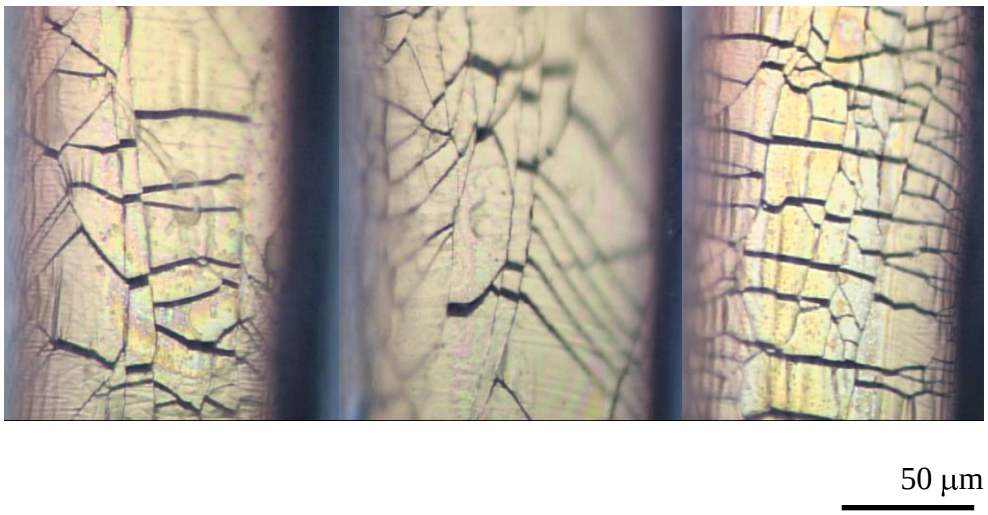

Figure 4.21: The 100 x view of the electrodes at 10% strain shown that while the gold islands are separated, there are still regions of connectivity.

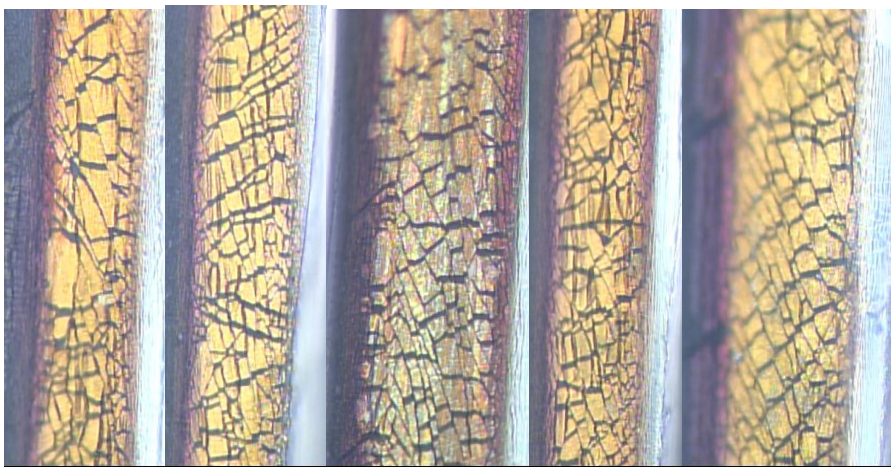

Figure 4.22: At 0.25 strain, the cracks appear to completely separate the gold islands.

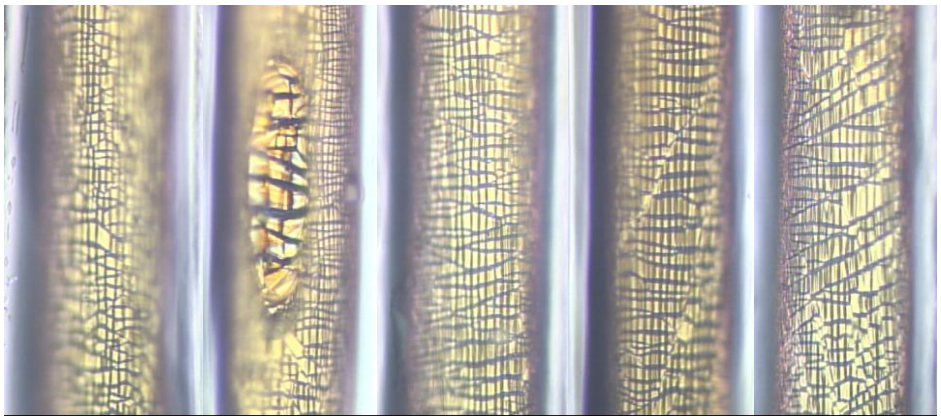

Figure 4.23: At 0.5 strain, the size of the gold islands decreases. The recording site/uninsulated region is visible in the electrode second from the left. The uninsulated region is shown to have larger cracks than the insulated region.

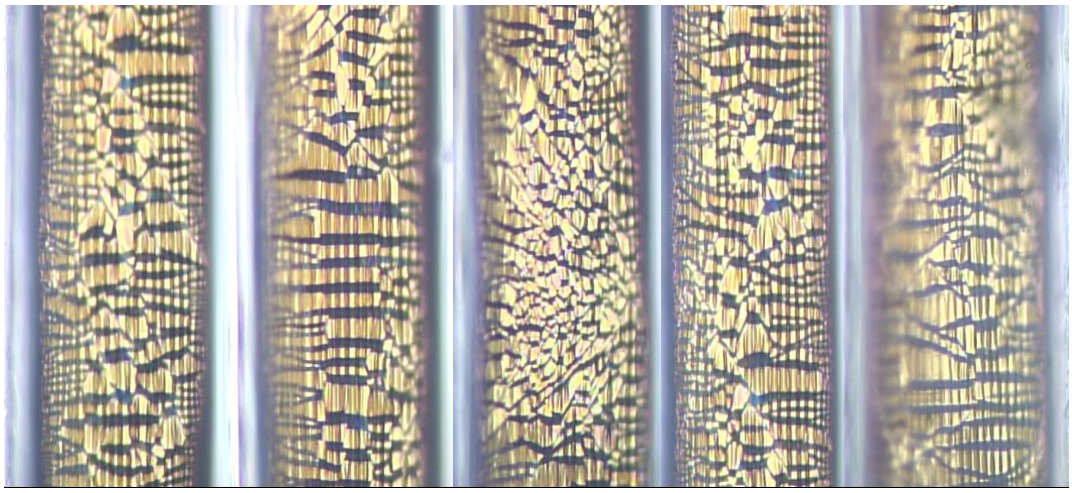

Figure 4.24: At 1.0 strain, the gold film is shows compressive wrinkles in the direction perpendicular to strain. This is likely due to the decrease in the cross-section of the PDMS strain under large strain.

4.3.1 Young's modulus of the patterned microcable array

The microcables patterned with gold and an insulating PDMS layer were tested at sequentially increasing strain levels (5, 10, 20, 30, & 40%) (Figure 4.25). The data displayed here are at 10 and 40% strain. The stress-strain curve of the 10% strain has a slightly higher slope than the 10% strain region in the 40% stress-strain curve. The 10% vs. 40% strain curves are shown together for three microcable samples. Hysteresis is visible in the 40% strain curves; however no change is visible from the first applied strain to the fifth as the cycles appear to have the same stress strain (the cycles are shown as overlapping traces). The difference in noise level between the 10% and 40% strains is due to the decreased sampling available for the 40% scan series. Higher sampling rates presented higher noise levels.

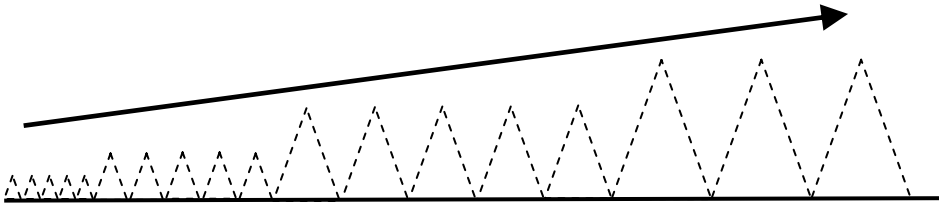

Figure 4.25: The strain was applied to the samples in the pattern shown above, increasing from five to forty percent.

The Young's modulus was calculated from the curve for both sets of scans. It was slightly higher for the 10% strain scans as shown in table 4.3 and in the data in Figure 4.26. The 10% strain region of the 40% curve diverges from the initial 10% strain curve, indicating that the microcable stiffness is changed over the course of the cyclically applied increasing strain.

Table 4.3 shows the Young's modulus fitted from the stress strain data of microcables.

Microcable	**E at 10% strain**	**Standard Deviation**	**E at 10% after 40% strain**	**Standard Deviation**
Sample 1	2.08 MPa	12 kPa	1.84 MPa	11 kPa
Sample 2	1.38 MPa	12 kPa	1.23 MPa	6.3 kPa
Sample 3	1.96 MPa	12 kPa	1.81 MPa	8.8 kPa
Average	1.81 MPa		1.62 MPa	

Table 4.4 lists the Young's modulus measurements from the unmetallized samples.

Sample	**Young's Modulus**	**Standard Deviation**
Sylgard 184 a	0.72 MPa	
Sylgard 184 b	0.78 MPa	
Sylgard 184 c	0.78 MPa	
Sylgard 184 d	0.60 MPa	
Average	**0.72 MPa**	**0.084 MPa**
Sylgard 184/186 a	0.58 MPa	
Sylgard 184/186 b	0.85 MPa	
Sylgard 184/186 c	0.60 MPa	
Sylgard 184/186 d	0.69 MPa	
Average	**0.68 MPa**	**0.18 MPa**

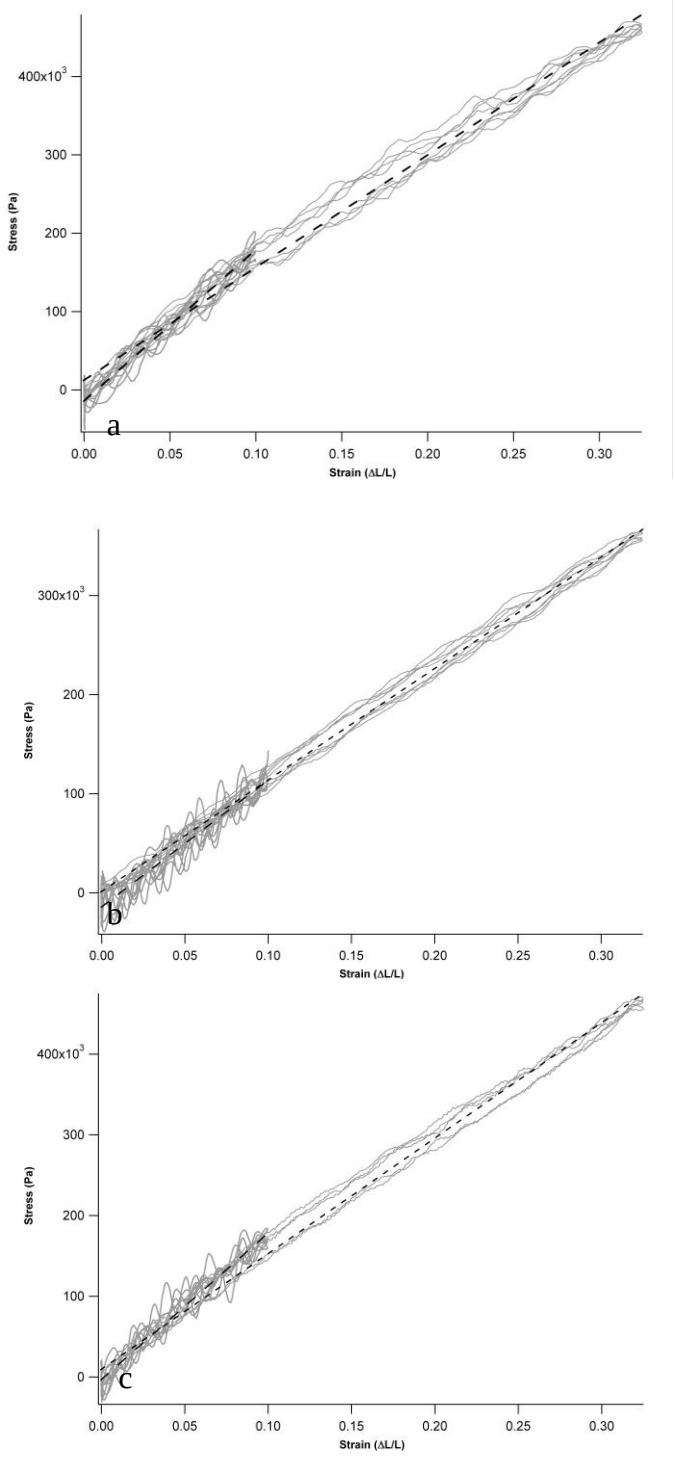

Figure 4.26: The 10 and 40% strains are shown overlaid for each microcable array. Some hysteresis is visible in the 40% strain, which was applied as a sequence of five triangle waves. The 10% strain was also applied as a sequence of five triangle waves.

The composite modulus was applied to the calculations for bending stiffness (EI) for comparison to the expected value. The expected values (from the dimensions and material properties) for silicon and polyimide electrodes are also given in table 4.5.

Table 4.5: Bending stiffness as a function of material and cross-sectional area for different microelectrodes

Electrode type	Bending stiffness ($MPa \cdot m^4$)
Michigan electrode-style silicon electrode [51]	$3.6 \cdot 10^{-9}$
Polyimide electrode [49]	$5 \cdot 10^{-10}$
Estimated PDMS microcable electrode	$2.8 \cdot 10^{-11}$
PDMS microcable electrode	$1.8 \cdot 10^{-11}$

4.3.2 The electromechanical response of the microcable array to applied strain

Microcables were measured in series because of the available resistance range of the data acquisition set up and for averaging purposes. To confirm these assumptions, measurements of individual microcables were compared to the parallel measurements. The electrode arrays tolerated cyclic stretching up to 200% strain. The resistance during 200% applied strain is shown in Figure 4.27. The resistance is shown after first few cycles (>10) and after 5, 1k, and 5k cycles. The increase in resistance happens rapidly with the applied strain, with a measurable conductivity up to approximately 6% strain in the initial cycles. After several thousand cycles, the resistance still returns to a low value at zero strain, but the increase in resistance happens at a lower strain as the number of cycles increases. After one thousand cycles, the conductivity can be measured essentially in the unstrained device and goes to unmeasurable resistance after approximately 1% strain. The resistance at five thousand cycles follows essentially the same path as the resistance after one thousand cycles. The measurable resistance spans a slightly larger

strain after the 5k cycle than the 1k cycle, however the difference is small. The difference may have been due to a temperature change in the room or a slight shifting of the mold in the clamps of the Instron machine. The microcables were measured as a pair in parallel, but because the resistance increased non-linearly, and very rapidly at 6% strain, the resistance of the individual microcables are expected to follow a very similar strain-resistance profile, loosing conductivity at 6%.

To examine the changes in resistance at low strain, the resistance of the microcables was measured at several cyclically applied strain increments at 4, 5, 6, 7, and 8 percent. The resistance data from these tests are shown in Figures 4.28-36. The uneven increase in resistance per applied strains is present in all the data, except at the lower strains (four and five). The data shown here are for a microcable measured individually and for two microcables measured in parallel. The parallel measurements were done in the interest of improving resolution in the recording; however, there is variation between microcables. The sequence of cyclic strains in Figures 4.34-36 show each microcable measured individually and then in parallel at 5% strain.

a

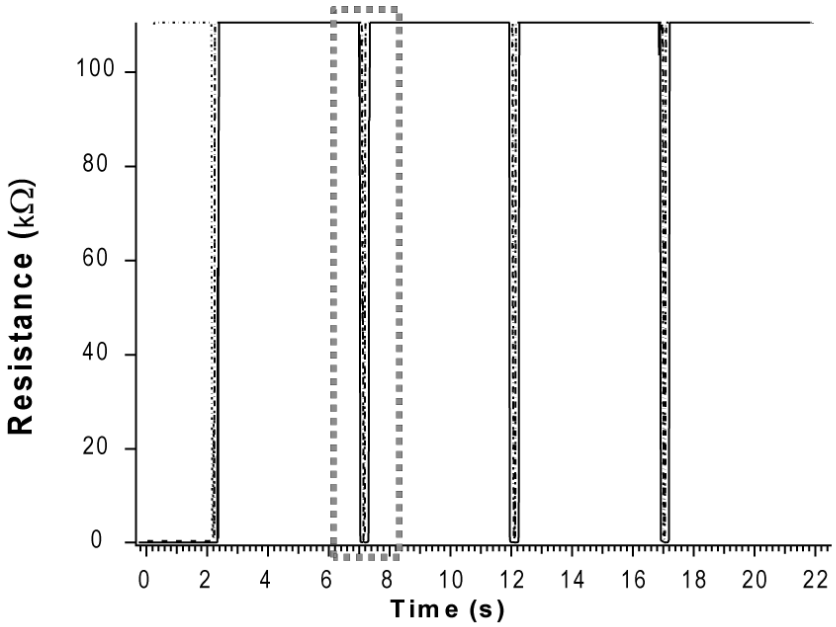

b

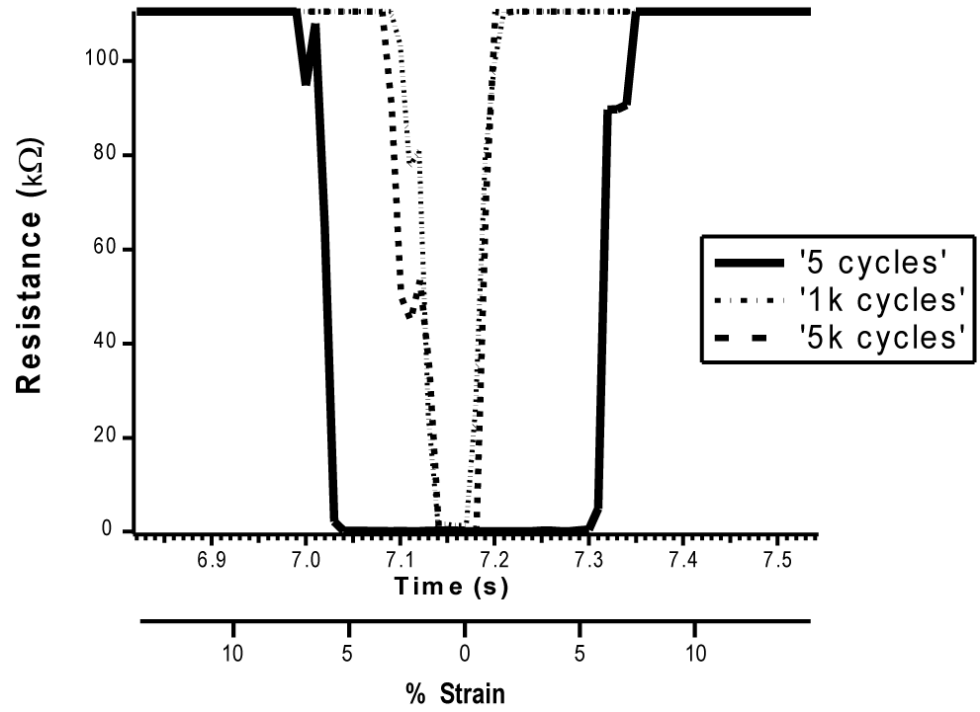

Figure 4.27 a-b: The electromechanical response to 200% applied strain is shown above. The strain rate is 80% per second (absolute displacement: 1.92 mm/s, 4.8 mm per 5 s, 0.2 Hz). The microcables have a measurable conductivity to approximately 6% strain in the initial cycles.

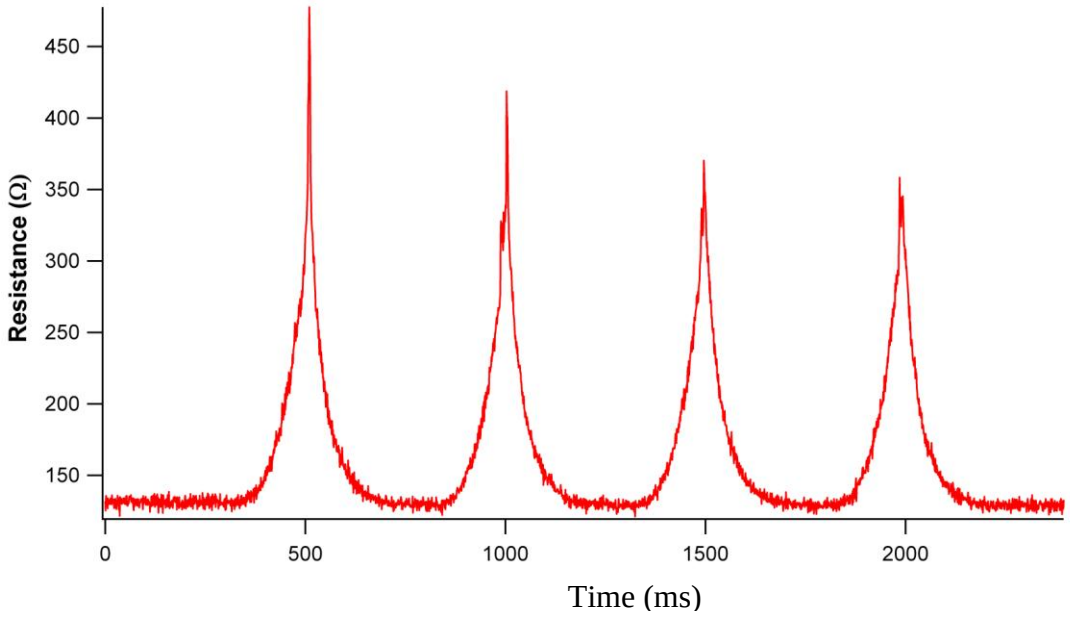

Figure 4.28: Two microcables four percent strain, measured in parallel.

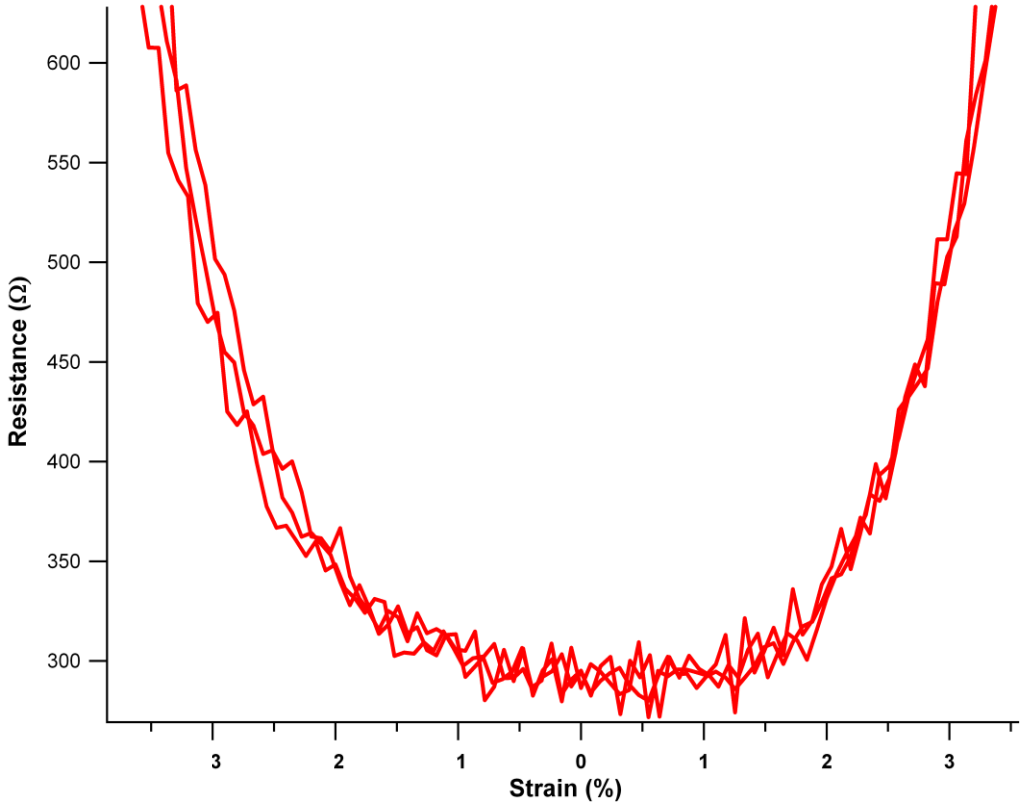

Figure 4.29: Expanded view of multiple cycles of 4% strain of a single microcable.

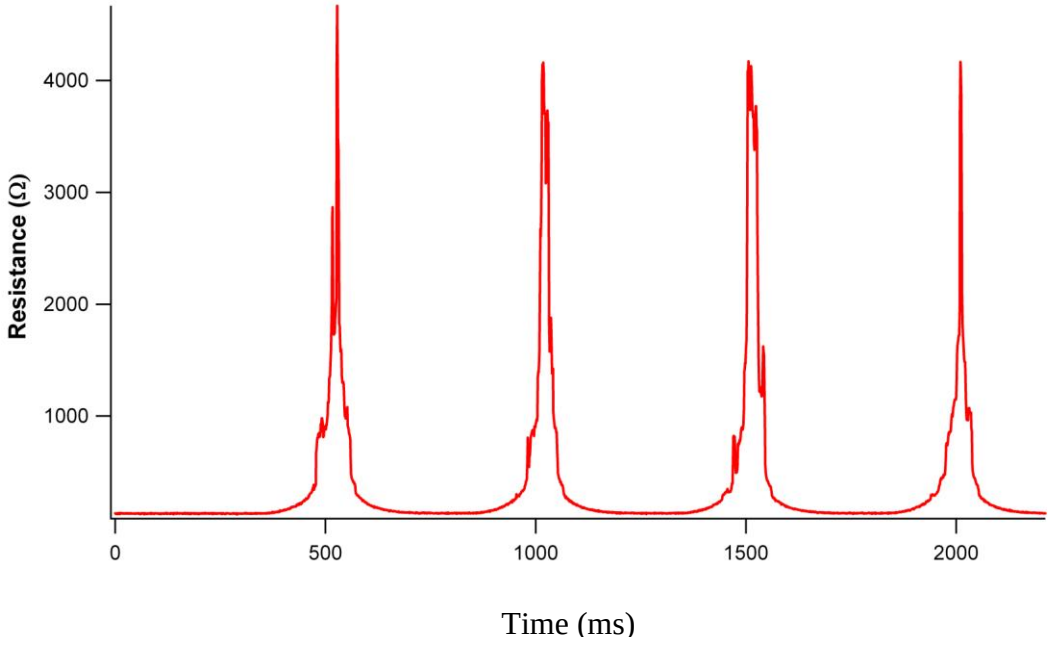

Figure 4.30: Two microcables at 5 percent strain measured in parallel

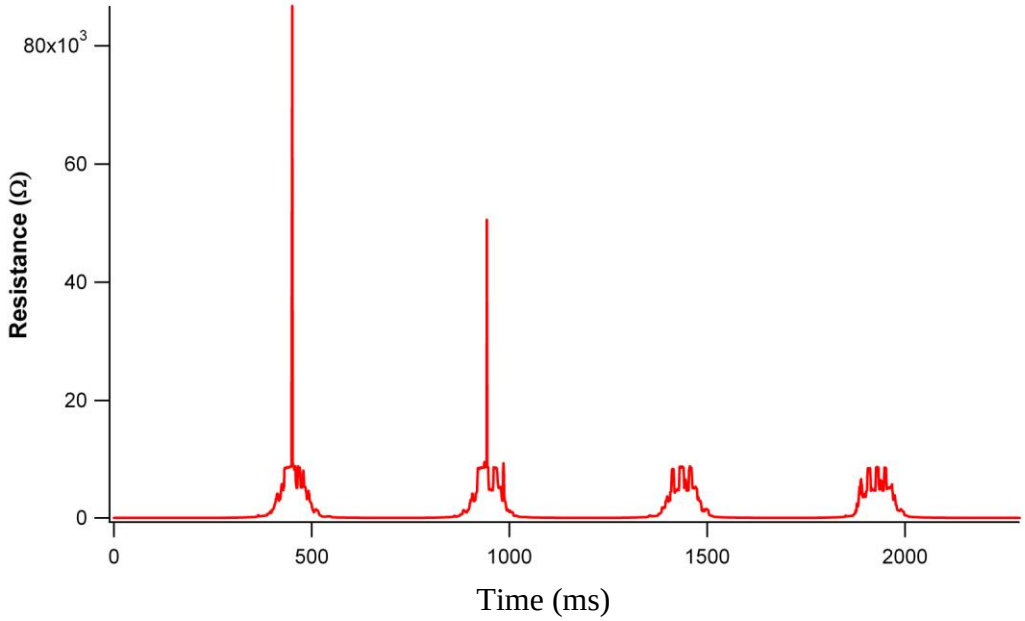

Figure 4.31: Two microcables at 6 percent strain, measured in parallel

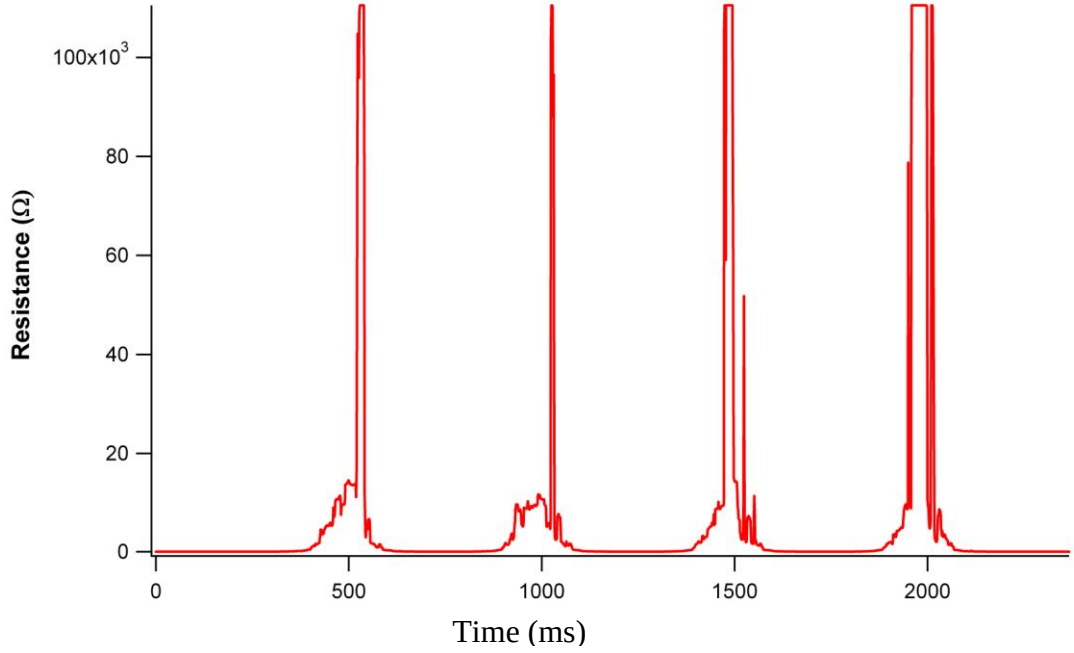

Figure 4.32: Two microcables at seven percent strain, measured in parallel

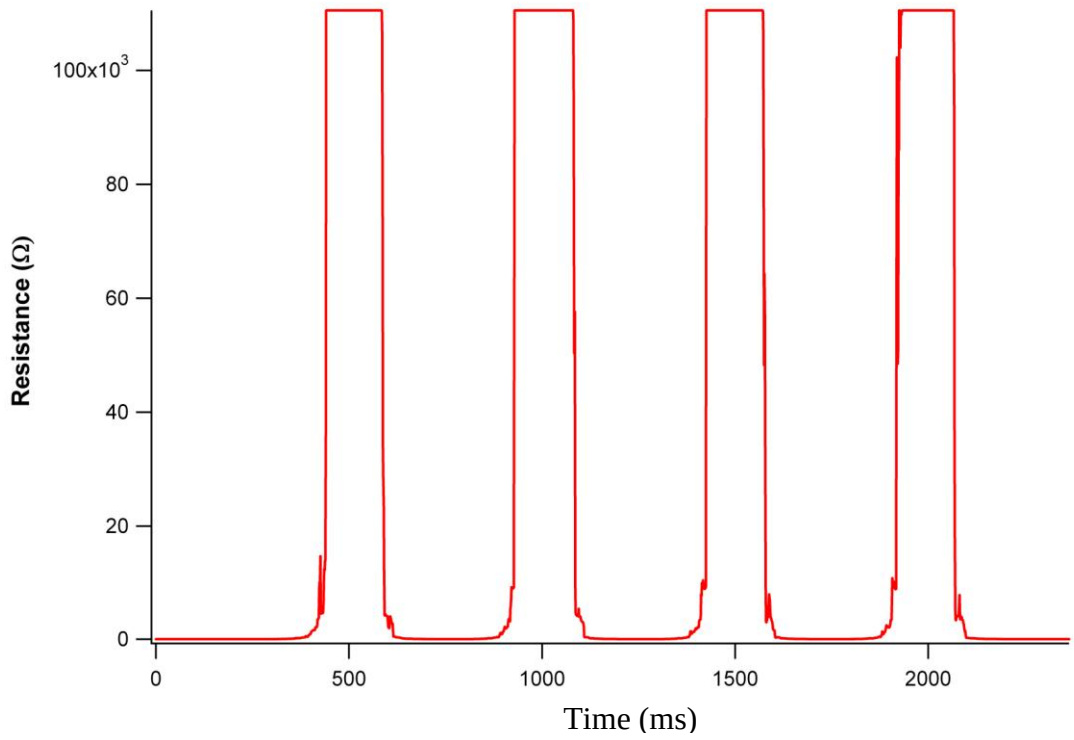

Figure 4.33: Two microcables at eight percent strain, measured in parallel

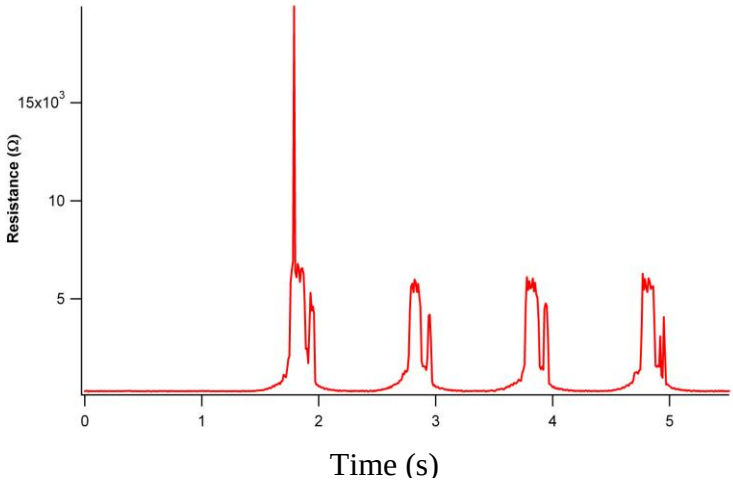

Figure 4.34: An individual microcable at five percent strain

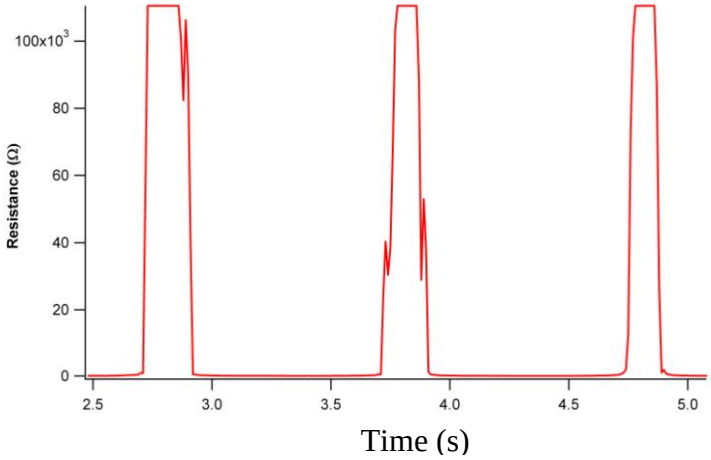

Figure 4.35: A second individual microcable at five percent strain

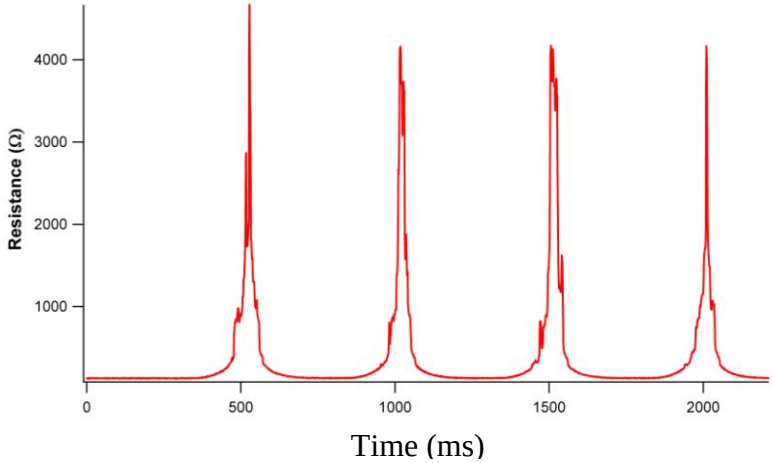

Figure 4.36:The two microcables measured individually above are shown in parallel here at five percent strain

4.4 Discussion

4.4.1. Morphology of the gold and qualitative response to stretch

The density of grain boundaries influences the tensile strength of a thin film as well as the film's fracture pattern [46]. In most instances, in the films shown here, at low strains, the shape is roughly trapezoidal, with larger islands often having a larger width. Also, at low strains, the height or continuity of the crack along the direction of strain, the vertical value, varies less than the horizontal value of the island size. This may be due to the formation of vertical cracks from defects in the film and stress-induced wrinkles, while the formation of horizontal cracks is primarily due to the applied strain. As the strain is increased, the horizontal crack density increases and the larger islands become smaller.

The cracks are not fully aligned or perpendicular to the axis of strain; rather, they have a diagonal component suggestive of shear fracture. Fracture data on thin films in the literature has also noted shear morphologies. The proposed mechanism is a slipping at intercolumnar grain boundaries [52]. As the islands spread apart under an applied strain, some electrical continuity is likely maintained by sliding contact. If the cracks are roughly aligned either parallel or perpendicular to the direction of strain, the parallel cracks are less likely to incur a separation than if they have a horizontal component as shown in the diagram in Figure 4.37. In a scenario with vertically aligned cracks, island separation will be delayed because of contact along the vertical axis. This assumes that the horizontal cracks are discontinuous across the width of the film, suggesting that films

with smaller cracks are conductive at higher strains than films with larger cracks.) If the horizontal crack is continuous across the width, as soon as edges of the crack loose contact, the film will not be electrically continuous. This suggests two ways to reduce the resistance in the film for a given strain, both based on the assumption that the islands maintain electrical continuity by physical contact at crack edges. 1) Increase the width of the gold film. The number of contacts is a function of area (within a certain strain region) and by increasing the width of the film, the number of parallel contacts will increase, decreasing the resistance for a given strain. 2) Increase the number of islands by decreasing the island size. For a given strain, as the number of islands increases, the separation between the islands decreases. Also, by the same logic that increasing the width will reduce the resistance for a given strain, increasing the number of islands will increase the probability that a subset will remain in contact at a given strain. Reducing the resistance for a given strain may also increase the ultimate strain at which resistance can be measured, although this relation is likely nonlinear.

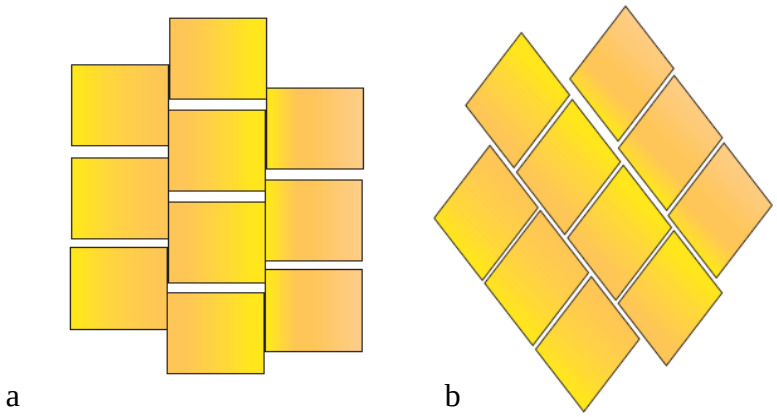

Figure 4.37: (a) If the crack patterns are aligned with the strain, contact can still be maintained between the islands. (b) If the cracks all have a significant horizontal component, the islands become separated at a similar strain.

4.4.2. Young's modulus of the patterned microcable array

The decrease in modulus confirms the theory outlined by Begley on the effect cracks in a film have on a sample when a metal film is attached to an elastomer substrate. The crack density increases with the applied strain as shown in Figures 4.17-23. As the crack density increases, the modulus decreases, eventually approaching the modulus of the elastomer substrate. The results on the tensile modulus also gave an indication of the difference in stiffness between the microcable electrode and brain tissue. The recorded tensile modulus for the microcables was consistently less than 2 MPa (averaging 1.81 MPa and 1.62 MPa for microcables stretched 10 and 40%, respectively.) The modulus of brain is less than 10 kPa [22]. The difference is still 2.5-3 orders of magnitude. However, this is a decrease of over two thirds, than that found with silicon, and about half that found with polyimide [10]. Whether the decrease is significant enough to avoid chronic inflammation as an implanted electrode is a question to be determined in a separate study.

4.4.3. The electromechanical response of the microcable array to applied strain

Repeated application of strain at 200% causes a degradation of the film. The resistance in the unstrained film increases with the number of cycles. The strain at which the resistance becomes unmeasurable also decreases with the number of cycles. The resistance was initially measurable up to 6% strain, but after five thousand cycles of 200% strain, the resistance was only measurable up to 1% strain. The degradation may be due to an increasingly degraded connection between islands and an increasing number of islands over which this degraded connection occurs. When in contact at very low or zero

strains, the cracks most likely do not have an electrical continuity as effective as that of an uncracked film. It may also be due to creep in the substrate. 200% strain is very close to the point of failure in the microcable substrates tested in chapeter two. As described in chapter two, the devices had a higher resistance after release and as seen in the micrograph in Figure 4.17, some cracks are present in the released samples from casual handling. The degradation may be because a small amount of plastic deformation occurs before the failure creating the crack occurs; when the faces of the crack are brought into contact, the plastic deformation prevents full contact at the interface. Additionally, because the substrate is compliant, the crack edges may not line up exactly in plane. The increase in resistance over both a large strain and several thousand cycles may be because of creep in the substrate or because of fatigue-induced changes in the crack interface. If it is the latter, the film likely has a gradual delamination from the substrate due to the continuous cyclic strain. When the film delaminates, it becomes much more brittle. The delaminated edges can crack or otherwise deform and the change in edge profile reduces the contact efficiency at low and zero strains. Furthermore, an increase in the number of islands, considering the concurrent increase in imperfect contacts, increases the total resistance of the unstrained film. Gold is a relatively soft metal; while the studies found in the literature generally use softer metals (Au or Cu), the overall durability may act as a limitation. The frictional force applied from the mismatched interfaces, or sliding islands could be expected to wear down the interface.

The resistance measurements under low applied strains (4-8%) show a transition from low resistance continuity to an increase in resistance that continues to a loss of continuity. A cracked gold film is conductive at low applied strains because the crack

edges are in contact. The transitional regime at low strains is consistent over repeated cycles for thin films but not for thicker films or bulk material, which is typically not conductive after fracture. The fracture behavior of a thin gold film may be different from that of a thicker (>100 nm) film or wire (i.e. bulk material) because bulk materials progress through a plastic deformation that occurs on a minimal level in thin films [53]. The gold in the thin film has less plastic deformation before it fractures relative to a thicker film. The edges of the cracks in a thicker film will have a plastic deformation proportional to the film thickness; therefore because of the change in the edge profile, the surfaces do not make full contact after the strain is released. Conversely, the cracked islands on a thin film, which suffer little plastic deformation, have a larger surface area that is able to make contact with neighboring islands after the strain is released.

The microcables were measured after a small number of strain cycles to verify the data acquisition was running and that the samples were accurately positioned at the zero strain point. The data shown are not from the very first cycle because it was past of the system verification done before recording was initiated. The intention of the cyclic strains was to demonstrate reproducibility and to examine the profile of the increase in resistance. Lacour *et al.* has described a linear increase in resistance [36]. The increases in resistance shown here are roughly hyperbolic. The increase is also not the same for sequential cycles of strain and varies with the microcable sample. As shown in Figures 4.28, 30 and 31, the resistance profile decreases in value for every cycle of applied strain. Figures 4.28, 30, 31, 34 and 35 show a smaller peak area for resistance at the fourth strain, relative to the first. In Figure 4.28, the two microcables measured in

parallel show a decreasing resistance at 4% strain over four cycles. The peak resistance decreases by 25%, from 500 ohms to 375 Ω.

The fourth strain is greater than the first for Figure 4.32, although there is some oscillation in the series. The change in the resistance-strain relation, therefore, is not consistent, but trends down in the data shown. The resistance increases depending on the fracture pattern. From the change in resistance, we can infer that the fracture pattern changes with each strain. With each cycle, the existing cracks propagate farther or new cracks form. The film has a finite stress tolerance (maximum stress prior to plastic deformation) that is exceeded by the applied strain. Each crack removes some of the applied strain from the metal film. The tension is not fully removed from the film in a single cycle. It can be expected that the decrease in strain on the film will asymptotically continue until the strain applied to the sample transfers a stress to the film that does not exceed its stress tolerance.

The fracture propagation is a stochastic process. The fractures are influenced by grain boundaries and variations in the film adhesion to the substrate, but these variables are not controlled for in the fabrication process. As such, and as seen in the micrographs, the fracture patterns vary by microcable. This variation will translate into varying conductivities under strain as shown by the recordings of individual microcables in Figures 4.34 and 4.35. The resistance at low strain values appears to be more consistent, at least within a single microcable, as shown by the overlaid resistance curves at low strain in Figure 4.29. At lower resistance the "redundancy" in connecting islands is high so fluctuation in the fracture patterns is less noticeable. As the number of connecting islands decreases with strain, changes in the connecting island pattern cause large

fluctuations in the resistance. In Figure 4.31, the microcables are measured at 6% strain. In the initial cycle, the resistance increases sharply, but by the forth cycle, the maximum resistance is an order of magnitude lower. Potentially, a large island in the first cycle, has been fractured into smaller islands in subsequent cycles. When the smaller islands separate under strain, they maintain contact with other islands at higher strains than the single large island.

The conductivity for microcables that have received only low (4-8%) strains follows a very similar profile to the microcables that have received higher strains (200%). The low strain microcables loose conductivity at 4-6% strain, while the high strain microcables loose conductivity at 6% strain. The two tests were done on different size frames. The 200% strain tests had a 1 mm window because the displacement was limited by the instron, while the 4-8% strain tests had a 2 mm window to maximize the resolution at low strain values. The high strain data was tested and showed similar results on two sets of microcables (each was mounted on a separate frame). The 6% ultimate strain with measureable resistance is lower some of the films in the literature, with reported conductivity to strains in excess of 30%. The films in the literature also reported a linear increase in strain. The difference may be due to the average length of the crack branches. The crack-branch length on the microcable electrodes is on the order of microns and tens of microns. Pictures in the literature of the film conductive to 30% show a small crack length (< 1 μm, Figure 4.38) [8]. Maximizing the conductivity under strain may to be an issue of minimizing crack length.

Durability is improved in the system described here compared to that described by Graz *et al.* [54]. The island size may be a mediating factor in degradation because the

surface area of the cracked faces increases with the island count, leaving more area available for degradation. The difference may also be due to the plasma treatment described here to improve adhesion of the metal film to the substrate. No adhesion promoting treatment was described by Graz or Lacour *et al.* [8, 54].

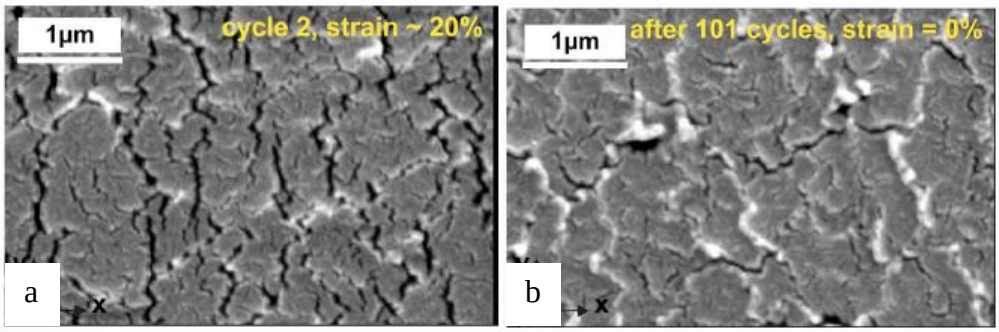

Figure 4.38: The films shown above, 25 nm of gold on 5 nm of chromium, were stretched to 32% strain. The branches of the microcracks are 0.2-0.6 µm long [8]. The relatively short length of the cracks may explain the measurable conductivity at 32% strain.

Another reason the thin gold film is stretchable on PDMS or other polymer substrates is the compliant substrate's inhibiting effect on localized propagation of strain. When the substrate is absent or when the gold is thick enough that its bulk mechanical properties dominate the crack propagation, as discussed previously, the initialization of a crack creates a stress concentration that favors the propagation of the crack. The thin film gold on PDMS has numerous small cracks that do not individually cross the width of the film. Thicker films or bulk material, which are inclined to have individual cracks that span the film's width, will lose continuity as soon as one crack looses contact at the crack faces in the film (Figure 4.39).

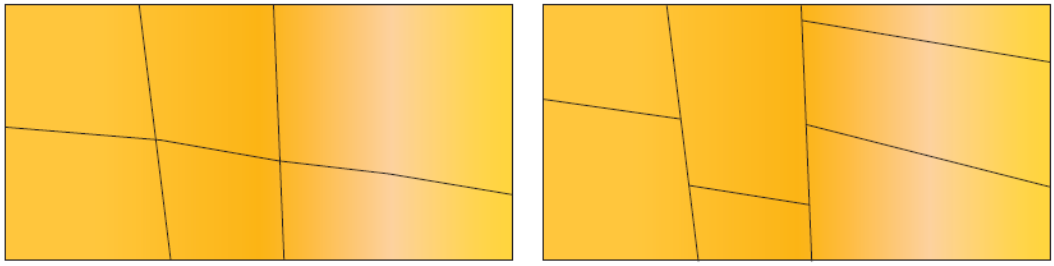

Figure:4.39: The long crack creates a full break in the film, while shorter cracks do not. Shorter cracks (and larger numbers of islands) have a lower increase in resistance for a given strain than longer cracks.

Because the contact is imperfect from the plastic deformation along the edges, the tolerance for strain is negligible before conductivity is lost. Literature on stretchable wave-shaped microwires (bulk material) do not describe the devices as conductive after the leads have cracked because their low tolerance for deformation renders them un-useful [40].

The pattern of small crack branches is expected to be more stretch tolerant for three possible reasons. The first is that at the same strain that the islands associated with the large crack loose contact, the set of smaller cracks has the displacement distributed along the length of the film. As the crack-branch number increases the average strain at which separation occurs decreases. Additionally, as the crack-branch length decreases, the probability that a path of crack separation extends across the width of the film also decreases. Third, strain applied to the substrate along the long axis, causes a Poisson ratio based compression in the perpendicular plane. The compression of the substrate likely helps the islands in the cracked film maintain contact because even though the separations are increasing in the longitudinal direction, the horizontal contact is improved. Because of the staggered and irregular crack pattern, the maximal strain

before loss of continuity is statistically determined. Additionally, because the crack-branch distribution changes slightly with each applied stretch, the variation is present in sequential strains on a single microcable. The film width has a statistical relationship with strain-related electrical continuity. The film widths tested here were approximately 100 μm wide. Increasing the width will increase the statistical likelihood that a path of islands is in contact under an applied strain, although because the increase is not linear, the benefit will not be linear either. The variables contributing to relation of resistance to strain include the applied strain, the island size and the crack orientation**.**

4.5 Conclusion

The mechanical and electromechanical properties of the microcables have been characterized. The Young's modulus was measures from the force generated by the tensile strain. As the strain is increased in the microcable, the crack density increases and the average island size decreases. The discontinuities in the gold film cause a small decrease in the modulus. This trend agrees with the theory described by Begley *et al* [42]. The electromechanical behavior is consistent for small and large strains, with an ultimate strain of 6% for electrical continuity. The microcables can tolerate large strains (200%) without a permanent loss of continuity. The strain tolerance is lower than some of the films reported in the literature and may be due to a difference in crack-branch length. If the crack-branch length correlation to strain-tolerance is correct, it suggests that the optimal film for stretchable electronics has a minimized crack length. The parameters that determine the morphology of a thin film, such as mechanism (e.g. sputtered, e-beam or thermal (used here), deposition pressure, and speed, could be optimized to create a morphology that cracks in short branches.

4.6 Citations

1. *Electronic skin for robots.* Chemical & Engineering News, 2005. **83**(34): p. 38-38.
2. Birringer, J. and M. Danjoux, *Wearable performance.* Digital Creativity, 2009. **20**(1-2): p. 95-113.
3. Someya, T., et al., *A large-area, flexible pressure sensor matrix with organic field-effect transistors for artificial skin applications.* Proceedings of the National Academy of Sciences of the United States of America, 2004. **101**(27): p. 9966-9970.
4. Watanabe, M., H. Shirai, and T. Hirai, *Wrinkled polypyrrole electrode for electroactive polymer actuators.* Journal of Applied Physics, 2002. **92**(8): p. 4631-4637.
5. Rogers, J.A., *Electronics - Toward paperlike displays.* Science, 2001. **291**(5508): p. 1502-1503.
6. Rogers, J.A. and Y.G. Huang, *A curvy, stretchy future for electronics.* Proceedings of the National Academy of Sciences of the United States of America, 2009. **106**(27): p. 10875-10876.
7. Someya, T., et al., *Conformable, flexible, large-area networks of pressure and thermal sensors with organic transistor active matrixes.* Proceedings of the National Academy of Sciences of the United States of America, 2005. **102**(35): p. 12321-12325.
8. Lacour, S.P., et al., *Mechanisms of reversible stretchability of thin metal films on elastomeric substrates.* Applied Physics Letters, 2006. **88**(20).
9. Lago, N., et al., *Assessment of biocompatibility of chronically implanted polyimide and platinum intrafascicular electrodes.* Ieee Transactions on Biomedical Engineering, 2007. **54**(2): p. 281-290.
10. Subbaroyan, J.M., D.C.;Kipke, D.R., *A finite-element model of the mechanical effects of implantable microelectrodes in the cerebral cortex.* Journal of Neural Engineering, 2005. **2**(4): p. 10.
11. Pornsin-Sirirak, T. and Y. Tai, *Flexible parylene actuator for micro adaptive flow control*, in *MEMS 2001*. 2001.
12. Shire, D.B., et al., *Development and Implantation of a Minimally Invasive Wireless Subretinal Neurostimulator.* Ieee Transactions on Biomedical Engineering, 2009. **56**(10): p. 2502-2511.
13. Nicolelis, M.A.L., et al., *Chronic, multisite, multielectrode recordings in macaque monkeys.* Proceedings of the National Academy of Sciences of the United States of America, 2003. **100**(19): p. 11041-11046.
14. NeuroNexus, *SIlicon microelectrode array research product catalog and manual*. 2008.
15. Lawrence, S.M., G.S. Dhillon, and K.W. Horch, *Fabrication and characteristics of an implantable, polymer-based, intrafascicular electrode.* Journal of Neuroscience Methods, 2003. **131**(1-2): p. 9-26.
16. Lefurge, T., et al., *CHRONICALLY IMPLANTED INTRAFASCICULAR RECORDING ELECTRODES.* Annals of Biomedical Engineering, 1991. **19**(2): p. 197-207.

17. Sun, J.Y., et al., *Inorganic islands on a highly stretchable polyimide substrate.* Journal of Materials Research, 2009. **24**(11): p. 3338-3342.
18. Lacour, S.P., et al., *Stiff subcircuit islands of diamondlike carbon for stretchable electronics.* Journal of Applied Physics, 2006. **100**(1).
19. Ko, H.C., et al., *A hemispherical electronic eye camera based on compressible silicon optoelectronics.* Nature, 2008. **454**(7205): p. 748-753.
20. Mathur, A.B., et al., *Endothelial, cardiac muscle and skeletal muscle exhibit different viscous and elastic properties as determined by atomic force microscopy.* Journal of Biomechanics, 2001. **34**(12): p. 1545-1553.
21. Borschel, G.H., et al., *Mechanical properties of acellular peripheral nerve.* Journal of Surgical Research, 2003. **114**(2): p. 133-139.
22. Green, M.A., L.E. Bilston, and R. Sinkus, *In vivo brain viscoelastic properties measured by magnetic resonance elastography.* Nmr in Biomedicine, 2008. **21**(7): p. 755-764.
23. Sun, Y.J., B. Akhremitchev, and G.C. Walker, *Using the adhesive interaction between atomic force microscopy tips and polymer surfaces to measure the elastic modulus of compliant samples.* Langmuir, 2004. **20**(14): p. 5837-5845.
24. Al-Halhouji, A.T., et al., *Nanoindentation testing of SU-8 photoresist mechanical properties.* Microelectronic Engineering, 2008. **85**(5-6): p. 942-944.
25. Kaliappan, S.K. and B. Cappella, *Temperature dependent elastic-plastic behaviour of polystyrene studied using AFM force-distance curves.* Polymer, 2005. **46**(25): p. 11416-11423.
26. DuPont, *Kapton Technical Data Sheet*.
27. Gracias, D.H. and G.A. Somorjai, *Continuum force microscopy study of the elastic modulus, hardness and friction of polyethylene and polypropylene surfaces.* Macromolecules, 1998. **31**(4): p. 1269-1276.
28. Meacham, K.W., et al., *A lithographically-patterned, elastic multi-electrode array for surface stimulation of the spinal cord.* Biomedical Microdevices, 2008. **10**(2): p. 259-269.
29. Cotton, D.P.J., I.M. Graz, and S.P. Lacour, *A Multifunctional Capacitive Sensor for Stretchable Electronic Skins.* Ieee Sensors Journal, 2009. **9**(12): p. 2008-2009.
30. Hitt, J., et al., *Robotic transtibial prosthesis with biomechanical energy regeneration.* Industrial Robot-an International Journal, 2009. **36**(5): p. 441-447.
31. Castellini, C. and P. van der Smagt, *Surface EMG in advanced hand prosthetics.* Biological Cybernetics, 2009. **100**(1): p. 35-47.
32. Bogue, R., *Exoskeletons and robotic prosthetics: a review of recent developments.* Industrial Robot-an International Journal, 2009. **36**(5): p. 421-427.
33. Li, T. and Z. Suo, *Deformability of thin metal films on elastomer substrates.* International Journal of Solids and Structures, 2006. **43**(7-8): p. 2351-2363.
34. Li, T., et al., *Stretchability of thin metal films on elastomer substrates.* Applied Physics Letters, 2004. **85**(16): p. 3435-3437.
35. Xiang, Y., et al., *High ductility of a metal film adherent on a polymer substrate.* Applied Physics Letters, 2005. **87**(16).
36. Lacour, S.P., et al., *Stretchable gold conductors on elastomeric substrates.* Applied Physics Letters, 2003. **82**(15): p. 2404-2406.

37. Xiao, J., et al., *Stretchable and compressible thin films of stiff materials on compliant wavy substrates.* Applied Physics Letters, 2008. **93**(1).
38. Bowden, N., et al., *Spontaneous formation of ordered structures in thin films of metals supported on an elastomeric polymer.* Nature, 1998. **393**(6681): p. 146-149.
39. Kim, H.J., C. Son, and B. Ziaie, *A multiaxial stretchable interconnect using liquid-alloy-filled elastomeric microchannels.* Applied Physics Letters, 2008. **92**(1).
40. Gray, D.S., J. Tien, and C.S. Chen, *High-conductivity elastomeric electronics.* Advanced Materials, 2004. **16**(5): p. 393-+.
41. Befahy, S., et al., *Stretchable helical gold conductor on silicone rubber microwire.* Applied Physics Letters, 2007. **91**(14).
42. Begley, M.R. and H. Bart-Smith, *The electro-mechanical response of highly compliant substrates and thin stiff films with periodic cracks.* International Journal of Solids and Structures, 2005. **42**(18-19): p. 5259-5273.
43. McClain, M., *Modulus of PDMS, measured in Chapter 1*. 2009.
44. Begley, M.R., et al., *The electro-mechanical response of elastomer membranes coated with ultra-thin metal electrodes.* Journal of the Mechanics and Physics of Solids, 2005. **53**(11): p. 2557-2578.
45. Hsia, K.J., Z. Suo, and W. Yang, *CLEAVAGE DUE TO DISLOCATION CONFINEMENT IN LAYERED MATERIALS.* Journal of the Mechanics and Physics of Solids, 1994. **42**(6): p. 877-896.
46. Van Swygenhoven, H. and J.R. Weertman, *Deformation in nanocrystalline metals.* Materials Today, 2006. **9**(5): p. 24-31.
47. Tsay, C.L., S. Wagner, S. Li, T. Suo, Z. *How Stretchable Can We Make Thin Metal Films?* in *Materials Research Symposium Proceedings*. 2005.
48. Lu, N.S., et al., *Metal films on polymer substrates stretched beyond 50%.* Applied Physics Letters, 2007. **91**(22).
49. Rousche, P.J., et al., *Flexible polyimide-based intracortical electrode arrays with bioactive capability.* Ieee Transactions on Biomedical Engineering, 2001. **48**(3): p. 361-371.
50. Young, W.C., *Roark's Formulas for Stress and Strain*. 6th ed. 1989, New York: McGraw-Hill.
51. NeuroNexus, *Silicon microelectrode array research product catalog and manual*. 2009, NeuroNexus Technologies: Ann Arbor, MI.
52. Bhowmick, S., et al., *Nature of contact deformation of TiN films on steel.* Journal of Materials Research, 2004. **19**(9): p. 2616-2624.
53. Espinosa, H.D. and B.C. Prorok, *Size effects on the mechanical behavior of gold thin films.* Journal of Materials Science, 2003. **38**(20): p. 4125-4128.
54. Graz, I.M., D.P.J. Cotton, and S.P. Lacour, *Extended cyclic uniaxial loading of stretchable gold thin-films on elastomeric substrates.* Applied Physics Letters, 2009. **94**(7).

CHAPTER 5

BIOLOGICAL TESTING

5. 1 Introduction

The microcable electrodes are tested here to assess the chronic tissue response after 28 days of implantation in the rat brain. Studies testing the cortical response to variations in electrode compliance have shown that more complaint electrodes induce less inflammation and neuronal loss. The microcable electrodes are too compliant to insert into cortical tissue without some additional modification. To that end, the electrodes were coated with fibrin so that they would be stiff enough to insert into the brain. The fibrin, which is dried after it is coated on one side of the electrode, becomes compliant once it is rehydrated and, as a biologically derived clotting component, is resorbed naturally by the body. Preliminary evidence suggests it is non-toxic to neurons [4]; however, this data is interpreted with caution because fibrin deposits are found in degenerative and neuroinflammatory states in the brain [5-6]. It should be noted, however, that the fibrinolytic process and the degradation of resorbable materials in general, is intertwined with inflammatory processes [6-8]. The background literature on fibrin's use as a tissue sealant and its relation to neurodegenerative pathology is discussed in the literature review below. The inflammation was measured with immunohistological staining. MRI scans were taken at the end of the four week study. The spatial intensity profile around the implanted electrode from T2 weighted images was found to correlate with the presence of inflammatory marker, glial fibrillary acidic protein (GFAP), in the immunohistology.

5.1.1 Background and rationale for chronic implant test

The motivation for this study is the loss in implanted electrode stimulation and recording ability over time. The loss of functionality is most commonly attributed to the inflammation and fibrosis at the implant site, as well as the decrease in neuron density with time near the electrode [9]. The chronic inflammation increases the electrodes' impedance and may contribute to the loss of near-by neurons. The hypothesized chronic injury to the surrounding tissue causes both inflammation and neuronal injury. Several electrode designs have been tested that mitigate either the inflammation alone or the mechanical trauma. One example, the floating electrode array, is commercially available for use in animals (Plexon; Dallas, TX). For clinical applications such as deep brain stimulation (DBS), there is much room for progress both in improving currently available therapies and in developing electrophysiological feedback loops for the implant to make the therapy more precise and therefore more effective [10-11]. As detailed in the introduction, a hypothesis tested in several studies postulates and shows that increasing the electrode compliance decreases the inflammation at the electrode site when examined at weeks-to-months post- implantation. Based on the intrinsic material properties, the thin-film gold and PDMS microcable electrodes are highly compliant relative to other electrodes described in the literature, which are made of stiffer polymers or silicon. The bending stiffness calculations from chapter four are reproduced here, in table 5.1 for reference. Based on the mechanical properties, it is expected that the microcable electrodes will have a reduced chronic inflammatory response compared to commercially available silicon. The testing described here investigates whether the PDMS-based electrodes with a resorbable coating for insertion create less injury to the tissue over a

four-week time period than conventional silicon electrodes. The resorbable coating is fibrin glue, which is a biologically derived, clinically-approved material used as a surgical tissue sealant. The *in situ* activity of fibrin as a clotting agent and the potential neurological effects are discussed. The tissue implanted with the fibrin-coated, PDMS microcables and the conventional silicon electrodes is compared using MRI (*in vivo*) and conventional histology techniques. The differences between the tissue exposed to either silicon or PDMS are compared and the effect of fibrin on the tissue is investigated.

Table 5.1: Bending stiffness as a function of material and cross-sectional area for different microelectrodes

Electrode type	**Bending stiffness ($MPa \cdot m^4$)**
Michigan electrode-style silicon electrode [12]	$3.6 \cdot 10^{-9}$
Polyimide electrode [13]	$5 \cdot 10^{-10}$
PDMS microcable electrode	$1.8 \cdot 10^{-11}$

5.1.2 Potential applications for highly compliant cortical electrodes

Deep brain stimulation (DBS) delivers electrical pulses to the brain for the suppression of tremors in movement related disorders such as Parkinson's, dystonia and the most common neurological movement disorder, essential tremor. DBS therapy suppresses tremor and bradykinesia (slowness of movement) and ridgity [14]. It also addresses dyskinesia (involuntary movement), a frequent side effect of levodopa-pharmacotherapy for Parkinson's patients [15]. DBS therapy is currently being investigated for the treatment of a number of affective disorders, including depression [16].

Current systems are open-loop with continuous stimulation (although the stimulator may be turned off, e.g. when the patient is asleep) [17] . There is little variability in the stimulus parameters and their application can introduce side-effects such

as tetanic muscle contraction, speech disturbance, and ocular deviation [10-11]. The open loop system could be made more effective and efficient by incorporating feedback though neural recording. Recording neural activity in pathological conditions, at the stimulation site creates a closed loop system with the stimulus driven by identified signatures of the diseased state. The feedback targets the application of the stimulus [18-19]. Recording-based feedback has the potential to reduce stimulation based side-effects, prolong battery life, and extend the range of symptoms DBS can inhibit though specific targeting.

5.1.3 Reducing Electrode Encapsulation

Clinical implants for DBS develop an encapsulation that occurs at the stimulation site that can reduce the volume of tissue activated by the stimulation [20]. The layer of fibrous tissue increases the electrical impedance of the region so that the electrical stimulus propagating outside the fibrous region is reduced [20]. Although clinical studies still have not explicitly correlated the required electrical stimulus with the degree of encapsulation, models of the encapsulated electrode show that after encapsulation, the volume of tissue activated by the electrode is reduced by approximately half, assuming the stimulus is held constant [21]. While encapsulation can be expected to occur with any implant, the effects of material selection and micromotion at the site can increase the inflammatory response and thickness of fibrous tissue surrounding the implant [21].

The encapsulating tissue of electrodes in the brain ranges from 0.1-1 mm thick. It is composed of a fibrous layer, approximately 25 μm thick and extends to a layer of fibrillary gliosis and an outer zone of GFAP positive astrocytes . While a glial scar is absent, gliosis and giant cell reactivity are consistently present, meaning the cellular

population around the electrode is defined by the immune response, and the neurons intended for stimulation are outside this layer [20]. An impedance increase normally occurs with time after implantation and is understood to be related to the tissue encapsulation [20]. Readjusting DBS stimulation levels interrupts the therapeutic effect and increases the power of stimulus, reducing the IPG (implantable pulse generator) battery life.

The histological evaluation of electrode implants generally has two primary goals: 1) to measure the scarring or inflammation and 2) to measure the neuronal loss. The inflammatory response has several markers: GFAP (activated astrocytes), ED-1 (activated rat microglia) Neuronal loss is frequently measured by measuring neurofilament or neuronal nuclear density (NuN). FluoroJade is a marker of neuronal degeneration and has not been used to date to evaluate degeneration around the electrode, but may provide an indicator of the neural integrity around the electrode, which may provide more information than assessing the neuronal population. In an investigation identifying the parameters of the tissue change, Biran *et al*. found ED-1 upregulation, and neuronal loss in implanted electrodes but not stab-wound controls[2]. When the electrodes were extracted, and the attached cells were ED-1/MAC-1 (macrophage markers) positive and release MCP-1 (monocyte chemotactic protein) and TNF- α (tumor necrosis factor) under serum free conditions in vitro. These four markers are commonly used as indicators of inflammation[22-25]. As shown by figure 5.5, the implant is characterized by the combination of inflammation and neuronal loss [2]. Similar findings were also confirmed by Griffith in microwire implants (50 μm diameter) in Rhesus macaque monkeys [26]. Extensive GFAP expression was found after three months and

three year time points. The microglial reaction present at three months had subsided by the three year time point. These data show that the initial injury persists for several months, as evidenced by the presence of microglia, which clear injured tissue and help initiate remodeling around the injury site [27]. The chronic astrocte response is typically regarded as a low-grade inflammation at the implant site [28]. Because electrode functionality is often lost at three-six months after implant, the long-term low-grade inflammation may be one of the barriers to successful chronic electrode implants in the brain.

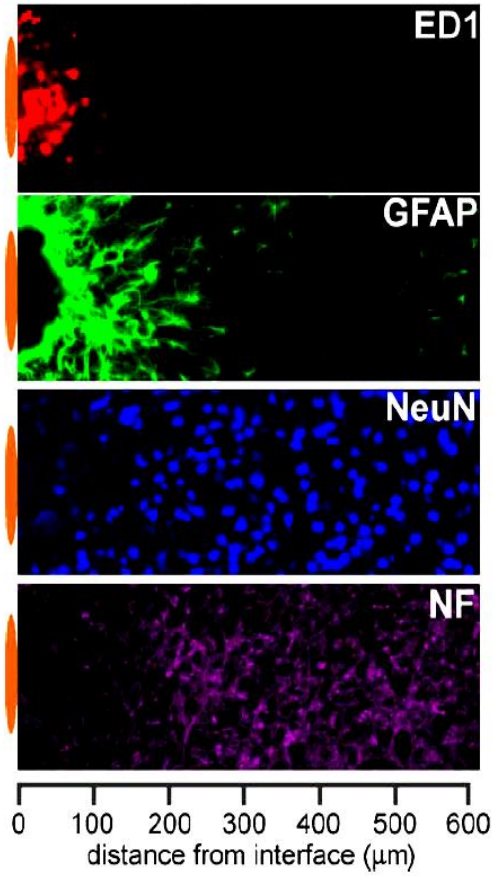

Figure 5.1: Biran *et al.* measured the histological response to silicon electrode arrays four weeks after implantation. The images shown above are subsets of the tissue extaned from the eletrode (denoted by the bars drawn to the left of each image). The inflammatory markers, ED1 and GFAP both increase around the electrode, with ED-1 contained within the penumbra of GFAP. The neuronal markers, NuN and neurofilament, are not present in the inflammatory region, which extends over 100 μm from the electrode [2].

The parameters of the electrode implant have been tested in the literature in multiple permutations to assess what minimizes inflammation and neuronal loss. The electrode geometry, material, coating and tethering have all been investigated. The configuration of the electrode based on each of these parameters can be improved to reduce the inflammatory response.

Polymer-based electrodes have shown a reduced inflammatory response compared to silicon. Cheung and Mercanzini both tested the inflammatory response of

implanted polyimide electrodes [29-30]. The expression of GFAP [29-30] (and CD-11 for microglia [30]) were described as low by the authors but direct comparisons are difficult because they did not include silicon or microwire controls. Reducing the electrode cross-sectional area has been shown to reduce GFAP staining in controlled studies, indicating that the chronic inflammation is reduced [31-32].

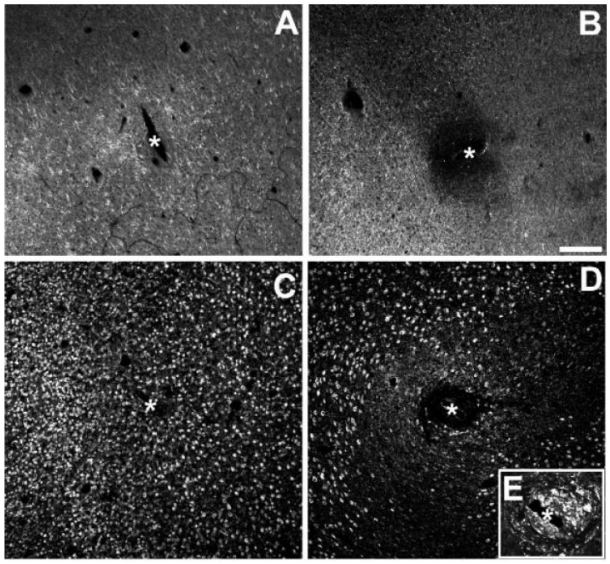

Figure 5.2: The influence of mechanical coupling between the electrode and the skull is tested on the influence of neuronal density around the electrode after four weeks. Neurofilament and NuN and shown top and bottom. The histology from the floating electrode is shown left, with no perceptible decrease in staining around the implant site. The traditionally fixed electrode, which is glued to the skull during implantation, has a noticeable zone around the implant without neuronal staining, similar to the images shown in figure 5.1.[3]

The tethering scheme that couples the implant to the electronics was made more compliant by allowing the electrode to "float" on the dura rather than being glued in place to the skull [3]. The inflammation was consistently lower at one, two and four week time points as measured by ED1 and GFAP. The reduction in NuN and neurofilament 160 relative intensity around the floating electrode was minimal; it is discernable in the image (showing the 4 week time point). In contrast, tethered

electrodes showed attenuation in staining intensity of both markers for approximately 100 μm around the implant site [3].

Coatings have inhibited inflammation but not reduced the neuronal loss. The addition of anti-inflammatory compounds locally at the electrode site reduces the inflammation in the short-term, but it is an acute-phase strategy. Coating the electrode with alpha-MSH (an endogenous tridecapeptide), an anti-inflammatory molecule that inhibits pro-inflammatory cytokines [33]. The alpha-MSH coated silicon electrode showed reduced ED1 and GFAP staining four weeks after implantation. TNF-alpha expression was also reduced [33]. Electrodes have also been coated with laminin [27]. *In vitro* cultures of microglia in the presence of laminin showed upregulation of proinflammatory cytokines [34]. It is thought that laminin has an acute effect on microglia, increasing the "clean-up response." The laminin-treated electrodes also showed reduced ED-1 and GFAP expression at four weeks *in vivo*, although the expression at one day and one week was not different (except for ED-1 expression at 1 day, which was increased for laminin) [27]. Differences in neuronal density around the probes for the same studies were not different, with both showing a decrease, suggesting that the neuronal cell loss occurs separately, at least in part, from the ability to attenuate inflammation. The micromotion from the electrodes is likely the same or similar because only the surface was modified. (Any difference in adhesion between the electrode and tissue may have altered the micromotion, although this is beyond the scope of the discussions in the papers [27, 33].)

5.1.4 Biological activity of fibrin

Fibrin was chosen to increase the electrode stiffness for insertion because it is a biologically derived, resorbable material with evidence suggesting minimal neurotoxicity [35]. Studies on the external application of fibrin applied on or adjacent to peripheral neurons or on the cortical surface shown that the subsequent resorption does not prove neurotoxic. It should be noted that all biodegradable materials cause inflammation during the resorption process. The cells that break down, digest, and clear the material are the same immune cells that arrive at a site of injury to clear and reconstruct damaged tissue. The success of fibrin as an electrode-insertion tool depends on its ability to degrade and be resorbed without harming the surrounding neuronal population. Carefully evaluating the application of fibrin as an electrode insertion tool is critical because the presence of fibrin in the brain in pathological conditions has been associated with neurodegeneration [5, 36]. It is unknown whether a resorption of the coating on the electrode will cause a loss in the surrounding neuronal population at the implant site.

5.1.5 Background on fibrin

Fibrin is a fibrillary protein that creates the mesh in wound-site clotting. It is found in the blood in its inactive form as fibrinogen, a soluble glycoprotein [37]. Clinically, the imbalance of fibrinogen or fibrin clotting can cause thrombosis, when it is in excess, and hemorrhage when it is insufficient or prematurely degraded. Fibrinogen levels have been monitored in the blood as an indicator for cardiovascular disease, and systemic inflammation [38-39]. It is an acute phase protein, meaning its concentration in the blood increases during an inflammatory response.

The clinically used fibrin glue combines fibrinogen with thrombin. Fibrinogen is a 340 kDa protein with three polypeptide chains connected in a fibril [1]. The central nodule of the fibril has N-terminal residues from all six chains. The chains are two sets of three-chained alpha-helical coils. At each end of the fibril, are D nodules, with beta and gamma folded chains. The conversion of fibrinogen to fibrin occurs when A alpha chains and the B beta chain are cleaved by thrombin[7]. The release of these peptides exposes polymerization sites. Fibrils polymerize in half-staggered pairs that continue to aggregate into larger structures, see figure 5.3 [1].

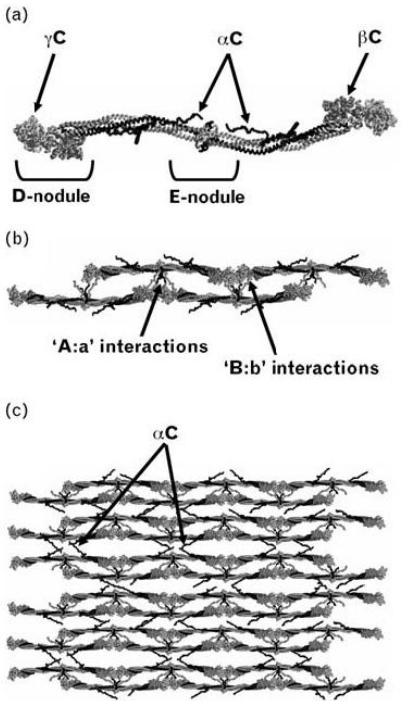

Figure 5.3: (a) The individual fibril of fibrinogen is shown top, and (b) after cleavage of the alpha and beta chains by thombin, the fibrils polymerize in a staggered formation that (c) repeats to form a clot structure [1].

An additional reaction is also catalyzed by thrombin: by activating FXIII (fibrin stabilizing factor), which is bound to the fibrin(ogen) molecule [37]. FXIII initiates cross-linking among the gamma chains- gamma-gamma dimmer formation, and between multiple alpha chains (alpha polymers). This additional polymerization, reinforces the strength of the clot.

The blood brain barrier (BBB) exists as an interface for metabolic regulation of nervous tissue, however, it is also a protective barrier, as exposure to blood-borne components has destructive effect on neural tissue. For example, the disruption of the BBB is associated with pathological conditions or traumatic events including stroke, Alzhemier's and Parkinson's disease, and multiple sclerosis [5, 40-42] (Although it must be noted that the etiology of these diseases is more complex than inflammation caused from exposure to blood borne species.)

When the BBB is compromised, one of the blood components that causes damage to nervous tissue is fibrinogen [6]. Fibrinogen is a normal component in the blood of a healthy organism, as it is necessary for blood to clot and initiates a response from immune and endothelial cells [37]. In the peripheral nervous system, it also initiates an adhesion and proliferation response from Schwann cells, the glial cells that myelinate neurons [6]. When fibrin extravasates, perivascular tissue factor converts it to fibrin, which, coagulates upon exposure to thrombin [7]. The conversion from fibrinogen to fibrin also occurs when it extravasates into the brain. The conversion exposes polymerization sites and the cleaved fibrinopeptide chain, ("chain B") attracts leukocytes, as part of an inflammatory response [6].

The application of coagulated fibrin has been studied for deleterious effects *in vivo* neuronal integrity. The breakdown of fibrin appears to initiate remyelination and repair. The toxicity of fibrin may also be associated as part of the cascade that includes tissue-type plasminogen activator (tPA). tPA converts plasminogen to plasmin, initating fibrinolysis. To test the side-effects of tPA as a therapeutic agent in thrombolytic events in patients with acute ischemic stroke, brain tissue was exposed to tPA via canula. There is a dose-dependent increase in lesion size around the canula [43]. (Although, it is important to note that the levels of tPA were higher than naturally found.) Physiological levels of tPA appear to be important in clearing fibrin. It was shown in transgenic mice with reduced tPA activity, that inflammation and fibrin deposition are both present in the tPA-deficient brain [44]. Additionally, in the transgenic mouse model of tPA deficency, fibrin depletion through a pharmaceutical agent (ancrod) was used to prevent proper fibrin polymerization to avoid fibrin deposits even in the absence of tPA [5]. The fibrin deposition was reduce along with the inflammation, and BBB permeability, compared the control group. Additionally, the inhibition of plasmin (i.e. inhibiting fibrinolysis) significantly increased microgliosis [5]. These findings do not show that the presence of fibrin in animals with normal plasmin and tPA activity is neurotoxic, however it does suggest that the accumulation of fibrin in the in pathological conditions brain is deleterious to neurons. Whether the presence of fibrin as an electrode coating, in animals with normal plasmin(ogen) regulation is harmful is not clear.

5.1.6 Fibrin as a tissue sealant

Tisseel (Baxter Scientific; Deerfield, IL) and other formulations of fibrin clots have been widely used for surgical repair in cardiac abdominal, vascular, and CNS

surgery. Tisseel has an antifibrinolytic additive (aprotinin) to slow the degradation [45]. It has been used for peripheral nerve repair in cases where the nerve has been cut and the ends must be put back in contact [46]. Neurosurgical applications include dural closure, treating subgaleal cerebrospinal fluid fisutlas, as a hemostatic agent during tumor resection surgeries, and use as a cranioplastic component (mixed with ground bone). It has also been used as a protective cover over intracranial nerves during laser-based surgery.

The effect of fibrin on central nervous tissue was explicitly tested by de Vrie *et al* [4]. Fibrin glue was applied to the subarachnoid space and the trigeminal nerve in rats, and examined for histological abnormalities at time points between one and 28 days. Three rats were sacrificed at each time point and the tissue was H&E stained. Compared to controls (rats that had the surgery, but no application of fibrin glue) no difference was found with respect to neuronal damage, gliosis, edema, fibroplasia, axonal or myelin damage. In both the fibrin and control group, mild to moderate damage was present, and at day 28, mild edema was visible around the trigeminal nerve. Mild fibroblast proliferation was continuously present in the fibrin group. At day 28, fibrin was found in one animal, but not in the other two at the same time point.

PEG-based hydrogels (DuraSeal (Covidien; Dublin, Ireland) and Coseal (Baxter Scientific) are newer alternatives, described as presenting a minimal inflammatory response and having adhesion inhibiting properties [47]. However, swelling of the hydrogels occurs, up to 50% for Duraseal and 400% for Coseal, which means the space constraints around their application must be carefully considered [47]. The literature has cited the potential for Duraseal to cause adverse neurological effects [47]. The nature of

these effects was not described; however the PEG molecule's low immunogenicity and adhesion-minimizing properties may inhibit its clearance in the central nervous system, leaving the molecules from the degraded gel in place. PEG can interfere with cell membranes and may locally disrupt the implant site [48-49].

Other sealants and adhesives include cyanoacrylates and bovine serum albumin (BSA) gluteraldehyde, sold as Bioglue (Cryolife, Kennesaw, GA). Cyanoacrylates are particularly durable, but are only used for topical application because of foreign body reaction concerns [47]. Bioglue is used as a durable bond for large blood vessels, but is not recommended for use near nerves because of potential injury from gluteraldehyde [47].

5.1.7 MRI imaging background

The MRI imaging was included in the electrode implant study to see whether changes in the tissue around the electrode were visible in the live animal. The tissue develops a fibrous layer around the electrode and chronic inflammation may be cause for a penumbral edema. The findings on the MRI will be correlated with the findings from the histology. The identification of changes relating to edema can be expected to correlate with chronic inflammation or resorption of the fibrin. The MRI was also used to electrode confirm placement at seven and 28 days.

The MRI signal uses the magnetic moment of the hydrogen nuclei in water molecules to differentiate tissue features. Under a magnetic field, the magnetic fields associated with the hydrogen atoms all align. Protons can be aligned with or against the applied field. The number of alignment states is

$$(2 \times I) + 1 \qquad \text{Eq (5.1)}$$

where I is the nuclear spin (I = 1/2); consequently there are two states. The frequency is set so that it will be transferred to the protons, i.e. the resonant frequency, and is equal to the energy difference between the two alignment states for a given magnetic field. The magnetic radiation is delivered in the radiofrequency range (MHz). The axis of rotation in the protons changes with time, and is referred to as precession. The radio frequency magnetic field is used to redirect the alignment of the protons on a temporal scale. When the field is removed, the speed of return of the protons to random rotational axes depends on the surrounding environment.

The spin of the proton has an angular momentum that resists a change in its rotational axis. The change in rotational axis, precession, occurs at a speed called the Larmor frequency. The Larmor frequency is a function of the strength of the applied field and the gyromagnetic ratio, which is intrinsic to the particle of interest.

$$W_o = \gamma_o \cdot B_o \qquad \text{Eq (5.2)}$$

By varying the strength of the magnetic field by an established gradient in a spatial dimension, the measured change in frequency can be used to create three dimensional reconstructions of biological tissue, among other samples. The degree of relaxation in the aligned spins that occurs in between the pulses of the magnetic field can be used to elicit different information about the water molecule's surrounding environment, i.e. the tissue. T1, T2 are reconstructions from commonly used pulse sequences.

The T1, spin-lattice, relaxation time is the time of recovery after the alignment through an applied field. The T2 spin-spin relaxation measures the temporal change in the transverse magnetic field (e.g. x-y plane), relative to the longitudinal field applied for T1 (z plane). The T1 relaxation time measures the ratio between the resonant frequency

and the Larmor frequency. Free water has a bigger difference in its resonant frequency than bound water from the larmor frequency, and so the T1 signal is stronger for free water. T2 spin-spin relaxation is the loss of spin coherence. If the water is bound or associated with other structures, the loss of coherence will be delayed compared to reversion in free water. In free water, there is not a field strong enough to count as a retarding element, so the T2 relaxation is comparatively short because of the rapid and random fluctuations among the freely associated molecules [50]. The difference in relaxation in T2 weighted MRI has been used to identify central venous thrombosis [51] and cerebral hemorrhaging [52]. The hemorrhage is identified as a excess of fluid in a confined space, and is hyper-intense in the T2 image. In the case of thrombosis, the clotted region is more intense than the normally flowing blood because the water in the clot looses coherence more quickly than that in the blood (blood actually shows no intensity because it is moving). Cerebral edema (the accumulation of water in the brain either intracellularly or extracellularly) shows up as hyperintense regions on T2 weighted images [53]. Intracellular edema is correlated with inflammation [37]. T2-weighted MRI may be a useful mechanism to track inflammation around the electrode during a study if it is accompanied by some level of edema. *In vivo* imaging, such as MRI, has the advantage of not requiring additional animals for every time-point collected. Using the same animal for multiple time points is desirable because it reduces the size of the study and can provide some continuity when interpreting the data because one animal's response can be observed and marked for changes over time.

5.2 Methods

5.2.1 Characterization of the viscoelastic properties of fibrin

Tisseel, the commercially available fibrin glue, consists of fibrinogen and thrombin powders, which are dissolved into solution separately and then combined for instantaneous coagulation. The mechanical properties were assessed using a frequency dependent measure of the sheer force when a sample in placed between two disks, one of which rotates at the specified frequency. The rheometer (CVO 120 High Resolution , Bohlin Instruments; East Brunswick, NJ) tested the coagulated fibrin samples at frequencies ranging from 0.1-1 Hz, which were chosen for their biological relevance. Two batches of fibrin were mixed. They were rheologically tested immediately after mixing. Two samples were tested in the first batch and a third sample was tested in the second batch.

5.2.2 Electrode preparation for implantation

The control electrodes were silicon pitchforks in the Michigan-electrode style. The controls were not functional electrodes, just the silicon substates, because electrical recording was not to be conducted in the study and ordering the substrates is considerably more economical than ordering fully functional probes. The silicon probes and microcable electrodes were sterilized using steam-pressure sterilization (Tuttnauer-Brinkmann autoclave, model 3850; Jerusalem, Isreal). The sterilization run was 30 minutes at 20 psi and 127° C. If the probes had been intended for electrophysiological recordings, low-temperature hydrogen peroxide, plasma sterilization, a more expensive, but more gentle alternative intended for sterilization of delicate medical equipment, would have been implemented (Sterrad , Advanced Sterilization Products; Irvine, CA).

The microcable electrodes were laid ontop of paper with center cut-outs prior to sterilization, as shown in figure 5.4. The fibrin was obtained from Hemaseel fibrin sealant kits (Hemaseel is another trade name for Tisseel); it was in aseptic packaging because it was intended for clinical use as a tissue sealant. The fibrin preparation and application to the electrodes was done using aseptic technique so that the electrodes did not require additional sterilization prior to surgery.

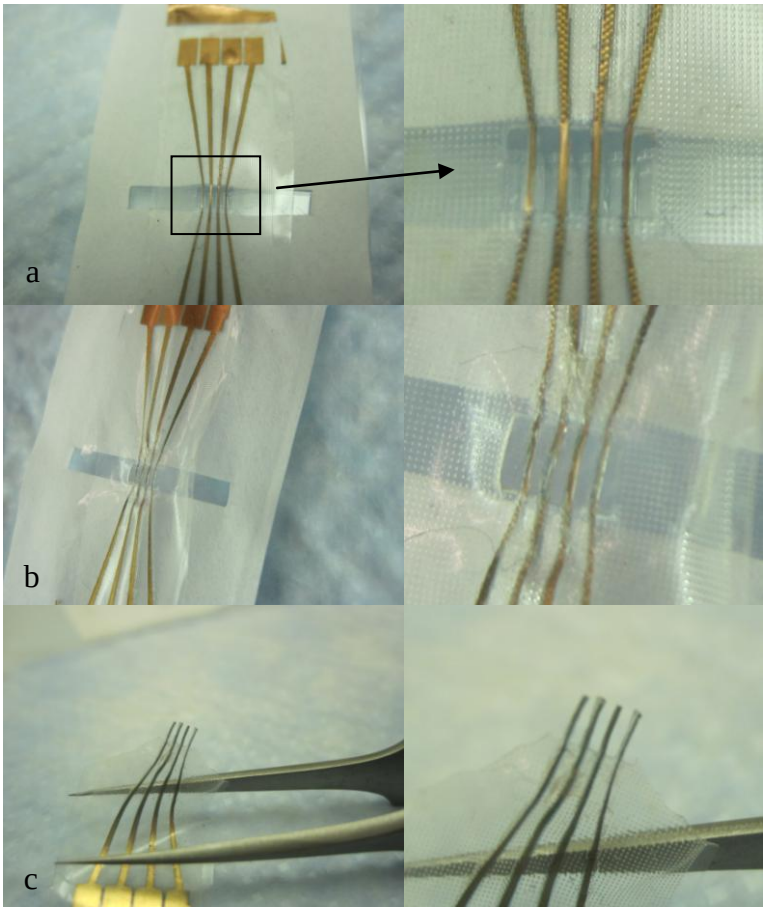

Figure 5.4. The microcable electrodes are shown (a) laid on the paper over the cut-out region, (b) after the fibrin has been applied and dried, and (c), after the microcables have been cut and pulled off the paper. For reference, the microcables are 2 mm long.

The preparation is as follows: 10 mg of Sealer protein concentrate (fibrin w/ polysorbate, sodium chloride, trisodium citrate, and glycine [45]) was mixed with 75 ul of fibrinolysis inhibitor solution (3,000 KIU/ml of aprotinin). The mixture was allowed to sit until it was dissolved. Ten mg of thrombin (also with sodium chloride and glycine) was dissolved in 75 µl of a 20 µMol calcium chloride solution. The dissolved fibrin, which has a mucus-like consistency, was applied to the non-recording side of the microcable electrodes. The thrombin, which dissolved into a solution, was pipette on to the fibrin to allow it to cross-link. The fibrin on the coated microcables was allowed to air dry, after which the microcables were cut into shank-style electrodes with a razor blade. The microcable array was laid on the paper to keep the microcables aligned during the fibrin application and drying. After the fibrin was dry, and the microcables were cut with a razor blade and the array was gently pulled off the paper with a pair of tweezers.

5.2.3 Surgical implantation of the electrodes

Male Sprague-Dawley rats (150-175 g) were deeply anesthetized with an intraperitoneal injection of ketamine cocktail (50 mg/kg ketamine, 10 mg/kg xylazine, 16.7 mg/kg acepromazine). Ketamine creates a deep sedation that is intensified by xylazine and acepromazine, which produce light sedation when used alone. Ketamine is an non-competitive NMDA-receptor anatagonist which as anesthetic doses, binds to mu-opoid receptors and sigma receptors, causing the loss of conscientiousness [54-56]. Acepromazine is used as a preanesthetic agent but may cause bradycardia and respiratory arrest [57]. Xylazine is used for analgesic effects. It is an adrenergic receptor antagonist, ($alpha_2$ class), as such it can cause bradycardia and myocardial depression. All

pharmaceuticals were obtained from Henry Schein (Indianapolis, IN.) If the rats had difficulty recovering from anesthesia, the quantity of xylazine was decreased by half.

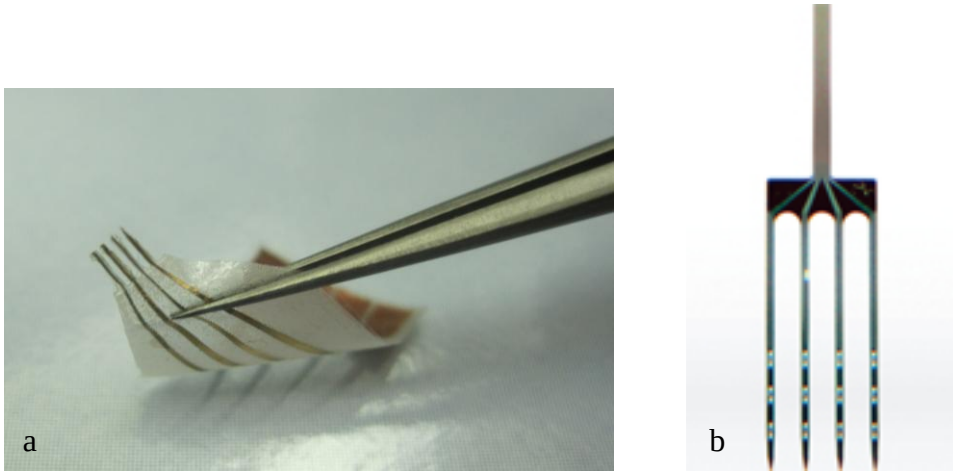

Figure 5.5: The PDMS electrode coated in fibrin and the silicon electrode used in the implants are shown above (a & b). The excess lead region shown in the photo of the PDMS electrode was trimmed prior to implantation. PDMS array dimensions: 2x2 mm, 85 μm thick, shank width: 200 μm. Silicon array dimensions: 0.8x2 mm, 15 μm thick, shank width: 100 μm.

Once the animal was sedated, the fur over the surgical site was removed with an electric razor. The head of the animal was mounted in a sterotaxic frame. The skin was disinfected with three alternate rinses each of isopropanol and toluidine blue. The skin was cut with a scalpel along the midline of the skull and pulled away from the skull with hemostats. The connective tissue over the skull was scraped away and a 2.5 mm hole was drilled into the skull with a hand-held trephine. The insertion side was 2mm lateral and caudal of the intersection of the intersection of the coronal and sagittal sutures (bregma). The dura was snipped to facilitate electrode insertion. A diagram of the surgical implantation is shown in Figure 5.6.

The electrode was inserted using a pair of forceps (care was taken to avoid rupturing blood vessels on the cortical surface). The skin was closed using would clips

and the surgical area was cleaned with hydrogen peroxide until residual blood was removed. The animal was removed from the stereotaxic frame and placed on a heating pad until recovering from anesthesia. At two and 18 hours after surgery, the animals were given injections of buprenorphine (opioid-derived analgesic, Buprenex, 0.1ml). Would clips were removed 10-14 days post surgery. Each treatment group had four animals.

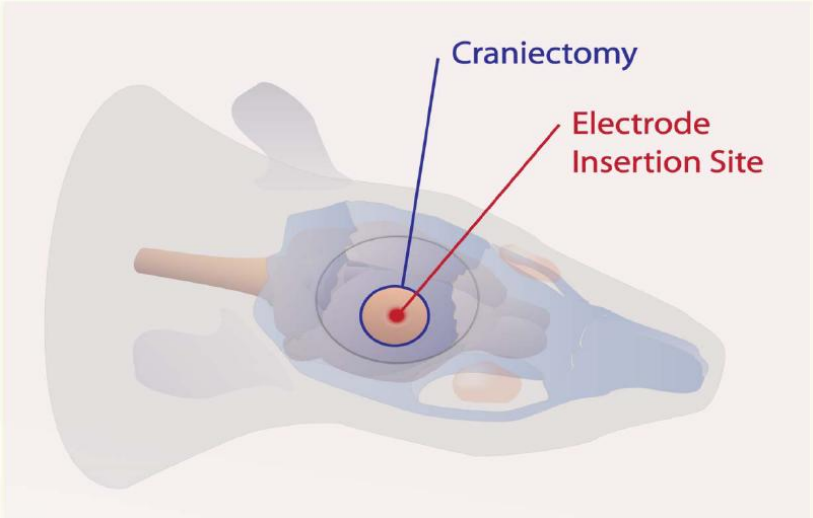

Figure 5.6: The craniectomy was performed with a hand-held trephine bit, 2mm to the side of the midline sutures. The dura were snipped to allow for insertion of the electrodes.

5.2.4 *In vivo* MR imaging

The animals were MR imaged at seven and 28 days post-implant. The MRI system was a 38 mm coil, seven Tesla, Pharmascan (Brucker; Billerica, MA). The animal was anesthetized with isoflurane. The animal was initially sedated in an induction chamber (5% in O_2) and the wound clips were removed from the animals imaged at the seven-day time point. The sedated animal was then transferred to the imaging station, where anesthesia was continued via nosecone (1-2% in O_2). The animal's heart rate was

monitored for the duration of the imaging process. Several T1 scans were taken to verify the placement of the electrode. First, a gross scan along three axes was taken to verify animal head placement. Re-adjustments were made during this period. The head was then imaged in the horizontal and coronal orientations to verify electrode placement. A spin-echo sequence was run for obtaining T2-weighted and spin-density-weighted images. After imaging, the wound clips were replaced as necessary, and the animal was allowed to recover from the anesthesia.

5.2.5 Histological staining

The tissue was cut on a cryostat 10 μm thick for staining. The immunohistology was run for activated astrocytes (GFAP), neurons (NeuN), and activated microglia (Iba-1) using monoclonal antibodies (Millipore, Billerica, MA). The tissue was first blocked with a horse serum (10%) and tween (2%) phosphate buffered saline (PBS) solution at room temperatures for 2 hours. The slides were rinsed 4x in PBS and incubated with the primary antibody overnight (1:100 dil) at 4 C in PBS with 2% horse serum and 1% tween. The primary antibody was rinsed from the slides 4x in PBS. The secondary antibody, TRITC-conjugated from donkey (Jackson Immunoresearch; West Grove PA), was incubated 1:80 in 2% horse serum PBS at room temperature for two hours. After the second incubation, the slides were rinsed 2x in PBS. The FluoroJade C (Histo-Chem; Jefferseon, AR) was used to assay for degenerating neurons. The tissue was incubated in 0.06% potassium permanganate for 10 min, and then rinsed in deioninzed (DI) water. The tissue sections were then incubated in 0.0001% FluoroJade C solution in 0.1% acetic acid for 20 minutes. The slides were rinsed in DI water 3x.

5.2.6 Histology analysis

Two types of neuronal staining were conducted. NuN stains for neuronal nuclei, and as such can be quantified by counting neurons within a specified region. FluoroJade C stains degenerating neurons, and depending on the density (i.e. if the cells are distributed enough to resolve individual cells) may be translated into cell counts. Because only very sparse FluoroJade staining was observed, it was not included in the analysis. Activated microglial and activated astrocyte markers (Iba-1 and GFAP) stain for proteins expressed after these cell types are activated. As such, the staining is not discrete like a nuclear stain. The quantity of visibly-stained stained Iba-1 was identified as positive or negative, although the presence of microglia appeared to be somewhat random, with adjacent microglia positive and negative electrodes. The GFAP staining was almost universally present in the samples and the amount of GFAP staining was measured the spatial profile of the staining. The absolute intensity of the GFAP staining was not quantified because of intensity variations between separate batches of immune-staining. Because the size and shape of electrode insertion sites varied in size for several reasons, the GFAP analysis was done on a segment extending from the edge of the insertion site outward. The image section was created in ImageJ (Figure 5.7). The segment was the same size in area for each image. If there was noticeable variation in intensity around the implant site, sections were taken of high and low intensity regions and averaged.

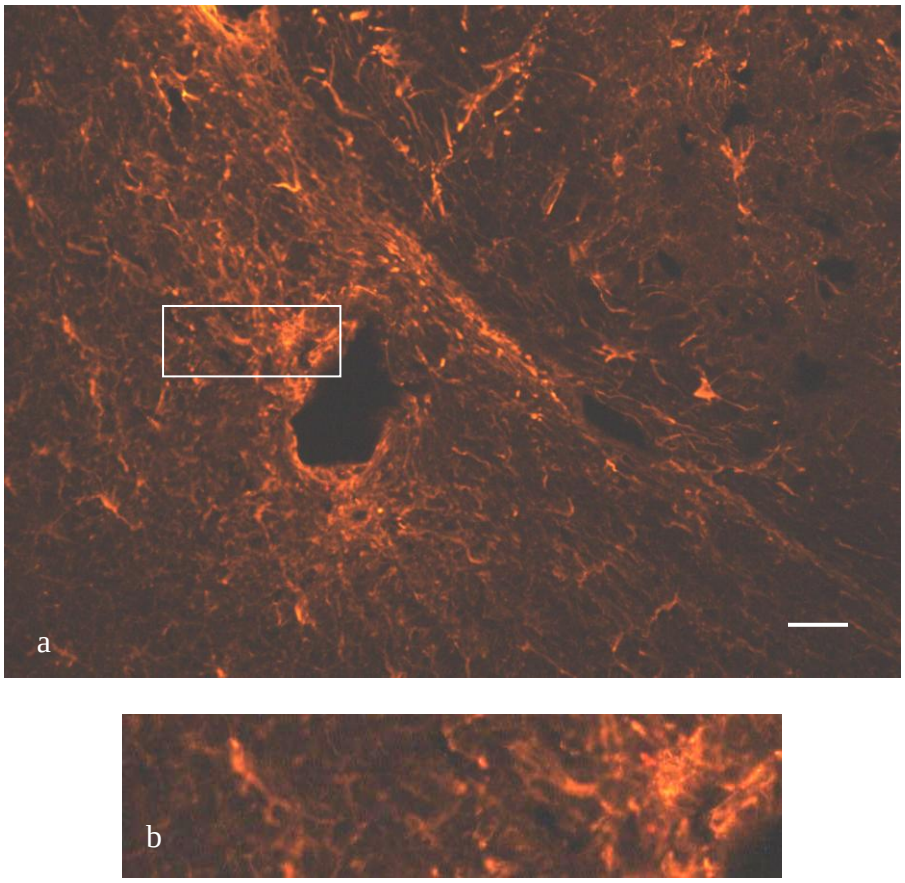

Figure 5.7 (a) A sample image with the implant site is shown with GFAP staining with the cropped section highlighted (~450 µm by 110 µm). (b) the cropped segment of the image to be used for intensity analysis. Scale bar: 50 µm

5.3 Results

5.3.1 Fibrin application and mechanical characterization:

The elastic and viscous modulus was calculated from the torque the sample generated from differential rotation between the two plates which move at a specified frequency. The torque is converted into shear stress, which is used to calculate the elastic and viscous moduli shown in table 5.1. The elastic modulus and viscous modulus are in the low kPa-Pa range. For comparison, brain tissue is ~ 3 kPa, [58].

Table 5.2: Fibrin viscoelastic characterization

Frequency (hz)	Sample 1 Elastic Modulus (Pa)	Sample 1 Viscous Modulus (Pa)	Sample 2 Elastic Modulus (Pa)	Sample 2 Viscous Modulus (Pa)	Sample 3 Elastic Modulus (Pa)	Sample 3 Viscous Modulus (Pa)
0.10	920.58	485.77	519.12	227.51	907.96	213.57
0.18	648.79	317.71	638.25	198.82	1213.80	272.08
0.32	539.33	217.93	828.16	212.50	1446.20	308.22
0.56	653.36	262.73	1043.30	240.08	1766.00	368.94
1.00	751.12	306.74	1285.60	288.86	1981.20	411.10

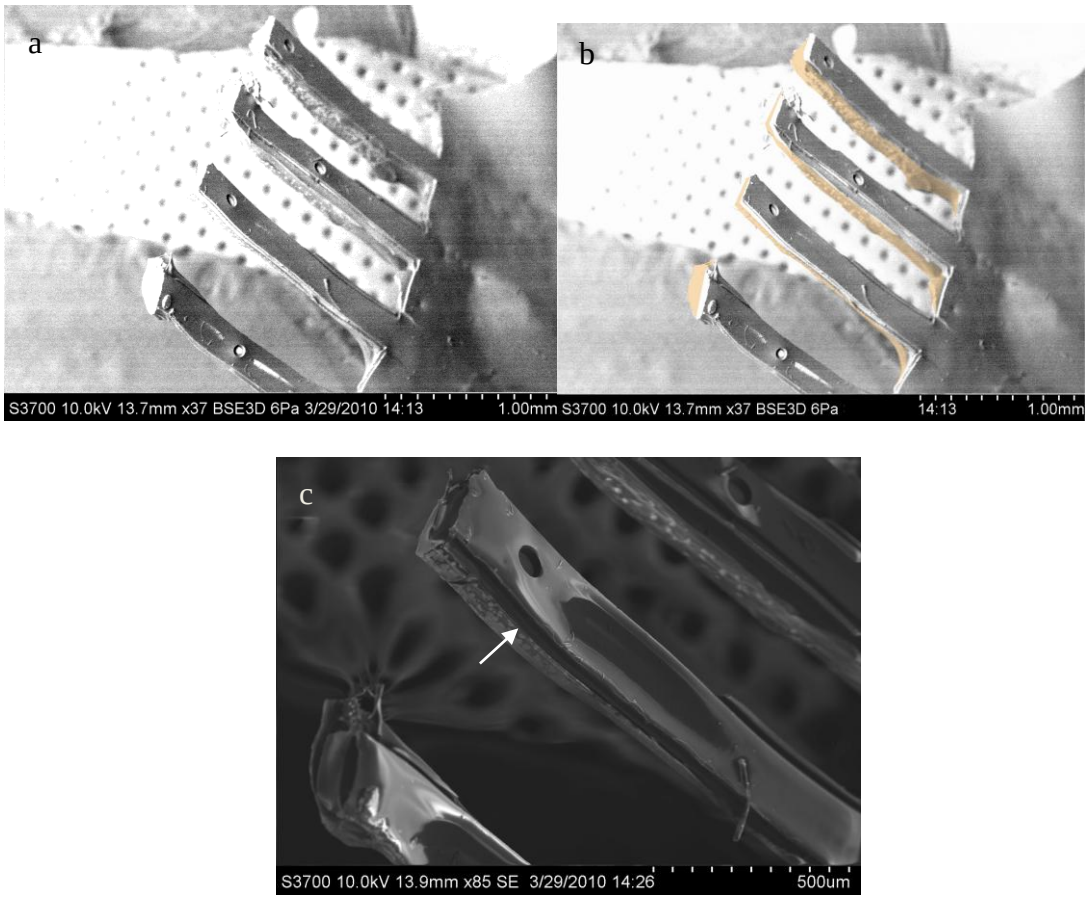

Figure 5.8: (a) The array of four electrodes is shown with a backside coating of fibrin. (b) The fibrin is highlighted using artificial shading. Some variation in the fibrin thickness occurs, and is due to the nature of the application process. (c) An expanded view of one of the fibrin coated electrodes is shown, where the delineation between the fibrin and the PDMS is shown with the arrow.

The electrodes after the application fibrin are shown in figure 5.8 (a-c). The fibrin was applied to the back of the electrode only. The localized application leaves the recording site exposed. The variation in fibrin thickness is due to the limitations of the coating-process. The thickness, form visual inspection, was estimated to vary from 50 µm to 100 µm after the fibrin had dried.

5.3.2 MR Imaging

Some sample images of the T1 are shown in Figure 5.9. The electrode implant site was clearly visible a majority of the scans. One of the animals with the silicon implant did not have a visible electrode in the T1 imaging sequence at either the seven or 28 day time points. At the end of the study, the electrode was found broken in pieces at the cortical surface. How the electrode escaped the cortical tissue is not clear; however it was not fixed in place and may have dislodged during post-surgical swelling. This animal was removed from the study.

The T2-weighted images showed increased intensities around both the PDMS microcable and silicon electrode implant sites at 28 days (Figures 5.10-14). No intensity increases at the implant site (relative to the surrounding tissue) were visible at seven days. At 28 days, the microcable implants had a more diffuse signal than the silicon electrodes, which had a more localized intensity.

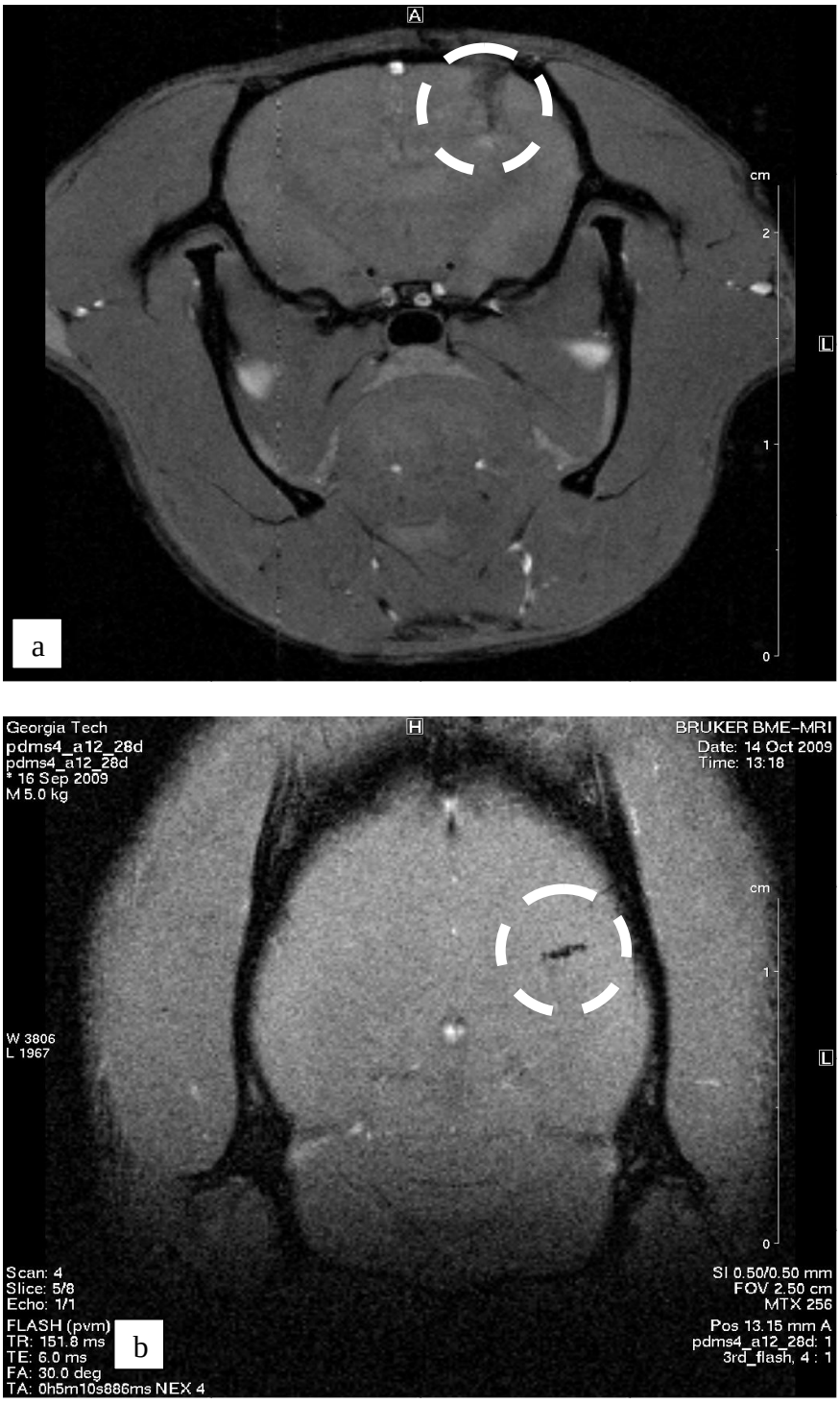

Figure 5.9: An example of the T1 images taken to verify placement are shown above at 29 days. The electrodes are highlighted in (a) the coronal and (b) the horizontal planes. The electrode shown here is a PDMS electrode.

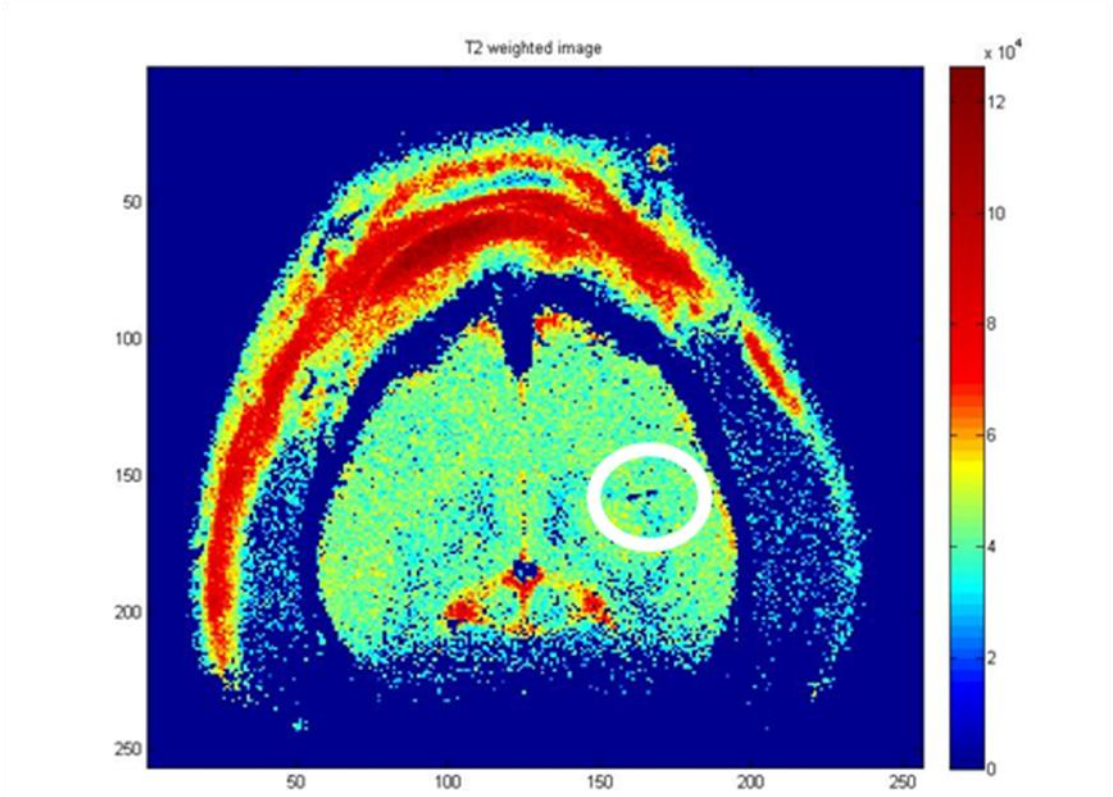

Figure 5.10: The T2 weighted images at seven days did not show any intensity differences between the region surrounding the electrode and the rest of the tissue. T2 weighting measures "bound" water density and has been correlated with edema in clinical settings. The electrode shown above is a PDMS/fibrin electrode.

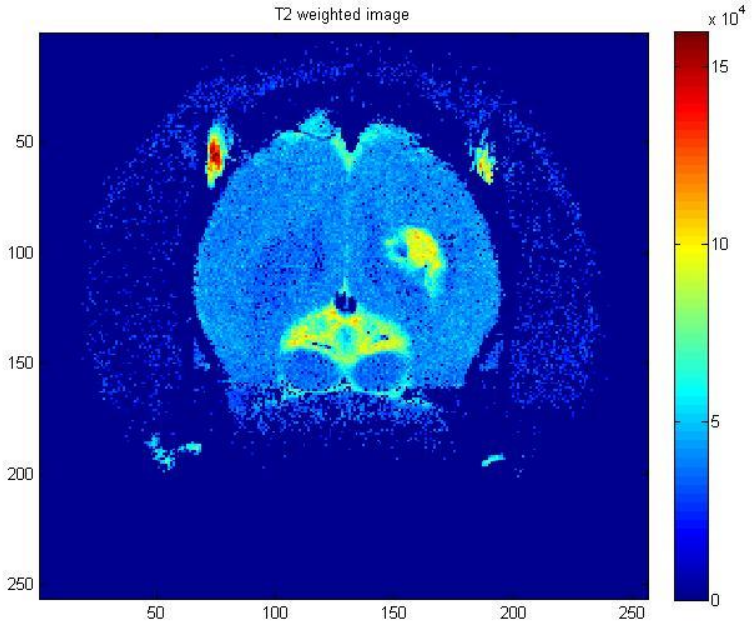

Figure 5.11: The T2 weighted image of a PDMS electrode is shown again at 28 days. A change in intensity around the electrode site is clearly visible.

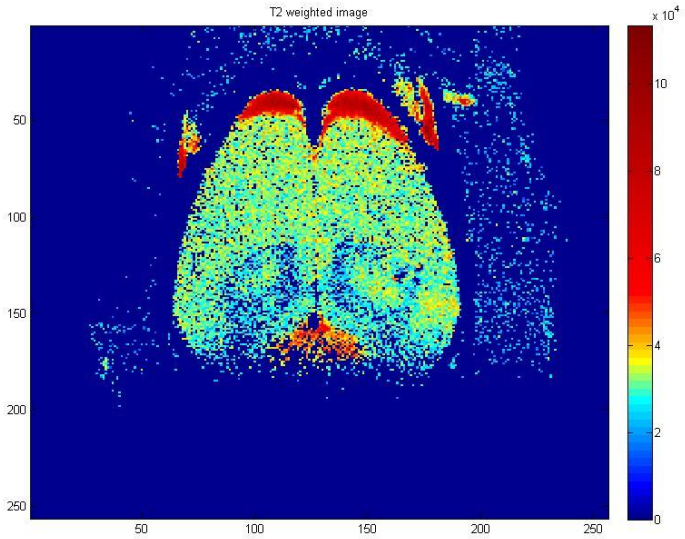

Figure 5.12: The T2 weighted image of a second PDMS electrode is shown again at 28 days. The intensity changes are not consistently present. The coloration scale was narrowed here to highlight any subtle changes, but none are visually evident.

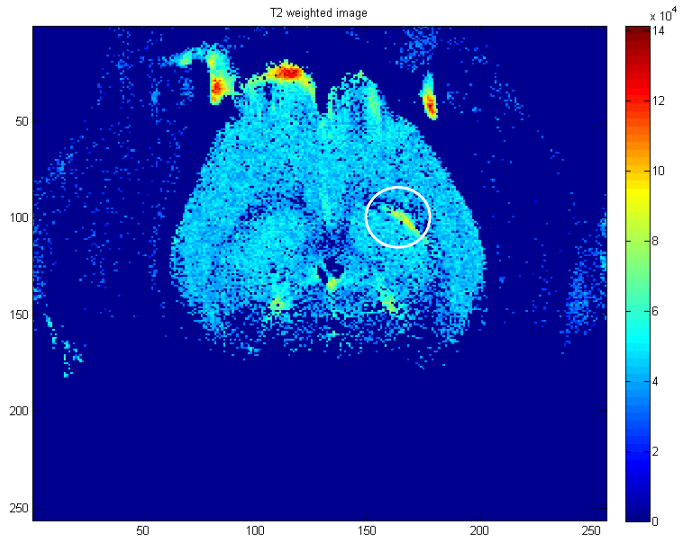

Figure 5.13: The T2 weighted image of a silicon electrode is shown again at 28 days.

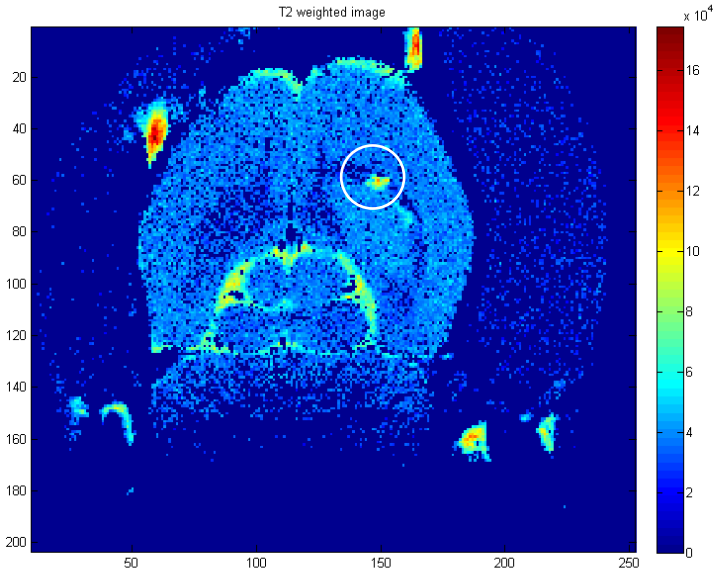

Figure 5.14: The T2 weighted image of a second silicon electrode is shown again at

Table 5.3: Visible T2 intensity change at the implant site from MR images

Sample	T2 7D	T2 28d
PDMS 1	No	Yes
PDMS 2	small	No
PDMS 3	No	Yes
PDMS 4	No	Yes
Si1	No	Bad scan
Si2	No	Yes
Si3	No	Yes

5.3.3 Histology Results

The histological staining for NeuN was not quantified because neurons were found in the vicinity of the implant site for both the fibrin-coated microcable electrodes and the silicon electrode implants. FluoroJade positive neurons were also not found in any density that might suggest local degeneration at the implant site. Microglia were present for both types of implants, although not in a consistent manner. When they were found, it was as a tightly-formed bundle around the electrode track (Figures 5.15). GFAP staining was positive for both the fibrin-coated microcable electrodes and the silicon electrode implants, although the degree of GFAP staining varied with the sample (Figure 5.15-16). The GFAP intensity profile was greater at the edge of the implant site, particularly for one of the silicon electrodes, which had a six-fold increase in GFAP intensity relative to the staining in the background. In general, GFAP intensity at the implant site was two-three times the intensity of the background for the other samples (Figure 5.17).

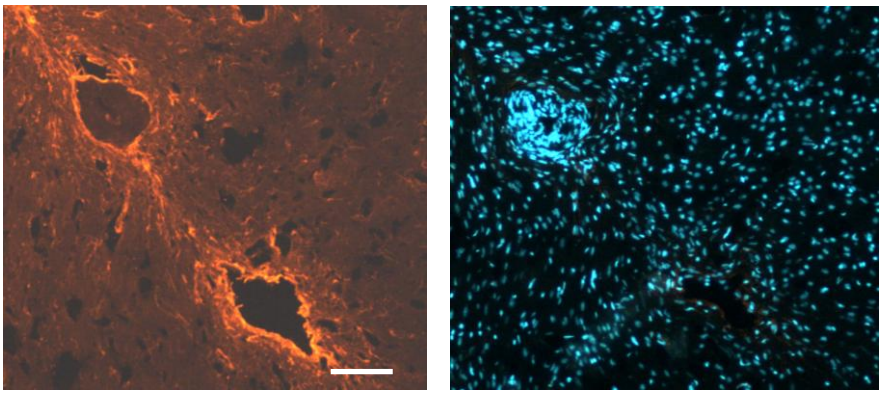

Figure 5.15: Two sections of the same implant (S1) are shown with GFAP and the nuclear stain for a silicon electrode implant. The bundle of cells surrounding one of the implant sites is microglia. Separate immunohistology with Iba-1 (microglia) done to confirm, not shown) The electrode cross-section was 85 x 15 µm Scale bar: 50 µm

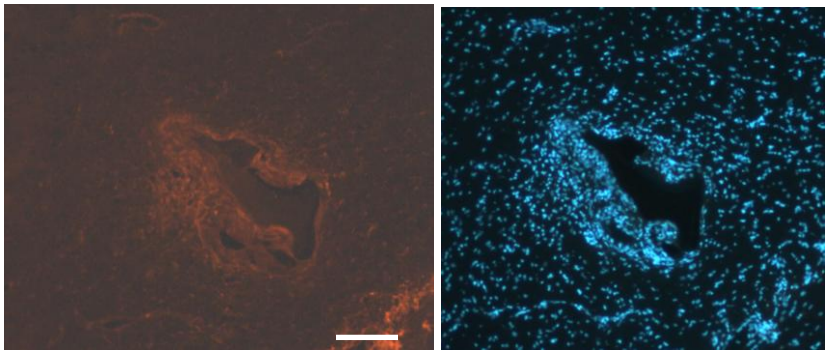

Figure 5.16: Two sections of the same implant (P1) are shown with GFAP and the nuclear stain for a silicon electrode implant. The nuclear density is coincident with the GFAP intensity. (Separate immunohistology with Iba-1done to confirm, not shown) The electrode cross-section was 200 x 85 µm. Scale bar: 50 µm

Additionally, the intensity values of the subsection were averaged along the y-axis to show how the intensity-profile changes as a function of distance from the implant site. The sections for each sample were averaged to provide an average intensity profile. The data from S1, S2, P1, P2, P3 and P4 is shown in figure 5.17. The intensity profile of S2 very visibly peaks and then decreases with the distance from the electrode. The intensity in P4 also peaks and decreases, while the intensity in P3 does not appear to decrease with

distance. This difference the GFAP staining pattern supports that idea the inflammatory response for the fibrin-coated microcables is different than the silicon implants. The fibrinolysis is expected to induce inflammation, however the inflammation is also expected to be temporary until the fibrin is completely cleared. After the fibrin is cleared, GFAP expression may be reduced at the microcable electrodes.

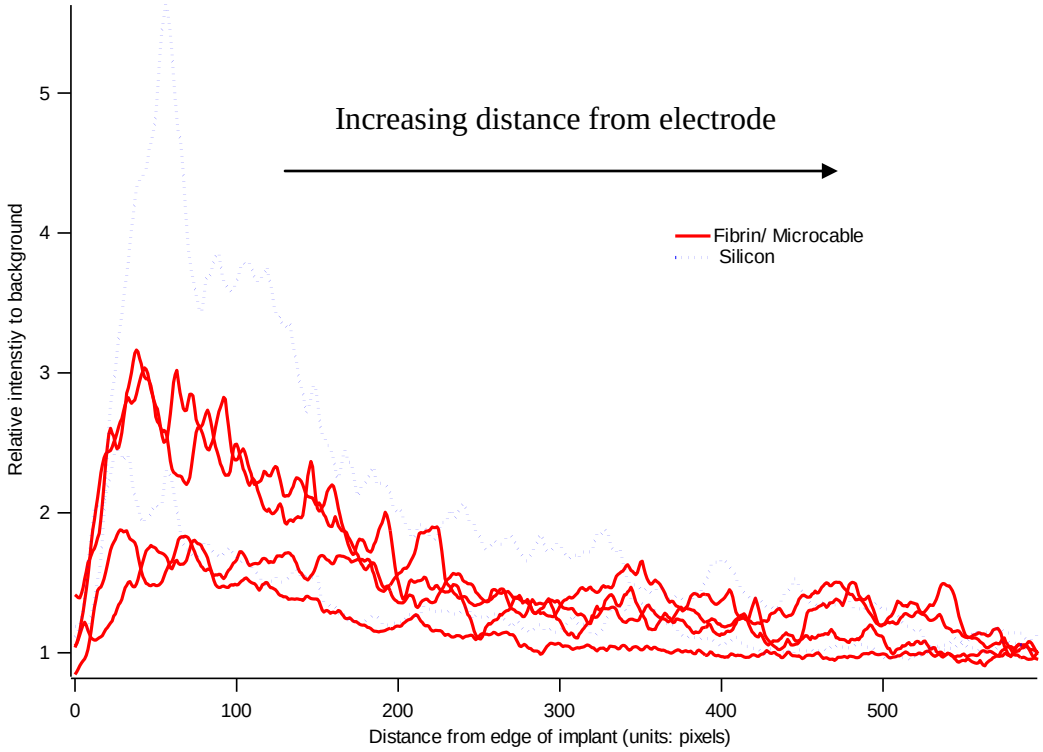

Figure 5.17: The average intensity profile is shown as a function of distance from the electrode. 450 µm = 600 pixels (length of sub-sampled image)

5.4 Discussion:

5.4.1 Rheology

The data show that coagulated fibrin has an elastic modulus less than 2 kPa, which less than the reported 3 kPa of brain tissue [58]. The fibrin rheology was done to assess the mechanical properties after rehydration. Its 2 kPa elastic modulus is also lower

than the 1.8 MPa composite modulus of the microcable electrodes. As such, it will not increase the stiffness of the electrodes after it has been inserted and rehydrated.

5.4.2 MR Imaging

The difference in the spatial spread of the intensity in the T2-weighted images between the PDMS microcables and silicon implants is likely due to the resorption of the fibrin but may also be due to the larger size of the microcable implants. Fibrinolysis was the likely cause of the larger T2 intensity area in the microcable implants. The degradation of fibrin is related to the inflammatory response through the initiators of fibrinolysis (via plasminogen activation) [8]. The localized fibrinolytic response appears to have caused some inflammation-based edema, as measured by the T2-weighted scans. The silicon implants had a much smaller region of edema, indicating inflammation [37, 53]. The inflammation in the silicon electrodes was likely due to the mechanical mis-match or foreign-body response [28, 31, 59].

5.4.3 Histology

GFAP staining, indicating activated astrocytes, was present for both the PDMS microcables and the silicon electrodes. One of the silicon electrodes had no significant GFAP staining or T2 intensity, while one electrode had intermediate staining and one showed significant staining. All fibrin-coated PDMS microcable electrodes showed some level of GFAP staining. The NeuN staining, highlighting the neuronal nuclei, showed neurons adjacent to the silicon electrodes. Previous studies have shown a loss of neurons after 28 days around the electrode site, although those electrodes were tethered to a head-stage, which is necessary for recording. The simulations that described the micromotion

of an electrode implanted in the cortex were designed to include the tethering scheme [60].

With a compliant, slack tethering scheme, the micromotion, and the consequent injury and inflammatory response is reduced [61]. From this finding, it follows that the tethering scheme will impact the outcome of the study. To examine the effect of the electrode stiffness in this study, the electrodes were tested without a tether. As such, the implants in this study targeted the low-range of inflammation.

Although it was desirable to decouple the electrode stiffness from other variables, it was not realistically possible to match the variables in each implant and the two groups. The silicon electrode implants were chosen because they were non-custom, commercially available for chronic applications. Polyimide and other polymeric electrodes are not found to be available in an off-the-shelf format. The PDMS microcable arrays could not be tested without testing an insertion mechanism also. In the microcable implants, the assessment convolves the inflammatory response of the fibrin as a resporbable implant with the biocompatibility of the microcable electrodes. Prior data shows that as electrode compliance increases, inflammation decreases. The expectation was held for the PDMS microcables, but testing their biocompatibility required the inclusion of an insertion mechanism. The silicon electrodes were intended to be tested as a third group with a fibrin coating, however, this was not included in the study because of difficulties in coating the silicon electrodes with comparable amounts of fibrin without inducing breakage from the coating process.

Evidence of fibrin was not generally apparent in the four microcable implants. The presence of fibrin was not tested using immunolohistological techniques, but bulk material was not present in three of the implants. In some sections, there was a residue that might have been an artifact from histological processing, but could also have been fibrin. The residue was not consistently present.

Based on the diffuse edema in the MR images, which is suggestive of inflammation, fibrin residue may have been present in the vicinity of the electrode site of the microcable implants at 28 days. Its presence would suggest that the fibrinolysis is not complete at four weeks. The relation between fibrinolysis and inflammation suggests that the inflammation will decrease once the fibrinolysis has completely resolved.

The MR images showed a perturbation in the tissue at the implant site at appears more pronounced and consistent than the inflammation found in the immunohistological staining. The functional impact of the edema is difficult to gauge without extending the time point beyond 28 days for histological or electrophysiological data. However, it is noticeable, with T2 intensity approximately double that of the tissue in the surrounding region, for the microcables, and the silicon microcables. Both groups had similar intensity ranges, although the silicon implants had a smaller T2-intensity foot-print.

5.5 Conclusion

The fibrin-coated microcable electrodes were successfully inserted into rat brains. The placement was verified at seven and 28 days by MR imaging. The MR imaging was

also used examine the tissue at the implant site. The larger area of the T2 signal in the fibrin coated microcables suggests a broader area of edema that may be due to fibrinolysis. The comparison of the two groups using immunohistology showed that inflammation as measured by GFAP staining was low in both groups, with an increase of 2-3 fold the staining intensity in both groups. The time point was also possibly too short to fully evaluate the steady-state response of the tissue to the microcable electrodes because the fibrinolysis may not have fully resolved. The small sample size limits the conclusions that can be drawn from the study, although the low level of inflammation suggests several ways to target the production of successful chronic electrodes. Studies in the literature documenting chronic long-term recording highlight the importance of an electrode tether that minimizes the transfer of micromotion to the implanted electrodes [3, 31]. A tethering scheme was not included in the study in the interest of simplicity. Showing the silicon electrodes low inflammatory response when untethered suggests that the connective tethering element can be improved to further reduce micromotion.

An advantage of using silicon probes is the recording density. Elastomer-based, stretch-tolerant electronics may not be able to approach the lead density possible with more traditional electronics. The lead density is a valuable asset in single unit recording of large populations of neurons. In these instances, a potential application for elastomeric leads may be as the tethering connector. The PDMS/thin film gold is more compliant than the currently used microwire or silicon cable and might serve to improve the long-term feasibility of recording large populations of single-unit activity.

5.6 Citations

1. Lord, S.T., *Fibrinogen and fibrin: scaffold proteins in hemostasis.* Current Opinion in Hematology, 2007. **14**(3): p. 236-241.
2. Biran, R., D.C. Martin, and P.A. Tresco, *Neuronal cell loss accompanies the brain tissue response to chronically implanted silicon microelectrode arrays.* Experimental Neurology, 2005. **195**(1): p. 115-126.
3. Biran, R., D.C. Martin, and P.A. Tresco, *The brain tissue response to implanted silicon microelectrode arrays is increased when the device is tethered to the skull.* Journal of Biomedical Materials Research Part A, 2007. **82A**(1): p. 169-178.
4. de Vries, J., et al., *Histological effects of fibrin glue on nervous tissue - A safety study in rats.* Surgical Neurology, 2002. **57**(6): p. 415-422.
5. Paul, J., S. Strickland, and J.P. Melchor, *Fibrin deposition accelerates neurovascular damage and neuroinflammation in mouse models of Alzheimer's disease.* Journal of Experimental Medicine, 2007. **204**(8): p. 1999-2008.
6. Adams, R.A., et al., *Manifold roles for fibrin.* Molecular Interventions, 2004. **4**(3): p. 163-176.
7. Mosesson, M.W., *Fibrinogen and fibrin structure and functions.* Journal of Thrombosis and Haemostasis, 2005. **3**(8): p. 1894-1904.
8. Medcalf, R.L., *Fibrinolysis, inflammation, and regulation of the plasminogen activating system.* Journal of Thrombosis and Haemostasis, 2007. **5**: p. 132-142.
9. McConnell, G.C., et al., *Implanted neural electrodes cause chronic, local inflammation that is correlated with local neurodegeneration.* Journal of Neural Engineering, 2009. **6**(5).
10. McIntyre, C.C., et al., *Uncovering the mechanism(s) of action of deep brain stimulation: activation, inhibition, or both.* Clinical Neurophysiology, 2004. **115**(6): p. 1239-1248.
11. McIntyre, C.C., et al., *How does deep brain stimulation work? Present understanding and future questions.* Journal of Clinical Neurophysiology, 2004. **21**(1): p. 40-50.
12. NeuroNexus, *Silicon microelectrode array research product catalog and manual*. 2009, NeuroNexus Technologies: Ann Arbor, MI.
13. Rousche, P.J., et al., *Flexible polyimide-based intracortical electrode arrays with bioactive capability.* Ieee Transactions on Biomedical Engineering, 2001. **48**(3): p. 361-371.
14. Kringelbach, M.L., et al., *Translational principles of deep brain stimulation.* Nature Reviews Neuroscience, 2007. **8**(8): p. 623-635.
15. Umemura, A., et al., *Role of subthalamic deep brain stimulation for levodopa-induced dyskinesia in Parkinson's disease.* Movement Disorders, 2007. **22**: p. 202.
16. Miller, J.P. and W.R. Selman, *Deep brain stimulation for depression.* Journal of Neurosurgery, 2009. **111**(6): p. 1207-1208.

17. Sotiropoulos, S.N. and P.N. Steinmetz, *Assessing the direct effects of deep brain stimulation using embedded axon models.* Journal of Neural Engineering, 2007. **4**(2): p. 107-119.
18. Boulet, S., et al., *Subthalamic stimulation-induced forelimb dyskinesias are linked to an increase in glutamate levels in the substantia nigra pars reticulata.* Journal of Neuroscience, 2006. **26**(42): p. 10768-10776.
19. Tass, P.A., et al., *Obsessive-compulsive disorder: Development of demand controlled deep brain stimulation with methods from Stochastic phase resetting.* Neuropsychopharmacology, 2003. **28**: p. S27-S34.
20. Butson, C.R., C.B. Maks, and C.C. McIntyre, *Sources and effects of electrode impedance during deep brain stimulation.* Clinical Neurophysiology, 2006. **117**(2): p. 447-454.
21. Butson, C.R. and C.C. McIntyre, *Tissue and electrode capacitance reduce neural activation volumes during deep brain stimulation.* Clinical Neurophysiology, 2005. **116**(10): p. 2490-2500.
22. Arumugam, T.V., et al., *Contributions of LFA-1 and Mac-1 to brain injury and microvascular dysfunction induced by transient middle cerebral artery occlusion.* American Journal of Physiology-Heart and Circulatory Physiology, 2004. **287**(6): p. H2555-H2560.
23. Kumagai, N., et al., *Involvement of pro-inflammatory cytokines and microglia in an age-associated neurodegeneration model, the SAMP10 mouse.* Brain Research, 2007. **1185**: p. 75-85.
24. Madinier, A., et al., *Microglial Involvement in Neuroplastic Changes Following Focal Brain Ischemia in Rats.* Plos One, 2009. **4**(12).
25. Neumann, H., M.R. Kotter, and R.J.M. Franklin, *Debris clearance by microglia: an essential link between degeneration and regeneration.* Brain, 2009. **132**: p. 288-295.
26. Griffith, R.W. and D.R. Humphrey, *Long-term gliosis around chronically implanted platinum electrodes in the Rhesus macaque motor cortex.* Neuroscience Letters, 2006. **406**(1-2): p. 81-86.
27. He, W., G.C. McConnell, and R.V. Bellamkonda, *Nanoscale laminin coating modulates cortical scarring response around implanted silicon microelectrode arrays.* Journal of Neural Engineering, 2006. **3**(4): p. 316-326.
28. He, W.B., R., *A molecular perspective on understanding and modulating the performance of chronic central nervous system recording electrodes*, in *Indwelling neural implants: strategies for contending with the in vivo environment*, W.M. Reichert, Editor. 2008, CRC Press: Boca Raton.
29. Cheung, K.C., et al., *Flexible polyimide microelectrode array for in vivo recordings and current source density analysis.* Biosensors & Bioelectronics, 2007. **22**(8): p. 1783-1790.
30. Mercanzini, A., et al., *Demonstration of cortical recording using novel flexible polymer neural probes.* Sensors and Actuators a-Physical, 2008. **143**(1): p. 90-96.
31. Stice, P., et al., *Thin microelectrodes reduce GFAP expression in the implant site in rodent somatosensory cortex.* Journal of Neural Engineering, 2007. **4**(2): p. 42-53.

32. Seymour, J.P. and D.R. Kipke, *Neural probe design for reduced tissue encapsulation in CNS.* Biomaterials, 2007. **28**(25): p. 3594-3607.
33. He, W., et al., *A novel anti-inflammatory surface for neural electrodes.* Advanced Materials, 2007. **19**(21): p. 3529-+.
34. Chamak, B. and M. Mallat, *Fibronectin and laminin regulate the invitro differentiation of microglial cells.* Neuroscience, 1991. **45**(3): p. 513-527.
35. Muhammad, A., et al., *Topical application of fibrin adhesive in the rat brain: Effects on different cellular elements of the wound.* Neurological Research, 1997. **19**(1): p. 84-88.
36. Cortes-Canteli, M. and S. Strickland, *Fibrinogen, a possible key player in Alzheimer's disease.* Journal of Thrombosis and Haemostasis, 2009. **7**: p. 146-150.
37. Guyton, A.H., J., *Human Physiology and Mechanisms of Disease*. 6th ed. 1997, Philadelphia: W.B. Saunders Company.
38. Myers, G.L., et al., *National Academy of Clinical Biochemistry Laboratory Medicine Practice Guidelines: Emerging Biomarkers for Primary Prevention of Cardiovascular Disease.* Clinical Chemistry, 2009. **55**(2): p. 378-384.
39. Rudez, G., et al., *Biological variation in inflammatory and hemostatic markers.* Journal of Thrombosis and Haemostasis, 2009. **7**(8): p. 1247-1255.
40. Bielekova, B., et al., *Treatment with the phosphodiesterase type-4 inhibitor rolipram fails to inhibit blood-brain barrier disruption in multiple sclerosis.* Multiple Sclerosis, 2009. **15**(10): p. 1206-1214.
41. Carvey, P.M., B. Hendey, and A.J. Monahan, *The blood-brain barrier in neurodegenerative disease: a rhetorical perspective.* Journal of Neurochemistry, 2009. **111**(2): p. 291-314.
42. Gilad, R., et al., *POST STROKE SEIZURES AND BBB (BLOOD-BRAIN BARRIER)-DTPA SPECT STUDIES.* Epilepsia, 2009. **50**: p. 135-136.
43. Goto, H., et al., *Neurotoxic effects of exogenous recombinant tissue-type plasminogen activator on the normal rat brain.* Journal of Neurotrauma, 2007. **24**(4): p. 745-752.
44. Tabrizi, P., et al., *Tissue plasminogen activator (tPA) deficiency exacerbates cerebrovascular fibrin deposition and brain injury in a murine stroke model - Studies in tPA-deficient mice and wild-type mice on a matched genetic background.* Arteriosclerosis Thrombosis and Vascular Biology, 1999. **19**(11): p. 2801-2806.
45. Baxter, *Fibrin sealant Tiseel Kit*. 1998, Baxter Scientific.
46. Isaacs, J.E., et al., *Comparative analysis of biomechanical performance of available "Nerve Glues".* Journal of Hand Surgery-American Volume, 2008. **33A**(6): p. 893-899.
47. Spotnitz, W.D. and S. Burks, *Hemostats, sealants, and adhesives: components of the surgical toolbox.* Transfusion, 2008. **48**(7): p. 1502-1516.
48. Herold, D.A., et al., *Evidence for the toxicity of polyethylene-glycol.* Veterinary and Human Toxicology, 1981. **23**(5): p. 363-363.
49. Montaguti, P., E. Melloni, and E. Cavalletti, *Acute intravenous toxicity of dimethyl-sulfoxide, polyethylene-glycol-400, dimethylformamide, absolute*

ethanol, and benzyl alcohol in inbred mouse strains. Arzneimittel-Forschung/Drug Research, 1994. **44-1**(4): p. 566-570.
50. Mitchell, D.G.B., D.L. Vinitski, S. Rifkin, M.D., *The biophysical basis in extracranial MR imaging.* American Journal of Roentgenology, 1987. **149**(4): p. 7.
51. Agostoni, E.A., A. Longoni, M, *Cerebral venous thrombosis.* Expert Reviews in Neurotherapy, 2009. **9**(4): p. 553-564.
52. Perl, J., et al., *Hemorrhage detected using MR imaging in the setting of acute stroke: An in vivo model.* American Journal of Neuroradiology, 1999. **20**(10): p. 1863-1870.
53. Gerstner, E.R., et al., *VEGF inhibitors in the treatment of cerebral edema in patients with brain cancer.* Nature Reviews Clinical Oncology, 2009. **6**(4): p. 229-236.
54. Harrison, N.L. and M.A. Simmonds, *QUANTITATIVE STUDIES ON SOME ANTAGONISTS OF N-METHYL D-ASPARTATE IN SLICES OF RAT CEREBRAL-CORTEX.* British Journal of Pharmacology, 1985. **84**(2): p. 381-391.
55. Hirota, K., et al., *Stereoselective interaction of ketamine with recombinant mu, kappa, and delta opioid receptors expressed in Chinese hamster ovary cells.* Anesthesiology, 1999. **90**(1): p. 174-182.
56. Narita, M., et al., *A putative sigma(1) receptor antagonist NE-100 attenuates the discriminative stimulus effects of ketamine in rats.* Addiction Biology, 2001. **6**(4): p. 373-376.
57. Baniadam, A., F.S. Afshar, and M.R.B. Balani, *Cardiopulmonary effects of acepromazine-ketamine administration in the sheep.* Bulletin of the Veterinary Institute in Pulawy, 2007. **51**(1): p. 93-96.
58. Green, M.A., L.E. Bilston, and R. Sinkus, *In vivo brain viscoelastic properties measured by magnetic resonance elastography.* Nmr in Biomedicine, 2008. **21**(7): p. 755-764.
59. Roitt, I.B., J. Male, D., *Immunology*. 2001, Edinburch: Mosby.
60. Subbaroyan, J.M., D.C.;Kipke, D.R., *A finite-element model of the mechanical effects of implantable microelectrodes in the cerebral cortex.* Journal of Neural Engineering, 2005. **2**(4): p. 10.
61. Musallam, S., et al., *A floating metal microelectrode array for chronic implantation.* Journal of Neuroscience Methods, 2007. **160**(1): p. 122-127.

CHAPTER 6

SUMMARY AND FUTURE WORK

6.1 Summary

The electrodes described in this work have made the following contributions to the fields of microfabrication and neural interfacing:

1) simple, rapid fabrication process for microcable electrodes
2) low-modulus electrodes for a number of potential electrophysiological applications
3) insertion mechanism for inserting microcables as shank-style cortical electrodes.

The fabrication of polymer-based electrodes often relies on plasma-based etching which requires optimization and is time consuming. Plasma etching and, another alternative, laser ablation are also high energy processes and require specialized equipment. The use of spin casting in a multilayer process uses common photolithography equipment and techniques. It is also low-energy, so that is does not degrade the PDMS or the thin gold film. SCμM is versatile in that is can be applied to different geometries. In this work, straight and sinusoidal microcables, recording sites, and a net-like-substrate have been fabricated using SCμM.

The microcable electrodes were fabricated from PDMS and thin film gold to make them both compliant and tolerant of stretch-based deformation. The PDMS had a measured tensile modulus of approximately 700 kPa. The addition of the gold film increased the effective composite modulus of the microcable electrode approximately 2.5

fold, to 1.8 MPa. The resulting bending stiffness is an order of magnitude lower than the estimated value for polyimide electrodes and two orders of magnitude lower than the estimated value for commercially available silicon electrodes. The compliance and small footprint lends the microcable electrodes to applications that are limited by either stiffer electrodes or larger-foot print sheet-style electrode arrays. The potential applications addressed in this work include relatively small features such as the peripheral nerve, that the microcable can be wrapped around. Compliant electrodes may be particularly useful in peripheral nerve prostheses for sensory and motor communication. Preliminary attempts to create an electrode interface have been described, but have been limited in their success, possibly by what appears to be tissue damage and scar-formation at the interface site. The implementation of an electrode with a tensile modulus closer to peripheral nerve might prove more successful.

The small foot-print of the microcables also means that they will conform to irregular surface more easily than a contiguous sheet-like array. The capacity to conform to irregular could be applied to cortical surface recording [1, 2], cardiac applications [3], or to prosthetics for smooth muscle to modulate bladder function [4, 5]. Electrically-active skins for prosthetic applications are another potential use for the microcable arrays [6, 7]. The electrodes can be made in a breathable sheet suitable for skin contact and could be applied either as strain sensors or surface electrodes.

The second potential electrophysiological application addressed in this work is cortical shank-style electrodes. An insertion mechanism was developed and tested for biocompatibility as measured by inflammation at the implant site. The inflammation was measured by two metrics: traditional immunohistological staining and MR imaging. The

immunohistology showed mild inflammation. The MR imaging showed edema at the implant sites, suggesting that the tissue was disrupted by the electrodes. The pattern of the edema was different for the fibrin-coated microcables and the silicon electrodes. The fibrin-coated microcables had a spatially broader, region around the site, while the silicon electrodes had a smaller T2 signal immediately at the implant site. The difference in size between the two signals suggests that the microcables' inflammatory influence may have been the fibrinolysis. The silicon electrodes small high intensity signal was localized very closely around the implant site and based on the findings from previous studies in the literature, was likely due to the mechanical mismatch between the electrodes and tissue.

6.2 Future Directions

The microcable electrodes could be optimized by the addressing some durability and packaging issues that were beyond the scope of this work. The stretch tolerance of the microelectrodes was characterized and it was determined that the devices were conductive up to 6% strain. Other similar devices in the literature have been described as conductive at over 30% strain [8]. The deposition of the film and the preparation of the PDMS substrate were not optimized. Additionally, the effect of the initial strain rate was not tested, although the strain rate for the high-strain tolerance devices is disconcertingly slow, suggesting there is a reason for its implementation. The film was deposited at a moderate rate using thermal evaporation. The deposition rate could be expected to modulate the grain size and crystallinity, which impacts the thin film's mechanical properties [9]. The use of a higher energy deposition mechanism, such as E-beam evaporation might also improve the strain tolerance of the film by increasing the tensile

modulus of the substrate at the surface. Increasing the modulus of the polymer substrate has also been correlated with improving the strain-tolerance of the metal film [10]. Other measures include introducing a Soxhlet extraction to remove unpolymerized oligomers from the substrate and optimizing the energy of the oxygen plasma pre-treatement [11].

The packaging of the elastomer-based microcables was only minimally addressed. The yield of the stretched, packaged arrays was not studied because the packaging was felt to be a contributor to the reliability of the devices. The electrical connection was made with aluminum-particulate embedded RTV silicone. The material was conductive and somewhat pliable, unlike the alternative conductive epoxies; however the mechanical mismatch between the device and the RTV silicone could be problematic. Effective packaging requires the connection site to be mechanically isolated in a slim-profile housing. The simple connections using the conductive RTV silicone were adequate for the testing in this thesis, but for many potential applications, a more durable housing would be desirable.

The packaging is also a prerequisite for implementation of the microcables as chronic electrodes. The use of compliant electrodes likely stands to help realize the promise in chronic, neuroprosthetic interfaces [12]. Current efforts are hampered by the damage the electrodes do to the tissue and limit the effectiveness of electrode to tissue communication [13, 14]. Although regenerative medicine [15-18] and non-invasive therapies [19-21] will address some of the function for which electrodes are currently being developed, electrodes have the advantage of being used as a direct connection to communicate with electrically functional tissue in a spatially targeted manner.

6.3 Citations

1. Myllymaa, S., et al., *Fabrication and testing of polyimide-based microelectrode arrays for cortical mapping of evoked potentials.* Biosensors & Bioelectronics, 2009. **24**(10): p. 3067-3072.
2. Yeager, J.D., et al., *Characterization of flexible ECoG electrode arrays for chronic recording in awake rats.* Journal of Neuroscience Methods, 2008. **173**(2): p. 279-285.
3. Nielsen, T.D., et al., *Epicardial mapping of ventricular fibrillation over the posterior descending artery and left posterior papillary muscle of the swine heart.* Journal of Interventional Cardiac Electrophysiology, 2009. **24**(1): p. 11-17.
4. Gaunt, R.A. and A. Prochazka, *Transcutaneously Coupled, High-Frequency Electrical Stimulation of the Pudendal Nerve Blocks External Urethral Sphincter Contractions.* Neurorehabilitation and Neural Repair, 2009. **23**(6): p. 615-626.
5. Matsushita, M., et al., *Evoked magnetic fields as a tool to optimize therapeutic electrical stimulation of the sacral surface.* Journal of Clinical Neuroscience, 2009. **16**(10): p. 1330-1333.
6. Cotton, D.P.J., I.M. Graz, and S.P. Lacour, *A Multifunctional Capacitive Sensor for Stretchable Electronic Skins.* Ieee Sensors Journal, 2009. **9**(12): p. 2008-2009.
7. Dorey, E., *Electronic skin gives robots a human touch.* Chemistry & Industry, 2005(17): p. 10-10.
8. Graz, I.M., D.P.J. Cotton, and S.P. Lacour, *Extended cyclic uniaxial loading of stretchable gold thin-films on elastomeric substrates.* Applied Physics Letters, 2009. **94**(7).
9. Van Swygenhoven, H. and J.R. Weertman, *Deformation in nanocrystalline metals.* Materials Today, 2006. **9**(5): p. 24-31.
10. Li, T. and Z. Suo, *Deformability of thin metal films on elastomer substrates.* International Journal of Solids and Structures, 2006. **43**(7-8): p. 2351-2363.
11. Befahy, S., et al., *Stretchable gold tracks on flat polydimethylsiloxane (PDMS) rubber substrate.* Journal of Adhesion, 2008. **84**(3): p. 231-239.
12. Micera, S., et al., *On the Use of Longitudinal Intrafascicular Peripheral Interfaces for the Control of Cybernetic Hand Prostheses in Amputees.* Ieee Transactions on Neural Systems and Rehabilitation Engineering, 2008. **16**(5): p. 453-472.
13. Ceballos, D., et al., *Morphologic and functional evaluation of peripheral nerve fibers regenerated through polyimide sieve electrodes over long-term implantation.* Journal of Biomedical Materials Research, 2002. **60**(4): p. 517-528.
14. Lago, N., et al., *Long term assessment of axonal regeneration through polyimide regenerative electrodes to interface the peripheral nerve.* Biomaterials, 2005. **26**(14): p. 2021-2031.
15. Bliss, T.M., R.H. Andres, and G.K. Steinberg, *Optimizing the success of cell transplantation therapy for stroke.* Neurobiology of Disease. **37**(2): p. 275-283.
16. Mukhatyar, V., et al., *Tissue Engineering Strategies Designed to Realize the Endogenous Regenerative Potential of Peripheral Nerves.* Advanced Materials, 2009. **21**(46): p. 4670-4679.

17. Orlacchio, A., G. Bernardi, and S. Martino, *Stem Cells: An Overview of the Current Status of Therapies for Central and Peripheral Nervous System Diseases.* Current Medicinal Chemistry. **17**(7): p. 595-608.
18. Salewski, R.P.F., E. Eftekharpour, and M.G. Fehlings, *Are Induced Pluripotent Stem Cells the Future of Cell-Based Regenerative Therapies for Spinal Cord Injury?* Journal of Cellular Physiology. **222**(3): p. 515-521.
19. Cogiamanian, F., et al., *Non-invasive brain stimulation for the management of arterial hypertension.* Medical Hypotheses. **74**(2): p. 332-336.
20. Bretlau, L.G., et al., *Repetitive transcranial magnetic stimulation (rTMS) in combination with escitalopram in patients with treatment-resistant major depression. A double-blind, randomised, sham-controlled trial.* Pharmacopsychiatry, 2008. **41**(2): p. 41-47.
21. Antal, A., et al., *Excitability changes induced in the human primary visual cortex by transcranial direct current stimulation: Direct electrophysiological evidence.* Investigative Ophthalmology & Visual Science, 2004. **45**(2): p. 702-707.